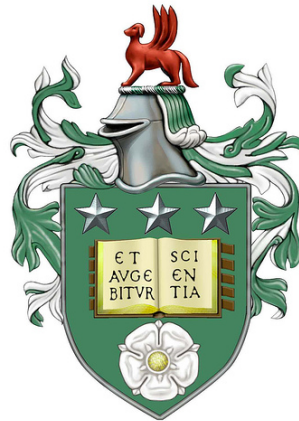# Use of Chirps in Medical Ultrasound Imaging

Sevan Harput

Ultrasound Group
School of Electronic and Electrical Engineering

University of Leeds

Submitted in accordance with the requirements for the degree of

Doctor of Philosophy

December 2012

The candidate confirms that the work submitted is his own, except where work which has formed part of jointly authored publications has been included. The contribution of the candidate and the other authors to this work has been explicitly indicated below. The candidate confirms that appropriate credit has been given within the thesis where reference has been made to the work of others.

Chapter 4 contains materials from Harput *et al.* (2009, 2011b).

Chapter 5 contains materials from Harput *et al.* (2011a).

Chapter 6 contains materials from Arif *et al.* (2011).

Chapter 7 contains materials from Arif *et al.* (2010a).

Chapter 9 contains materials from Harput *et al.* (2012).

This thesis is dedicated to Meline Harput and Dr. Yekvart Harput.

Acknowledgements

I should first thank my PhD. supervisors Dr. Steven Freear and Prof. Stephen Evans for their help during my PhD. and especially for Steve for his generous support and guidance throughout this research.

I want to thank my officemates and colleagues Dr. David M. J. Cowell and Dr. James R. McLaughlan. I also want to thank my colleagues Dr. Paschalis Sofotasios, Dr. Muhammad Arif, Benjamin Raiton, and Peter R. Smith. Without their valuable support, contributions, and company, my PhD. would not have been as productive.

I thank my girlfriends Eva Ryndova and my friend Theodoros Karamanos for their support and help while going through the stressful times of my PhD.

I thank my friends Dr. Tamer Ovutmen and Arda Kuzu for their indirect stimulating inputs on this work.

For the work presented in chapter 4 and chapter 5, I would like to thank Dr. Tony Evans, Dr, Nigel Bubb, Prof. Richard M. Hall, Khalid Sindi, and Ondrej Holub of University of Leeds for their valuable support during this work. The use of human teeth for this study was approved by the Leeds Dental Institute Skeletal Tissues Bank which is in turn approved by the National Health Service Research Ethics Committee (UK) (ref: 07H130693), according to the Human Tissues Act 2004 (UK).

For the work presented in chapter 6 and chapter 7, I would like to give special thanks to Dr. Muhammad Arif for his valuable discussions and substantial contributions.

I want to thank the former head of school and current dean of postgraduate research studies Prof. Paul Harrison for starting the "Graduate Teaching Assistantship" scheme.

Abstract

A "chirp" is a frequency modulated signal widely used in ultrasound imaging to increase the signal-to-noise ratio and penetration depth. In medical ultrasound imaging, resolution and penetration are two major criteria that are inversely proportional. Because of this inverse relation, short duration pulses cannot achieve a high resolution with good penetration. The reasons for this trade-off are the decrease in signal energy due to shorter pulse duration and the attenuation in tissue, which increases with the excitation frequency. The chirp coded excitation however can increase the total transmitted energy using longer pulse durations, while the resolution can be recovered by decoding on receive. Therefore, chirp signals offer potential advantages over single carrier short duration pulses for medical imaging.

This work addresses the possible problems encountered in medical ultrasound imaging with chirps and offers new solutions to these problems in terms of signal processing. These proposed solutions are then applied to three major categories of medical ultrasound imaging; hard-tissue ultrasound imaging, soft-tissue ultrasound imaging and contrast-enhanced ultrasound imaging.

The application of coded excitation in medical ultrasound imaging is the main motivation behind this work. Therefore, the concepts of frequency modulation and matched filtering are introduced first, and ultrasound specific problems for pulse compression of chirps are discussed. Examples are given on specific applications and circumstances, where the performance of the traditional pulse compression techniques drops significantly.

Alternate methods of pulse compression and filtering of frequency modulated chirps using the Fractional Fourier transform (FrFT) and the Fan Chirp transform (FChT) are presented. Rather than restricting the chirp

analysis in the time or frequency domain; these proposed methods transform the signal of interest into a new domain, which is more suitable to analyse frequency modulated chirps.

Contents

I Hard-Tissue Ultrasound Imaging

4 Ultrasound Dental Imaging using Chirp Coded Excitation

5 Detection of Restoration Faults under Fillings in Human Tooth

List of Figures

List of Tables

Abbreviations

CTR	contrast-to-tissue ratio
FBW	fractional bandwidth
FChT	the Fan Chirp transform
FFT	the fast Fourier transform
FrFT	the Fractional Fourier transform
FT	the Fourier transform
iFChT	the inverse Fan Chirp transform
LCT	the Linear Canonical transform
LFM	linear frequency modulation
MB	microbubble
MF	matched filter
MI	mechanical index
SHMF	second harmonic matched filter
SNR	signal-to-noise ratio
TBP	time bandwidth product
TMM	tissue mimicking material
UARP	ultrasound array research platform
UCA	ultrasound contrast agents

List of Symbols

$A(t)$	amplitude modulation function
B	sweeping bandwidth of the signal
$B(f_1, f_2)$	bispectrum
$\mathcal{B}_n$	harmonic amplitude (n-th harmonic)
$C_M(x, y)$	the Linear Canonical transform kernel
$K_\alpha(x, y)$	the Fractional Fourier transform kernel
$\mathcal{M}$	matrix representing the LCT parameters
M	number of captured signals
N	length of the discrete signal, number of samples
$P(f)$	power spectral density
$R_{ss}(\tau)$	autocorrelation function
$S(f, \sigma)$	the Fan Chirp transform of the signal $s(t)$
$S(y)$	transformation of the signal $s(t)$ (generic)
$S_\alpha(y)$	the Fractional Fourier transform of the signal $s(t)$
$S(\omega), S(f)$	frequency domain signal, the Fourier transform of the signal $s(t)$
$S^*(f)$	complex conjugate of the frequency domain signal
T	duration of the signal
Z	acoustic impedance
$b(f_1, f_2)$	bicoherence index
c_r	r-th cumulant
c_0	speed of sound
f	frequency
f_c	centre frequency
$f_i(t)$	instantaneous frequency
f_s	sampling frequency

$f_{-3\mathbf{dB}}$	the half-power width of the frequency domain signal
$f_{-60\mathbf{dB}}$	the -60 dB width of the frequency domain signal
$h(t)$	impulse response
m_r	r-th moment
n_{win}	the ratio between the window width
$r(t)$	received echo signal
$s[n]$	discrete signal
$s(t)$	time domain signal
t	time
t_d	time delay
z	propagation distance
Γ	reflection coefficient
α	the FrFT transform order
α_{opt}	the optimum FrFT transform order
β	attenuation coefficient
η_α	offset between the FrFT axis and the time axis
μ_α	scaling factor between the FrFT axis and the time axis
σ	chirp rate ($\sigma = B/T$)
$\tau_{-3\mathbf{dB}}$	the half-power width of the time domain signal
ϕ	the FrFT rotation angle
$\phi(t)$	phase function of the chirp
$\varphi_\sigma(t)$	time warping function or phase function of the FChT kernel
ω	radial frequency

Chapter 1

Introduction

The first attempts to use ultrasound for medical diagnosis date back to 1940s (Dussik *et al.*, 1947). However, the diagnostic medical ultrasound imaging started to gain popularity in 1970s, where the use of real-time scanners with hand-held transducers and a coupling oil was reported by Griffith & Henry (1974) and McDicken *et al.* (1974). The grey scale images acquired by those systems were usually referred to as B-mode images or B-scans, where the amplitude of received echoes were mapped to the ultrasonic properties and the time delays were mapped to the locations of the reflectors or the scatterers. These images were formed line by line with the pulse-echo method, which is based on the measurement of the elapsed time between the transmission of a short pulse and the reception of the echo.

The axial resolution[1] of these pulse-echo imaging systems were determined by the duration of the ultrasonic pulse. Better resolution can be achieved by decreasing the pulse length, which is limited by the ultrasonic frequency. The penetration depth is also a function of the excitation frequency, since the attenuation of ultrasound in the tissue is frequency-dependant. Therefore the resolution improves as the excitation frequency is increased, but this increase results in reduced penetration depth.

Frequency modulated excitation, which is usually referred to as a "chirp", can be used to overcome these limitations introduced by the classical pulse-echo imaging technique. In medical imaging with ultrasound, chirp excitation is used to increase the penetration depth by increasing the total transmitted energy using longer pulse durations, while the resolution is controlled by the signal bandwidth.

---

[1]The resolution in the direction of propagation. Also known as resolution in depth.

1.1   Literature Review

Coded signals are common in all types of ultrasound applications including medical imaging, sonar and non-destructive evaluation (Kino, 1987; Szabo, 2004). The first application of coded excitation in medical ultrasound systems was by Takeuchi (1979) using Golay codes. O'Donnell (1992) used chirp coded excitation for the first time for B-mode imaging on a real-time phased-array system to improve the penetration and SNR. He also calculated a theoretical $15 - 20$ dB SNR improvement for medical ultrasound applications. A simulation study by Rao (1994) highlighted the advantages of coded excitation and also investigated the limitations of pulse compression technique for medical ultrasound imaging. Passmann & Ermert (1996) showed the superiority of chirp excitation for high frequency broadband applications, where the major concern was the strong attenuation. They designed a 100 MHz dermatologic and ophthalmologic diagnostics ultrasound imaging system and used chirp excitation to improve the SNR. Misaridis *et al.* (2000) presented the potential of coded excitation in medical ultrasound imaging by using a new pre-distorted chirp signal. The advantages of chirps became clearer, after Pedersen *et al.* (2003) performed the clinical evaluation of chirp-coded excitation by comparing it with conventional pulsed excitation using a modified commercial ultrasound scanner. Chiao & Hao (2005) reviewed various coded excitation techniques by considering the effects of frequency-dependent attenuation, dynamic focusing, and nonlinear propagation for diagnostic ultrasound. During the same year, Misaridis & Jensen (2005a,b,c) published the most extensive study on coded excitation in medical ultrasound. This work was based on simulations, theoretical analysis and experimental measurements for waveform design, signal modulation, match filters, mismatched filters, and pulse compression under frequency and depth dependant attenuation specifically for medical imaging applications.

After these studies, chirps have found applications in many types of medical ultrasound imaging including classical B-mode imaging of soft tissue, tissue harmonic imaging, synthetic aperture imaging, intravascular imaging, bone imaging, contrast imaging, contrast harmonic imaging, subharmonic imaging, etc.

There are several examples on soft-tissue imaging. Jensen *et al.* (2006) used a chirp signal to overcome one of the biggest problems in synthetic aperture ultrasound imaging; the limited signal energy and penetration depth due to the use of single element

and un-focused waves. Arshadi *et al.* (2007) tried to improve the spatial resolution in ultrasound imaging by applying coded excitation methods for ultrasound harmonic imaging. Mamou *et al.* (2009) preferred chirp excitation for high frequency ophthalmologic and small-animal imaging to compensate for the attenuation. Recently, Maresca *et al.* (2012) utilized coded chirp excitation for intravascular ultrasound (IVUS) imaging because of the high attenuation observed at high frequencies used in IVUS.

Not as many examples can be found for hard-tissue imaging but chirps are used for imaging inside the bone with pulse compression techniques (Iriea *et al.*, 2003).

The application of chirp excitation in contrast imaging has attracted the attention of many researchers. Sun *et al.* (2006) performed the simultaneous optical-acoustical observation of contrast agent response to chirp insonation with a high-speed digital streak camera at 100 million frames per second. After getting promising results, they used chirped excitation for contrast imaging (Sun *et al.*, 2007). Borsboom *et al.* (2005) proposed a harmonic chirp imaging method for ultrasound contrast agents, mainly focusing on second harmonic component. Zhang *et al.* (2007) however used chirps for subharmonic imaging and showed that subharmonic emission from encapsulated microbubbles can be enhanced by using a chirp excitation technique.

Several new techniques have been proposed on pulse compression with chirp excitation and specific problems associated with ultrasound contrast imaging. A new nonlinear compression technique was proposed by Borsboom *et al.* (2003) for ultrasound contrast imaging that selectively compresses the second harmonic component to improve contrast-to-tissue ratio (CTR) and SNR. Chetty *et al.* (2006) performed simulations of the microbubble response to chirp multi-pulse sequences with pulse inversion and power modulation. Their results showed that the extra energy carried by chirps results in an increased SNR for contrast imaging. Novell *et al.* (2009) combined the time reversal technique with chirp excitation to improve CTR and SNR by sacrificing the axial resolution for contrast imaging. Shen & Chiu (2009) designed a dual-frequency chirp excitation waveform for contrast harmonic imaging to suppress the tissue harmonics.

Recent studies have focused in more detail on sidelobe reduction and issues associated with non-linear propagation in tissue. Song *et al.* (2010) applied coded excitation for ultrasound tissue harmonic imaging for sidelobe reduction. They observed that the coded excitation with pulse inversion gives better suppression of peak sidelobe levels

for tissue harmonic imaging. They later used quadratic nonlinear chirps to further improve their results on tissue harmonic imaging with coded excitation (Song *et al.*, 2011). Park *et al.* (2013) combined chirp coded tissue harmonic and fundamental ultrasound imaging for intravascular ultrasound to reduce range sidelobe levels.

Even though coded excitation techniques have been applied to ultrasound imaging for over three decades, researchers could not overcome the main limitations of using chirps in medical ultrasound imaging. Image resolution and dynamic range have always been an issue for coded excitation systems. The axial resolution is usually much worse than the theoretical prospect because of the limited bandwidth of the transducer. Also, the transfer function of the transducer is usually asymmetrical; therefore the range sidelobes in the compressed signal appear in an unexpected manner. Most of the recent studies still focus on improving image quality by suppressing compression sidelobes, where time-bandwidth limitations of ultrasound systems and frequency-dependent attenuation in tissue result in sub-optimal compression.

1.2 Motivation

The identification, evaluation, and processing of frequency modulated chirps are still challenging for classical signal analysis. Several methods were proposed to overcome these challenges (Cohen, 1989; Daubechies, 1990; Jaynes, 1996; Mann & Haykin, 1995). Most of the solutions for these specific chirp related problems have surprisingly come from a broader field; the time-frequency analysis. Therefore, this study focuses on the application of these alternative solutions to the ultrasound related problems on pulse compression of chirps. Especially the chirp-based transforms are given precedence, since they provide a broader picture of the time-frequency content of the chirp signal.

A precise and fine representation of signals in the time-frequency plane is of great importance in many fields such as radar, sonar, speech processing, optics, seismology, oceanography, etc. Time frequency representation of signals or data is usually achieved by spectrograms, which is a time varying spectral estimation of the signal power density. Conventional Fourier-type techniques and new spectral estimation methods will be discussed in this section including their advantages and disadvantages for processing chirp signals. Although these spectral estimation methods were not developed for medical ultrasound imaging, their main purpose is similar to imaging applications; to

improve the compression and representation of non-stationary signals or chirps in the time-frequency plane.

The *conventional* spectrum analysis[1] is based on the Fourier transform and a lag window. The Fourier transform has a sinusoidal kernel[2] that is suitable for analysing monochromatic signals. Chirps however have a quadratic phase function[3] whose frequency content changes by time, therefore the Fourier transform is not ideal for analysing the chirps (Jaynes, 1996). For this reason, the first fundamental shortcoming of the conventional approach is that chirp signals are analysed by an algorithm appropriate to detect single-frequency stationary signals.

The second shortcoming of this method is that a Blackman-Tukey spectrum uses a fixed-length lag window to cut the noise contribution from long time domain signals, where the total noise energy is small for the shorter durations. When the data set is tapered by a window, the spectrum becomes smooth and the sidelobes disappear. By removing those unwanted sidelobes, the estimated power spectrum will have a more *pleasing appearance* (Jaynes, 1996). The final representation of the time-frequency plane will be equivalent to the convolution of the spectrogram and the Fourier transform of the lag window, thus reducing the resolution and making it impossible to represent sharp spectral lines correctly.

Instead of using a conventional Fourier based spectral analysis; new algorithms were proposed to extract more information from the data and to make better use of *a priori* information. The most common example is the Wigner-Ville spectral analysis (Martin & Flandrin, 1985). Wigner-Ville distribution achieves better resolutions than Blackman-Tukey spectrum for a single chirp signal. Choi & Williams (1989) however, pointed out a problem with these time-frequency distributions which are members of the generalized Cohen's class; multicomponent signal artefacts. The artefacts appear between multiple signals at Wigner distribution as an interference between the cross-terms (Cohen, 1989). Other Cohen class distributions such as the Smoothed Pseudo Wigner-Ville distribution can be used to attenuate this interference at the expense of decreased resolution due to the smoothing.

---

[1] The Blackman-Tukey spectrum analysis is referred to as conventional spectrum analysis. Blackman & Tukey (1958) have introduced the usage of windows into spectral analysis and it is still the one of the most common methods of estimating the spectrum of a signal.

[2] The Fourier transform is given in Eq. (3.1).

[3] The phase function of a linear frequency modulated chirp is given in Eq. (2.2).

These interfering cross-terms are negligible for multiple chirps in the Choi-Williams distribution, since they used a quadratic exponential transformation kernel and a running window (Choi & Williams, 1989). However the window parameters must be chosen carefully, since the weighting of the window controls the amplitude of the cross term by spreading it out in a selective manner. After Choi & Williams (1989) presented the importance of the transformation kernel, several more time-frequency techniques with different properties have been proposed specifically for chirp analysis. The most common ones are the Wavelet transform, the Chirplet transform, the Fractional Fourier transform, and the Fan Chirp transform.

The Wavelet transform uses a kernel consisting of wavelets having similar time-frequency properties to the analysed signal (Daubechies, 1990). This technique can achieve multiple resolutions on different parts of the time-frequency plane, however it has serious limitations for fast chirp rates when applied to non-stationary signals (Képesi & Weruaga, 2006).

The Chirplet transform (Mann & Haykin, 1995) and the Fractional Fourier transform (McBride & Kerr, 1987) can achieve optimum compression and resolution for a single linear frequency modulated chirp thanks to their chirp-based transformation kernels. Both transformations can obtain a non-Cartesian tiling by rotating or shearing the time-frequency plane that matches with the chirp rate of interest (Ozaktas *et al.*, 1994). In the presence of harmonics however, these transformations cannot achieve optimum compression for all the harmonically related chirps (Cancela *et al.*, 2010).

In the case of harmonics, the Fan Chirp transform offers optimal resolution simultaneously for all harmonic chirps by warping the time-frequency plane in a "fan" geometry (Weruaga & Képesi, 2007). But interpolation may be necessary after warping the time-frequency plane by the Fan Chirp transform, which can result in degraded resolution, aliasing or extra computational load.

1.3 Objectives of this work and the organization of the thesis

The chirp coded excitation has been proven to be useful in medical ultrasound imaging. Nevertheless, the design of an efficient coded excitation system is not trivial. Designing the excitation signal and the pulse compression pair are equally important for this

process. The matched filter is usually preferred for the pulse compression to maximize the SNR. The matched filter[1] response can also be further improved by compensating for the depth-dependant attenuation, frequency-dependant attenuation, and transducer response. However, it is impossible to design a perfect matched filter for medical ultrasound imaging, because of the nonlinear behaviour of tissue[2]. Human tissue also generates harmonics that reduces the performance of the matched filter for soft-tissue imaging and ultrasound harmonic imaging. For contrast-enhanced ultrasound imaging microbubbles alters the phase, the amplitude, and the frequency content of the scattered echoes that makes pulse compression even more challenging. Therefore, alternative methods are proposed for the compression of chirps and these techniques are applied in different fields of medical ultrasound imaging.

The concepts of frequency modulation and matched filtering are described in chapter 2. Chapter 3 explains the Linear Canonical transform and two of its special cases used in this work; the Fractional Fourier transform (FrFT) and the Fan Chirp transform (FChT). The following chapters present the applications of these techniques on different problems encountered in chirp coded excitation for three major categories of medical ultrasound imaging; hard-tissue ultrasound imaging, soft-tissue ultrasound imaging and contrast-enhanced ultrasound imaging.

In part I, the chirp coded excitation is applied to dental imaging and characterisation of tooth layers. A method of pulse compression and filtering based on the FrFT is used to improve the resolution and SNR. In chapter 4, an imaging technique to measure the thickness of the enamel layer in human teeth is proposed. The FrFT is used for pulse compression of overlapping chirps due to reverberations inside the tooth layers. In chapter 5, detection of the restoration faults under the fillings in a human tooth is performed with ultrasound. For this application, the FrFT is used for filtering rather than pulse compression. The results of this study were published in the following papers:

- Sevan Harput, D.M.J. Cowell, J.A. Evans, N. Bubb and S. Freear, "Tooth Characterization using Ultrasound with Fractional Fourier Transform," *IEEE Int. Ultrasonics Symposium (IUS)*, 2009, pp. 1906 - 1909.

---

[1]In this context, it is also called as a mismatched filter.

[2]Tissue is inhomogeneous and anisotropic, for this reason variations in the density, compressibility, attenuation, and speed of sound is usually observed in medical imaging.

- Sevan Harput, J.A. Evans, N. Bubb and S. Freear, "Detection of Restoration Faults under Fillings in Human Tooth using Ultrasound," *IEEE Int. Ultrasonics Symposium (IUS)*, 2011, pp. 1443 - 1446.

- Sevan Harput, J.A. Evans, N. Bubb and S. Freear, "Diagnostic Ultrasound Tooth Imaging using Fractional Fourier Transform," *IEEE Transactions on Ultrasonics, Ferroelectrics, and Frequency Control*, vol. 58, no. 10, pp. 2096 - 2106, 2011.

The idea of using ultrasound to measure the enamel thickness and to detect the restoration faults was conceived as result of a group discussion with D.M.J. Cowell, J.A. Evans, N. Bubb and S. Freear. All authors contributed on these three publications by giving their insights on possible applications of ultrasound to dentistry. J.A. Evans and N. Bubb assisted on supplying a real human teeth and preparing it for ultrasound measurements. However, the experimental setup, ultrasound measurements and the signal processing were performed by the first author. All three publications were written and edited by the first author after considering the comments and corrections of co-authors.

In part II, the problems encountered on pulse compression of chirp signals for ultrasound soft tissue imaging is investigated. Chapter 6 presents a common problem in second harmonic imaging; spectral overlapping. The FrFT is used for the extraction of the overlapped second harmonic and fundamental components in tissue harmonic imaging. In chapter 7, a similar problem is addressed for superharmonic imaging. The FChT is found to be more suitable for filtering and separating the spectrally overlapped harmonics. The results of these two studies and performance analysis of frequency modulated signals for ultrasound imaging were published and will be submitted as:

- M. Arif, Sevan Harput and S. Freear, "Experimental Investigation of Chirp Coded Excitation in Ultrasound Superharmonic Imaging," *IEEE Int. Ultrasonics Symposium (IUS)*, 2010, pp. 2187 - 2190.

- M. Arif, Sevan Harput, P.R. Smith, D.M.J. Cowell, and S. Freear, "Extraction of an Overlapped Second Harmonic Chirp Component using the Fractional Fourier Transform," *IEEE Int. Ultrasonics Symposium (IUS)*, 2011, pp. 405 - 408.

- Sevan Harput, J. McLaughlan, P.R. Smith, D.M.J. Cowell, S.D. Evans and S. Freear, "Analysis and Applications of the Fan-Chirp Transform to Chirp Excitation for Super Harmonic Imaging," *IEEE Transactions on Ultrasonics, Ferroelectrics, and Frequency Control*, (Manuscript in Preparation).

Using chirp coded excitation for second harmonic and superharmonic imaging was suggested by M. Arif. M. Arif and Sevan Harput contributed proportionally while solving the problems encountered during the experiments, calibrating the instruments, performing the measurements, and processing the data. First two publications were mostly written by the first author. Sevan Harput contributed to the write-up process by correcting and editing the final manuscript.

Part III focuses on contrast-enhanced ultrasound imaging and microbubble behaviour. The nonlinear behaviour of the microbubbles and their effect on pulse compression is described in chapter 8. The pulse compression with the matched filter and filtering using the FrFT and the FChT techniques are compared and analysed for contrast-enhanced ultrasound imaging and contrast-enhanced second harmonic imaging. In chapter 9, a new method is proposed to separate the second harmonic response of tissue and microbubbles using the bispectral analysis. The theoretical background for this work is given in chapter 8 by explaining the nonlinear behaviour of microbubbles. The results of these studies were published in the following papers and will be submitted as:

- Sevan Harput, M. Arif and S. Freear, "Experimental Investigation of the Subharmonic Emission from Microbubbles using Linear and Nonlinear Frequency Modulated Signals," *IEEE Int. Ultrasonics Symposium (IUS)*, 2010, pp. 1724 - 1727.

- Sevan Harput, J. McLaughlan, P.R. Smith, D.M.J. Cowell, S.D. Evans and S. Freear, "Separating the Second Harmonic Response of Tissue and Microbubbles using Bispectral Analysis," *IEEE Int. Ultrasonics Symposium (IUS)*, 2012, pp. 1930 - 1933.

- Sevan Harput, M. Arif, J. McLaughlan, P.R. Smith, D.M.J. Cowell, S.D. Evans and S. Freear, "Evaluation of Frequency Modulated Chirp Excitation for Contrast-

Enhanced Harmonic Imaging," *IEEE Transactions on Ultrasonics, Ferroelectrics, and Frequency Control*, (Manuscript in Preparation).

The first publication was a team effort between all authors, however it was the first author who shaped the idea and carried out most of the work. M. Arif and Sevan Harput contributed proportionally while performing the measurements with contrast agents. The signal processing and the formation of subharmonic images were performed by the first author. For the second publication, the idea of using higher order spectral techniques to analyse ultrasound data was conceived by the first author. The experimental setup, ultrasound measurements and the signal processing for this study were performed by Sevan Harput. Co-authors contributed by preparing contrast agents, calibrating the instruments, supplying technical support while using the UARP and giving feedback during all stages of this study. Both publications were written and edited by the first author and reviewed by co-authors.

The research performed in this work on frequency modulated chirps, medical ultrasound imaging, and microbubble behaviour contributed to other publications that are not presented in this thesis. One patent application was submitted, and one journal paper and six conference papers were published:

- S. Freear, B. Raiton, J.R. McLaughlan, D.M.J. Cowell, P.R. Smith, and Sevan Harput, "Acoustic Tap for Microbubbles," International Patent Application No. PCT/GB2013/050738, 2012.

- Sevan Harput, P.C. Sofotasios and S. Freear, "A Composite Statistical Model for Ultrasound Application," *IEEE Int. Ultrasonics Symposium (IUS)*, 2011, pp. 1387 - 1390.

- Sevan Harput, B. Raiton, J.R. McLaughlan, S.D. Evans and S. Freear, "The Periodicity between the Aggregated Microbubbles by Secondary Radiation Force," *IEEE Int. Ultrasonics Symposium (IUS)*, 2011, pp. 1630 - 1633.

- P.R. Smith, Sevan Harput, D.M.J. Cowell, J. McLaughlan, and S. Freear, "Pre-Distorted Amplitude Modulated (PDAM) Chirps for Transducer Compensation in Harmonic Imaging," *IEEE Int. Ultrasonics Symposium (IUS)*, 2012, pp. 459 - 462.

- G. Leaute, J. McLaughlan, Sevan Harput, D.M.J. Cowell, and S. Freear, "Comsol Modelling of Non-Spherical Microbubble Dynamics Near a Soft Membrane," *IEEE Int. Ultrasonics Symposium (IUS)*, 2012, pp. 2286 - 2289.

- B. Raiton, J.R. McLaughlan, P.R. Smith, D.M.J. Cowell, Sevan Harput and S. Freear, "Counter flow microbubble channeling using acoustic radiation force funnel," *IEEE Int. Ultrasonics Symposium (IUS)*, 2011, pp. 2432 - 2435.

- M. Arif, Sevan Harput and S. Freear, "Performance Evaluation of Nonlinear Frequency Modulated Signals in Ultrasound Harmonic Imaging," *IEEE Int. Ultrasonics Symposium (IUS)*, 2010, pp. 2016 - 2019.

- B. Raiton, J.R. McLaughlan, Sevan Harput, P.R. Smith, D.M.J. Cowell, and S. Freear "The capture of flowing microbubbles with an ultrasonic tap using acoustic radiation force," *Applied Physics Letters* 101, 044102, 2012.

Chapter 2

Coded Excitation and Pulse Compression

Coded excitation was originally introduced in radar (Cook & Bernfeld, 1967; Skolnik, 1981) and was adapted to ultrasound imaging systems within the last three decades (Chiao & Hao, 2005; Misaridis *et al.*, 2000; O'Donnell, 1992). In medical imaging with ultrasound, coded excitation is used to increase the SNR and penetration by increasing the total transmitted energy while maintaining the same peak intensity level using a longer pulse duration (O'Donnell, 1992).

In medical ultrasound imaging, pulsed excitation is usually utilized to enhance the image quality by improving the axial resolution (Misaridis & Jensen, 2005a). By transmitting short pulses, high resolution can be achieved at the expense of poor penetration. In order to improve the penetration, the energy of the excitation signal must be increased by increasing either the duration or amplitude of the pulse. Extending the pulse duration will decrease the axial resolution, which is a trade-off between resolution and penetration for pulsed excitation. Increasing the pulse amplitude or peak pressure level can potentially cause bio-effects. The food and drug administration FDA (30-09-1997) has set a limitation on mechanical index[1] (MI), where large values of MI can cause inertial cavitation and therefore tissue damage (Szabo, 2004). Therefore, the main challenge for the pulsed excitation is to achieve a good penetration without exceeding

---

[1]$MI = P_-/\sqrt{f}$, where P_- is the peak value of the attenuated rarefactional pressure in MPa and f is ultrasonic working frequency in MHz (Abbott, 1999). Note that MI is always normalised by 1 MPa·MHz$^{-1/2}$ and dimensionless.

the safety limits.

For hard tissue, the speed of sound is much higher than in any soft tissue, which effectively increases the wavelength at a specific frequency. This may not be an issue for bone imaging, where the features are coarse; however it introduces a great challenge for dental imaging. Two of the greatest problems encountered by researchers who have applied medical ultrasound imaging techniques to dentistry are the dimensions of teeth and the varying speed of sound in the different tooth layers (Barber *et al.*, 1969; Ghorayeb *et al.*, 2008). These two facts inevitably suggest the use of high frequency excitation and short pulse duration to achieve better resolution. However, the ultrasonic attenuation in dental tissue makes signal detection more difficult for high frequency pulses, since the attenuation values are more than 10 dB/mm for dental tissue at high frequencies (> 20 MHz) (Kossoff & Sharpe, 1966; Singh *et al.*, 2008). The excitation pressure may be increased to achieve better penetration depth, but this is at the cost of increased intensity levels and the likely generation of harmonic signals. Long duration excitation provides better penetration and improved SNR by increasing the excitation energy without changing the peak pressure level.

In ultrasound contrast imaging, long duration excitation is preferred since it triggers nonlinear microbubble oscillations and induces a stronger response from microbubbles. Coded excitation can also provide the opportunity for real-time *in-vivo* contrast imaging at low MI. In non-destructive contrast imaging, the peak pressure level is limited due to UCA disruption. The destruction threshold of the microbubbles is significantly lower than the maximum allowed MI (Chomas *et al.*, 2002). The low pressure approach works well without destroying the microbubbles, because the response of the microbubbles is still nonlinear at low pressure levels (< MI 0.2). In a similar manner, coded excitation techniques can be used for contrast agent detection in tissue (Sun *et al.*, 2007). Therefore, the main advantages of coded excitation over conventional short pulse excitation are the improvement in SNR and contrast-to-tissue ratio, which leads to better image quality and penetration depth (Borsboom *et al.*, 2005).

Although coded excitation has numerous advantages over pulsed excitation, it is not easy to employ and design a coded signal. A *good* code must be easily detectable at the receiver, which can be accomplished by choosing the appropriate bandwidth for the coded signal according to the application. The decoding stage is performed on the receiver side by applying a pulse compression technique. Bandwidth of the excitation

signal is the key for achieving a substantial compression, where the axial resolution of the coded excitation system becomes comparable to a conventional pulse system. However, if the coded signal and decoding stage is not well designed, the rising sidelobe levels can decrease the image quality (Borsboom *et al.*, 2005).

2.1 Comparison of Frequency and the Phase Modulation for Ultrasound Imaging

In a pulse compression system, the signal coding schemes are based on either frequency modulation or phase modulation. Signals based on phase modulation are binary coded sequences that use sinusoidal bursts of one to several cycles with an alternating phases of 0° and 180°. Takeuchi (1979) investigated the coded excitation method for the first time for medical ultrasound imaging based on Golay sequences. Later on, it has been shown that the most practical codes for ultrasound imaging systems are the Golay sequence, Barker codes and frequency modulated chirps (Chiao & Hao, 2005; Leavens *et al.*, 2007; Misaridis & Jensen, 2005b).

The main differences between radar and medical ultrasound system are the wavelength and time-bandwidth product (TBP) restrictions imposed by the relatively narrowband ultrasound transducers. Long codes can be implemented on radar systems, where achieving a TBP as high as 1000 is possible (Cook & Bernfeld, 1967). In ultrasound, the TBP is usually limited to 80 or 100 (Misaridis & Jensen, 2005b) and the code lengths must be shorter because of the finite transducer bandwidth and hardware limitations. The level of the range sidelobes for the binary coded signals is a function of the TBP. For this reason, the phase coded signals will perform poorly for ultrasound applications due to limitations on both signal duration and bandwidth. The sidelobe levels of the frequency modulated chirps after compression depend on the amplitude modulation or weighting function rather than TBP. However, achieving a reasonably TBP is still a necessity, because it determines the SNR gain after the pulse compression (Chiao & Hao, 2005; Misaridis & Jensen, 2005b).

The sidelobe levels can be significantly improved by employing complementary codes that require multiple transmissions. The sidelobes of the complementary codes have opposite signs after compression and they can be cancelled by addition; however transmitting two reciprocal waves degrades the system frame-rate and may lead to poor

cancellation of range sidelobes under tissue motion. Golay and Barker codes are also more affected by dynamic focusing and motion artefacts than frequency coded signals (Chiao & Hao, 2005).

Implementation of a binary coding scheme in ultrasound contrast imaging is also challenging as the phase of the transmitted signal is not preserved due to the nonlinear scattering from microbubbles (Eckersley *et al.*, 2007; Leavens *et al.*, 2007). A similar challenge exists for harmonic imaging, since the code phase are not maintained in the harmonic domain. In contrast, frequency modulated chirp signals can be employed for the ultrasound harmonic imaging as the chirp signal maintain its phase according to second order distortion model or square law (Arshadi *et al.*, 2007; Kim *et al.*, 2001). Finally, chirps are more robust to the distortion caused by the frequency dependent attenuation as the ultrasound wave propagates through soft tissue (Misaridis & Jensen, 2005b).

2.2 Linear Frequency Modulation (LFM)

In this section, the linear frequency modulated excitation technique will be described and formulated. Its response after pulse compression will be evaluated in the next section by considering sidelobe performance and resolution.

The representation of a linear frequency modulated *real* signal is

$$s(t) = A(t) \cdot \cos(2\pi\phi(t)), \quad -\frac{T}{2} \leq t \leq \frac{T}{2} \tag{2.1}$$

with a phase

$$\phi(t) = \left(f_c + \frac{B}{2T}t \right) t, \tag{2.2}$$

where $A(t)$ is the amplitude modulation function, f_c is the centre frequency, B is the sweeping bandwidth, T is the duration of the signal, $\sigma = B/T$ is the chirp rate, and $f_c - B/2$ is the starting frequency. A sample linear frequency modulated chirp is shown in Figure 2.1 with the waveform parameters given in Table 2.1, where a Hann window is used to design the envelope of the signal $A(t)$.

The *uncertainty principle* dictates that a time-limited signal cannot be also band-limited. A function can only have a finite support either in time domain or the frequency domain, but not in both domains. For this reason, the duration of the signal is defined as T from Eq. (2.1), where more than 99% of the signal's energy is located. The
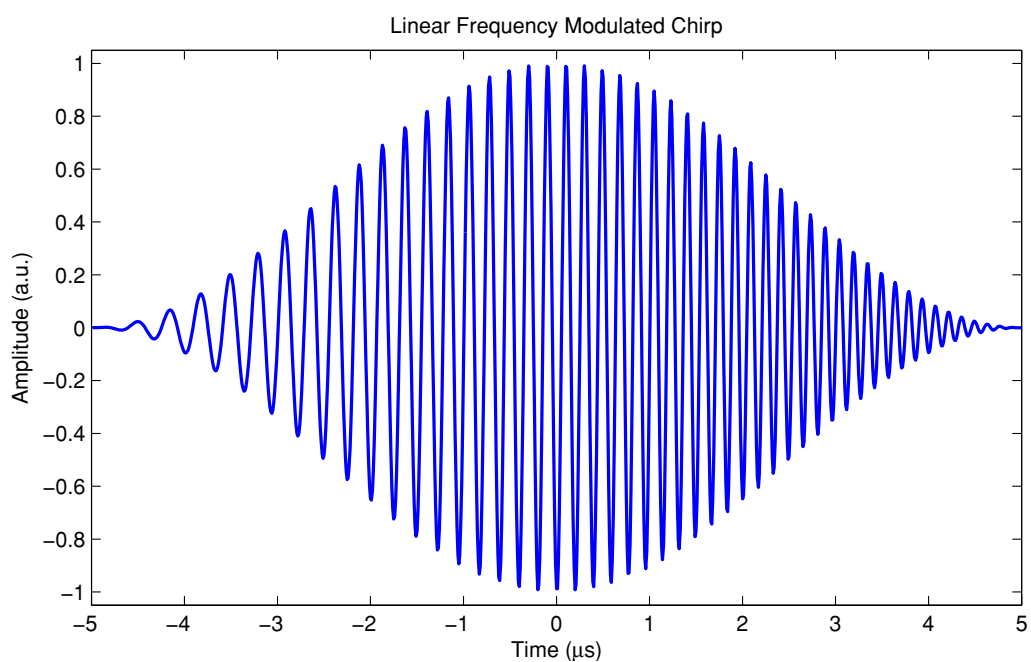
Figure 2.1: Illustration of a linear frequency modulated chirp with a Hann window. The waveform has a centre frequency of 5 MHz, a fractional bandwidth of 100%, and a duration of 10 μs.

bandwidth of the signal, B, is defined as the sweeping bandwidth at -20 dB points in the frequency domain, where 99% of the signal's energy is located.

Table 2.1: Signal parameters

PARAMETER	VALUE
Sampling frequency	100 MHz
Centre frequency	5 MHz
Fractional bandwidth	100%
Duration	10 μs

To differentiate between different types of frequency modulated signals, one must consider the instantaneous frequency of the signal. The instantaneous frequency, $f_i(t)$, of the signal can be found by calculating the derivative of its phase

$$f_i(t) = \phi'(t) = f_c + \frac{B}{T}t. \tag{2.3}$$

The instantaneous frequency of a frequency modulated signal includes all the necessary information about a signal, such that the signals are named after the shape of their instantaneous frequency. Three chirps with different instantaneous frequencies are illustrated in Figure 2.2 for descriptive purposes.

2.2.1 Received Echo

For ultrasound imaging in human tissue, the received echo, $r(t)$, from a plane wave can be expressed in the following form

$$r(t) = \mathcal{R}e\left\{ \sum_{k=1}^{K}\sum_{n=1}^{\infty}\Gamma_k \cdot \underbrace{\mathcal{B}_n \cdot s(t)^n}_{1} \cdot \underbrace{e^{-\beta zf}}_{2} \cdot \underbrace{e^{-j2\pi f(z/c_0)}}_{3} \right\}. \tag{2.4}$$

Γ_k is the reflection coefficient for the k-th reflection due to scatterers in tissue or reflections from different tissue layers. K is the total number of reflections.

According to second order distortion model (Arshadi *et al.*, 2007), the harmonic generation in tissue can be modelled as the summation of all harmonic terms as given in part 1 of Eq. 2.4. $\mathcal{B}_n$ is the amplitude of the harmonic generated due to nonlinear
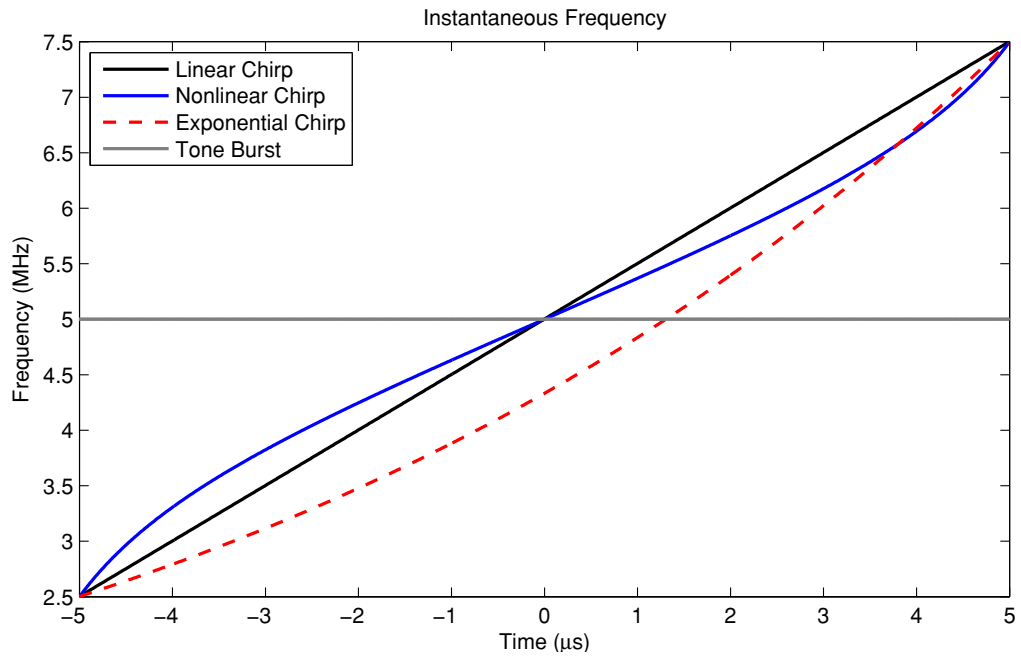
Figure 2.2: Instantaneous frequency functions of tone-burst, linear frequency modulated chirp, nonlinear frequency modulated chirp, and exponential frequency modulated chirp are shown. All waveforms have a duration of 10 μs. The centre frequency of the sinusoidal tone-burst is 5 MHz and its instantaneous frequency is constant. The chirp waveforms have a centre frequency of 5 MHz, a fractional bandwidth of 100%. The frequency of the sinusoidal chirps changes linearly, nonlinearly or exponentially with time therefore the instantaneous frequencies are linear, nonlinear and exponential for the given chirps.

propagation in tissue as explained in appendix B. n is the number of the harmonic that also increases the phase of the signal by a factor of n.

The part 2 of the Eq. 2.4 is due to the depth and frequency dependant attenuation, where β is the attenuation coefficient, z is the total propagation distance, f is the frequency. For human tissue the frequency dependant attenuation is assumed to be linear, *i.e.* attenuation is scaled by $f^{1.0}$. For wideband signals, such as chirps, the attenuation completely alters the shape of the applied window, $A(t)$. This change in the window shape creates problems for pulse compression with matched filters, which will be explained in the next section.

The part 3 of the Eq. 2.4 shows the phase change observed by the signal after propagating the distance of z and c_0 is the speed of sound in human tissue.

2.3 Pulse Compression with a Matched Filter

The main problems encountered in target detection by pulse compression are the straddling loss and the separation between multiple targets. The straddling loss is the loss in SNR because the target is not centred with the transmitted beam. The separation problem is due to the proximity of the targets and the shadowing of weak reflectors by stronger reflectors because of the undesirable sidelobes. Therefore the performance of a pulse compression system can be measured by its detection range, SNR, range resolution, dynamic range, and Doppler resolution[1]. These parameters depend on the waveform design and the pulse compression pair. The excitation waveform determines detection performance and accuracy of measurement. The detection range and SNR can increased by using longer waveforms and high transmit energy. The long duration signals however, reduce the range resolution. The resolution is recovered back by using a matched filter with an appropriate window, which also determines the sidelobe levels and hence the dynamic range.

A matched filter[2] is a linear time-invariant filter that works by correlating a known signal with an unknown signal to detect the presence of the known signal. A matched filter optimizes the probability of the detection by maximizing the SNR in the presence

---

[1]The Doppler resolution was not taken into consideration, because the Doppler effect was not observed in any of the applications presented in the later chapters of this work.

[2]A matched filter is also known as a North filter.

of white Gaussian noise (Misaridis & Jensen, 2005a). Therefore, in this study matched filtering is used for pulse compression of the linear frequency modulated signals.

The ideal filter at the receiver side must be the same as the transmitted signal according to the likelihood criterion. In order to design an optimal receiver, the matched filter's impulse response[1], $h(t)$, must be equal to the time reversal of the transmitted signal with a time shift, t_d. For the real signal $s(t)$, defined in Eq. (2.1), the impulse response of the matched filter is given by:

$$h(t) = s(t_d - t). \tag{2.5}$$

Thus the time-domain output of the pulse compression is the convolution of the input signal with the matched filter, which is the autocorrelation function of the input signal as given in Eq. (2.6).

The match filter has a processing gain or SNR gain, which equals to the time bandwidth product of the excitation signal (Misaridis & Jensen, 2005a). In order to maximise the SNR and the probability of detection, one should increase the signal bandwidth and duration; however the transducer's response and hardware performance will place limitations on both duration and bandwidth. For an ultrasound system; pulse duration is usually adjusted according to power requirements and necessary penetration depth, and the bandwidth is maximised to increase the resolution. The matched filter response has a resolution approximately in the order of $1/B$, so the maximum achievable resolution is limited with the bandwidth of the system.

Unlike a typical frequency domain filter that simply passes all energy within a certain bandwidth, the matched filter detects not only the frequency but also the modulation. The matched filter in effect calculates the probability of the signals presence, compressing the energy contained within the signal into a single pulse. The pulse compression system provides a gain in SNR at the receiver that in turn provides an improvement in measurement; such as an increase in measurement range or through the use of media with higher attenuation, allowing measurements not feasible with pulsed excitation.

---

[1]For a complex signal, matched filter response is the complex conjugate time reversal of the transmitted signal, $h(t) = s^*(t_d - t)$.

2.3.1 Sidelobe suppression using windowing functions

If the noise of the system is negligible and the matched filter does not have a translation in time ($t_d = 0$), the input signal of the matched filter will be the same as its transfer function. Therefore, the response of the matched filter will be equal to the autocorrelation of the transmitted signal as

$$R_{ss}(\tau) = \int_{-\infty}^{+\infty} s(t)s(t-\tau)dt \, , \tag{2.6}$$

or in discrete form as

$$R_{ss}[k] = \frac{1}{N}\sum_{n=1}^{N} s[n]\, s[n-k], \tag{2.7}$$

where N is the total number of samples, and $s[n]$ is the real valued discrete signal.

The autocorrelation function can also be defined as the inverse Fourier transform of the power spectral density, $P(f)$.

$$R_{ss}(\tau) = \int_{-\infty}^{+\infty} P(f)e^{j2\pi f\tau}df \, , \tag{2.8}$$

where it is obvious that all the phase information of the signal is cancelled. Since the output of the pulse compression system is the autocorrelation of the excitation signal, the final shape of the compressed pulse does not depend on the modulation function and the sidelobe levels are independent of signal duration and bandwidth (exceptions can occur for low TBP < 10). The mainlobe width and the sidelobe levels on a pulse compression system are therefore controlled by a windowing function that changes the effective signal bandwidth and envelope.

A windowing function, tapering function or amplitude modulation function is usually applied on the excitation signal to reduce the spectral leakage and sidelobe levels after compression. The choice of windowing functions available is extensive with each possessing different sidelobe suppression properties, mainlobe widths and spectral leakage. An extensive study performed by Harris (1978) gives a better understanding on windows and a thorough comparison between a wide variety of windowing functions. For this study, some of the most commonly used windows are chosen for comparison. The windowing has been performed in the time domain on a LFM chirp signal and the same window is also applied on the matched filter. Parameters given in Table 2.1 and rectangular, Hann, Hamming, Kaiser-Bessel, Blackman and Dolph-Chebyshev windows
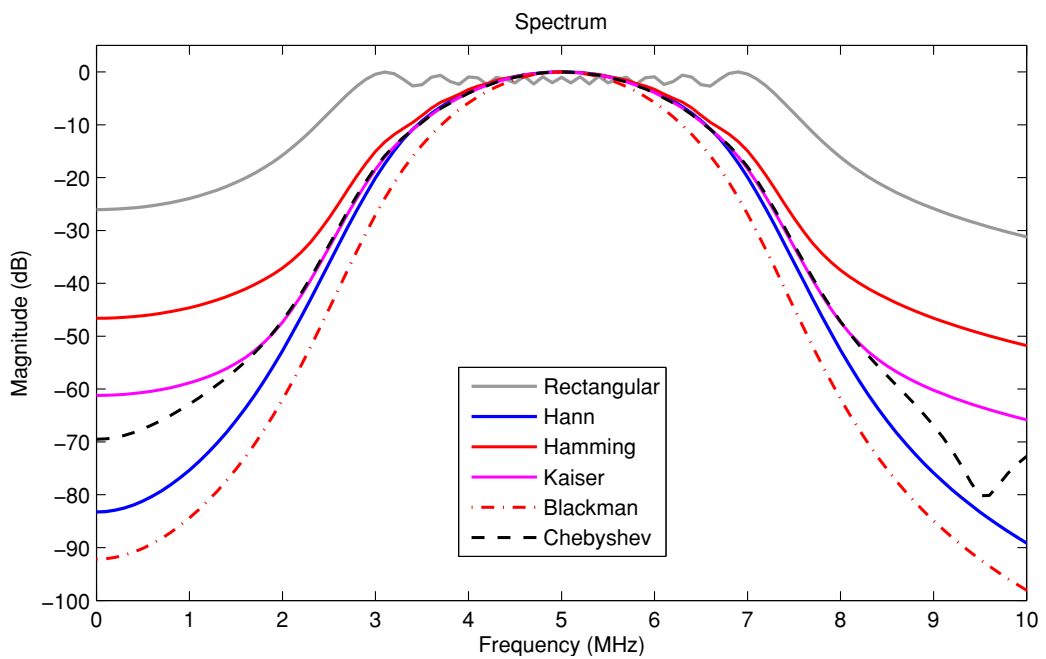
Figure 2.3: Frequency spectra of linear frequency modulated chirps with rectangular, Hann, Hamming, Kaiser-Bessel, Blackman and Dolph-Chebyshev window are shown. All waveforms have a centre frequency of 5 MHz, a fractional bandwidth of 100%, and a duration of 10 μs.

are used for this comparison. A more detailed comparison of windowing functions are given in appendix A.

In order to compare the performance of the windowing functions, a rectangular window, a Hann window, a default Hamming ($a = 0.54$) window and an exact Blackman ($a_0 = 0.42$, $a_1 = 0.5$, $a_2 = 0.08$) window are chosen. The Kaiser-Bessel ($\beta = 6$) and Dolph-Chebyshev (sidelobe attenuation= 55) windows are designed to have the same -6 dB bandwidth with the Hann and Hamming windows. Figure 2.3 shows the spectral leakage for rectangular, Hann, Hamming, Kaiser-Bessel, Blackman and Dolph-Chebyshev windows. Figure 2.4 shows the effect of windowing on the pulse compression. Rectangular window or no windowing achieves the best compression by having the narrowest mainlobe width; however it gives sidelobe levels as high as -13 dB which is unacceptable for ultrasound imaging applications.

Windowing on the transmitting signal reduces the transmitted energy which also reduces the SNR and penetration depth, whilst windowing on the matched filter reduces the SNR gain and axial resolution. Therefore the Kaiser-Bessel, Blackman and Dolph-Chebyshev windows, which can achieve better than -60 dB sidelobe levels, usually perform worse than the Hann window in terms of axial resolution.

Figure 2.5 is presented for a better comparison of sidelobe levels and mainlobe width. These two parameters are important for all imaging applications, where the mainlobe width corresponds to the image resolution and the sidelobe levels corresponds to the image dynamic range. There is a trade-off between mainlobe width and sidelobe levels, so none of the windowing functions is superior to another.

The rectangular window has the widest bandwidth (Figure 2.3), however the compressed waveform with a rectangular window has the highest sidelobe levels as shown in Figure 2.5. However, for applications such as second harmonic imaging, preventing the spectral leakage and minimising the sidelobe levels are crucial. It can be observed in Figure 2.3 that Blackman and Hann windows better concentrate the signal energy at the desired frequency band and cause less spectral leakage, since they have the highest sidelobe roll-off as explained in appendix A. Signal bandwidth is also important for imaging applications, where the wider bandwidth produces better image resolution. The Blackman window has the narrowest bandwidth compared to the other windows, which significantly reduces the image resolution. For this reason, Hann window is preferred for most of the applications, where sidelobe suppression of -40 dB is adequate.
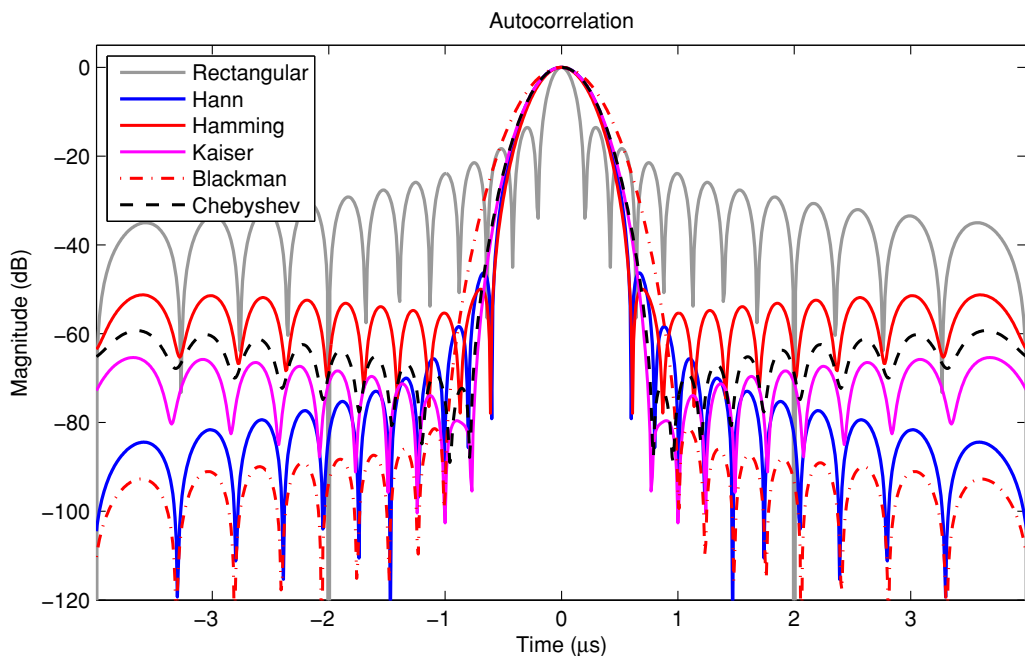
Figure 2.4: Autocorrelation functions of the linear frequency modulated chirps with rectangular, Hann, Hamming, Kaiser-Bessel, Blackman and Dolph-Chebyshev windows are shown. The autocorrelation functions are obtained after pulse compression by a matched filter with the same windowing function. All waveforms and designed match filters have a centre frequency of 5 MHz, a fractional bandwidth of 100%, and a duration of 10 μs.
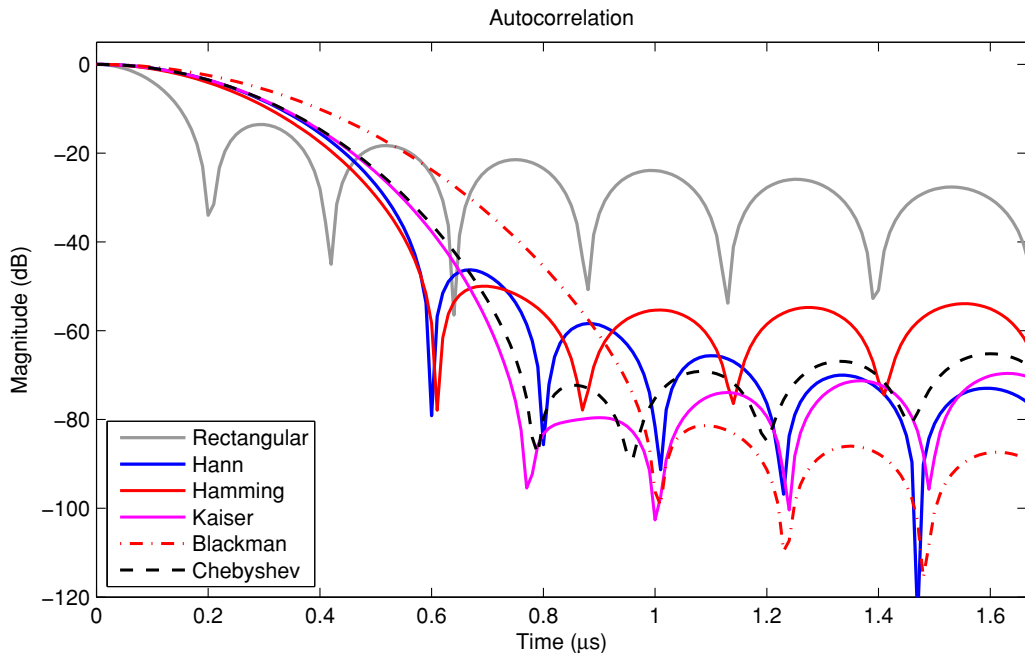
Figure 2.5: Figure 2.4 zoomed in for a more detailed comparison. Autocorrelation functions of the linear frequency modulated chirp with rectangular, Hann, Hamming, Kaiser-Bessel, Blackman and Dolph-Chebyshev windows are shown. The autocorrelation functions are obtained after pulse compression by a matched filter with the same windowing function. All waveforms and designed match filters have a centre frequency of 5 MHz, a fractional bandwidth of 100%, and a duration of 10 μs.

It is also possible to design *mismatched* filters to improve the compression of chirps for the measurements deteriorated by experimental factors. For example, the amplitude modulation function of the matched filter can be re-shaped to compensate for frequency-dependant attenuation in tissue. A mismatched filter can also be designed to rectify the phase corruption introduced by the receiver hardware and transducer element. However, in chapters 6, 7, 8 and 9 individual inverse filters are designed to compensate for the transducer's impulse response, depth-dependant attenuation and frequency-dependant attenuation. The received signals are first processed by these filters, and then compressed by a matched filter.

Chapter 3

Linear Canonical Transform

Transformations have been used in signal processing for over two centuries with the most commonly used transformation for signal analysis being the Fourier transform (Oppenheim & Schafer, 1975).

Fourier transform can be defined as a simple integral transformation as

$$S\left(\omega\right) = \int_{-\infty}^{\infty} s(t) \, e^{-j\omega t} \, dt. \tag{3.1}$$

It actually has a kernel formed by sine and cosine functions, which becomes evident after using the Euler's formula;

$$e^{-j\omega t} = \cos(\omega t) - j\sin(\omega t). \tag{3.2}$$

Since the Fourier transform has a sinusoidal kernel, it works effectively for analysing single-frequency signals. However, it treats the time and frequency as two completely disjoint domains, which is not the optimum strategy for analysing non-stationary chirp signals. For this reason, in this study a generalized transform called the Linear Canonical transform is proposed as an alternative signal processing tool over conventional techniques.

The main motive for preferring the Linear Canonical transform is that it can realize a range of transformations rather than a single one. Although the Linear Canonical transform is not directly employed in this work, two of its special cases are used for analysing the chirp signals.

3.1 Linear Canonical Transform (LCT)

Linear Canonical transform (LCT) is a family of integral transforms that can represent first degree and quadratic phase transformations. The LCT generalizes many classical transforms such as; the Fourier transform, the Fractional Fourier transform, the Fresnel transform and the Fan Chirp transform (Koç *et al.*, 2008).

The LCT of a signal $s(x)$ is given by Moshinsky & Quesne (1971) as

$$S(y) = \int_{-\infty}^{\infty} s(x)\, C_{\mathcal{M}}(x, y)\, dx, \tag{3.3}$$

where $C_{\mathcal{M}}$ is the canonical transformation kernel, which is defined as

$$C_{\mathcal{M}}(x, y) = A_{\mathcal{M}}\ \exp\left[j\pi\left(\frac{a}{b}x^2 - 2\frac{1}{b}xy + \frac{d}{b}y^2\right)\right], \tag{3.4}$$

$$A_{\mathcal{M}} = \sqrt{\frac{1}{b}}\ \exp\left(-\frac{j\pi}{4}\right). \tag{3.5}$$

The LCT has a special representation for $b = 0$, which is beyond the scope of this work and thus not presented here.

The transformation parameters are defined by the matrix $\mathcal{M}$ with determinant $ad - bc = 1$ as

$$\mathcal{M} = \left[\begin{array}{cc} a & b \\ c & d \end{array}\right]. \tag{3.6}$$

The Fourier transform (FT), the Fractional Fourier transform (FrFT), and the Fan Chirp transform (FChT) are all special cases of the Linear Canonical transform. When the LCT kernel is modified as

$$\mathcal{M}_{\mathrm{FT}} = \left[\begin{array}{cc} 0 & 1 \\ -1 & 0 \end{array}\right], \tag{3.7}$$

the transform becomes the same as the Fourier transform.

Sometimes there is a discrepancy between the original definition of FT, FrFT, FChT and the FT, FrFT, FChT derived by the LCT. For example, FT as a special case of the LCT differs from the conventional definition by a factor of $\exp(-j\pi/4)$ (Koç *et al.*, 2008). This usually introduces a phase shift or a scaling factor that does not affect the main transformation kernel, so for the sake of simplicity these discrepancies are not mentioned for each individual case.

Most of the *known* operations on the time-frequency distribution of signals can be represented in matrix form such as shifting, dilation, shearing, rotation and twisting. The LCT can also perform scaling and chirp multiplication operations, which is a special case with $b = 0$. This allows the realisation of physical systems and complicated algorithms to be decomposed into cascade combination of elementary LCT blocks with different $\mathcal{M}$ matrix parameters (Koç *et al.*, 2008). Although the Linear Canonical transform is a powerful signal processing tool just two special cases of the LCT are utilized since the focus of this study is only chirp signals.

3.2 Fractional Fourier Transform (FrFT)

The Fractional Fourier transform was first introduced by Namias (1980) in its incomplete form. An extended analysis of FrFT was published by McBride & Kerr (1987) upon which most recent work is based. The FrFT can be expressed as

$$S_\alpha \left(y \right) = \int_{-\infty}^{\infty} s(x) \, K_\alpha(x, y) \, dx, \tag{3.8}$$

where α defines the order of the transform, $K_\alpha(x, y)$ is the two dimensional transform kernel and y denotes the fractional Fourier-axis for the α-th order fractional Fourier domain, which is the frequency, f, for conventional Fourier transform with a kernel of

$$K_{\alpha=1}(x, y) \equiv K(t, f) = e^{-j2\pi ft}. \tag{3.9}$$

Whereas the conventional Fourier transform is only a shift from time to frequency domain with $\alpha = 1$, the FrFT enables transformation on to any line of angle in time-frequency space, which is achieved by modifying the kernel to the form (Candan *et al.*, 2000; Ozaktas *et al.*, 1996)

$$K_\alpha(x, y) = K_\phi \, \exp \left[j\pi \left(x^2 \cot \phi - 2xy \csc \phi + y^2 \cot \phi \right) \right], \tag{3.10}$$

where

$$K_\phi = |\sin \phi|^{-1/2} \exp \left[\frac{-j\pi \, \mathrm{sgn}(\sin \phi)}{4} + j\frac{\phi}{2} \right] \tag{3.11}$$

and

$$\phi = \frac{\alpha\pi}{2} \,. \tag{3.12}$$

The FrFT can also be represented as a special case of the LCT with the following transform parameters;

$$\mathcal{M}_{\text{FrFT}} = \left[\begin{array}{cc} \cos\phi & \sin\phi \\ -\sin\phi & \cos\phi \end{array} \right]. \tag{3.13}$$

with Eq. (3.4) and Eq. (3.5).

3.2.1 Compression in the Fractional Fourier Domain

When analysing overlapped LFM signals, the FrFT can be used to separate the signals by rotating the waveforms to another domain between time and frequency. The transform order is optimum when it is matched to the chirp rate of the signal. The waveform can be rotated in the fractional Fourier domain by the optimum transform order α_{opt}, which is defined by Capus & Brown (2003) as

$$\alpha_{opt} = -\frac{2}{\pi} \tan^{-1} \left(\frac{1}{2\sigma} \right) , \tag{3.14}$$

where σ is the chirp rate. For a LFM signal the chirp rate is $\sigma = B/T$ where B is the sweeping bandwidth and T is total signal duration. However, in order to calculate the optimal transform order for the discrete FrFT, the resolution of the signal both in time and frequency must be known. For the discrete case, the optimal transform order can be expressed as

$$\alpha_{opt} = -\frac{2}{\pi} \tan^{-1} \left(\frac{\Delta f/\Delta t}{2\sigma} \right) , \tag{3.15}$$

for a system with a time resolution of Δt and frequency resolution of Δf in the interval of $\alpha = [-2, 2]$. This interval covers all transformation angles for $\phi = [-\pi, \pi]$ according to Eq. (3.12) and beyond these limits the FrFT is repetitive. For $\alpha = [-2, 2]$ the FrFT produces an unique output, however two transformation orders can have the time-reversed pairs of the same output such as the axis rotations α and $2 - \alpha$.

The FrFT output has the maximum magnitude and hence peak compression when the transform order is optimized as given in Eq. (3.15). In the case of chirp signals the transform order is optimized when it is matched to the chirp rate of the linear frequency modulated chirp signal. Therefore, this transformation results in maximum compression at the fractional Fourier domain as illustrated in Figure 3.1.

Since the maximum compression is achieved in the fractional Fourier domain, this domain can be used for analysing the signals by recovering the time information. However, direct analysis in the fractional Fourier domain is complicated by the geometrical
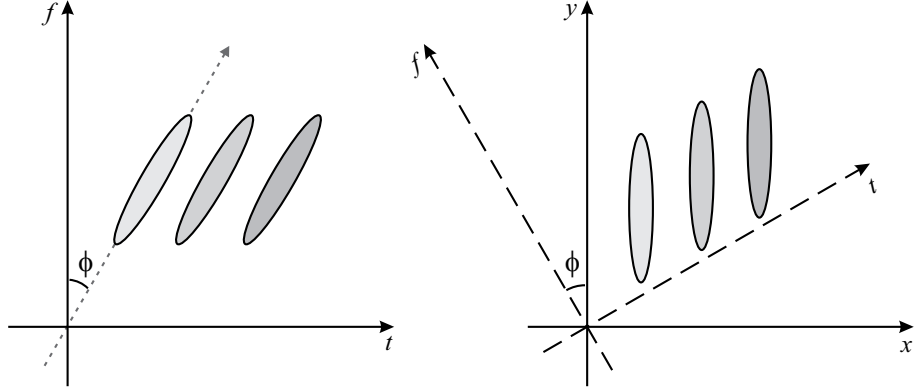
Figure 3.1: (Left) Illustration of three overlapping chirps both in frequency and time domains. (Right) Rotation of the time-frequency plane and overlapping chirps using the FrFT. The rotation angle ϕ matches the chirp rate of the illustrated waveforms.

transformation constituting the FrFT transform. Direct comparison of time and fractional Fourier domain data is complicated by scaling, offsets and rotations. Scaling of the time domain onto the fractional Fourier domain can be achieved using trigonometric transformations. The projection of the time axis, μ_t, onto the fractional Fourier axis, μ_α, is calculated as

$$\mu_\alpha = \mu_t \cos(\phi) , \tag{3.16}$$

where ϕ the transform angle in radians. There is an offset between the origins of the fractional Fourier and time domains. For a discrete sampled waveform this offset can be calculated as (Capus & Brown, 2003)

$$\eta_\alpha = \frac{(f_c - B/2)N}{f_s} \sin(\phi) , \tag{3.17}$$

where $f_c - B/2$ is the chirp start frequency, f_s is the sampling frequency, and N is the total number of samples. Analysis of the ultrasound signals in the fractional Fourier domain without the aid of the time domain projection will be offset and erroneously scaled as the chirp characteristics change.

3.2.2 Filtering in the Fractional Fourier Domain

Windowing in the fractional Fourier domain enables isolation of individual chirp signals that can be used for filtering purposes (Cowell & Freear, 2010). After achieving the

maximum compression in the fractional Fourier domain as described in the previous section, the overlapping chirp signals can be isolated and filtered.

The method for extraction of overlapping chirps is illustrated in Figure 3.2. Using the Fractional Fourier transform, the waveform can be rotated in the time-frequency plane by the optimum transform order to achieve maximum compression of the individual chirp components in the fractional projection. Windowing in the fractional Fourier domain enables isolation of individual chirp signals. Windowing in the fractional Fourier domain is very powerful as a linear time-frequency selective window is created (Almeida, 1994; Candan *et al.*, 2000; Kutay *et al.*, 1997; Ozaktas *et al.*, 1994, 1996). The windowed signal can then be rotated by $-\alpha_{opt}$ degrees, the inverse FrFT, to restore the signal to the time domain thus extracting the chirp from overlapped data.

3.2.3 Examples

Two examples are given to illustrate the compression capability of the FrFT. Figure 3.3 and Figure 3.4 show the fractional Fourier spectrum of two LFM chirp signals with white Gaussian noise. In both figures, each horizontal line of the image shows the envelope of the signal at the specific fractional Fourier domain with the transform order of α, where $\alpha = 0$ is the envelope of the time domain signal and $\alpha = 1$ is the signal's frequency spectrum. The optimum transform order is calculated according to Eq. (3.15), which is $\alpha_{opt} = 0.5$ for this example. Note that the optimum transform angle can be between $\alpha = -2$ and $\alpha = 2$, where both angles correspond to the time domain, beyond these boundaries the fractional Fourier domain is repetitive.

In Figure 3.3, two frequency modulated chirps are shown with a duration of 2 μs, centre frequency of 15 MHz, and bandwidth of 10 MHz, where there is a 10 μs delay between each chirp signal. This signal is transformed to the fractional Fourier domain for all α values between time domain ($\alpha = 0$) and frequency domain ($\alpha = 1$) with 0.05 increments. The maximum compression is observed at $\alpha_{opt} = 0.5$, where the chirp signal has the narrowest width in fractional time. Since both chirps have the same centre frequency and bandwidth, they overlap in the frequency domain at $\alpha = 1$. In Figure 3.4, two chirp signals exist with a duration of 2 μs and starting time of 6 μs and 7 μs. The interfering chirps overlap both in the time and the frequency domains; hence separation of the chirps is not possible in these domains. However, by using FrFT at
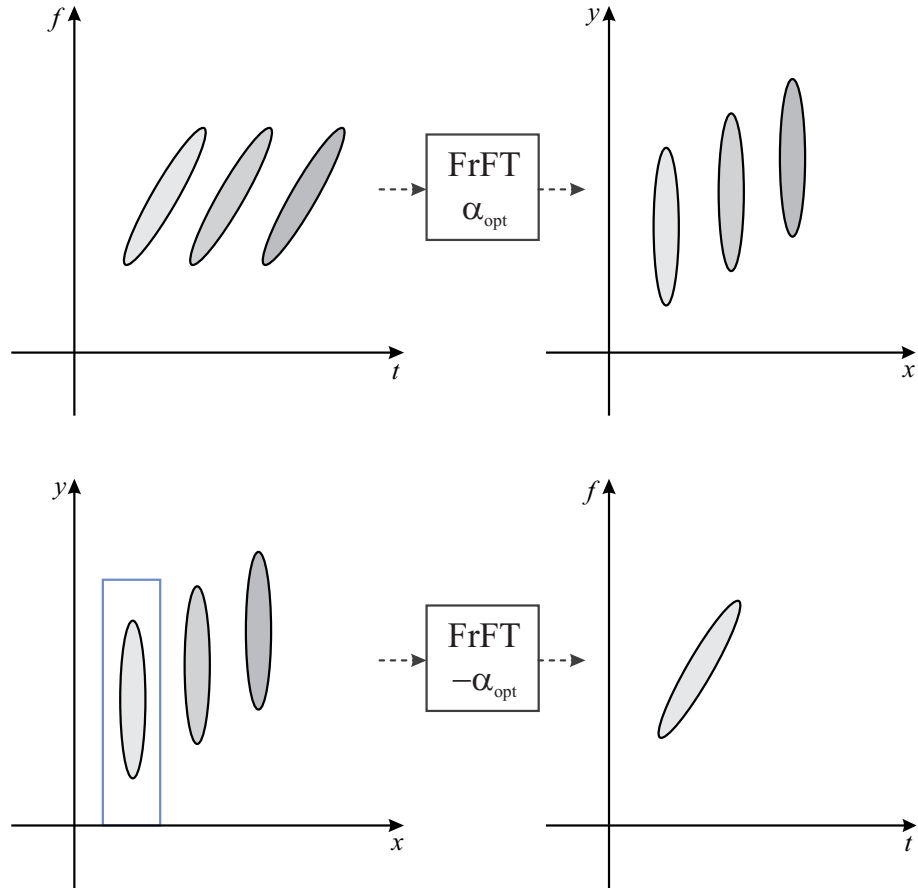
Figure 3.2: Isolation of overlapping chirps in time and frequency domain. (Top-left) Time-frequency representation of three overlapping chirps both in frequency and time domains. (Top-right) Compressed chirps in the fractional Fourier domain after rotating the time-frequency plane. (Bottom-left) Windowing in the fractional Fourier domain. The blue rectangle shows the filtering window applied around the compressed waveform. (Bottom-right) The filtered chirp on time-frequency plane after the inverse FrFT.
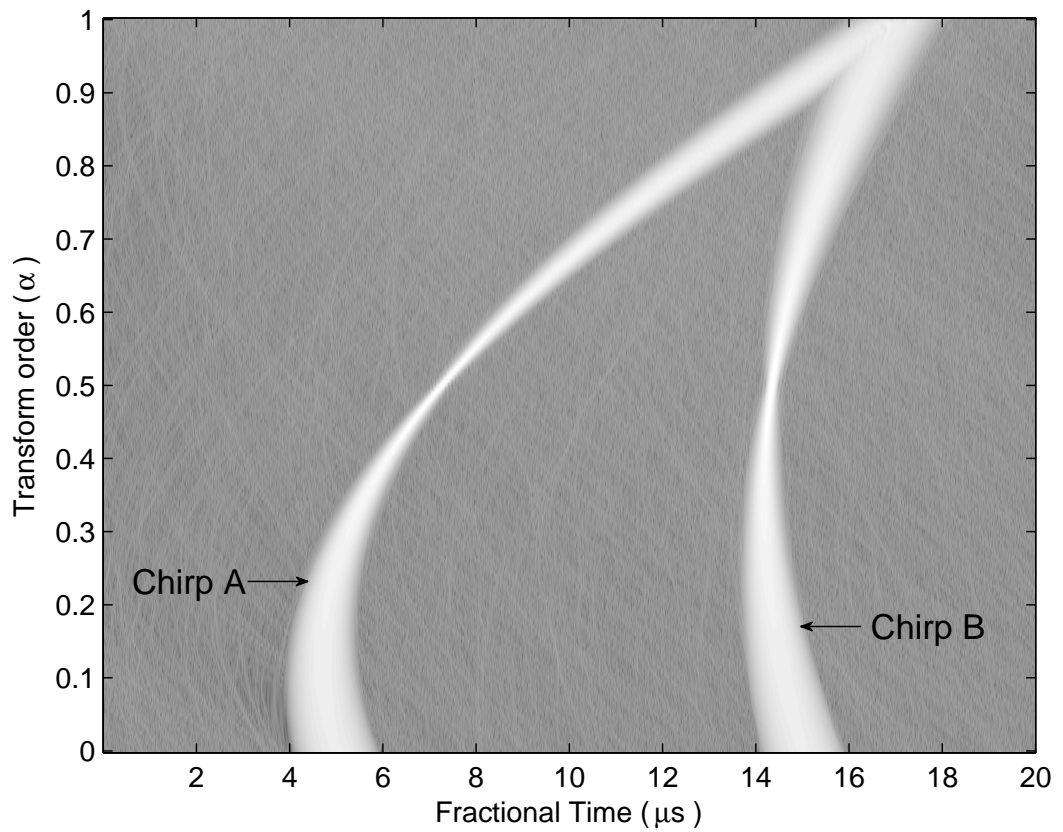
Figure 3.3: The Fractional Fourier transform of two different non-interfering linear frequency modulated chirps. Two chirp signals have a duration of 2 μs, centre frequency of 15 MHz, bandwidth of 10 MHz and starting time of 4 μs and 14 μs.
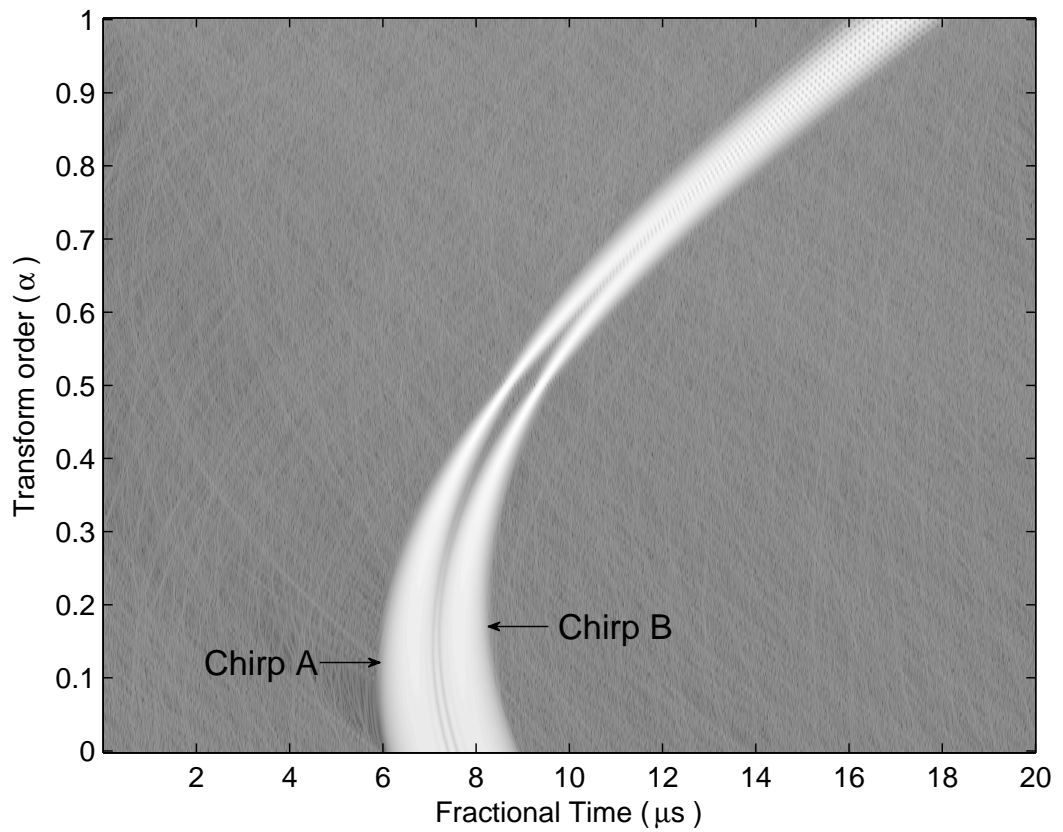
Figure 3.4: The Fractional Fourier transform of two interfering linear frequency modulated chirps. Two chirp signals have a duration of 2 μs, centre frequency of 15 MHz, bandwidth of 10 MHz and starting time of 6 μs and 7 μs.

the optimum transform order ($\alpha = 0.5$), the chirp signals are maximally compressed and separation can be achieved.

3.3 Fan Chirp Transform (FChT)

The Fan Chirp transform was recently introduced into chirp analysis by Képesi & Weruaga (2006); Weruaga & Képesi (2007). It has been shown to improve the resolution and fidelity of time-frequency representations of frequency modulated chirps. The name of the FChT comes from its unique *fan-shaped* transformation kernel, which is best explained visually.

Figure 3.5 represents the simplified behaviours of the Fourier transform, the FrFT, and the FChT on the time-frequency plane. Imagine an observer standing orthogonal to the frequency axis at the infinite. The Fourier analysis corresponds to the sight of the observer, where the time information carried by the signal is unclear. If the observer stands with an angle ϕ to the time-frequency plane at the infinite, he can see the FrFT of the signal as shown in Figure 3.5(B). For this case, it is possible to utilize both time and frequency information carried by the signal and the observer can achieve the best possible resolution for a linear frequency modulated chirp located with an angle of ϕ on the time-frequency plane.

In order to realize the FChT, the observer must stand *inside* the time-frequency plane as represented in Figure 3.5(C), where the resulting projection gives rise to the FChT power spectrum for σ/f. The observer can achieve the finest representation for linear frequency modulated chirps located with a fan geometry on the time-frequency plane, *i.e.* harmonically related chirps (Weruaga & Képesi, 2007).

Rather than rotating the time-frequency plane as the FrFT, the FChT reshapes the time-frequency plane by twisting it into a fan geometry. Therefore the FChT can compress a linear chirp with all of its harmonic content. This property of the FChT makes it an indispensable tool for characterisation of harmonically related chirplets. Harmonically related chirps are common in ultrasound imaging, especially in harmonic imaging, however the use of FChT has not been reported for ultrasound applications. It has been mostly employed in speech analysis (Képesi & Weruaga, 2006) and used for music representation (Cancela *et al.*, 2010), signal parameter estimation (Dunn *et al.*, 2009), and time-frequency representation of the chirps (Weruaga & Képesi, 2007).
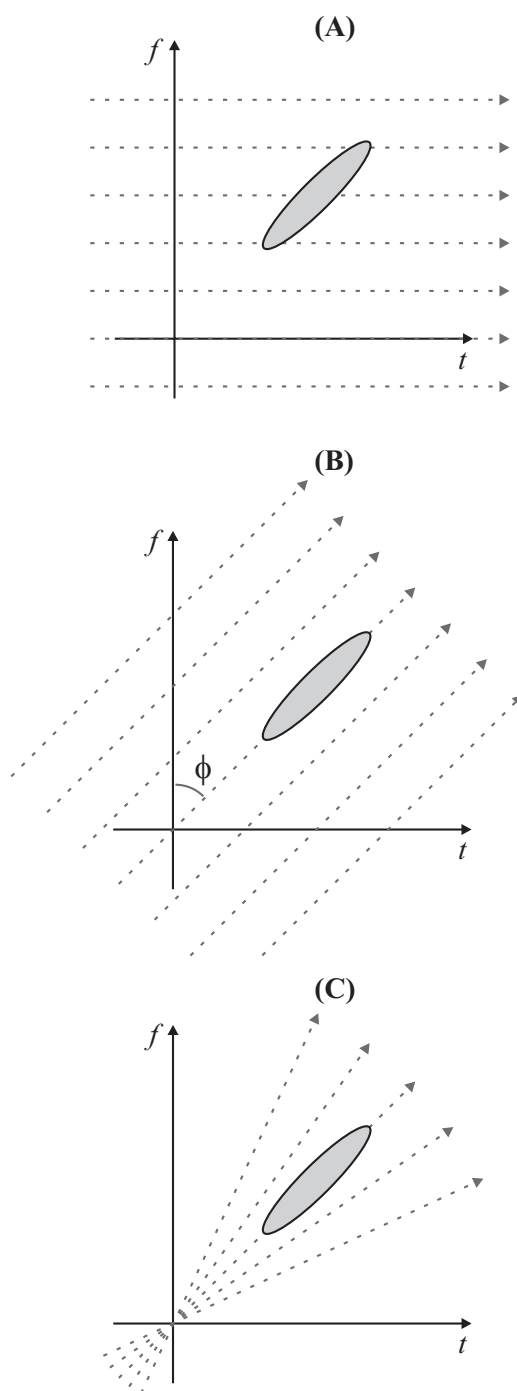
Figure 3.5: Graphical explanation of (A) the Fourier transform, (B) the Fractional Fourier transform (FrFT), (C) the Fan Chirp transform (FChT). The dashed arrows show the behaviour of each transformation on the time-frequency plane.

The Fan Chirp transform of the signal $s(t)$ can be expressed as (Weruaga & Képesi, 2007)

$$S(f, \sigma) = \int_{-\infty}^{\infty} s(t) \sqrt{|\varphi'_{\sigma}(t)|} \, e^{-j2\pi f \varphi_{\sigma}(t)} \, dt, \qquad (3.18)$$

where t is time, f is frequency and $\varphi_{\sigma}(t)$ is the phase function or time warping function, which is controlled by the normalized chirp rate, σ/f, as

$$\varphi_{\sigma}(t) = \left(1 + \frac{\sigma}{2f}t\right)t. \qquad (3.19)$$

$\varphi_{\sigma}(t)$ can be represented as the frequency normalized phase function associated with a LFM chirp with the same chirp rate as defined in Eq. (2.1). $\varphi_{\sigma}(t)$ is equal to $\phi(t)/f$ when $f = f_c$ and the transformation kernel given in Eq. (3.18) matches perfectly with the signal of interest. For $f = 2f_c$, the best match for the transformation kernel will be a new chirp with twice the centre frequency and chirp rate. For this case, the second harmonic component generated by the same chirp will have similar phase parameters with the FChT kernel; hence the optimum compression will be achieved.

For any given chirp rate the FChT can achieve optimum compression including all harmonics of the chirp of interest. For $\sigma = 0$ however, the FChT kernel becomes the same with the Fourier transform kernel. This mathematical relation between the transformations is more obvious, when the Linear Canonical transformation matrix $\mathcal{M}$ is given. The FChT can be realized by the LCT using Eq. (3.4), Eq. (3.5) and the following parameters;

$$\mathcal{M}_{\text{FChT}} = \begin{bmatrix} -\sigma & 1 \\ -1 & 0 \end{bmatrix}, \qquad (3.20)$$

where σ is the chirp rate of the LFM signal.

3.3.1 Compression by the FChT

Since this study focuses on finite duration signals, for the real signal $s(t)$, centred at the origin with duration T the limits of the integral in Eq. (3.18) reduce to $-T/2$ and $T/2$ as (Dunn *et al.*, 2009);

$$S(f, \sigma) = \int_{-T/2}^{T/2} s(t) \sqrt{|\varphi'_{\sigma}(t)|} \, e^{-j2\pi f \varphi_{\sigma}(t)} \, dt. \qquad (3.21)$$

It is possible to change the limits of the integral, because the harmonics of the signal of interest are distributed on the time-frequency plane as shown in Figure 3.6(B). Rather than computing the FChT for the whole received signal, it can now be calculated for a shorter duration. Although computation time reduces significantly for this case, the transform needs to be calculated at different time delays. For the FrFT however it is more practical to apply the transformation over the whole signal, since the signal of interest is made up of consecutive chirps with the same chirp rate as illustrated in Figure 3.6(A). For this reason a different methodology is used to compress the chirps with harmonic content.

When the FChT is computed according to Eq. (3.21), the best compression is achieved for an LFM chirp with a chirp rate of σ and for all of its harmonics. The first step is to compute the FChT for a zero centred signal in time with a transformation origin located at $\langle 0, -1/(\sigma/f) \rangle$ as depicted in Figure 3.6(B). After the transformation, the chirp and all of its harmonics appear as narrowband sinusoidal on the warped frequency domain by maintaining their centre frequencies, which is shown in Figure 3.6(B).

For the next step, the signal is shifted in time and the FChT is applied on the signal centred at the origin. It is similar to a running window approach, where the window length is chosen to be the duration of the chirp. However, this approach does not affect the resolution of the compression, since the window is not for reducing the effect of long t but to reduce the computation time.

3.3.2   Filtering in the FChT Domain

Filtering in the FChT domain is essential if there is spectral overlapping between the harmonic chirp components. When this overlap exists between the harmonic and the fundamental chirps, artificial sidelobes appear after pulse compression with a match filter. This will be explained in the next section and chapter 7.

In order to perform filtering in the FChT domain, the optimum compression in the FChT domain for the chirps of interest must be achieved. After achieving the optimum compression for a given chirp and for its harmonics, the compressed chirps can be filtered in the FChT domain as represented in Figure 3.7(middle). The window length used for filtering is selected according to the LFM chirp used as excitation. Note that narrower windows will result in higher SNR and reduced sidelobe levels and wider

(A)

(B)
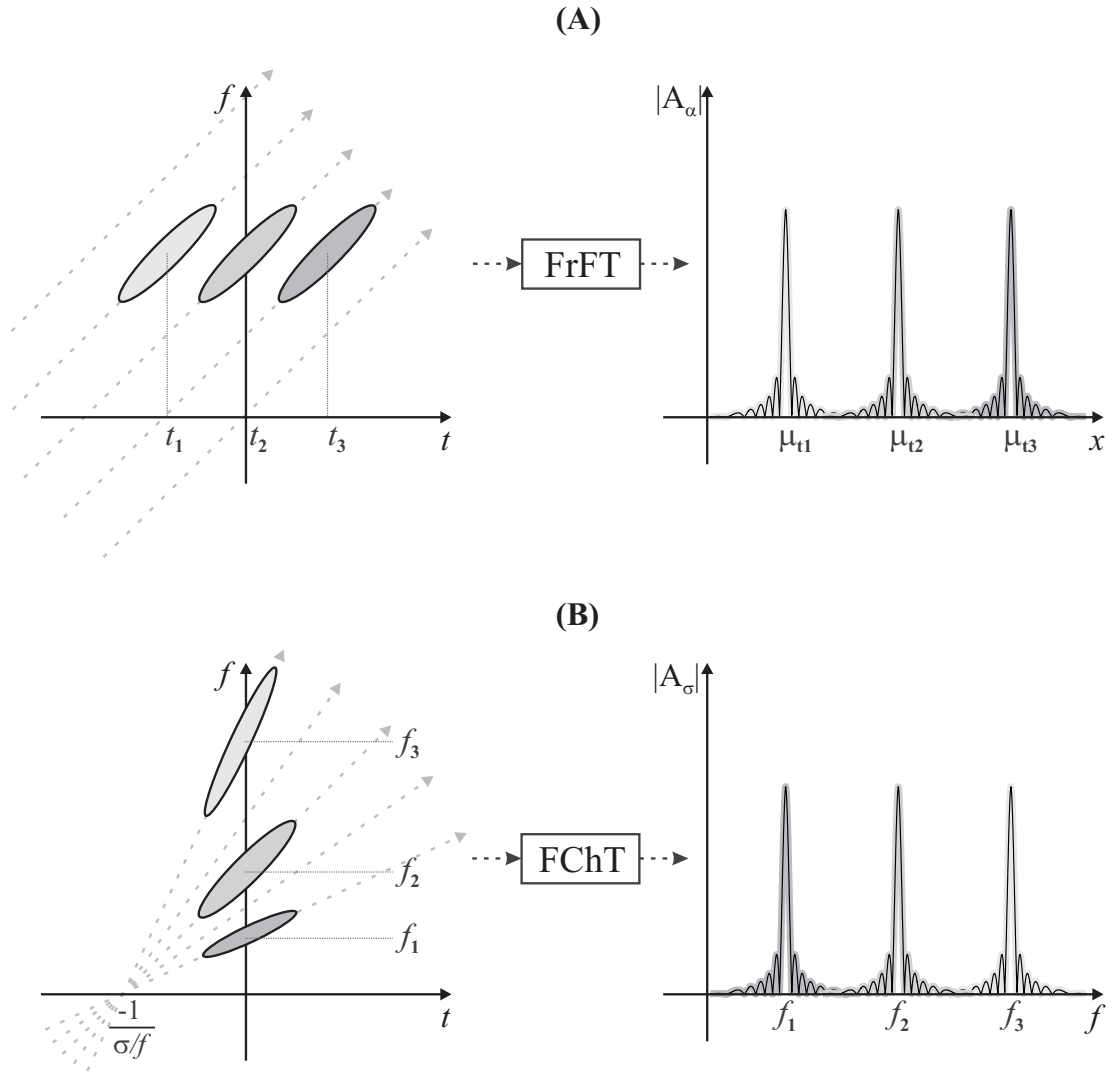
Figure 3.6: Compressed chirp signals by the Fractional Fourier transform and by the Fan Chirp transform. (A) Illustration of the compressed LFM chirps with same duration, centre frequency and bandwidth with different time delays by the FrFT. The time delays are scaled according to Eq. 3.16. (B) Illustration of the compressed LFM chirps with same duration and temporal location, but harmonically related centre frequency and bandwidths by the FChT.

windows will result in higher bandwidth and hence better axial resolution. Therefore, choosing the right window size is crucial for filtering in the FChT domain.

The compression ratio for a LFM chirp is the time-bandwidth product of the signal. In time domain, the width ratio between an uncompressed pulse and a compressed pulse is $T \times B$, where the approximated half-power width of the autocorrelation function is given by Misaridis & Jensen (2005a) as

$$\tau_{-3\mathbf{dB}} = \frac{\pi/2}{B}.$$ (3.22)

In the frequency domain, the compression ratio achieved by the FChT is also the time-bandwidth product of the signal, where the compressed signal in the FChT domain approximately has a half-power width of

$$f_{-3\mathbf{dB}} = \frac{\pi/2}{T}.$$ (3.23)

The length of the filtering window however is chosen to be the signal width at -60 dB[1] as

$$f_{-60\mathbf{dB}} = \frac{\pi/2}{T} n_{win},$$ (3.24)

where n_{win} is the ratio between the -60 dB pulse width and -3 dB pulse width of the autocorrelation function measured form Figure 2.4.

After applying the filtering windows designed according to the Eq. (3.24) in the FChT domain, the filtered chirp and harmonics must be transformed back to the time domain by using the inverse Fan Chirp transform (iFChT), which is defined as

$$s(t) = \int_{-\infty}^{\infty} S(f,\sigma) \sqrt{|\varphi'_{\sigma}(t)|} \, e^{-j2\pi f \varphi_{\sigma}(t)} \, df.$$ (3.25)

Separation between the spectrally overlapping harmonics can be achieved as shown in Figure 3.7(bottom). The filtered fundamental and harmonic chirps can now be compressed by a matched filter without any artefacts.

Effect of the finite duration FChT and the running window approach

When Eq. (3.21) is used for a signal longer than the duration of the excitation chirp, the process is repeated by shifting the time domain signal and computing the FChT

---

[1]For a window length equals to the pulse width at -3 dB, the half of the signal's power will be filtered out. Therefore, the -60 dB figure is decided after the experimental measurements performed in later chapters.
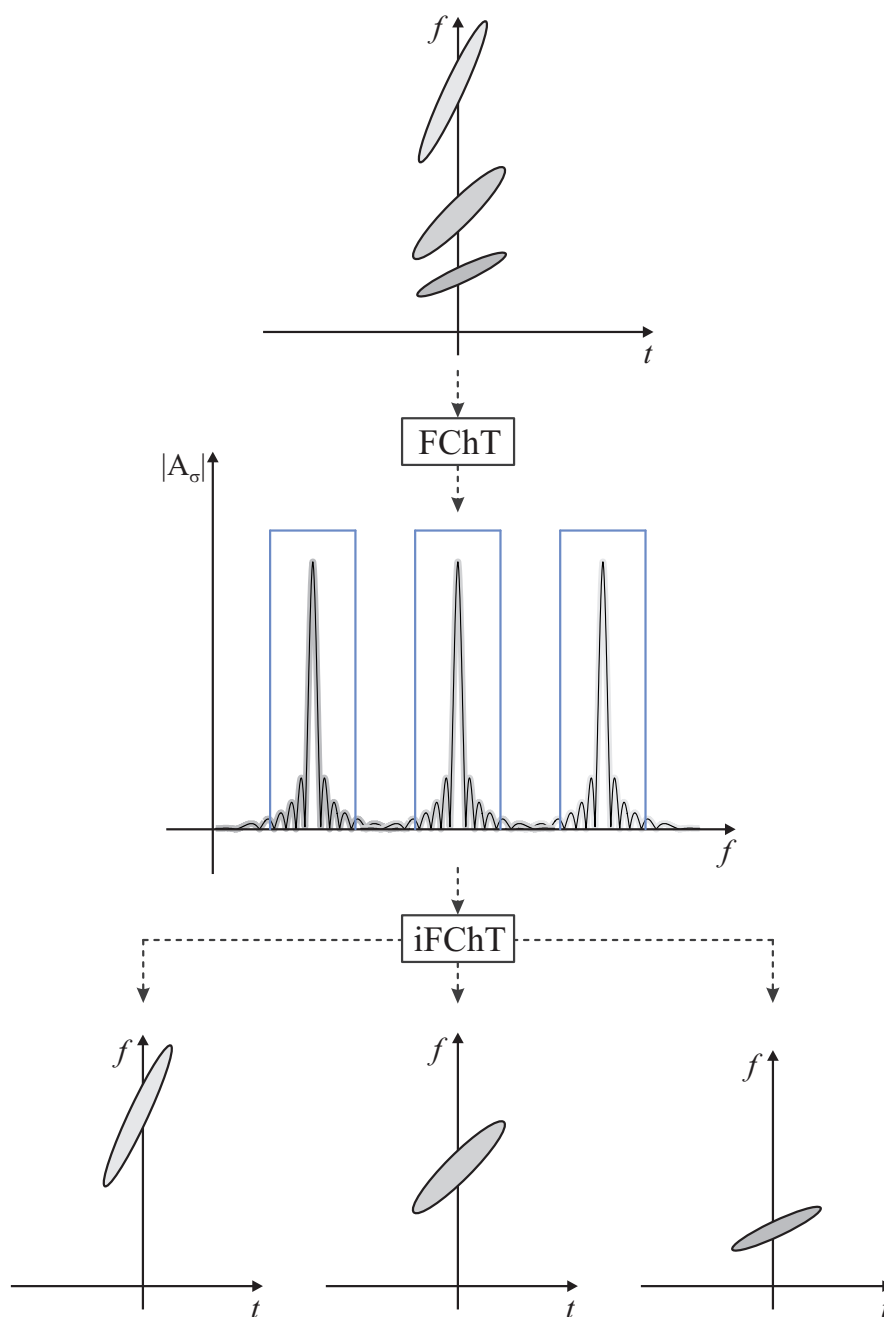
Figure 3.7: Isolation of harmonically related multiple chirps is described. (Top) Time-frequency representation of the signal. (Middle) Compressed chirps in the FChT domain. The blue rectangle shows the filtering window applied around the compressed waveform. (Bottom) Filtered chirps are shown on time-frequency plane after the inverse FChT.
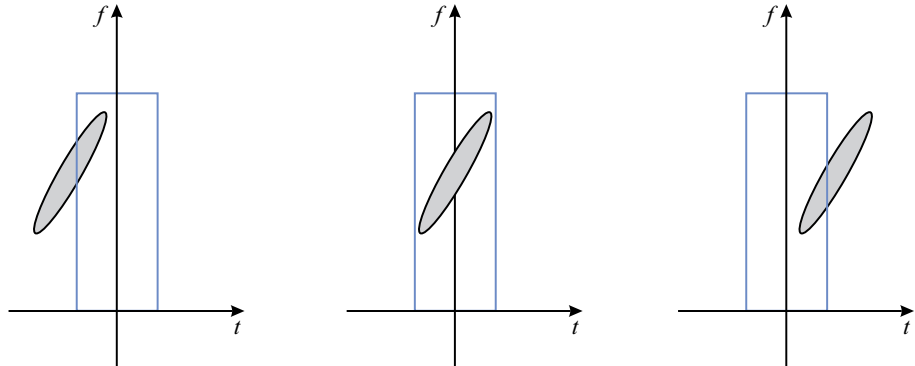
Figure 3.8: Time-frequency representation of time delayed linear frequency modulated chirps. (Left) The waveform has a time delay of $t = -\tau$. (Middle) The waveform has no time delay and centred at $t = 0$. (Right) The waveform has a time delay of $t = +\tau$.

several times to cover the whole signal length. While performing this computation, the same chirp appears in the FChT computation window for several times as illustrated in Figure 3.8.

The chirp waveforms, whose time-frequency representations are illustrated in Figure 3.8, have the same duration, centre frequency, and bandwidth, but different time delays. When these waveforms are transformed into the FChT domain, the time delayed chirps result in frequency shifted components in the warped-frequency domain similar to the example given in Figure 3.9. Figure 3.9 shows the FChT spectrum of five simulated linear frequency modulated chirps with a duration of 20 μs, a centre frequency of 5 MHz, and a bandwidth of 5 MHz, but different time delays.

When the filtering is performed in the FChT domain with the window length calculated with Eq. (3.24) and illustrated in Figure 3.9, the same chirp appears inside the filtering window for several times with a frequency shift. To overcome this problem, a peak detection algorithm is used to differentiate between the desired waveform and time delayed waveforms.

It is known that the waveform with a specific chirp rate centred at $t = 0$ will appear in the FChT domain exactly at its centre frequency, unlike the time delayed waveforms. Therefore, the peak detection algorithm is used to find the location of the compression peak and this location is compared with the centre frequency of the chirp. If the waveform is not maximally compressed at the expected frequency location, but still inside the filtering window, these signals are discarded. Therefore, in Figure 3.9,
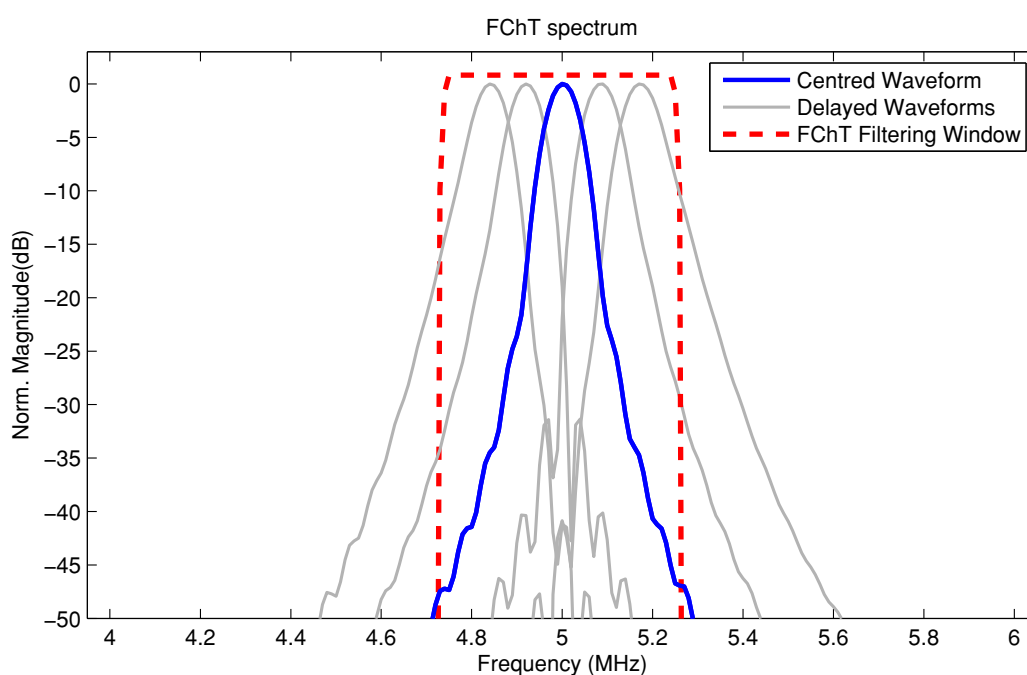
Figure 3.9: FChT spectrum of a simulated linear frequency modulated chirp with a duration of 20 μs, a centre frequency of 5 MHz, and a bandwidth of 5 MHz with different time delays. The thick blue line is the FChT spectrum of the chirp with no time delay. The thin grey lines are the FChT spectrum of the time delayed chirps. The red dashed line is the window applied in the FChT domain for filtering purposes.

the grey signals are omitted since they do not have a peak at 5 MHz and the blue signal is selected.

3.3.3   Example
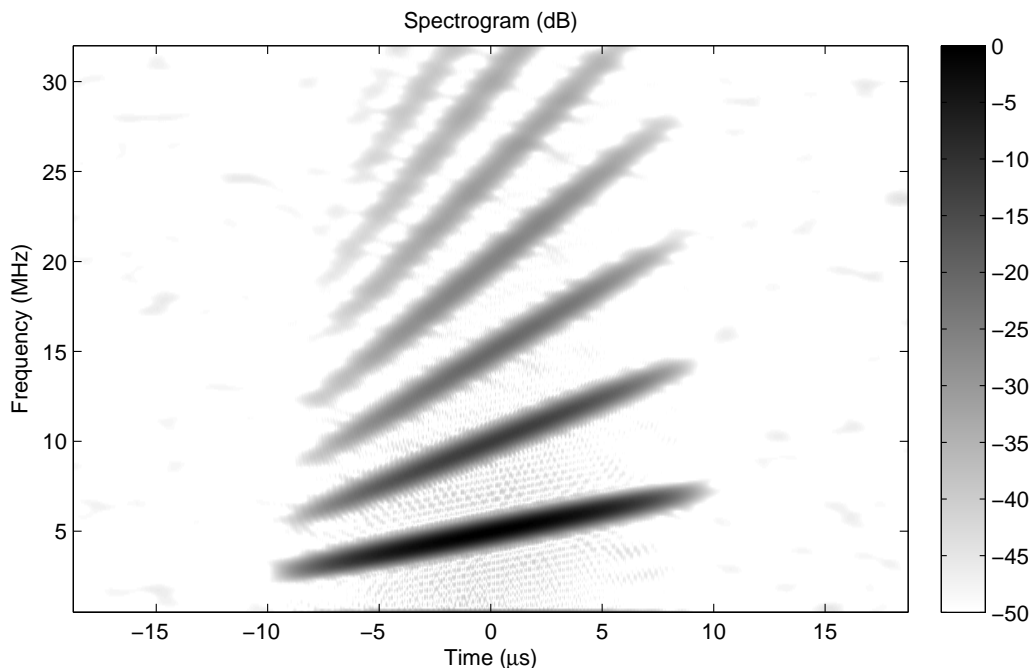
Figure 3.10: Spectrogram of the simulated chirp signal with harmonic content. The fundamental component of the simulated linear frequency modulated chirp has a duration of 20 μs, centre frequency of 5 MHz, and bandwidth of 5 MHz.

A chirp waveform with harmonic content and white Gaussian noise, whose time-frequency representation is given in Figure 3.10, is generated. The fundamental component of the simulated linear frequency modulated chirp has a duration of 20 μs, centre frequency of 5 MHz, and bandwidth of 5 MHz. The harmonic components of the simulated waveform is generated to have an asymmetric wave shape and decaying harmonic power by considering the wave propagation in dispersive media and weak shock theory (Hamilton & Blackstock, 2008). The shock wave formation will be presented and explained in chapter 7 and appendix B. For the sake of simplicity, it is assumed that n^{th} harmonic will have n times the centre frequency and bandwidth (for $n = 2, 3, 4...$) and the frequency dependant attenuation is ignored.
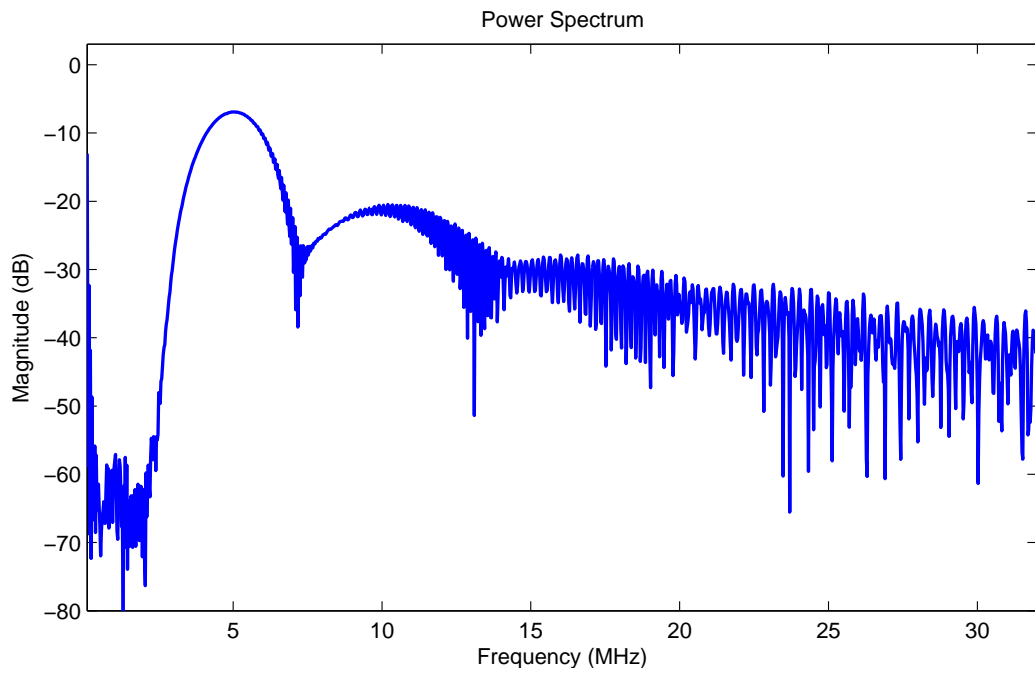
Figure 3.11: Power spectrum of the simulated chirp signal with harmonic content. The spectrum is calculated according to modified periodogram method explained in appendix A.

The fundamental component of the simulated linear frequency modulated chirp has a duration of 20 μs, centre frequency of 5 MHz, and bandwidth of 5 MHz. The rich harmonic content of the simulated waveform results in spectral overlap between the fundamental and harmonics, as shown in Figure 3.11.
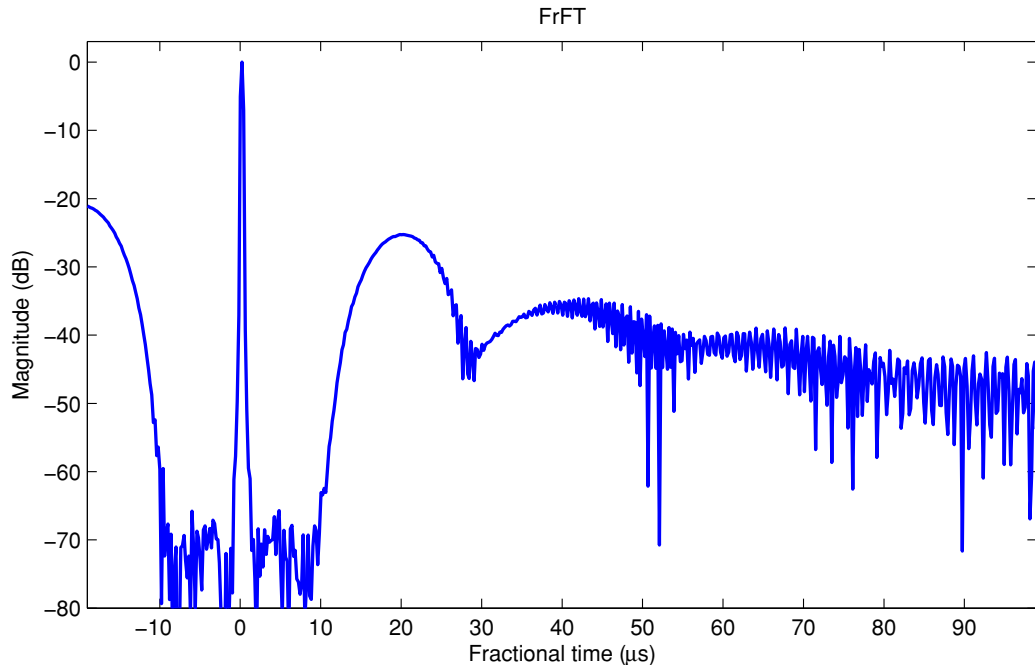
Figure 3.12: Fractional Fourier domain representation of the simulated chirp signal after applying the FrFT with a transform order that matches with the fundamental component.

The FrFT can achieve the maximum compression for the fundamental *or* any harmonic component when the optimum transform order α_{opt}, Eq. (3.15), is set accordingly. Figure 3.12 shows the transformation of the simulated waveform into fractional Fourier domain for the transform order that matches with the parameters of the fundamental component. The compressed fundamental component appears at $t = 0$ μs and does not overlap with any of the harmonics. To extract the fundamental and harmonic components individually, the FrFT must be recalculated with a different transform order that matches with the harmonic of interest.

The FChT can achieve the maximum compression for the fundamental *and* all harmonic components. Figure 3.13 shows the new frequency spectrum after applying
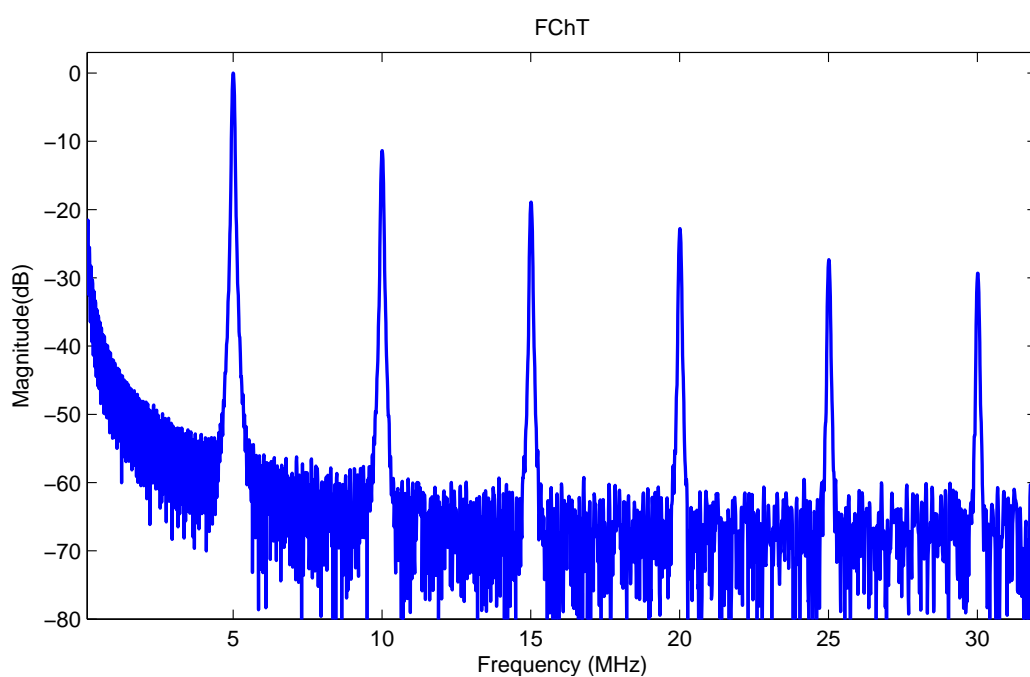
Figure 3.13: Frequency domain representation of the simulated chirp signal after applying the FChT with a normalised chirp rate that matches with the fundamental and harmonic components. The frequency domain is not the same with Figure 3.11, since the time-frequency plane is warped by the FChT.

the FChT, which effectively warps the time-frequency plane.

When the example waveform with high harmonic content was compressed by a matched filter designed for the fundamental chirp component, the compression artefacts would appear on the final waveform. These artefacts can be observed between $t = -15$ μs and $t = -10$ μs in Figure 3.14. Separating the fundamental chirp from the spectrally overlapping harmonics, as explained in the previous section on filtering in the FChT domain, these artefacts can be suppressed. Figure 3.15 shows the compressed waveform without any artefacts thanks to processing with the FChT before pulse compression.
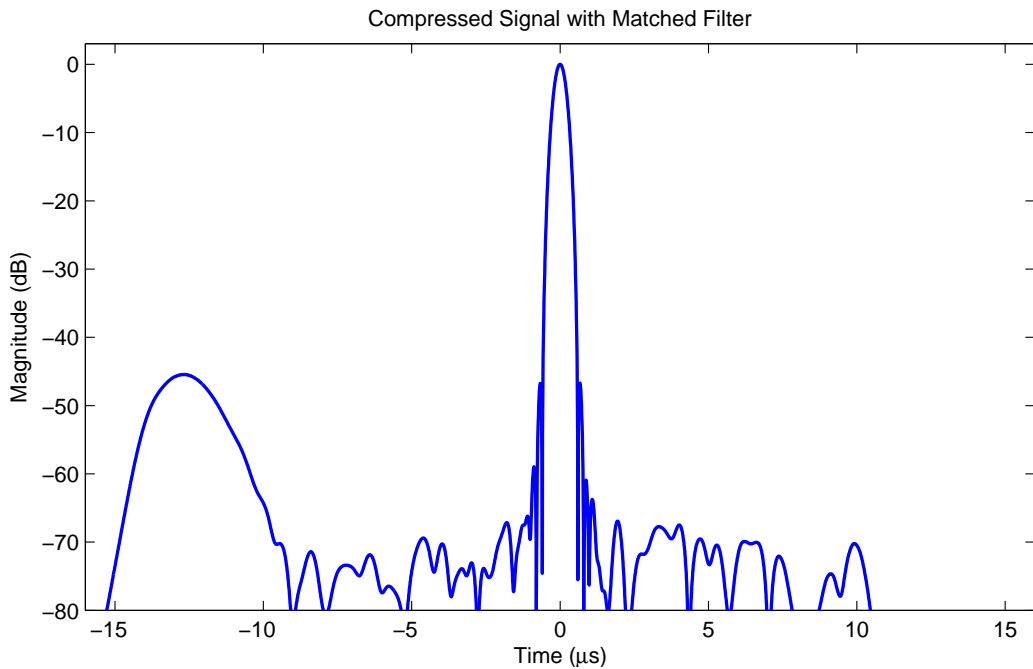
Figure 3.14: Pulse compressed fundamental component of the simulated chirp signal with matched filter.
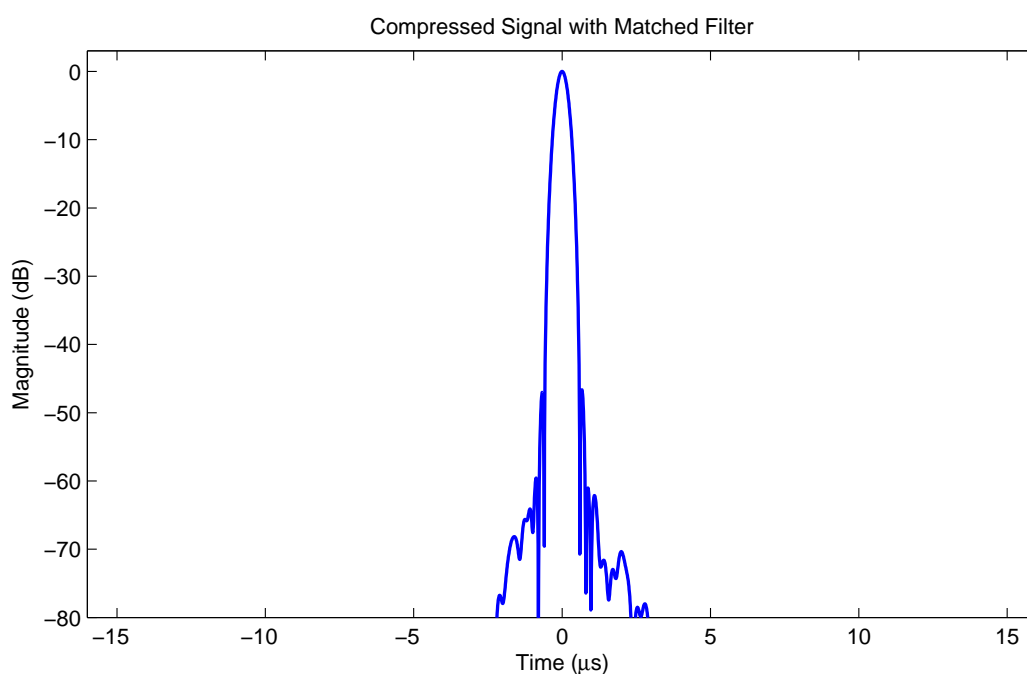
Figure 3.15: Pulse compressed fundamental component of the simulated chirp signal with matched filter after processing with the FChT.

Part I

Hard-Tissue Ultrasound Imaging

Ultrasound is mostly preferred for characterisation of the osseous tissue by scattering and attenuation measurements to determine velocity, attenuation and density values (Evans & Tavakoli, 1990). The use of ultrasound for hard-tissue imaging is not very common except in dentistry, where access to teeth is easily achievable.

Two of the greatest problems encountered by researchers who have applied medical ultrasound imaging techniques to dentistry are the dimensions of teeth and the varying speed of sound in the different tooth layers. In addition, the speed of sound in enamel and dentine layers is much higher than in any soft tissue (Barber *et al.*, 1969). These two facts encourage the use of high frequency excitation and short pulse duration for better resolution. However, the ultrasonic attenuation in dental tissue makes signal detection more difficult for high frequency pulses. The excitation pressure may be increased to achieve better penetration depth, but this is at the cost of increased intensity levels and the likely generation of harmonic signals.

Long duration excitation provides a better penetration and improved SNR by increasing the excitation energy without changing the peak pressure level, but introduces another problem when the duration of the ultrasound signal is longer than the time of the round trip in that tooth layer. The signal overlapping caused by the successive reflections inside the enamel and dentine layers makes time and frequency analysis nearly impossible, since both constructive and destructive interference occur between individual reflections. Due to these reverberations, the received echoes are not identifiable in the time domain. In the frequency domain all reflections completely overlap with each other, where they are not in phase with the successive reflections. Without filtering, the resulting waveform cannot be used to determine the tooth layers. The proposed solution in this work is to use LFM chirp excitation by exploiting the Fractional Fourier transform (FrFT). The FrFT allows frequency modulated signals overlapping in time and frequency to be separated.

Chapter 4 and chapter 5 are based on the publications (Harput *et al.*, 2009, 2011a,b), where the FrFT is used for compressing and for filtering the chirp signals.

Chapter 4

Ultrasound Dental Imaging using Chirp Coded Excitation

An ultrasound contact imaging method is proposed to measure the enamel thickness in human tooth. A delay-line transducer with a working frequency of 15 MHz is chosen to achieve a minimum resolvable distance of 400 μm in human enamel. To confirm the contact between the tooth and the transducer, a verification technique based on the phase shift upon reflection is used. Because of the high attenuation in human teeth, linear frequency modulated chirp excitation and pulse compression are exploited to increase the penetration depth and improve the signal-to-noise ratio. Preliminary measurements show that the enamel-dentine boundary creates numerous internal reflections causing the applied chirp signals to interfere arbitrarily. In this work, the Fractional Fourier transform (FrFT) is employed for the first time in dental imaging to separate chirp signals overlapping in both time and frequency domains. The overlapped chirps are compressed using the FrFT and matched filter techniques. Micro-CT, also known as the X-ray microtomography, is used for validation of the ultrasound measurements for both techniques. For a human molar, thickness of the enamel layer is measured with an average error of 5.5% after compressing with the FrFT and 13.4% after compressing with the matched filter based on average speed of sound in human teeth.

4.1 Introduction

The first ultrasonic observations in dental tissue started in the 1960s using the pulse-echo technique to evaluate the tooth enamel, dentine-enamel junction (DEJ) and dentine-pulp interface (Barber *et al.*, 1969; Kossoff & Sharpe, 1966). Most of these studies used simple time of flight measurements by calculating time delay between the peaks of consecutive reflections utilizing little or no signal processing techniques (Barber *et al.*, 1969; Ghorayeb & Valle, 2002; Kossoff & Sharpe, 1966). Traditionally, short-duration pulses are preferred by researchers to achieve better axial resolution. Some signal and image processing techniques, such as filtering and envelope detection, were subsequently used to improve image quality (Culjat *et al.*, 2005a; Hua *et al.*, 2009). However, the use of coded excitation techniques in echodentography[1] is not reported. In this work, a linear frequency modulated (LFM) chirp is chosen as an excitation technique to improve the signal-to-noise ratio (SNR), penetration depth and thus the image quality.

The first studies in echodentography started with the frequency range of $6 - 18$ MHz with basic pulse-echo measurements (Barber *et al.*, 1969; Kossoff & Sharpe, 1966). Later, some researchers focused on high frequency ultrasound to achieve a better resolution. Hughes *et al.* (2008) reported on the use of a 35 MHz focused ultrasound piezo-composite transducer for tooth measurements. Scanning acoustic microscopy (SAM) has been successfully used to image the elastic properties of carious human teeth, characterize the enamel and detect the enamel-dentine interface (Maev *et al.*, 2002; Peck & Briggs, 1987; Raum *et al.*, 2007). SAM has been described at frequencies around 50 MHz (Maev *et al.*, 2002), but the highest frequency ever reported was 900 MHz by Raum *et al.* (2007) for tooth characterization. SAM can easily achieve sub-millimetre resolution, however it is not a practical diagnostic method for dentistry. Recently, the frequency range of $10 - 20$ MHz has been favoured by researchers due to the high attenuation in human tooth at higher frequencies (Culjat *et al.*, 2003; Ghorayeb & Valle, 2002; Löst *et al.*, 1992; Singh *et al.*, 2006). For this reason, a delay-line transducer with a 15 MHz centre frequency is chosen in this study for the experiments. An extended and well detailed literature review of all diagnostic applications of ultrasound in dentistry has been published by Ghorayeb *et al.* (2008).

---

[1]Ultrasound dental imaging.

The aim of this work is to measure the thickness of the enamel layer, locate discontinuities and produce an image of the tooth *ex-vivo* using ultrasound that can provide significant benefits to patients and dentists. *A priori* knowledge of tooth anatomy allows the early identification of cracks, decays, enamel loss or other tooth defects, which can cause inflammation or infection. According to the American Association of Endodontics, it is estimated that 15 million teeth receive endodontic treatment each year in the USA (Rosenberg *et al.*, 2007); early diagnostic information may help dentists reduce this number. By considering the significance of early detection of these anomalies on prevention, this work will focus on dental erosion. Dental erosion or acid erosion is mostly related to the consumption of carbonated drinks and it can cause irreversible tooth loss. It is one of the most common chronic diseases in children with 32% of 14 year old showing erosion of permanent dentition (Dugmore & Rock, 2004). The rise in consumption of sugar, coffee, and acidic beverages and disorders, such as Gastroesophageal Reflux Disease, causes dental erosion and enamel loss (Hua *et al.*, 2009). Monitoring the enamel thickness can provide dentists with sufficient information to prevent the enamel loss (Louwerse *et al.*, 2004).

In this study, LFM excitation is used to achieve better penetration without degradation of the resolution and the Fractional Fourier transform is utilized to analyse overlapping echoes, which are caused by the successive reflections inside the enamel and dentine layers. A tooth phantom is constructed to test the effectiveness of the proposed technique and the experimental measurements are performed in the tooth phantom and an extracted human molar. To perform pulse compression on overlapping chirps, the FrFT and matched filter techniques are applied. Micro-CT, again a non-destructive imaging method, is used for validation of the proposed technique.

4.2 Materials and Methods

4.2.1 Experimental Setup

The experimental measurements were carried out with a 15 MHz Sonopen replaceable delay line transducer with 1 mm polystyrene tip (Olympus NDT Inc., Waltham, MA, USA) in contact with the sample. All experiments were performed with glycerine couplant at a temperature between 21°C and 22°C. The transducer was characterized before designing the excitation waveform, where the centre frequency was 14 MHz

Table 4.1: Acoustic properties of materials

MATERIAL	Velocity (m/s)	Density (kg/m^3)	Impedance (MRayl)
Enamel[a]	6250	3000	18.8
Dentine[a]	3800	2000	7.6
Pulp[a]	1570	1000	1.57
Glass, borosilicate*	6025	2475	14.9
Dental Composite*	3350	2200	7.4
Water[b]	1482	1000	1.5
Glycerine*	1910	1265	2.42
Delay-line, polystyrene*	2310	1070	2.47
Transducer, PZT-5A[b]	4350	7750	33.7

[a] values are taken from Ghorayeb *et al.* (2008).

[b] values are taken from Kino (1987).

* values are determined in our laboratory.

and the -3 dB fractional bandwidth was 86%. To generate the excitation signals a 33250A Arbitrary Waveform Generator (Agilent Technologies Inc., Santa Clara, CA, USA) was used and the signals were amplified by using E&I A150 RF Power Amplifier (Electronics & Innovation Ltd., Rochester, NY, USA). Transmitted and received signals were separated by using a RDX-6 diplexer (Ritec Inc., Warwick, RI, USA). Then the received signal was amplified by 30 dB for phantom measurements and 50 dB for tooth measurements, due to the higher attenuation in enamel, with a Panametrics 5072PR Pulser/Receiver (Olympus NDT Inc., Waltham, MA, USA). All measurements were saved by a LeCroy Waverunner 64xi oscilloscope (LeCroy Corporation, Chestnut Ridge, NY, USA) for further processing in Matlab (Mathworks Inc., Natick, MA, USA).

Two different set of measurements were performed on a tooth phantom and a human molar with the same experimental setup.

Phantom Measurements

The tooth phantom was constructed by bonding a 1 mm thick borosilicate glass to a 1 mm thick dental composite Herculite XRV Unidose dentine (Kerr, Scafati, Italy) instead of enamel and dentine (Singh *et al.*, 2008). The acoustic properties of the materials are given in Table 4.1. The thickness of the phantom layers were measured with a micrometre screw gauge (Table 4.2). To replicate the effect of the pulp, the tooth phantom was partially immersed in water during the experiments.

Tooth Measurements

For the tooth measurements, an extracted human molar with intact enamel layer was acquired from the Leeds Dental Institute Skeletal Tissues Bank. The tooth sample has been stored in a 1% aqueous thymol solution for 6 months. Before the experiments the human molar was scanned first with an X-ray scanner μCT 80 (Scanco Medical AG, Brüttisellen, Switzerland) with 40 μm resolution. Micro-CT data was used to validate the accuracy of the ultrasound measurements. To perform the experiments a screw thread was bonded to the tooth samples using a dental composite and cured by UV light. A high precision computer numerical controlled (CNC) positioning system with a positioning accuracy of 50 μm was used to scan the tooth sample with the ultrasound delay line transducer, as shown in Figure 4.1.
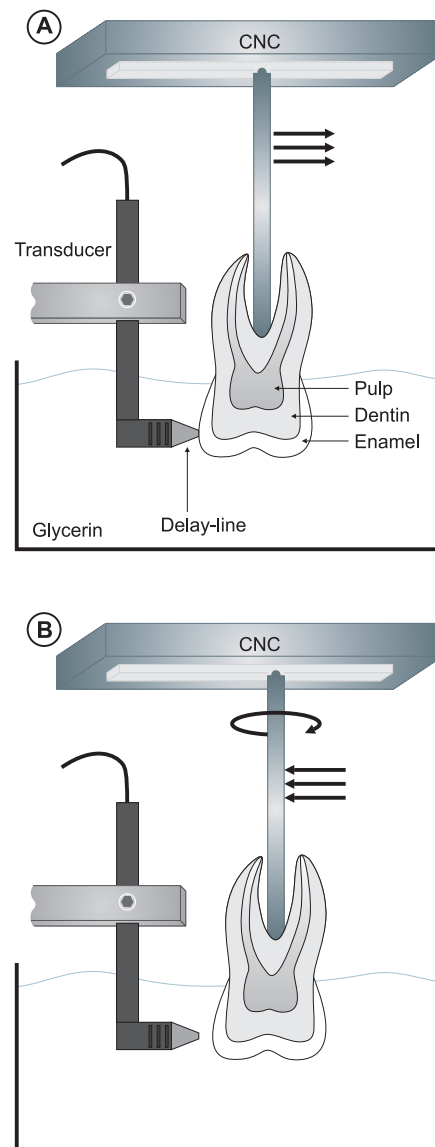
Figure 4.1: Experimental setup used for enamel thickness measurements. The tooth sample is mounted on the moving arm of the CNC positioning system. The transducer is fixed by a metal profile to a stationary stage. (A) Pulse-echo measurement is performed in a tank filled with glycerine. Then the tooth is moved away from the transducer after the measurement. (B) The CNC positioning system rotates the tooth sample and moves in the opposite direction to achieve a contact with the transducer. After repositioning the tooth sample with a different angle consecutive measurement is performed.

4.2.2 Coupling Material

Human tooth is a porous material. Without using any coupling material, the small air pockets between the transducer and tooth would prevent the ultrasonic energy transmission due to the acoustic impedance mismatch between air and enamel. In order to facilitate the transmission of ultrasound waves into the sample, a coupling material must be used. Although various acoustic couplants have been evaluated for tooth imaging (Culjat *et al.*, 2005b), water is usually preferred as a coupling medium for non-contact ultrasound tooth measurements (Ghorayeb & Valle, 2002; John, 2005; Kossoff & Sharpe, 1966; Löst *et al.*, 1992). However, the acoustical mismatch between the water, polystyrene delay-line and enamel would interfere with echoes from the target tissue and decrease the transmission efficiency. In this study, glycerine is chosen as the coupling material to fill the small pores on the tooth surface. Since glycerine and polystyrene have similar acoustic impedances (Table 4.1), the transfer efficiency is improved by minimizing the impedance mismatch.

4.2.3 Contact Imaging

For the measurements, the tooth sample and the transducer were immersed in a tank filled with glycerine and controlled by a CNC positioning system. Even though there was glycerine couplant between delay-line and tooth sample, the measurements were performed in contact mode, where the glycerine was only used to fill the microscopic pores on the surface of the tooth sample.

For the proposed contact imaging technique, transducer positioning to achieve a good contact with the tooth sample is crucial for accurate measurements. The human tooth however has a rough and curved surface, which makes it difficult to achieve a good contact with the probe tip. This contact problem between the tooth and transducer was solved by checking the phase of first reflected echo. In the experiments, the acoustic impedances of the polystyrene, glycerine and enamel was used to validate contact between the delay-line and enamel by considering the 180° phase shift of the returned echo while the transducer was coupled to the enamel. Measurements were also performed on the tooth phantom to test the proposed contact verification method with results given in the next section.

A similar contact problem was reported by Louwerse *et al.* (2004), where they showed the error in enamel thickness measurements due to variations in the positioning of the probe tip. In this work, the contact problem was solved by checking the phase of the reflected signal and by using a CNC positioning system to increase measurements reproducibility. The importance of the reproducibility of ultrasonic enamel thickness measurements and the variations is further discussed by Louwerse *et al.* (2004).

4.2.4 Coded Excitation and Pulse Compression

Coded excitation has been shown to be effective in radar applications (Skolnik, 1981) as well as some medical ultrasound systems (Misaridis & Jensen, 2005a) by improving the SNR, penetration depth or image quality. Different methods such as frequency modulation, phase modulation and Golay codes were compared to find the most suitable coded excitation technique for ultrasound dental imaging. The linear frequency modulated chirp signal was chosen as an excitation technique, since it was reported to have lower side-lobe levels after compression under high attenuation and nonlinearity (Chiao & Hao, 2005).
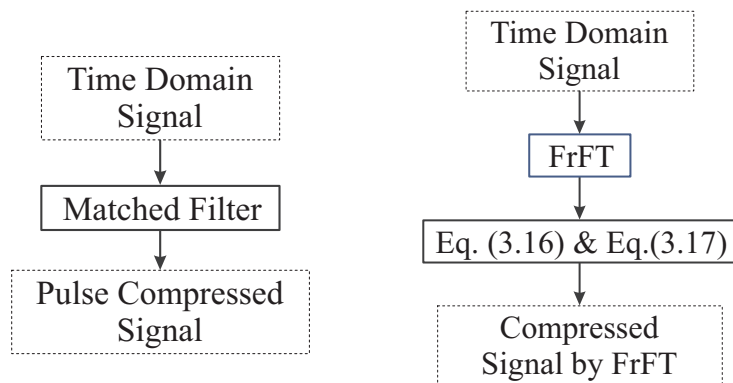
Figure 4.2: (Left) Diagram illustrates the pulse compression method by a matched filter. The time domain signal is convolved with a matched filter to achieve pulse compression. (Right) Diagram illustrates the compression method by the FrFT. First, the time domain signal is transformed into fractional Fourier domain, where the compression is achieved. As the second step, Eq. (3.16) and Eq. (3.17) are used to calculate the projection of the FrFT axis in time axis, so that the temporal information can be recovered.

The matched filter (MF) is the most common method for filtering and compressing

chirp signals as it optimizes the probability of detection and maximizes the SNR (Misaridis & Jensen, 2005a). Therefore, the MF was chosen as the golden standard pulse compression technique for comparison with the FrFT. Both methods are explained in Figure 4.2.

The main advantage of the FrFT over the MF is that the FrFT can be used without the *a priori* knowledge of the transmitted signal. The FrFT does not rely on the phase of the signal but the chirp rate, which can be obtained at the receiver side. The FrFT technique becomes more effective, if the phase distortions induced by experimental equipment needed to be eliminated.

4.3 Experiments

To verify the accuracy of the proposed coded excitation scheme and the FrFT technique, measurements were first performed on a tooth phantom of known dimensions. The excitation method was also compared with a Gaussian pulse of the same bandwidth, which is widely used by researchers to measure the thickness of the tooth layers (Barber *et al.*, 1969; Culjat *et al.*, 2003; Ghorayeb & Valle, 2002; Ghorayeb *et al.*, 1997; John, 2005, 2006; Löst *et al.*, 1992).

Table 4.2: Thickness measurements for different excitation signals and pulse compression techniques.

	Glass	Dental composite	A.E.	M.A.E.
Actual Size	0.998 mm	1.016 mm		
Gaussian Pulse	1.006 mm	0.951 mm	36 μm	65 μm
MF (Short LFM)	1.039 mm	1.050 mm	37 μm	41 μm
FrFT (Short LFM)	1.048 mm	1.060 mm	46 μm	50 μm
MF (Long LFM)	1.030 mm	0.975 mm	36 μm	41 μm
FrFT (Long LFM)	0.970 mm	1.012 mm	16 μm	28 μm

* (A.E.) Average error, (M.A.E.) Maximum absolute error
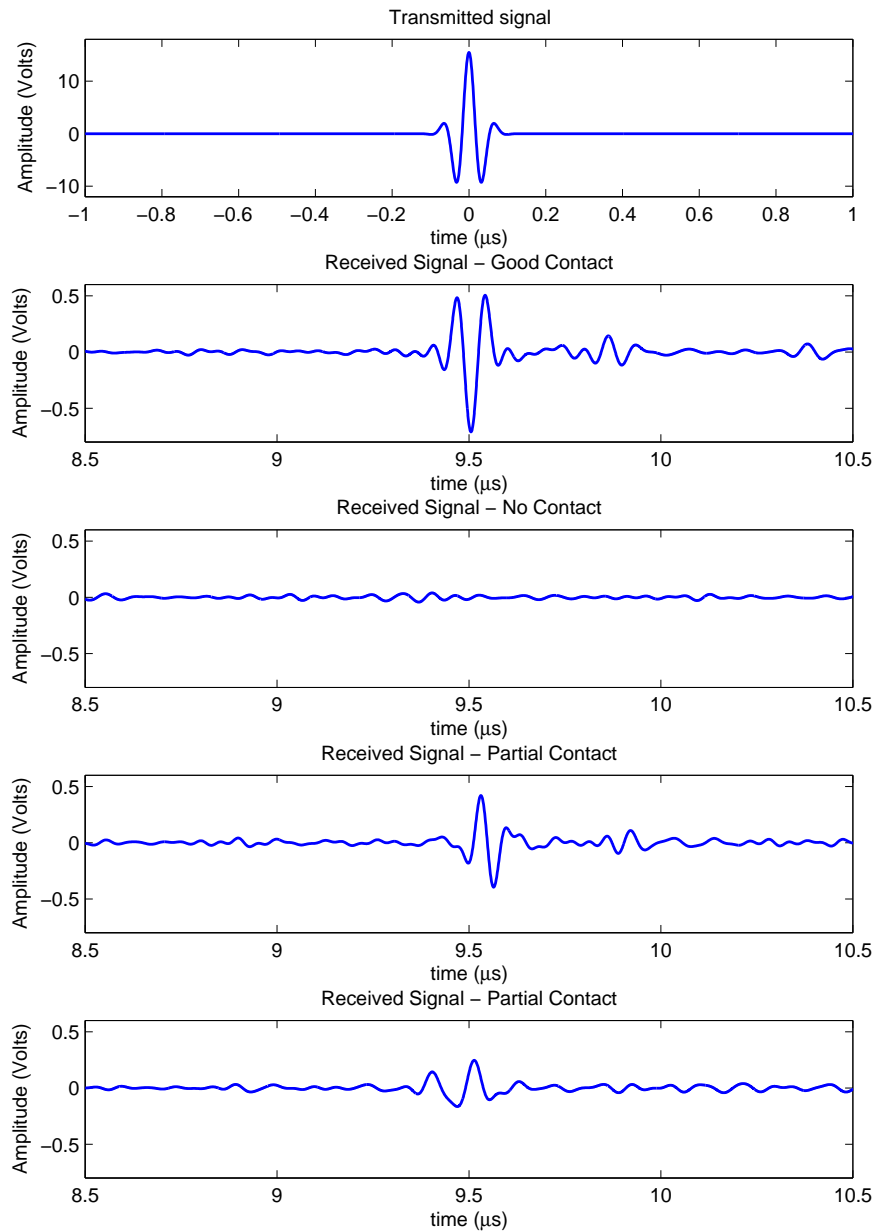
Figure 4.3: (First) Transmitted Gaussian pulse. (Second) Received signal from a good contact, where a phase-shifted Gaussian pulse can be seen at 9.5 μs. (Third) Received signal without any contact, where no reflections can be observed. (Fourth) Received signal from a partial contact, where the observed phase shift is not 180°. (Fifth) Received signal from a partial contact, where the shape of the Gaussian pulse is distorted.

4.3.1 Contact Verification

In all experiments, the phase of the first reflected echo was used to verify contact between the transducer delay-line and tooth sample or tooth phantom. However, before performing the thickness measurements, the contact verification method was tested on the tooth phantom. The transmitted signal was captured as shown in Figure 4.3(first) and this measurement was used as a control signal, whilst a $180°$ phase shift must be observed when the contact between the delay-line and enamel is achieved. This phase shift appears, because the imaging system has two physical interfaces; 1) between the transducer and the delay-line, 2) between the delay-line and the tooth sample. The polystyrene delay-line has a lower acoustic impedance than the transducer (PZT-5A) resulting in a negative reflection coefficient,

$$\Gamma = \frac{Z_{\text{polystyrene}} - Z_{\text{transducer}}}{Z_{\text{polystyrene}} + Z_{\text{transducer}}} < 0, \tag{4.1}$$

where Z is the acoustic impedance of the given material and Γ is the reflection coefficient.

However for the coupling from the polystyrene delay-line to the enamel, the reflection coefficient is positive;

$$\Gamma = \frac{Z_{\text{enamel}} - Z_{\text{polystyrene}}}{Z_{\text{enamel}} + Z_{\text{polystyrene}}} > 0. \tag{4.2}$$

Since two reflection coefficients have a different sign, a $180°$ phase shift is expected between the signal at $t = 0$ and $t = 9.5$ μs in Figure 4.3. For a good contact, a $180°$ phase shift was observed between Figure 4.3(first) and Figure 4.3(second), which was considered as a valid measurement. However if the waveform is distorted or the phase shift is not $180°$, the ultrasound measurement was discarded. Figure 4.3(third), Figure 4.3(fourth) and Figure 4.3(fifth) are some examples, where the measurements were discarded due to the aforementioned phase shift technique.

4.3.2 Thickness Measurements on Tooth Phantom

The tooth phantom was measured with three different excitation signals; a Gaussian pulse, a short LFM signal with 0.5 μs duration, and a long LFM signal with 2 μs duration. All signals were designed to match the transducer frequency response, and therefore a centre frequency of 14 MHz and a fractional bandwidth of 80% were chosen.
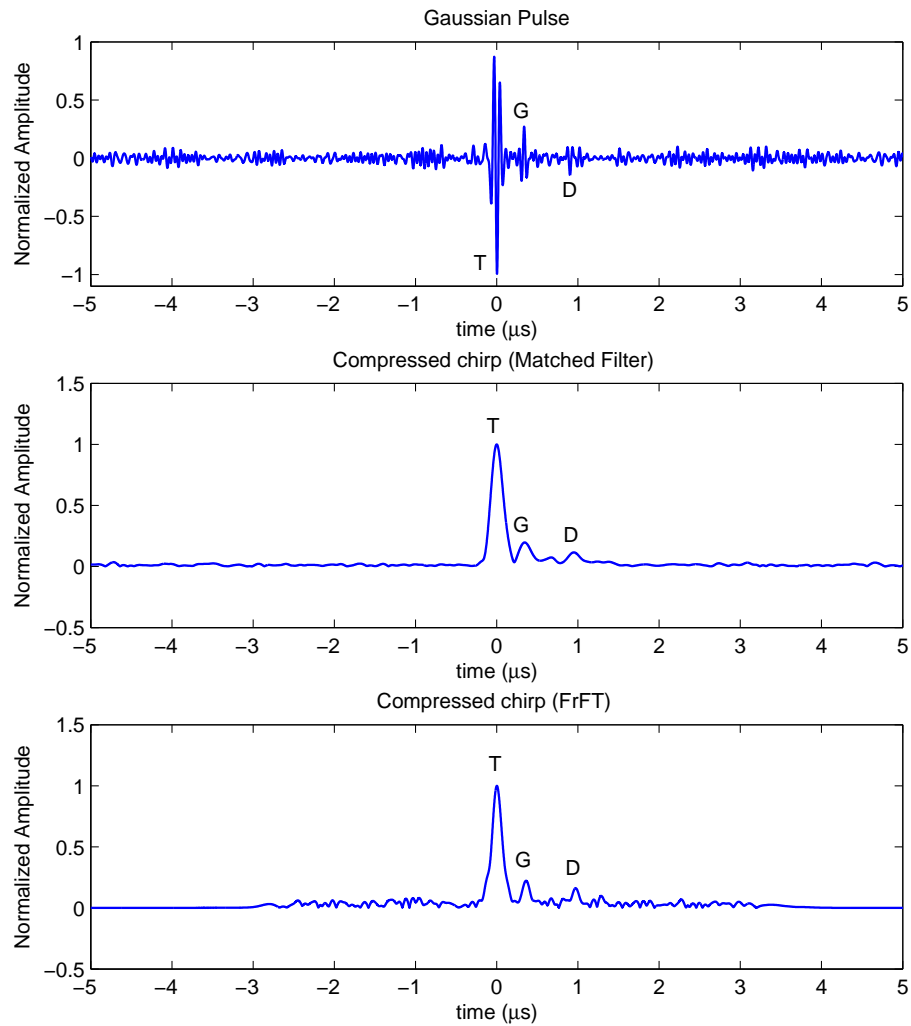
Figure 4.4: Comparison of (Top) a Gaussian pulse with (Middle) an LFM chirp compressed with matched filter and (Bottom) an LFM chirp compressed with the FrFT. (T) denotes the reflection from transducer tip and glass boundary. (G) denotes the reflection from glass and dental composite boundary. (D) denotes the reflection from dental composite and water boundary.

A Hann window was applied to the LFM signals to reduce the side lobe levels after compression. The same excitation voltage of 25 V_{pp} was used in each measurement.

The Gaussian pulse was chosen to demonstrate the basic pulse-echo technique and the measurements performed with the Gaussian pulse were filtered using a band-pass filter. However, to compress the interfered chirp signals, the LFM measurements were first filtered using a band-pass filter and then processed using the FrFT technique or matched filter. Two different matched filters were designed for short and long duration LFM signals. These were then used to pulse compress the received signals. FrFT was performed at $\alpha = 1.7421$ for the short LFM and at $\alpha = 1.3360$ for the long LFM with the rotation angle calculated according to Eq. (3.15).

The received echoes for the Gaussian pulse and the envelope of the received signal for the LFM excitation after compression with the MF and the FrFT are shown in Figure 4.4, respectively. The time-of-flight between consecutive pulses or compressed chirps, which are denoted as **T**, **G** and **D** in Figure 4.4, were measured. The time-of-flight information for the signals in the fractional Fourier domain was recovered by using Eq. (3.16). The layers thickness were calculated through prior knowledge of the speed of sound in that material as given in Table 4.1. The average error and maximum absolute error for each method was calculated and the accuracy of the techniques is compared using the results given in Table 4.2. Of the tested techniques, it is found that the LFM signal with 2 μs duration processed with the FrFT technique gives the lowest error.

4.3.3 Enamel Thickness Measurement

To measure the enamel thickness of the human molar, the tooth sample was mounted to the moving arm of the CNC positioning system. The transducer was fixed on a stationary stage and pulse-echo measurements performed with chirp excitation. Measurement data was obtained through automated CNC scanning performed in steps of 5°, as shown in Figure 4.1. Only the LFM signal was used for excitation with a duration of 2 μs, centre frequency of 14 MHz, fractional bandwidth of 80%, and excitation voltage of 25 V_{pp}, which approximately generates a pressure of 150 kPa inside the enamel.

The measurement data was processed in two different ways to plot the ultrasound images shown in Figure 4.5. The tooth was scanned with the CNC and individual scan lines captured for each angle were combined. For better visualisation, the spatial
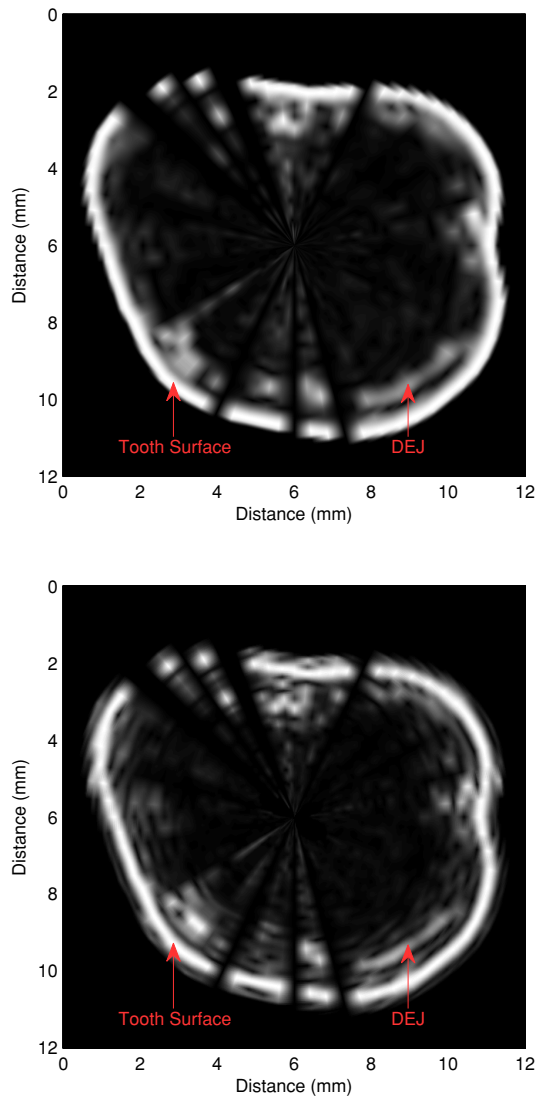
Figure 4.5: Ultrasound image of the tooth scanned with the LFM chirp and (Top) processed with a matched filter technique and (Bottom) processed with the FrFT technique. This scan is performed to determine the enamel thickness of the tooth by measuring the difference between the tooth surface and dentine-enamel junction (DEJ).

position of the tooth was recorded by the CNC and was used to offset the individual scan lines on the image. To plot the final ultrasound images, the measurement plot was converted from polar coordinates to Cartesian coordinates.

In Figure 4.5(top), the matched filter technique was used to compress the received ultrasound echoes. In Figure 4.5(bottom), the received signals were transformed to the fractional Fourier domain where the rotation angle was calculated by Eq. (3.15). The temporal information was recovered by scaling the time axis according to Eq. (3.16). By comparing these figures, it can be observed that the FrFT technique gives a better compression with a smaller main lobe width and hence better resolution in the final image, where the features of the tooth are more distinguishable such as the DEJ at the north-east of Figure 4.5(bottom).

For the tooth measurements, the received signal is attenuated not only because of depth and frequency dependant attenuation, but also because of scattering, dispersion and absorption (Barber *et al.*, 1969). The structure of the dental tissues absorbs and scatters the sound wave due to roughness and the irregular curved shape of the tooth. The overall effect on the received echo is degraded SNR, change in the envelope shape and reduced bandwidth, which will result in a discrepancy between the MF and chirp signal. This phenomenon was observed in the real tooth measurements. Figure 4.6 shows the worst case observed in the measurements, where it was not possible to measure the enamel thickness correctly with the compression achieved by the matched filter. In Figure 4.6(middle) the reflected echoes from enamel surface, enamel-dentine boundary and second reflection from enamel-dentine boundary appear as a single lobe after compression. In this case, the search algorithm, which uses the *findpeaks* function in Matlab to find the local maxima, located the false DEJ according to the second reflection from enamel-dentine boundary. However, in Figure 4.6(bottom) the compression achieved by the FrFT clearly separates each reflection. In this example, the advantage of the FrFT over the MF becomes more obvious; transforming the signals into the fractional Fourier domain gives a better compression and hence increases the probability of detection.

In order to compare the accuracy of the FrFT and the MF, the enamel thickness measurements processed with both techniques were plotted on the X-ray scan of the tooth, as shown in Figure 4.7. The registration of the Micro-CT slice with the ultrasound data was done by using the positional information of the transducer relative to
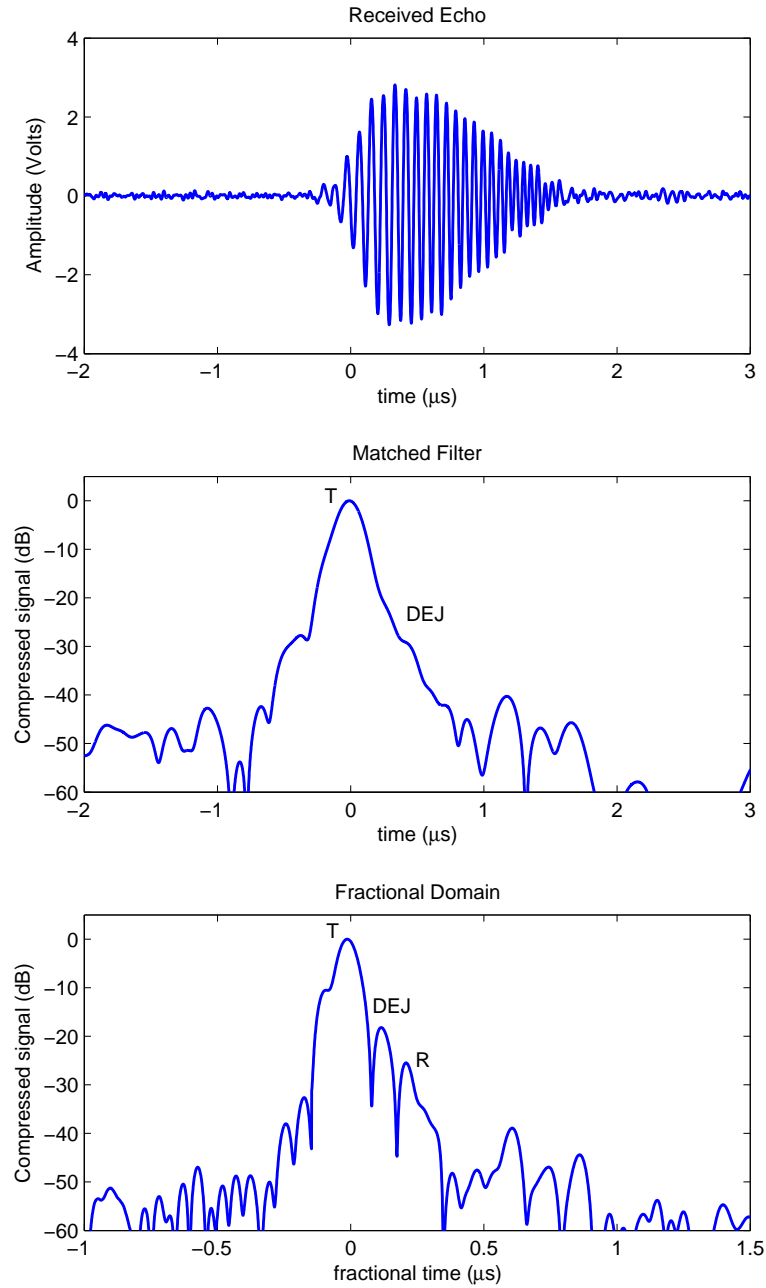
Figure 4.6: (Top) Received signal, (Middle) compressed with matched filter and (Bottom) signal transformed to the FrFT domain to achieve compression. (T) denotes the reflection from transducer tip and enamel boundary. (DEJ) denotes the reflection from dentine-enamel junction. (R) denotes the reverberation (secondary internal reflection) caused by the enamel-dentine boundary.

the tooth sample, which was controlled by the CNC system. In the Table 4.1 the typical acoustic properties of the materials used are shown. The thickness of the tooth layers were calculated according to these values by using the time-of-flight measurements.
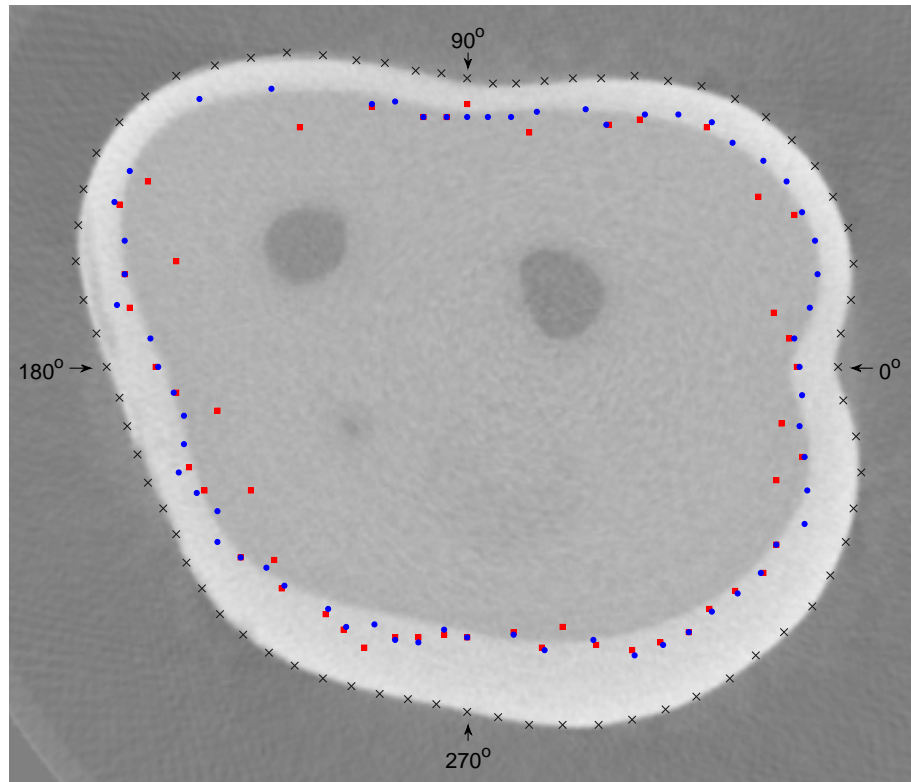
Figure 4.7: Figure shows the ultrasound enamel thickness measurements mapped on the Micro-CT image. Black crosses represent the outer surface of the tooth. Blue dots show the ultrasound measurements processed with the FrFT. Red squares show the ultrasound measurements processed with the matched filter. The image dimensions are 14 mm × 12 mm.

In the Figure 4.7, some measurement points between $115°$ and $145°$ are missing, because good contact between the enamel and the transducer tip could not be achieved due to the curvature of the tooth surface. A similar problem was also observed for the measurement points $70°$, $235°$, $275°$, and $290°$. The measurement data for these angles were discarded after checking the phase of the reflection from the enamel surface. The compression problem explained in Figure 4.6 was observed at $10°$, $30°$, $125°$, $160°$, $190°$, $210°$ and $340°$, which increases the error for the MF technique.

In order to compare the real values with the data processed by the FrFT and MF techniques, an edge detection algorithm was used to measure actual enamel thickness from the Micro-CT image. The edge detection was performed by the *edge* function based on the Sobel method in Matlab, which finds edges in the image using the Sobel approximation to the derivative of the Micro-CT data. The maximum relative error observed for the MF was 113% and the maximum absolute error was 860 μm, which was expected because of the aforementioned compression problem. However the maximum relative error for the FrFT was 33% and the maximum absolute error was 370 μm. The average relative error values are also calculated in order to make a fair comparison between the phantom and tooth measurements. The mean absolute error for the FrFT was 45 μm and the average relative error was calculated as 5.5%, which was higher than the 1.6% error achieved in the phantom measurements for the same technique. The mean absolute error calculated for the MF was 109 μm and the average relative error was 13.4%, which was more than double the error observed for the FrFT.

4.4 Discussion

In this work, time-of-flight measurement for a human molar was performed with a delay-line transducer in contact mode. The use of similar transducers, such as delay-line or thickness gauge, is common for dental measurements (Huysmans & Thijssen, 2000; Louwerse *et al.*, 2004; Yanıkoğlu *et al.*, 2000). Researchers, who used similar transducers, concluded that ultrasonic measurement of enamel thickness is feasible without any enamel preparation. This improves the *in-vivo* applicability of the proposed contact imaging technique, since teeth can be examined without cleaning or any further processing. Although, SAM can achieve better resolution and perform more accurate measurements (Marangos *et al.*, 2011; Raum *et al.*, 2007), it cannot be used practically for real-time *in-vivo* diagnostic imaging in dentistry.

The main limitation of this method, time-of-flight measurement, is that the velocity of the medium must be known *a priori*. However, without knowing the exact speed of sound in tooth layers, the average velocity values can be used with a cost of increased error. In this study, experiments were performed on two different samples; a phantom with known material properties and a human tooth. Tooth phantom measurements showed that the thickness of the glass and dental composite can be measured with a

1.6% error, where the average error increased to 5.5% for the real tooth sample using the FrFT technique. The average error for the matched filter was calculated as 3.6% for the tooth phantom and 13.4% for the real tooth measurements. The error for the FrFT technique is within the speed of sound variations observed for different tooth samples. The average speed of sound measured by several researchers is 6250 m/s with a deviation of $\pm$ 410 m/s (Barber *et al.*, 1969). In a study focused on enamel thickness measurements, researchers used an average speed of sound of 6500 m/s and reported an average error of 50 μm (Huysmans & Thijssen, 2000). This is similar to the mean absolute error of 45 μm for the FrFT technique observed in this study, which is based on using averaged speed of sound values.

For the experiments performed with human teeth, it is difficult to evaluate the accuracy of the measurement technique since this study was based on the average sound velocities in dental tissues. The speed of sound varies in different sections of enamel and dentine layers even within the same sample (Ghorayeb *et al.*, 2003). It was previously reported that there is a significant variance between measured tooth samples (Barber *et al.*, 1969; Ghorayeb & Valle, 2002). Additionally, ultrasonic wave propagation in human teeth is not trivial due to the anisotropic structure of tooth, where the speed of sound can vary within the same tooth in different directions (Ghorayeb *et al.*, 2003; Lees & Rollins, 1972). In Figure 4.7, for angles between 300° and 325° the ultrasound measurements did not match with the X-ray scan of the tooth. The reason for the mismatch is the anisotropic structure of the tooth. It was measured that the density of the enamel layer between these angles was 9% higher than the average enamel density. Rose *et al.* (2005) showed the correlation between sound velocity and bone mineral density in teeth, where higher mineral density increases the speed of sound. This is the reason why the enamel thickness was measured to be less in this region.

For *in-vivo* tooth measurements, the expected error will be similar with the *ex-vivo* measurements performed in this study. It is shown that by storing the tooth sample in aqueous solutions, the mechanical properties of the tooth samples can be protected (Raum *et al.*, 2007). The speed of sound will be similar for a moist extracted tooth and non-extracted tooth, where the hardness and the sound velocity of the tooth will crucially change after drying (Totah, 1942). In this study, the tooth sample was always stored in an aqueous solution in order to eliminate the drying effect. Temperature will be another important variable for the *in-vivo* and *ex-vivo* measurements. However, it

was proven by Huysmans & Thijssen (2000) that measurements performed at 21°C and 34°C do not have significant differences for a human incisor teeth.

4.5 Conclusions

In optics and signal processing the Fractional Fourier transform has many applications, although there are only a few examples of the application of FrFT in ultrasound (Bennett *et al.*, 2004; Cowell & Freear, 2010; Harput *et al.*, 2009). In this study, the ultrasonic non-destructive evaluation of human teeth using chirp coded excitation together with FrFT was performed. The FrFT was used for the first time to analyse the received echoes by separating chirp signals overlapping in both the time and the frequency domains in dental imaging. The proposed technique was used to measure the thickness of the enamel layer in human teeth. The results obtained with the proposed method was compared with a Gaussian pulse, which is the *de facto* standard in thickness measurements, and with a chirp excitation processed by a matched filter for pulse compression. The Gaussian pulse and the chirp waveform processed by a matched filter had an average error of 3.6%. The proposed method achieved more accurate results with an average error of 1.6%, since the chirp signal was transformed into the fractional Fourier domain and the temporal information was recovered by using Eq. (3.16) and Eq. (3.17). The results for different waveforms and compression techniques are presented in Table 4.2.

Besides measuring the thickness of tooth layers, other possible applications for this method could be locating cracks inside tooth and analysing the restoration faults under the fillings. Dentists rely on visual and endodontic examination methods or dental radiographs to diagnose cracked teeth. These methods are usually not effective in the early detection of cracks before the crack causes an infection (Culjat *et al.*, 2005a); however the coded excitation improves the detectability of small cracks by increasing the SNR. Another major problem encountered in dentistry is the bonding faults between dental composite and tooth. Conventional radiography cannot be used for imaging of radiopaque restoration material, but the ultrasound is able to penetrate into the hard structures and can detect cavities under existing restorations (Culjat *et al.*, 2003; Singh *et al.*, 2007). The proposed contact imaging method combined with coded excitation and the FrFT technique could be used as a diagnostic tool in dentistry to measure the

enamel thickness, locate the cracks inside the tooth and analyse the possible restoration faults.

Chapter 5

Detection of Restoration Faults under Fillings in Human Tooth

An ultrasound contact imaging technique for detecting the restoration faults under fillings in human teeth is proposed. A linear frequency modulated chirp signal is used to improve the signal-to-noise ratio and increase the penetration depth to allow the detection of the echoes from restoration-tooth boundary at 200 kPa acoustic pressure. Although the detection threshold is improved, it is observed that the duration of the excitation signal is longer than the duration of time of flight in the restoration, which causes signal overlapping between consecutive internal reflections. Due to these reverberations, the applied chirp signals interfere arbitrarily with the successive reflections, where the received echoes are not identifiable in the time domain. Separation in the frequency domain is not possible, since all reflections have the same bandwidth and centre frequency.

In this work, the Fractional Fourier transform (FrFT) is employed to separate chirp signals overlapping in both time and frequency domains. By analysing the received echoes with the FrFT, this work presents the ultrasonic non-destructive evaluation of dental restorations in human teeth.

5.1   Introduction

For dental imaging, conventional X-ray radiography and computed tomography (CT) remain dominant while micro-CT has been used for *in-vitro* applications achieving

a resolution of a few microns. The use of ultrasound in dentistry is not common even though the first diagnostic applications of ultrasound were described in the 1960s (Barber *et al.*, 1969; Ghorayeb *et al.*, 2008; Kossoff & Sharpe, 1966). In radiography, the primary limitations of X-rays are the risks associated with ionizing radiation and their inability to detect small cracks and faults in dental restorations. However, due to its non-ionizing nature and high resolution, ultrasound offers an explicit advantage over conventional radiography as an imaging technique in clinical dentistry (Culjat *et al.*, 2003; Ghorayeb & Valle, 2002; Löst *et al.*, 1992).

One of the major problems encountered in tooth restoration is the bonding faults between the restoration material and tooth. The restorative insertion placed in the tooth must completely reach the base and form a flawless bond, otherwise a cavity will be created inside the tooth, which can cause an infection requiring repetition of the restoration procedure (Ghorayeb & Valle, 2002). Small cavities are challenging for conventional X-ray imaging, because dental radiographs are usually not effective in the early detection but often rely on the subsequent damage after infection (Culjat *et al.*, 2005a). On the other hand ultrasound is highly effective in detecting discontinuities in the tooth, even if they are smaller than the acoustic wavelength. The advantage of ultrasound becomes more apparent if the restoration material is radiopaque and hence cannot be imaged by conventional radiography. Ultrasound however is able to penetrate the hard structures and can detect hard tissue pathosis and cavities under existing restorations (Culjat *et al.*, 2003; Singh *et al.*, 2007).

The aim of this work is to detect the possible restoration faults under fillings in human teeth using ultrasound. A linear frequency modulated chirp signal is chosen for excitation to increase the penetration depth. On the receiver side, the Fractional Fourier transform is used to filter the received echoes and separate overlapping LFM chirps.

5.2 Materials and Methods

5.2.1 Experimental Setup

A dentist performed two different restorations on an extracted human molar. Two cylindrical cavities were formed using a dental drill on the tooth crown with a depth of 2.4 mm. Dental composite Herculite XRV Unidose enamel (Kerr, Scafati, Italy) was
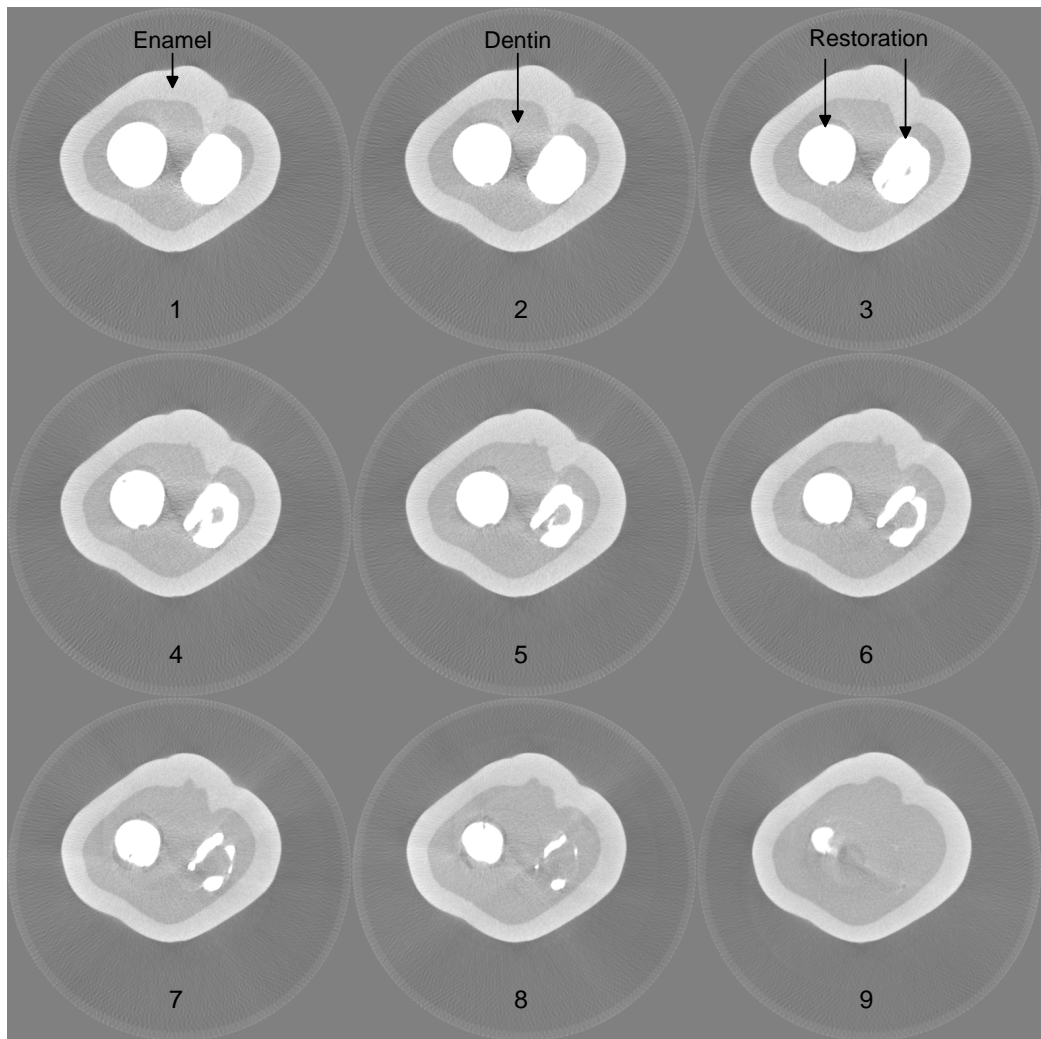
Figure 5.1: X-ray image of tooth with restorations. The enamel, dentine and restoration material appear in a different colour, since they all have different density values. Each scan is separated by 80 μm and the scan direction is from the crown to the root of the tooth. The restoration on the right has a cavity between the restoration material and the tooth sample.

used as the restoration material. For restoration **A**, a bonding agent was applied before filling the cavity with restorative material. For restoration **B**, in order to create a poor filling, the cavity was covered with glycerine. After filling the cavities, the restorative material was cured by UV light and the surfaces of the fillings were flattened using dental instruments. After the restoration process, the tooth sample was scanned by the X-ray scanner μCT 80 (Scanco Medical AG, Brüttisellen, Switzerland) with 40 μm resolution. Figure 5.1 shows the X-ray scan of the tooth with restorations. The shape of the filling on the left hand side of the X-ray image matches the cavity shape. However, for the filling on the right hand side it can be observed on the bottom of the cavity that it is not bonded well with the dentine.
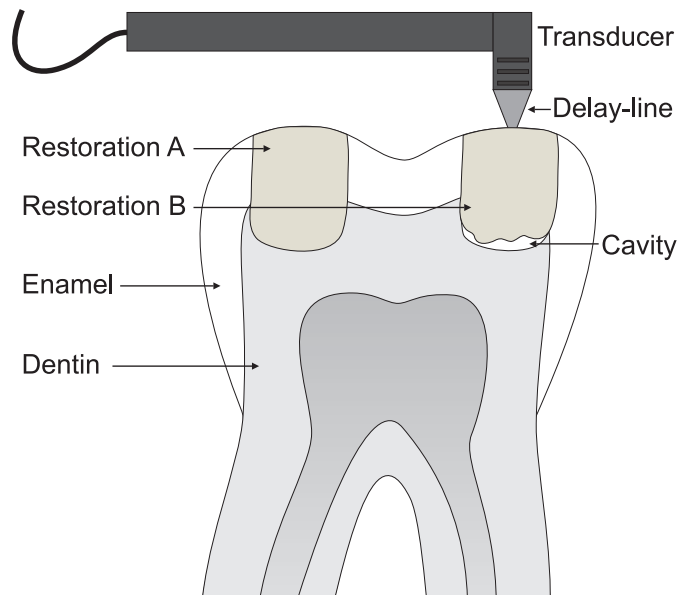
Figure 5.2: Experimental setup used for detection of restoration faults. The transducer is mounted to the moving arm of the CNC positioning system. The tooth sample is fixed by a metal profile to a stationary stage. The measurements are performed by using a glycerine couplant between the transducer's delay line and the tooth sample. Restoration **A** represents a good restoration and Restoration **B** represents a restoration with bonding problems.

The measurements were carried out with a 15 MHz Sonopen delay line transducer with 1 mm polystyrene tip (Olympus NDT Inc., Waltham, MA, USA) using a glycerine couplant in contact mode as shown in Figure 5.2. The excitation signal was designed to

match the transducer frequency response, and therefore a centre frequency of 14 MHz and a fractional bandwidth of 80% were chosen. The excitation voltage of 25 V was used with a signal duration of 2 μs, which generates a pressure of 200 kPa. The excitation signal was tapered with a Hann window to reduce the side lobe levels after compression. A 33250A Arbitrary Waveform Generator (Agilent Technologies Inc., Santa Clara, CA, USA) was programmed to generate the excitation signal and then amplified by using E&I A150 RF Power Amplifier (Electronics & Innovation Ltd., Rochester, NY, USA). The received signal was amplified by 50 dB with a Panametrics 5072PR (Olympus NDT Inc., Waltham, MA, USA) after separating the transmitted and received signals by a RDX-6 diplexer (Ritec Inc., Warwick, RI, USA). The received ultrasound echoes from the tooth sample were saved by a Waverunner 64xi oscilloscope (LeCroy Corporation, Chestnut Ridge, NY, USA) and the signals were processed in Matlab (Mathworks Inc., Natick, MA, USA). The contact mode imaging and the importance of glycerine couplant is explained by Harput *et al.* (2011b).

In order to perform the ultrasound scan, the tooth sample was fixed on a stationary stage and the transducer was held by a mounting frame on the high precision CNC positioning system. The tooth sample was scanned by the automated CNC with a step size of 0.5 mm through the surface of both fillings on the scan lines **A** and **B** as shown in Figure 5.3.

5.2.2 Filtering with the Fractional Fourier Transform

It was previously reported by Singh *et al.* (2007) that ultrasound can penetrate most of the dental restorative materials such as amalgam, resin-composite, porcelain and gold. However, the authors observed that gold restorations transmit minimal acoustic energy to the tooth behind the restoration due to their large acoustic impedance. In this study, a coded excitation technique is chosen to overcome such penetration problems.

Coded excitation has been effectively used in radar applications and medical ultrasound systems to improve the image quality (Misaridis & Jensen, 2005a). However, the use of coded excitation in echodentography is not common except some recent studies by Harput *et al.* (2009, 2011b). In this work, a LFM chirp is used as an excitation signal to improve the SNR and penetration depth.

The coded excitation improves the penetration and SNR, but introduces another problem when the duration of the ultrasound signal is longer than the time of the round
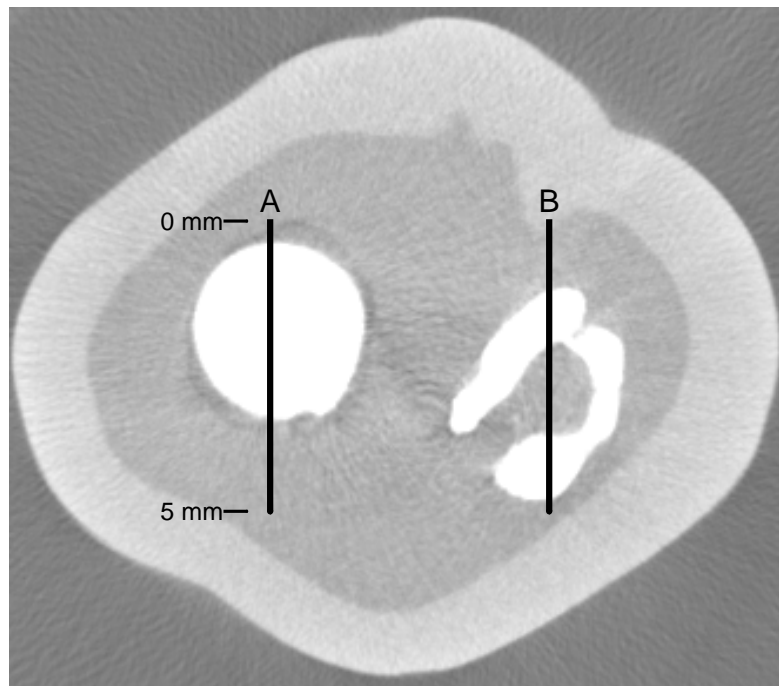
Figure 5.3: Scan lines for the ultrasound measurements are represented on an X-ray slice of the tooth sample. The transducer mounted on the moving arm of the CNC positioning system is moved between the 0 mm and 5 mm points with a step size of 0.5 mm. **A** represents the scan line for the good restoration and **B** represents the scan line for the restoration with bonding problems.

trip in the restorative material. Due to the signal overlapping inside the restorative material, the received echoes are not identifiable in the time domain. In the frequency domain all reflections completely overlap with each other, since they all have the same bandwidth and the centre frequency. The proposed solution in this work is to use the Fractional Fourier transform with long duration LFM chirp excitation. The FrFT allows frequency modulated signals overlapping in time and frequency to be separated.

To isolate individual chirp signals windowing is used in the fractional Fourier domain as explained in the section 3.2 and illustrated in Figure 3.2. As recently presented by Cowell & Freear (2010), after windowing in the fractional Fourier domain the waveform can be rotated by $-\alpha_{opt}$ degrees to restore the signal to the time domain hence extracting the chirp from overlapped data.

5.2.3 Calculating the Power of Received Echoes

The power level of the received echo can be estimated by using the acoustic impedance and attenuation coefficient of the medium in which the ultrasonic wave is travelling with the material properties given in Table 5.1. The transmitted ultrasonic wave into the restoration, which has exactly 3 dB less energy than the incident wave for this case, reflects from the back of the restoration-dentine boundary with different power levels according to the quality of the bonding.

The received signal power is reduced as determined by the reflection coefficient, Γ, and the reflected echoes are further attenuated by 1 dB/mm in the resin based restorative material. Therefore, the total power of the echo can be calculated as

$$\text{Received Power(dB)} = -10\log(\Gamma^2) - \text{Attenuation(dB)} \tag{5.1}$$

for

$$\Gamma = \frac{Z_1 - Z_0}{Z_1 + Z_0} \tag{5.2}$$

where the wave is propagating from a medium of impedance Z_0 into a medium of impedance Z_1.

The main problem with this type of techniques based on reflected power calculations is that the received signal must be compressed accurately. However for the tooth measurements, the received signal energy is still spread in time after compression with a matched filter (MF). The compression is not ideal, since the received signal is deformed because of frequency dependant attenuation, scattering and dispersion in tooth

layers and dental restorative material (Barber *et al.*, 1969). The overall effect on the received echo is usually observed as a change in the envelope shape and reduction in the bandwidth, which will result in a discrepancy between the MF and chirp signal. For this reason, rather than measuring the peak power of the compressed signals, the total power of individual echoes is calculated in the time domain after separating with the FrFT as

$$\text{Power} = \frac{1}{t_2 - t_1} \int_{t_1}^{t_2} s(t)^2 dt \, . \tag{5.3}$$

Table 5.1: Acoustic properties of materials

MATERIAL	Velocity (m/s)	Attenuation (dB/mm)	Impedance (MRayl)
Dentine	3800^d	8^c	7.6^d
Restorative Material	3530^a	1^a	14.5^a
Glycerine	1910^a	-	2.42^a
Delay-line, polystyrene	2310^a	0.18^b	2.47^a

[a] values are determined in our laboratory.

[b] values are taken from Kino (1987).

[c] values are measured by Kossoff & Sharpe (1966) at 18 MHz.

[d] values are compiled by Ghorayeb *et al.* (2008).

5.3   Experimental Results and Discussion

To separate the interfered chirp signals, the LFM measurements were processed either using the FrFT or the MF technique. The matched filter was chosen as a reference, since it is the most common method for filtering and compressing chirp signals as it optimizes the probability of detection and maximizes the SNR (Misaridis & Jensen, 2005a). The received signal, shown in Figure 5.4(top), was first processed with a matched filter. However, it was not possible to distinguish the reflection from restoration-dentine boundary clearly from the compressed signal shown in Figure 5.4(middle).
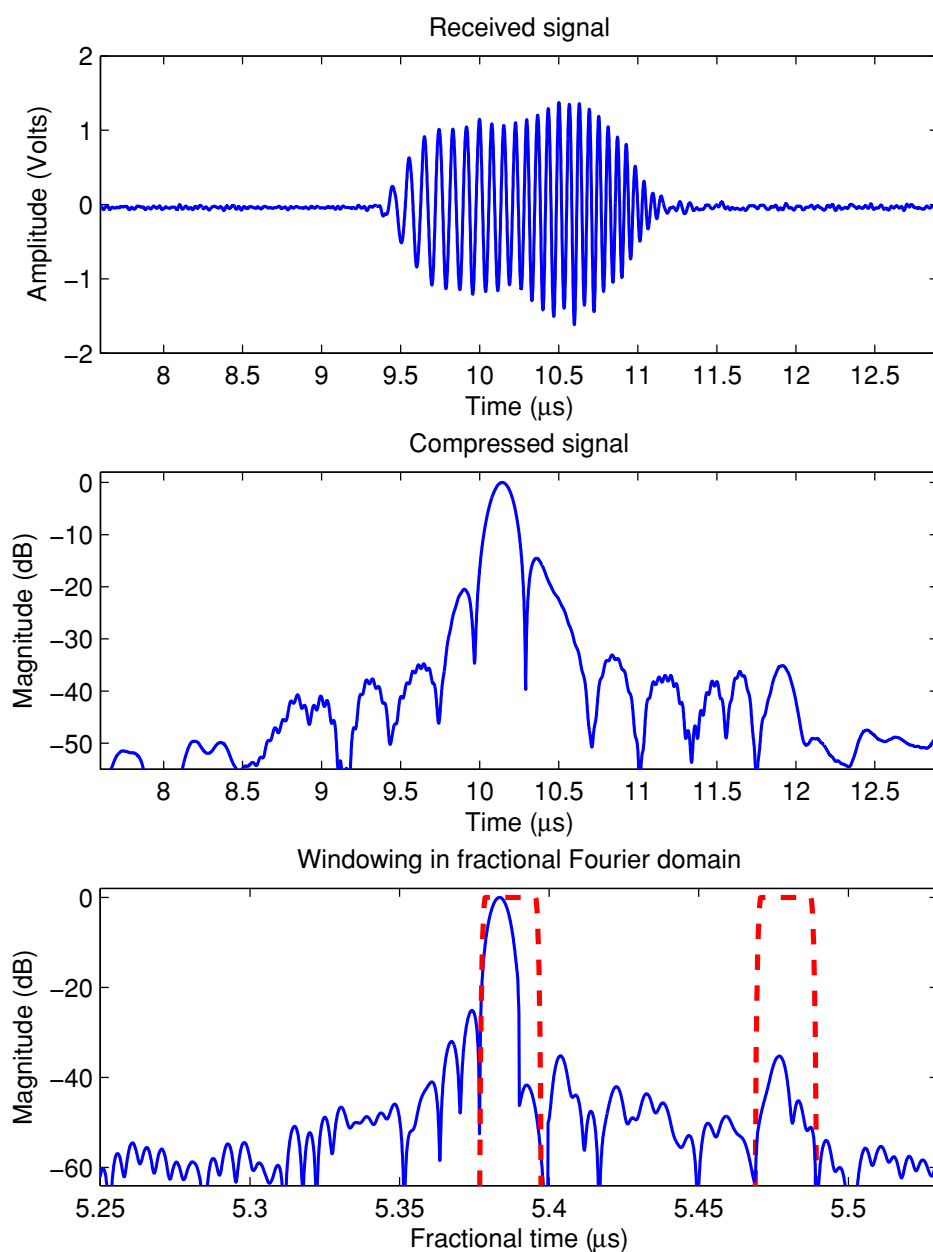
Figure 5.4: Figure shows (Top) the received signal from the restoration material, (Middle) compressed waveform with matched filter, (Bottom) the waveform transformed into the fractional Fourier domain. The dashed lines on the bottom figure show windows applied in the fractional Fourier domain.
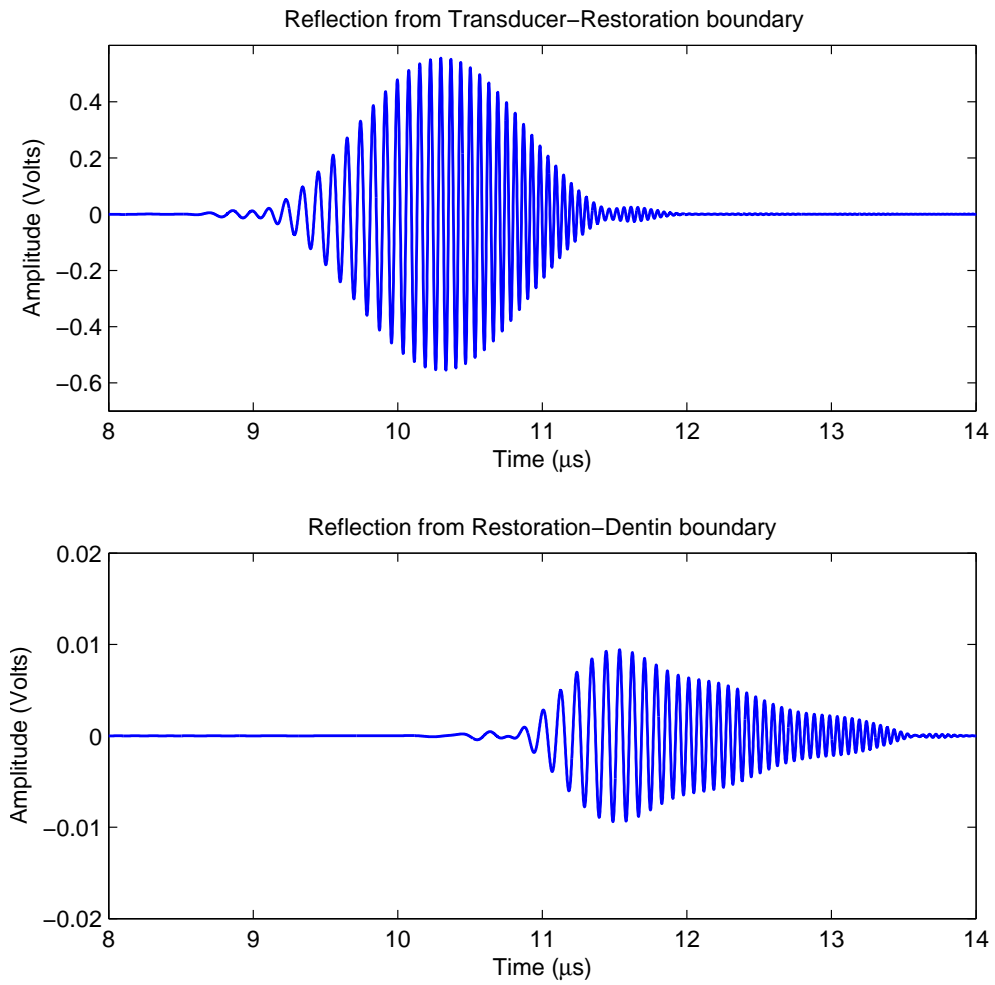
Figure 5.5: Received signal in the time domain after filtering in the fractional Fourier domain is shown. (Top) The filtered echo from the transducer-restoration boundary. (Bottom) The filtered echo from the restoration-dentine boundary.

The FrFT was performed at $\alpha = 1.336$ with the rotation angle calculated according to Eq. (3.15). Unlike the MF, the first echo from the transducer-restoration boundary and the second echo from the restoration-dentine boundary were clearly visible in the fractional Fourier domain. The individual echoes were separated by windowing as shown in Figure 5.4(bottom), and the filtered signal was transformed back to the time domain by applying the inverse FrFT. The separated chirps are plotted in Figure 5.5, where the total power of the signals were calculated by integrating in the time domain using Eq. (5.3).

The reflected echoes from the bottom of the fillings were normalized and the power level of the reflected echoes are plotted in Figure 5.6 for each scan lines.

By assuming a perfect reflector geometry, a threshold value of -14.91 dB is calculated for a good bonding according to Eq. (5.1) as

$$-10 \log \left(\frac{7.6 - 14.5}{7.6 + 14.5}\right)^2 - (1 \text{ dB/mm} \times 4.8 \text{ mm}) = -14.91 \text{ dB},$$

by using the material properties given in Table 5.1.

The maximum power of the reflected echo observed for the scan line **A** was -17.3 dB, which is below the threshold and does not indicate any bonding problems. For the scan line **B**, the echoes between 3.0 mm and 4.5 mm show the reflections from the bottom of the filling and the reflected power was between -13.1 dB and -7.8 dB. For restoration **B**, the reflections from the filling were always above the threshold for each scan point, which shows an adhesion problem between filling and tooth.

The level of reflected power indicates that the restorative material inside this filling is not bonded with the tooth. The calculation of the threshold for the echo power is possible with the knowledge of the average material properties of the restoration material and tooth.

The proposed fault detection technique was successfully validated on a real extracted human tooth. The simulated tooth restoration was realistic, since it was performed by a dentist using dental instruments and dental composites. In order to achieve a good contact with the restoration material, the surface of the restoration material was kept flat. For a real filling however, the surface of the restoration will have the complementary shape of the opposing tooth. This will significantly reduce the total surface area that can be used to achieve a good contact with the ultrasound probe. The accuracy of the proposed method will not be affected by the surface geometry of
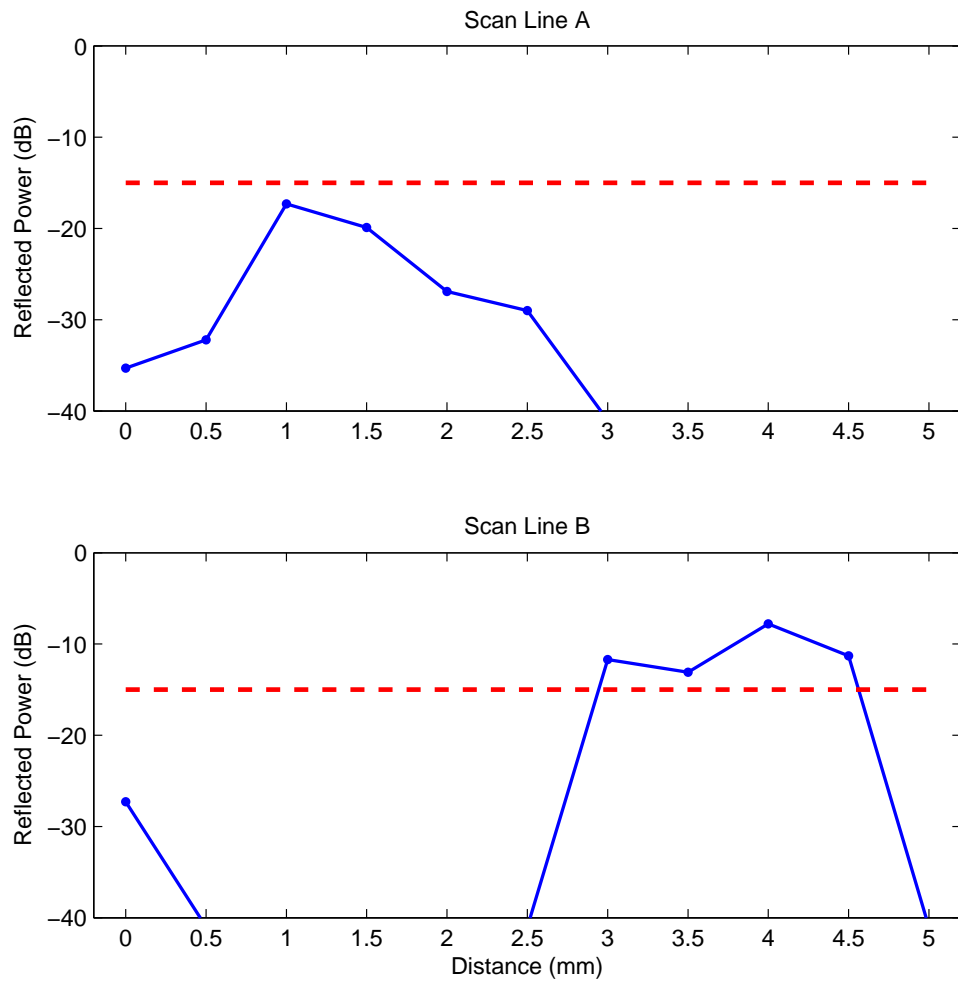
Figure 5.6: The reflected power from the bottom of the fillings (Top) for scan line **A** and (Bottom) for scan line **B**. Red dashed line shows the detection threshold for restoration failures. Signal power above this threshold indicates a bonding problem.

the restoration, but the efficiency will decrease since the proposed method is based on perfect reflector geometry. In order to increase the possibility of achieving a good contact and recovering the efficiency, a smaller delay line with a sharper tip can be designed and manufactured.

The main difficulty of using the proposed contact imaging system in practice will be the positioning system. In this study, the experimental measurements were performed by a CNC system which is impossible to use in clinical practice. This system must be modified and turned into a hand-held device that can be easily used by a dentist. Even though the current measurement setup is not suitable for practical use and cannot perform *in-vivo* scans, the proposed coded excitation method and signal processing technique is effective in detecting restoration faults.

5.4 Conclusions

Medical ultrasound is used for diagnostic imaging of almost all kind of soft-tissue structures in human body. The ultrasound is widely preferred since it is cheaper than other modalities, it does not use ionizing radiation, and it is safe and painless for the patient. However, the use of ultrasound as a diagnostic tool is not very common in dentistry. In this study, a contact imaging technique using a single element ultrasound probe was developed and the ultrasonic non-destructive evaluation of human teeth using chirp coded excitation was performed. The FrFT was used for the first time to analyse and filter the received echoes in dental imaging. The proposed technique was used for imaging purposes to detect restoration faults in human teeth and measure the thickness of the enamel layer as presented in chapter 4.

Radiography is currently the most dominant diagnostic imaging technique in dentistry. Dental X-ray scanners can achieve $50-100$ μm spatial resolution and the process takes from seconds to minutes for a single tooth (Farman & Farman, 2005). It is possible for ultrasound imaging systems to achieve faster frame rates and similar image resolution. The imaging method used in this work can easily resolve 200 μm in dental composite without any modifications and can scan a filling within a few seconds. However, the main advantage of ultrasound over radiography is the risks associated with ionizing radiation. Ultrasound is a non-ionizing modality and can be safely used for dental measurements.

Dental radiography is based on the absorption of X-rays and measures the density. Small discontinuities are challenging for conventional X-ray imaging, because dental radiographs are usually not effective in the early detection but often rely on the subsequent tissue damage after infection (Culjat *et al.*, 2005a). For this reason, radiography cannot accurately detect small cracks, air pockets and faults in dental restorations (Culjat *et al.*, 2003; Ghorayeb & Valle, 2002; Löst *et al.*, 1992). Ultrasound however, is based on the reflection of the acoustic waves and it detects the difference in acoustic impedance between the structures of the tooth. Therefore, the second advantage of the echodentography over radiography is the susceptibility of ultrasound in detecting discontinuities, even if they are smaller than the acoustic wavelength.

Another advantage of the ultrasound is the capability of imaging radiopaque materials, which cannot be imaged by X-rays. Ultrasound is cost effective, since the imaging systems and price of an individual scan are less expensive than radiography.

Beside having several advantages over radiography, echodentography has its limitations. The buccal and palatal surfaces, which are the sides of a tooth adjacent to the cheek and the palate, of the tooth are easy to make contact. Therefore, the proposed contact imaging method is suitable for imaging the buccal and palatal surfaces of the tooth. The proximal surfaces, which are adjacent to other teeth, however cannot be reached by the ultrasound probe and it is nearly impossible to image these sections. The occlusal surface, which is the direction towards the biting surface of posterior teeth, can be reached by the ultrasound probe but it is usually hard to make a good contact because of its irregular and uneven shape. For this reason, the proposed contact imaging method cannot attain the complete image of the tooth, since the ultrasound probe is unable to achieve a good contact with all surfaces of the tooth.

Part II

Soft-Tissue Ultrasound Imaging

It was demonstrated in chapter 4 and chapter 5 that the FrFT is an effective signal processing tool for separating chirp signals overlapping in both time and frequency domains. However, the reverberation artefacts and the separation of consecutive reflections are not an issue for soft-tissue imaging with chirps. The acoustic impedances of the fat, muscle, blood and internal organs are close to that of water, so they do not generate strong echoes. For this reason, the application of the FrFT for dental imaging with chirps as explained in the previous chapters cannot be directly employed for soft-tissue imaging.

In soft-tissue imaging, the attenuation is lower and the wavelengths are smaller due to the lower speed observed in soft tissue, but the image resolution and penetration depth are still an issue. For example, $2-3$ mm penetration will be sufficient for most cases in dental imaging, however a penetration depth of up to 300 mm may be necessary for abdominal imaging (Siemens AG, 2007). For such cases, high pressure low frequency wideband excitation will be the best candidate for optimizing the penetration depth and image resolution. Low frequencies will experience less attenuation. High pressure excitation will maximize the reflections from the features deep inside the body with likely generation of harmonics. Wideband signals will increase the axial resolution, but also cause spectral overlap between the fundamental and harmonic components.

Similar problems are also encountered in second harmonic imaging or tissue harmonic imaging, which can be considered as a commercial imaging standard (Rosenthal et al., 2001; Tranquart et al., 1999). Kim et al. (2001) used a wide bandwidth chirp signal for ultrasound harmonic imaging. The problem they have observed was the spectral overlapping between the fundamental and harmonic components which causes higher range sidelobes after pulse compression. The FrFT can still be employed to separate overlapping harmonic chirp components and suppress the compression sidelobe artefacts , but the signal processing becomes quite different to the case of hard-tissue imaging since the problem is not the separation of consecutive reflections any more.

In chapter 6 the FrFT was used to extract the second harmonic component by filtering in the fractional Fourier domain. The suppression of the fundamental chirp component was achieved for second harmonic imaging and the results were published by Arif et al. (2011). Chapter 6 also includes further improvements to the previous technique described in Arif et al. (2011).

Chapter 7 focuses on a new imaging modality called superharmonic imaging, where the common problems encountered in superharmonic imaging with chirps were published by Arif *et al.* (2010a). In this study, the signal processing was performed by using harmonic matched filters, which suffered from high sidelobe levels due to spectral overlap between the harmonics.

The transformations described in chapter 3 can be used to improve these results. Using the FrFT to separate the harmonic chirps however may not be practical for this application. Filtering in the fractional Fourier domain needs a clever windowing technique that must be applied manually or by using complex search algorithms. Also the process must be repeated individually for each harmonic component, which will increase the redundancy, computation time and accumulated error. Instead of computing several Fractional Fourier transforms, the FChT can compress all spectrally overlapping harmonic chirp components with one transformation. For this reason, a signal processing method based on the FChT is proposed in chapter 7 to improve the image quality in superharmonic imaging.

Chapter 6

Extraction of Spectrally Overlapped Second Harmonic using the Fractional Fourier Transform

In medical ultrasound imaging, the spatial resolution of an image is defined by the minimum resolvable distance between two points in space that can be distinguished by the system. The axial resolution of a coded excitation system can be improved by increasing the bandwidth of the excitation waveform. To improve the lateral resolution, the aperture size of the ultrasound probe or the excitation frequency[1] must be increased. Second harmonic imaging however can improve both lateral and axial resolution without changing the excitation bandwidth. The second harmonic image is formed by exploiting the second harmonic generated in tissue through nonlinear propagation, which effectively has twice the centre frequency and the bandwidth of the excitation waveform. In this study a linear frequency modulated chirp excitation is used for ultrasound harmonic imaging to improve the image resolution.

Even though the image resolution is better with second harmonic imaging, it is still desirable to use wideband excitation. Increasing the bandwidth will cause overlapping between the second harmonic component and the fundamental component of the received signal. For the spectrally overlapping harmonics, signal decoding using a

---

[1] Increasing the frequency of excitation effectively increases the aperture size in terms of wavelength.

matched filter typically produces higher range sidelobe levels, which reduces the image dynamic range.

In this study, the Fractional Fourier transform (FrFT) is used with chirp coded excitation for the extraction of the overlapped second harmonic component. The experimental results indicate at least a 13 dB improvement in the range sidelobe levels of the compressed second harmonic component when filtered in the FrFT domain. Later, these results have been found unsatisfactory and the filtering method with the FrFT has been altered in order to further improve the results.

6.1   Introduction

Medical ultrasound imaging techniques such as tissue harmonic imaging and contrast-enhanced harmonic imaging provide better spatial resolution by producing the image with the second harmonic component of the received signal. The extraction of the second harmonic from the received signal can easily be achieved by using a band-pass filter. Narrow-band signals are good candidates for this approach as the spectral boundaries of fundamental and second harmonic component are well separated; *i.e.* the second harmonic does not overlap with the fundamental component. However, using excitation signals with narrow bandwidths will result in poor axial resolution and decreased image quality.

The coded excitation has been applied to harmonic imaging and showed improvements over the pulsed excitation. Arshadi *et al.* (2007) reported that when applying coded excitation methods to ultrasound harmonic imaging the spatial resolution can be improved. Song *et al.* (2010) applied coded excitation for ultrasound tissue harmonic imaging for sidelobe reduction. They observed that the coded excitation with pulse inversion gives better suppression of peak sidelobe levels for tissue harmonic imaging.

Pulse inversion is a commonly used multi-pulse detection scheme that can be used to extract the second harmonic component (Burns *et al.*, 2000b). Pulse inversion requires the transmission of two consecutive pulses; the waveform itself and the complementary waveform with a relative phase of 180°. Summation of the two received echoes will result in the suppression of odd harmonics and of the linear fundamental frequency component mainly generated by the tissue whilst enhancing the second harmonic response. The suppression can be achieved even for wide bandwidth signals with spectral overlap

amongst the harmonic components. However, the main drawbacks of the pulse inversion are the reduction of the system frame-rate by a factor of two and the fact that the complete cancellation of the fundamental component under tissue motion cannot be achieved (Arshadi *et al.*, 2007; Cobbold, 2007; Shen & Li, 2002). Therefore, coded excitation technique is chosen to provide improved SNR and penetration depth with a single transmission which will not reduce the system frame-rate and therefore will be less susceptible to tissue motion (Chiao & Hao, 2005).

In this work, a wideband linear frequency modulated chirp excitation is used to achieve high spatial resolution. For wideband excitation, a spectral overlap between the second harmonic and the fundamental components of the received signal is inevitable. In this case, signal decoding using the second harmonic matched filter (SHMF) typically produces higher range sidelobe levels. Therefore, the FrFT is proposed as a filtering tool, with wideband chirp coded excitation, for the extraction of the overlapped second harmonic component.

6.2 Materials and Methods

In order to validate the proposed method, experiments were conducted both in transmission and pulse-echo configurations. The first experiment was performed to validate the accuracy of the technique. The second experiment in pulse-echo configuration was performed to analyse to feasibility of the proposed technique for real applications by comparing B-mode ultrasound images.

6.2.1 Experimental Setup and Procedure

Experimental Setup-I: In a transmit-receive configuration, a transducer was aligned coaxially with a 1 mm needle Polyvinylidene Fluoride (PVDF) hydrophone (Precision Acoustics Ltd., Dorchester, UK) at a distance of 110 mm in a water tank using a custom built computer numerical control (CNC) system. A 2.25 MHz single element V323-SM immersion transducer (Olympus-NDT Inc., Waltham, MA, USA) was used as a transmitter as shown in Figure 6.1. A 33250A Arbitrary Waveform Generator (Agilent Technologies Inc., Santa Clara, CA, USA) was set to generate a Hann windowed linear chirp with a centre frequency of 2.25 MHz, duration of 10 μs, and bandwidth of 2 MHz as the excitation signal. The signals were amplified by an A150 E&I RF Power Amplifier
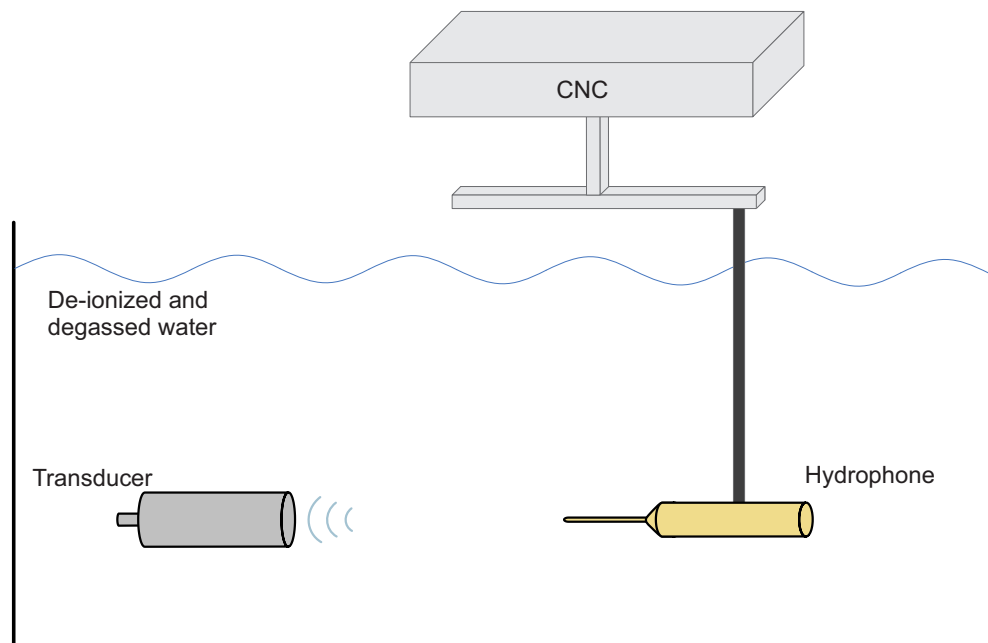
Figure 6.1: Schematic diagram of the experimental setup-I. The experiments are performed in a tank filled with de-ionized and degassed water. The alignment of the transducer and the needle hydrophone is performed by a CNC system.

(Electronics & Innovation Ltd., Rochester, NY, USA) to generate 340 kPa peak negative pressure in water. The signals received by the hydrophone were acquired at 100 MHz sampling rate using a Waverunner 44xi oscilloscope (LeCroy Corporation, Chestnut Ridge, NY, USA). The captured data was stored in a computer and processed off-line using the Matlab software (MathWorks Inc., Natick, MA, USA). The received echoes were corrected using an inverse filter designed in Matlab according to the frequency response of the hydrophone.

The distance, excitation frequency, and pressure levels for this experiment were chosen specifically to generate a second harmonic to fundamental ratio of −15 dB. The calculations were performed according to appendix B. The −15 dB figure was selected according to previous work by other researchers, where a second harmonic to fundamental ratio between −20 dB to −10 dB was reported (Burns *et al.*, 2000a; Couture *et al.*, 2008; Ma *et al.*, 2005).
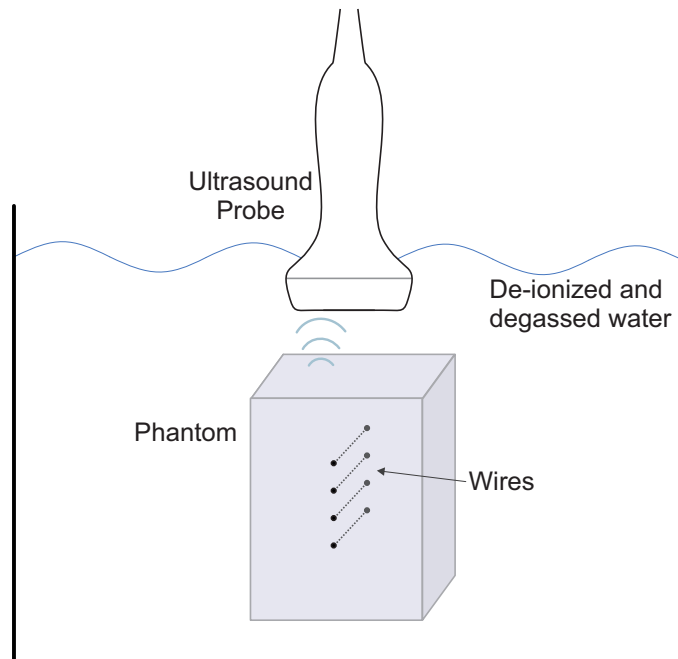
Figure 6.2: Schematic diagram of the experimental setup-II. The experiments are performed in a tank filled with de-ionized and degassed water. A commercial ultrasound probe connected to the UARP is used to scan the wire phantom.

Experimental Setup-II: In a pulse-echo configuration, an L3-8/40EP medical

probe (Prosonic Co., Korea) was used to scan the wire phantom as shown in Figure 6.2. The wire phantom consisted of four 120 μm thick aluminium wires within tissue mimicking material, which was prepared by mixing 3% (36 gr.) Agar powder (Sigma-Aldrich Co., Buchs SG, Switzerland) and 97% de-ionized water by volume. The wires were located at a depth of 42 mm, 50 mm, 60 mm, and 70 mm, where the first wire was mis-located during the manufacturing process. The focal depth was set to 55 mm, which was the centre of the wire phantom.

The medical probe was connected to the Ultrasound Array Research Platform (UARP) to perform a linear scan of the phantom. The UARP is a custom 96 channel ultrasound imaging system developed by the Ultrasound Group at the University of Leeds (Smith *et al.*, 2010, 2012), specifically for the research environment. The photograph of the instrument is given in Figure 6.3. The UARP was designed to be an highly flexible system based on an Altera Stratix III FPGA (Altera Corporation, San Jose, CA, USA), in order to support various ultrasound applications from non-destructive testing (NDT) to medical ultrasound imaging. The transmitter front-end architecture and the switched-mode MOSFET excitation method was previously described by Cowell & Freear (2008); Smith (2013). The UARP is capable of simultaneous excitation on 96 channels with arbitrary waveforms and transfer of the received raw RF data from individual channels to a computer.

For this experiment, the UARP was programmed to generate a Hann windowed linear frequency modulated chirp with a centre frequency of 3.5 MHz, duration of 10 μs, and bandwidth of 3 MHz.

The captured data was stored in a computer and processed off-line using the Matlab software (MathWorks Inc., Natick, MA, USA). All received signals were corrected using an inverse filter designed in Matlab according to the frequency response of the medical probe.

6.2.2 Extraction of the Second Harmonic using the FrFT

The FrFT was used as a filtering tool to extract the second harmonic component as explained in section 3.2. The received echoes with the hydrophone or the RF signals received by the individual array elements were processed in the fractional Fourier domain before pulse compression. The time domain signal was transformed into the fractional Fourier domain, where the transform order α_{opt} was calculated according to

Figure 6.3: University of Leeds 96-channel Ultrasound Array Research Platform (UARP) system. The front panel of the UARP is removed for this photograph.

the excitation waveform using Eq. (3.15). In the fractional Fourier domain, the second harmonic component was extracted by applying a window, which acts like a band-pass filter. The extracted second harmonic was transformed back to the time domain using the FrFT with a transform order of $-\alpha_{opt}$. The extracted second harmonic was then decoded using the SHMF in order to perform pulse compression to restore axial resolution. The SHMF was designed with twice the centre frequency and bandwidth of the fundamental component by using the same window function applied to the excitation signal (Borsboom *et al.*, 2003; Misaridis & Jensen, 2005a). Extraction of the second harmonic components both with the FrFT filtering and without the FrFT filtering is explained in Figure 6.4.

6.2.3 Fundamental and Harmonic B-mode Images

The phantom geometry can be studied from grey-scale B-mode images, where the reflection and scattering from individual wires are displayed. Since the geometry of the wire phantom is known, the image quality can be compared for the ultrasound image before and after filtering by the FrFT.

Time Domain Signal

Matched Filter

Pulse Compressed Signal

Time Domain Signal

FrFT

Filtering

iFrFT

Matched Filter

Pulse Compressed Signal
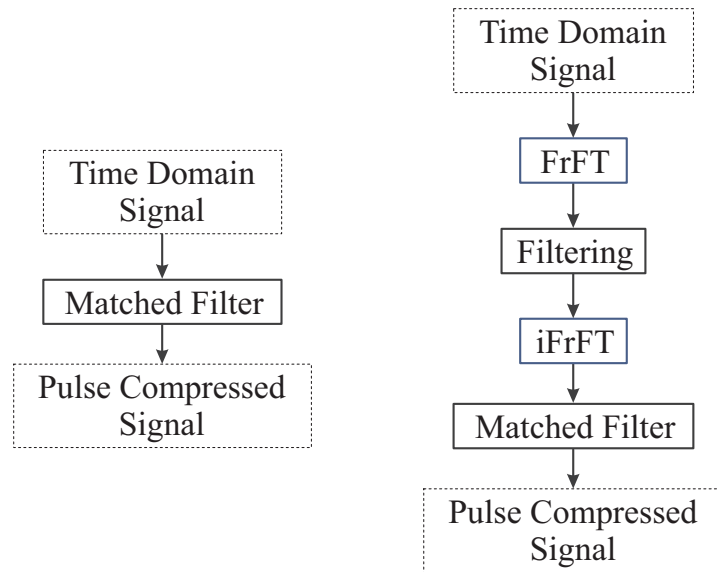
Figure 6.4: (Left) Diagram illustrates the pulse compression method by a matched filter. The time domain signal is convolved with a matched filter to achieve pulse compression. (Right) Diagram illustrates the filtering method by the FrFT. First, the time domain signal is transformed into the fractional Fourier domain, where the compression is achieved. Second, the signal is filtered in the fractional Fourier domain. Third, the filtered signal is transformed back to the time domain. As the last step, the time domain signal is convolved with a second harmonic matched filter to achieve pulse compression.

In order to form the B-mode images, the medical probe was used to perform a linear scan. The 96 element array was divided into 49 sub-apertures, which were consisted of 48 elements. E.g. the first sub-aperture includes the array elements $1 - 48$, the second sub-aperture includes the array elements $2 - 49$. Each sub-aperture was used to transmit a delayed version of the excitation waveform to generate a focussed acoustic pressure field at a predetermined depth. The waves reflected by the acoustic impedance mismatch caused by the presence of the wires were received by the same sub-aperture. The raw RF signals received by the individual array elements were filtered by the proposed method. The processed echo signal from 48 elements was combined by using a delay-and-sum beamforming technique. After acquiring the first scan line with the first sub-aperture, the same procedure was repeated with the second sub-aperture. To form a B-mode image 49 scans were performed. Therefore the final ultrasound image maps the strength of the reflected echoes to image intensity, the time delay between the echoes to axial distance, and the physical position of the sub-apertures to lateral distance.

Later, the pulse compression was performed on each beamformed scan lines by using a matched filter or a harmonic matched filter to form a fundamental or a harmonic B-mode image, respectively. The 49 scan lines were combined to form a single image, which was normalised and log-compressed to generate the final B-mode ultrasound image. The dynamic range of the image was set to 40 dB and linearly mapped to 64 levels of grey scale values, where 0 dB was encoded as white and -40 dB was encoded as black.

6.3 Experimental Results and Discussion

The received signal acquired with experimental setup-I in transmit-receive configuration is shown in Figure 6.5. Figure 6.6 shows the power spectrum of the received signal, where the fundamental component is centred at 2.25 MHz and the second harmonic component is centred at 4.5 MHz. The spectral overlap between the fundamental and second harmonic components may not be clear in the Figure 6.6, however a spectral overlap at the frequency range of $2.5 - 3.25$ MHz was expected. The excitation waveform was generated to sweep the bandwidth of $1.25 - 3.25$ MHz and the second harmonic component had an *estimated* bandwidth of $2.5 - 6.5$ MHz as explained in appendix B.
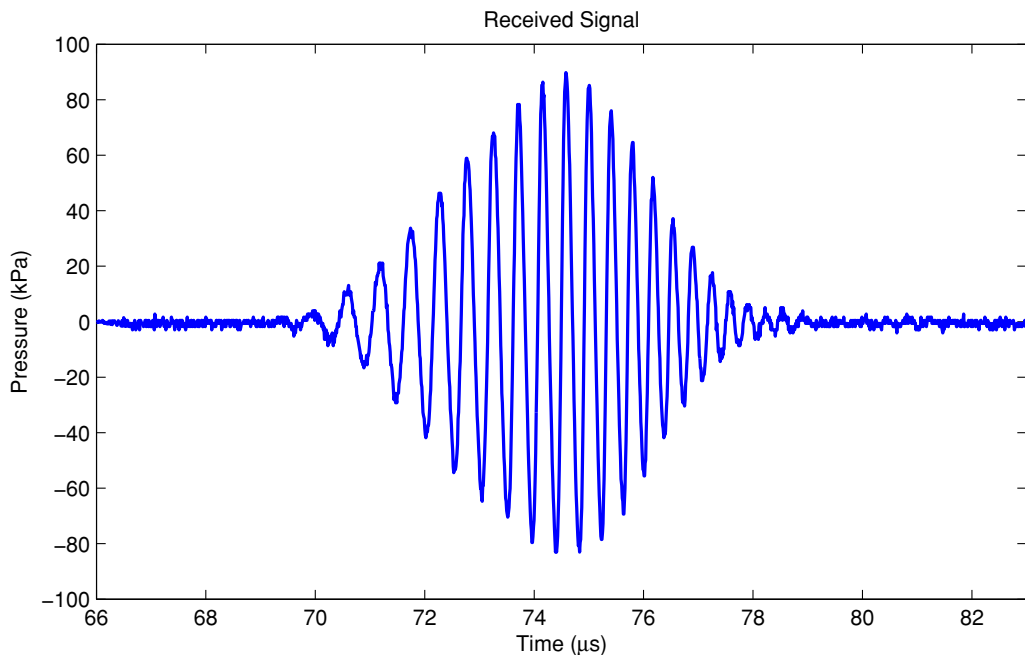
Figure 6.5: The received signal acquired with experimental setup-I is shown. The excitation signal is a Hann windowed linear chirp with a centre frequency of 2.25 MHz, duration of 10 μs, and bandwidth of 2 MHz.
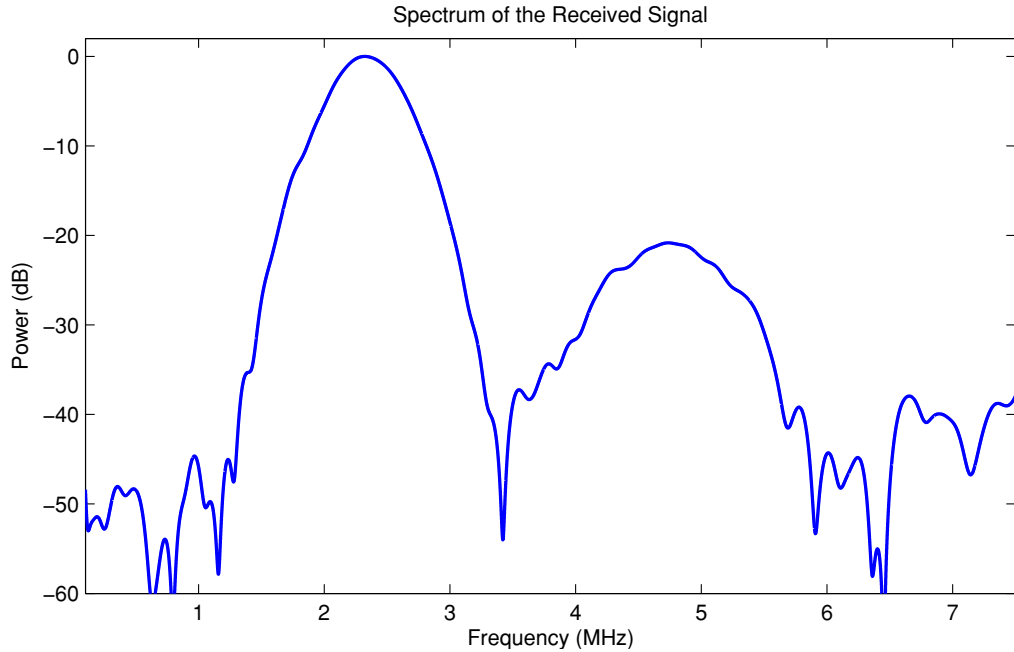
Figure 6.6: Frequency spectrum of the received signal acquired with experimental setup-I is shown.

To separate the overlapped harmonics, the received signal was transformed into the FrFT domain with a transformation order of $\alpha = 1.2422$. The value of α was computed according to the excitation chirp rate $\sigma = 0.2$ MHz/μs. The fractional Fourier domain signal after the transformation is shown in Figure 6.7. In the fractional Fourier domain, maximum compression for the fundamental component of the excitation waveform was achieved and the second harmonic component was separated. Any bandpass filter applied in the frequency domain (Figure 6.6) would either reduce the bandwidth of the second harmonic or will not completely filter the fundamental, in the fractional Fourier domain (Figure 6.7) however the second harmonic can be extracted without any energy loss.

The second harmonic component was then extracted by the application of a rectangular window as depicted in Figure 6.7. The extracted second harmonic signal was transformed back to the time domain by computing the FrFT with a transform order of $\alpha = -1.2422$. The extracted second harmonic component in the time domain with twice the chirp rate of the excitation waveform is shown in Figure 6.8.

The effect of the FrFT filtering on the pulse compression was evaluated by decod-
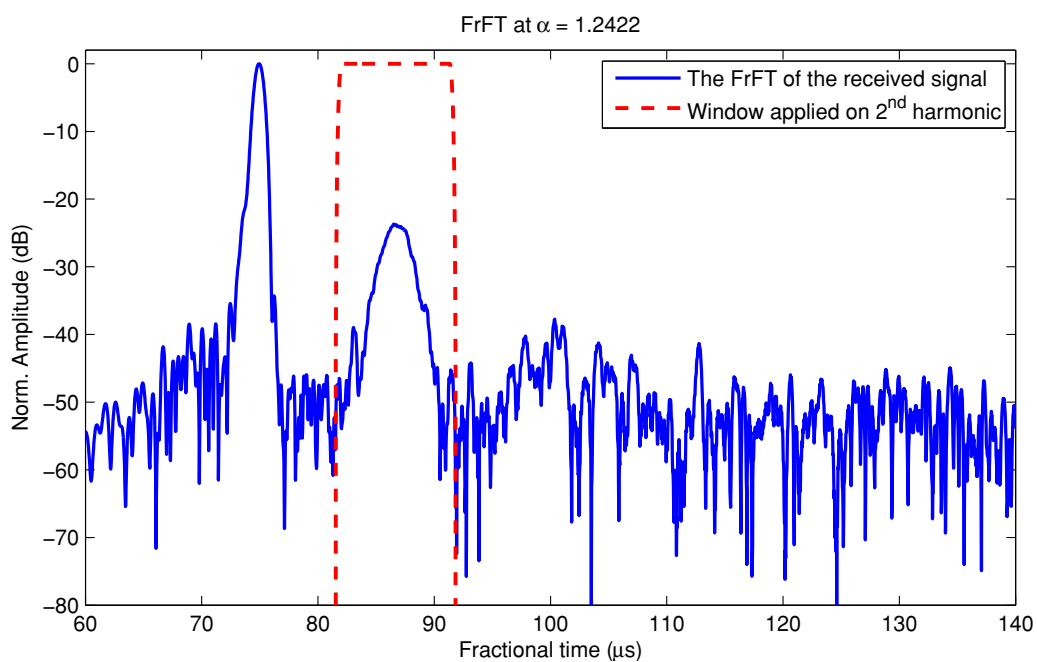
Figure 6.7: Figure shows the received signal in the fractional Fourier domain with the transformation order of $\alpha = 1.2422$. The red dashed lines show the window applied around the second harmonic component for filtering.
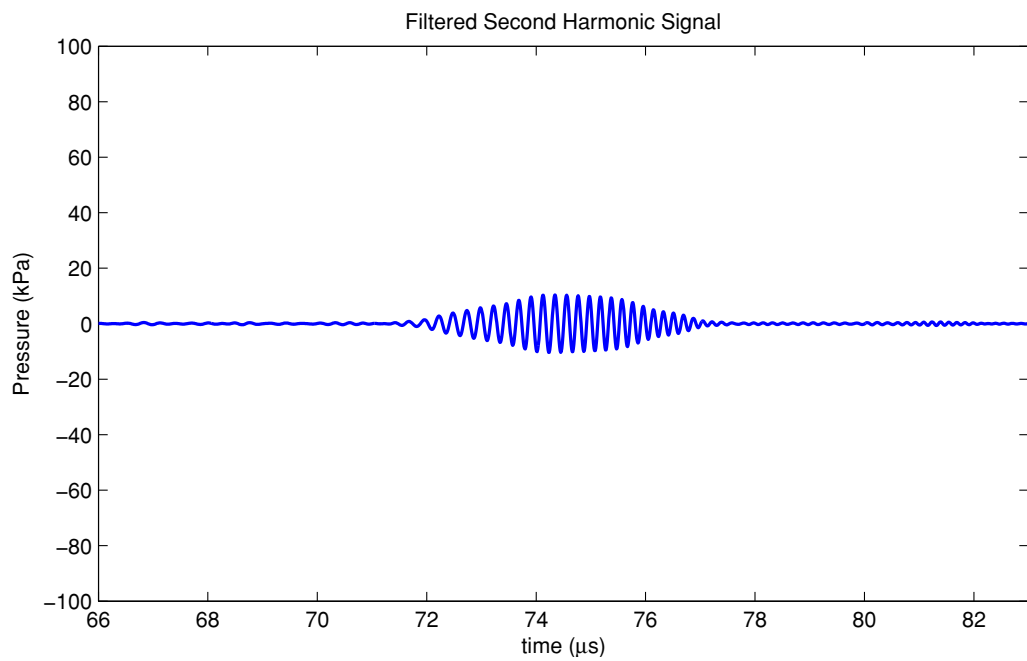
Figure 6.8: The extracted second harmonic component is shown in time domain. The FrFT is applied with a transformation order of $\alpha = -1.2422$ on the signal windowed in the fractional Fourier domain as shown in Figure 6.7.

ing the extracted second harmonic chirp signal using the harmonic matched filtering technique. Figure 6.9 shows the effect of the FrFT filtering on the compressed second harmonic chirp signal. The un-filtered compressed second harmonic signal exhibits a peak sidelobe level of -15 dB, whereas the FrFT filtered compressed second harmonic signal exhibits a peak sidelobe level of -32 dB. The reason for the higher sidelobe level in the un-filtered compressed signal is the spectral overlapping between fundamental and second harmonic components. An extra 17 dB reduction in the peak sidelobe level has been achieved on the compressed second harmonic chirp signal by filtering in the fractional Fourier domain, when compared with the un-filtered compressed signal.
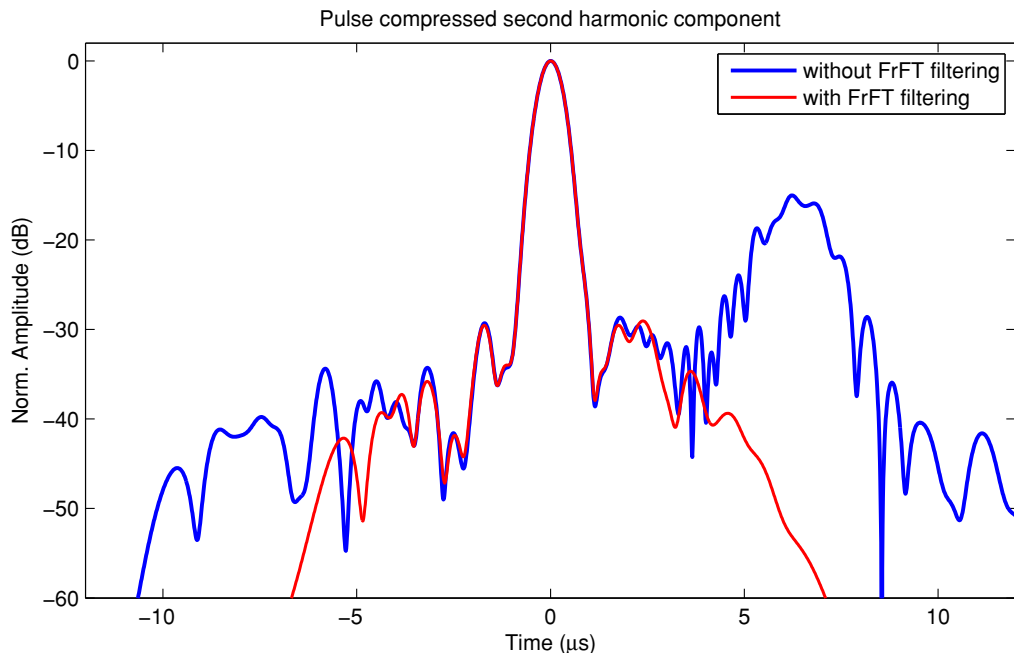
Figure 6.9: Pulse compression of the un-filtered signal and of the extracted second harmonic component after filtering with the FrFT are shown. The pulse compression is performed by a second harmonic matched filter, which is designed with twice the centre frequency and bandwidth of the excitation signal.

After verifying the validity of the proposed filtering technique, new measurements were performed by using the UARP on a wire phantom. The received signals were filtered by using the FrFT and the extracted second harmonic chirp signal was decoded using the SHMF. The FrFT filtered and un-filtered compressed second harmonic chirp signals are shown in Figure 6.10.
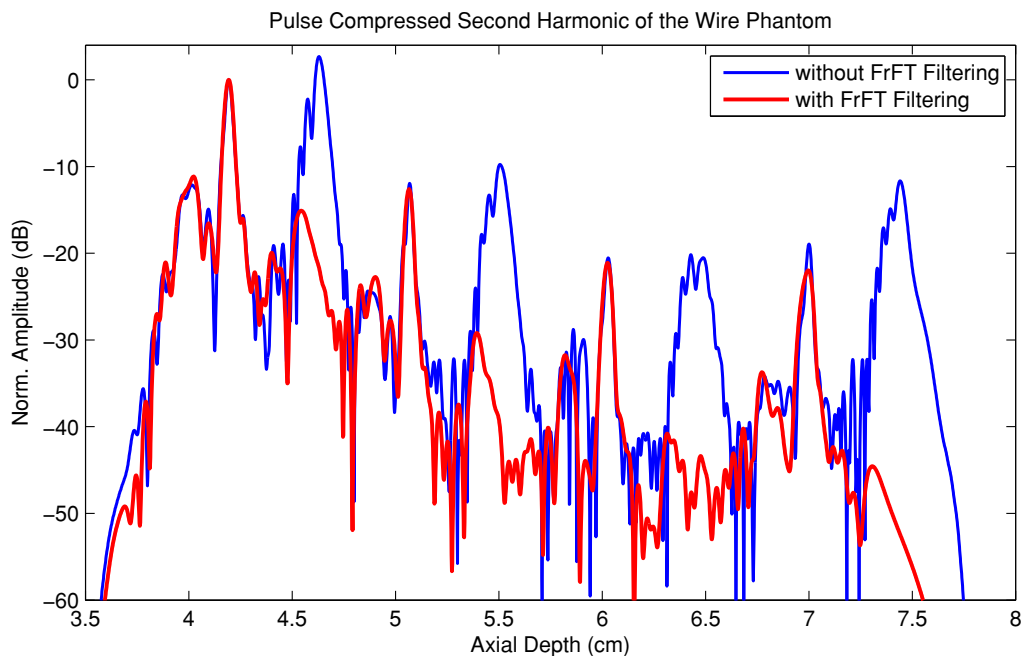
Figure 6.10: Figure shows the pulse compressed second harmonic component of the received signal for the measurements performed with the wire phantom. Pulse compression of the un-filtered signal and of the extracted second harmonic component after filtering with the FrFT are shown for comparison. The pulse compression is performed by a second harmonic matched filter, which is designed with twice the centre frequency and bandwidth of the excitation signal.

For this measurement, filtering by the FrFT was not as effective as the previous experiment. Both fundamental and second harmonic components suffered spectral energy loss, because of the narrower bandwidth of the transducer as compared to the hydrophone. A significant reduction in peak sidelobe level and fundamental suppression were observed in the FrFT-filtered compressed second harmonic chirp signal when compared with the un-filtered compressed signal. However, the complete cancellation of the fundamental component could not be achieved, which can be observed in Figure 6.10 at 45 mm and 54 mm.

6.4 Further Improvements to the Existing Study
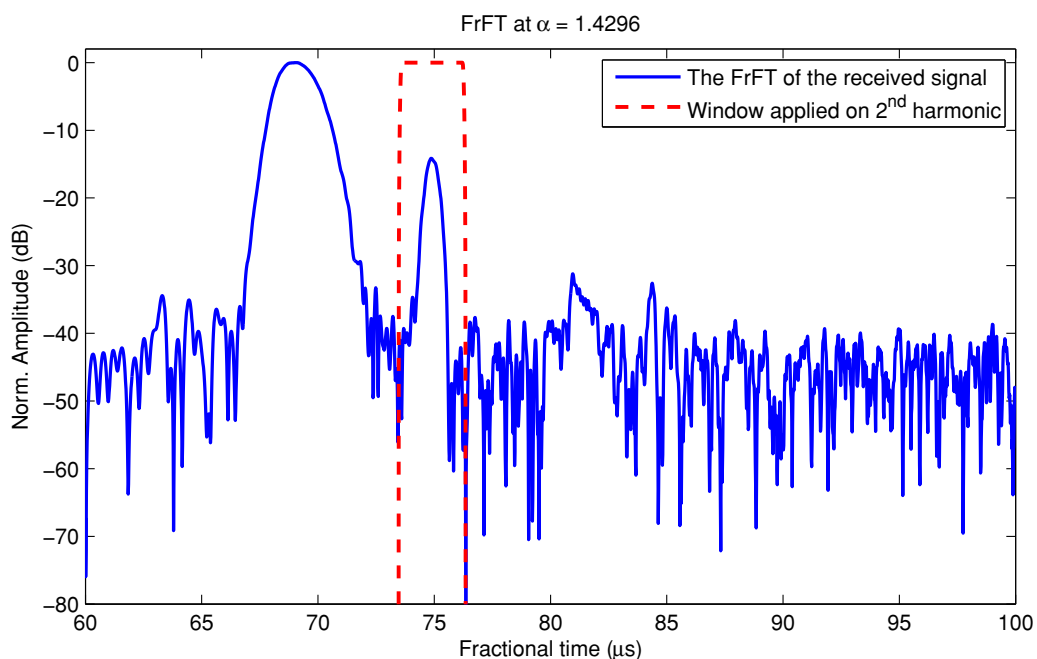
Figure 6.11: Figure shows the received signal in the fractional Fourier domain with a transformation order of $\alpha = 1.4296$. The red dashed lines show the window applied around the second harmonic component for filtering.

This work has been published in the proceedings of IEEE Ultrasonics with the results presented in the previous section (Arif *et al.*, 2011). Despite the aforementioned technique showing improvements over conventional filtering methods, there was a flaw in the extraction process. The optimum transform order α_{opt} was calculated according

to the excitation waveform, not according to the second harmonic component to be extracted. In this section, the flow of the second harmonic extraction sequence was kept the same, however the transform order α was calculated according to the expected chirp rate of the second harmonic, $\sigma = 0.4$ MHz/μs.

After re-calculating the transform order as $\alpha = 1.4296$, the maximum compression for the second harmonic was achieved in the fractional Fourier domain as shown in Figure 6.11. By achieving a better compression, a narrower window can be applied over the second harmonic component, which results in lower sidelobe levels and minimal contribution from the other frequency components.
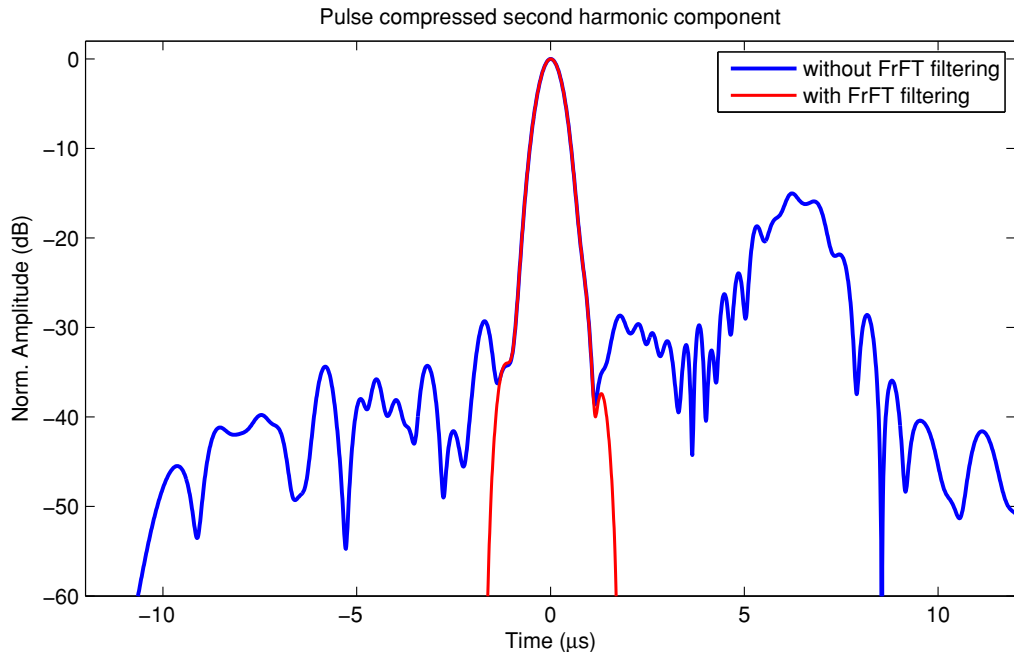
Figure 6.12: Pulse compression of the un-filtered signal and of the extracted second harmonic component after filtering with the FrFT are shown. The pulse compression is performed by a second harmonic matched filter, which is designed with twice the centre frequency and bandwidth of the excitation signal.

The second improvement over the previous technique was the automation of the filtering process by computing the second harmonic location in the fractional Fourier domain. The signal processing described in the previous section was performed manually. To extract the second harmonic component a window was applied in the fractional Fourier domain, after manually finding the location of the second harmonic. However,

by changing the transform order to compress the second harmonic component, it is now possible to estimate the location of the second harmonic in the fractional Fourier domain.

The relation between the fractional time and time axes was calculated by using the Eq. (3.16) and Eq. (3.17), so a window can be automatically applied on the signal of interest. The compressed second harmonic component will have the same temporal location with the received signal, after scaling the fractional time axis and removing the offset. Since the received signal is centred around $t = 74.8\ \mu$s as shown in Figure 6.5, the compressed second harmonic component appears at the fractional time of $t = 74.8\ \mu$s as shown in Figure 6.11. A similar relation can also be observed in Figure 6.7 for the fundamental component, since the figure was re-processed and the fractional time axis was re-calculated for consistency.

After verifying the accuracy of the new filtering technique, the measurements performed with the wire phantom were re-processed. A peak detection algorithm, which uses the *findpeaks* function in Matlab to find the local maxima, was used to detect the locations of the reflectors from the fundamental image, as in Figure 6.13. The locations of these peaks were used to generate windows in the fractional Fourier domain around the second harmonic components. By using these locations, including the ghost locations, the received signal was filtered in the FrFT domain. The ghost objects do not result in a compressed second harmonic component in the fractional Fourier domain, since they are just compression artefacts.

Figure 6.14 shows the image data compressed by using a second harmonic matched filter. Figure 6.15 was filtered by the FrFT before compression by the second harmonic matched filter. When the two images are compared, the effectiveness of the filtering in the fractional Fourier domain becomes obvious. Even though, the FrFT successfully filtered out the range sidelobes generated due to the spectral overlapping, it did not reduce the peak sidelobe level for all scatterers. The range and near-field sidelobe levels of the wires located at 50 mm and 60 mm were improved, since they were closer to the focal point of the acoustic beam. However, for the wires located at 42 mm and 70 mm, the near-field sidelobe levels were the same before and after filtering with the FrFT. The reason for this is the beamforming algorithm used to form the ultrasound images, where the received echoes from each array element was not perfectly aligned for the
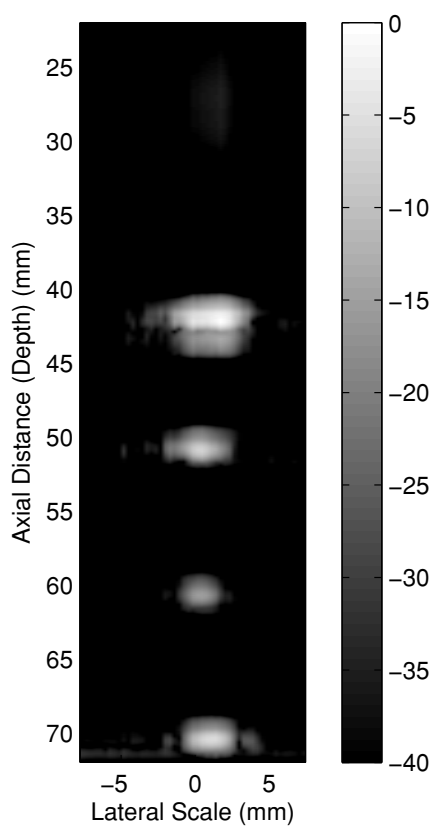
Figure 6.13: Fundamental image of the wire phantom is shown with a 40 dB dynamic range. The received signal is compressed by a matched filter designed with the same parameters as the excitation signal.

out-of-focus regions. The beamforming artefacts can be reduced by using methods such as synthetic beamforming and multiple foci on transmit and receive.

Pulse compression of the bandpass filtered signal and of the extracted second harmonic component after filtering with the FrFT are shown in Figure 6.16 for comparison. The pulse compression of the blue signal was performed by a second harmonic matched filter, which was designed with twice the centre frequency and bandwidth of the excitation signal. Red signal was first filtered with the FrFT according to the proposed method and the filtered signal was pulse compressed by the same second harmonic matched filter.

The effect of the spectrally overlapping fundamental component is increased range sidelobe level after pulse compression, which can be observed at $t = 6.2$ μs in Figure 6.11. When the location of these range sidelobes were calculated for the second harmonic image, a 4.6 mm difference between the real reflection from the wires and the ghost reflections was found. These ghost reflections can be clearly observed in the Figure 6.16 around 46.5 mm, 55 mm and 64.5 mm for the wires located at 42 mm, 50 mm and 60 mm, respectively.

The range sidelobe levels can be as high as -17 dB for the blue signal in Figure 6.16 because of the spectral overlap between the fundamental and second harmonic components. For the red signal in Figure 6.16 however, the range sidelobe levels were below -60 dB, which was the signal-to-noise ratio for these measurements. Filtering with the FrFT before pulse compression by a second harmonic filter completely cancels the range sidelobe levels without reducing the axial resolution.

6.5 Conclusions

The main advantages of the second harmonic imaging over B-mode imaging at fundamental frequency are the increased image resolution, and the reduced reverberation and near-field artefacts. The reverberations are caused by the ultrasound waves bouncing back and forth between tissue boundaries under the skin. The near-field artefacts are caused by the scattering and reflection form the first few layers of skin, fat and muscle tissue close to the ultrasound probe. The second harmonic field gradual builds up in the body through nonlinear propagation and the second harmonic energy is significantly lower than the fundamental energy for the first couple of centimetres in the body. For
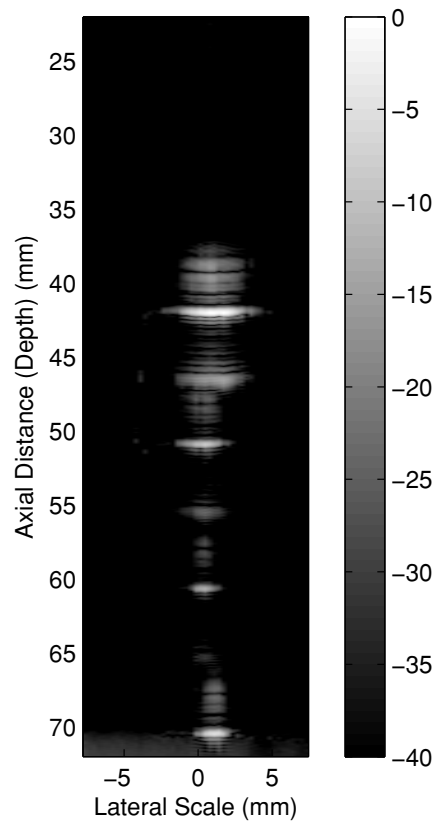
Figure 6.14: Second harmonic image of the wire phantom is shown with a 40 dB dynamic range. The second harmonic component is compressed by a second harmonic matched filter designed with twice the centre frequency and bandwidth of the excitation signal.
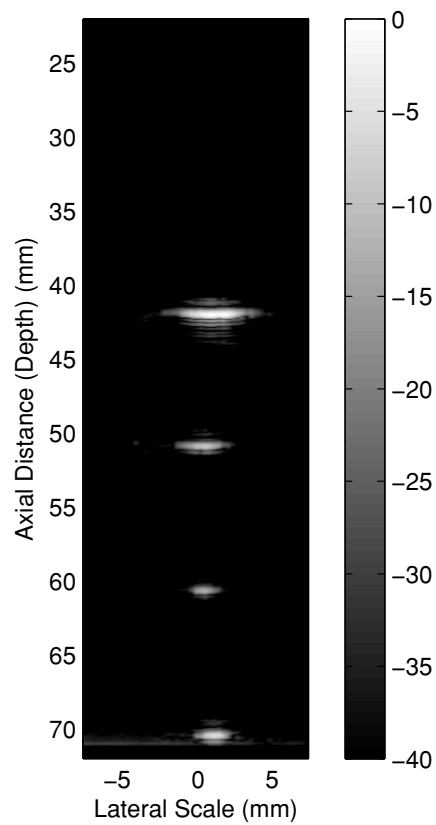
Figure 6.15: Second harmonic image of the wire phantom is shown with a 40 dB dynamic range. The second harmonic component is filtered by the FrFT before compression by a second harmonic matched filter designed with twice the centre frequency and bandwidth of the excitation signal.
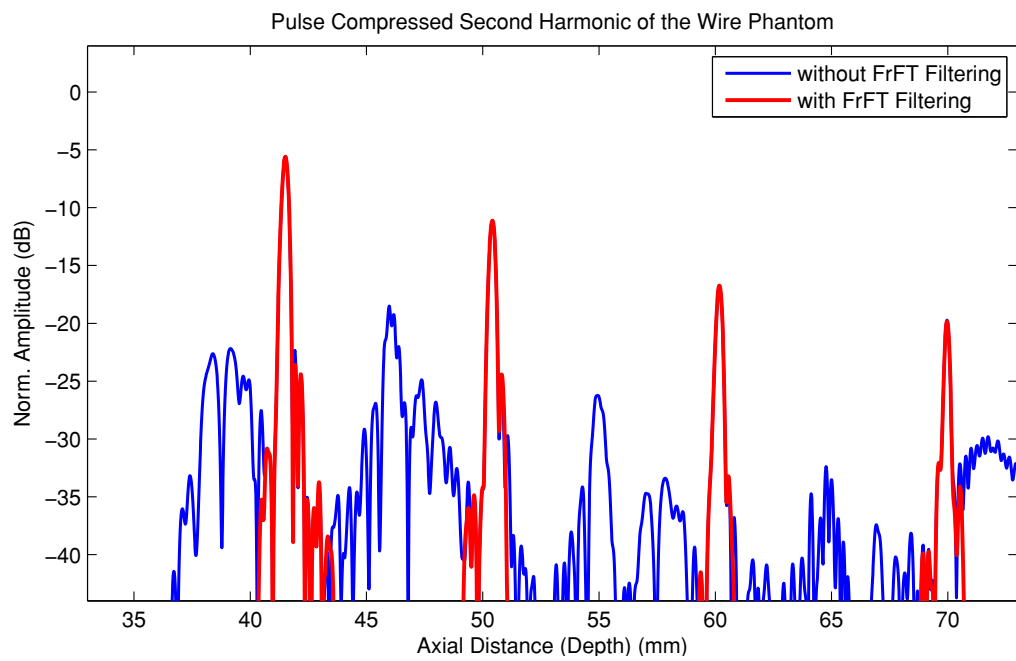
Figure 6.16: Figure shows the pulse compressed second harmonic component of the received signal for the measurements performed with the wire phantom. The signal in blue corresponds to the central line of the second harmonic image given in Figure 6.14. The signal in red corresponds to the central line of the second harmonic image given in Figure 6.15.

this reason, second harmonic imaging considerable improves the image quality. Eliminating these artefacts are especially important in echocardiography, where the imaging window is usually restricted by the ribs and lungs, and the presence of the intermediate skin and fat layers and proximity to the ribs substantially increases these artefacts.

Doubling the centre frequency and signal bandwidth provides better spatial resolution than conventional B-mode imaging; however separation between the spectrally overlapping second harmonic and fundamental components is crucial for imaging. Conventional filtering techniques such as a bandpass filter can separate the harmonic components at the expense of reduced bandwidth. Pulse inversion or similar multiple excitation methods can cancel the effect of the fundamental component by halving the image frame rate. If there is no tissue motion, the PI can achieve complete cancellation of the fundamental component that allows the use of whole transducer bandwidth. This significantly improves the image resolution for pulsed excitation; however for chirp excitation a tapering window is always necessary to reduce the sidelobe levels after pulse compression. Therefore, pulse inversion can only remove the image artefacts, but cannot further improve the spatial resolution and sidelobe levels for coded excitation. The FrFT performs more efficiently than these multiple excitation methods, where it can be used as a filtering tool with a wideband chirp excitation in order to extract the overlapped second harmonic component without reducing the system frame-rate and bandwidth.

Besides increasing the spatial resolution by working at the second harmonic frequency, second harmonic imaging also introduces some limitations; increased sidelobe levels due to the spectral overlap between the harmonic and fundamental components, decreased penetration depth, and reduced signal-to-noise ratio. The proposed coded excitation scheme and filtering method based on the FrFT mostly overcomes these limitations. The coded excitation was used to increase the SNR and penetration by increasing the total transmitted energy while maintaining the same peak intensity level using longer pulse duration. The FrFT was utilized to reduce the range sidelobe levels by filtering the fundamental component.

Results show that the range sidelobe levels in the compressed second harmonic can be reduced by filtering in the fractional Fourier domain. It was also presented that a narrower window can be applied on the compressed waveform in the fractional Fourier domain by choosing a transform order that matches the chirp rate of the signal of

interest. By calculating the transform order according to the signal parameters of the second harmonic component, further reduction in sidelobe levels are achieved for second harmonic imaging with chirp excitation.

Chapter 7

Superharmonic Imaging with Chirp Excitation

Tissue harmonic imaging improves spatial resolution of traditional B-mode images by utilizing the second harmonic generated in tissue. It is possible to take advantage of higher order harmonics and further increase the image quality. Superharmonic imaging provides improved spatial resolution by combining the third, fourth and fifth harmonics of the nonlinear received signal. The aim of this study is to increase the signal-to-noise ratio and improve the axial resolution of the superharmonic image using chirp coded excitation.

Experiments were performed by using linear chirp excitation with different bandwidths to observe the effect of spectral overlap between the higher harmonics. Harmonic matched filters were designed and applied to the received signal to perform pulse compression of the individual harmonic chirp components. To obtain the superharmonic image, the third to fifth harmonic components were combined in the time domain after pulse compression.

The results indicate that the processed superharmonic components with chirp excitation of 20% and 40% fractional bandwidths improved the axial resolution by 35% and 65%, respectively, when compared to the superharmonic component of a tone-burst. The wideband excitation achieves a better resolution as expected, however the spectral overlap between the harmonic components increases the peak sidelobe levels. To overcome this limitation and reduce the artefacts caused by spectral overlapping, the Fan Chirp transform (FChT) has been employed.

7.1 Introduction

A new ultrasound imaging technique called "superharmonic imaging" was proposed in the last decade by Bouakaz *et al.* (2002). The superharmonic image relies on the sum of the third, fourth, and fifth harmonic components of the received signal. These higher order harmonic components are produced due to the nonlinear propagation of ultrasound waves through biological tissue at high acoustic pressure (Duck, 2002). Superharmonic imaging provides improved axial and lateral resolution with reduced near-field artefacts.

The main issues with superharmonic imaging are the requirement for a large transducer bandwidth and sensitivity to accommodate fundamental to fifth order harmonics of the nonlinear received signal, and the reduced SNR due to the poor energy content of the higher order nonlinear harmonic components.

An interleaved phased array transducer having a -6 dB bandwidth of 144% was recently developed for superharmonic imaging with improved transmission efficiency and better reception sensitivity (van Neer *et al.*, 2010). The recent developments in capacitive micromachined ultrasound transducers (CMUTs) research showed that it is possible to make very wideband transducers with small harmonic distortions on transmit even at high pressure levels (Satir & Degertekin, 2012; Yamaner *et al.*, 2012). This makes CMUTs suitable for superharmonic imaging applications.

To improve the SNR, a multi-pulse excitation scheme based on the frequency compound method was proposed in the area of superharmonic imaging (Matte *et al.*, 2008; van Neer *et al.*, 2011). This technique showed improved image resolution with suppressed ripple artefacts; however it is susceptible to motion artefacts and reduces the system frame-rate. For this reason, in this study a linear frequency modulated (LFM) excitation is proposed to improve the SNR and image resolution.

7.2 Materials and Methods

7.2.1 Excitation Signals

In the experiments, a LFM chirp and tone-burst were used as excitation signals. Chirp signals had a centre frequency of 2.25 MHz, a duration of 10 μs, and fractional bandwidths (FBW) of 20% and 40%. A Hann window was also applied to reduce spectral

leakage. For comparison, a 2.25 MHz tone-burst signal of same duration and amplitude was used as an excitation, where all three signals had the same energy and similar SNR on receive. However, the tone burst had the narrowest bandwidth and was expected to yield the worst resolution.

7.2.2   Experimental Setup

Experiments were performed to measure the harmonic components generated due to the nonlinear propagation of ultrasound waves through water. The experimental setup is shown in Figure 7.1. The experiments were performed in a tank containing deionised and degassed water. The transducer and hydrophone were aligned coaxially in a pitch-catch configuration. An axial scan was performed, between the depths of $1-10$ cm, using a custom built computer numerical control (CNC) system. A programmable 33250A Arbitrary Waveform Generator (Agilent Technologies Inc., Santa Clara, CA, USA) was set to generate excitation signals. The signals were amplified by an A150 E&I RF Power Amplifier (Electronics & Innovation Ltd., Rochester, NY, USA). The amplified chirp signals were transmitted by a 2.25 MHz single element V323-SM immersion transducer (Olympus-NDT Inc., Waltham, MA, USA) with 56% fractional bandwidth. The nonlinear signals were detected using a Polyvinylidene Fluoride (PVDF) needle hydrophone with an active element diameter of 0.2 mm (Precision Acoustics Ltd., Dorchester, UK). The peak negative pressure level of each waveform was 1.125 MPa at 2.25 MHz with a MI of 0.75 at the focus of the transducer. The received signals were acquired at 1 GHz sampling rate using a LeCroy Waverunner 44xi oscilloscope (LeCroy Corporation, Chestnut Ridge, NY, USA) with 32-times averaging to improve the SNR. The captured data was processed offline in Matlab (MathWorks Inc., Natick, MA, USA). All received signals were corrected using an inverse filter designed in Matlab according to the frequency response of the hydrophone.

7.2.3   Processing the Superharmonic Component

Individual harmonic matched filters were designed and applied on the received signal to perform pulse compression of each harmonic component. The centre frequency and bandwidth of the desired harmonic matched filter were set by multiplying the centre frequency and bandwidth of the excitation signal with that harmonic number according to the second order distortion model or square law (Arshadi *et al.*, 2007;
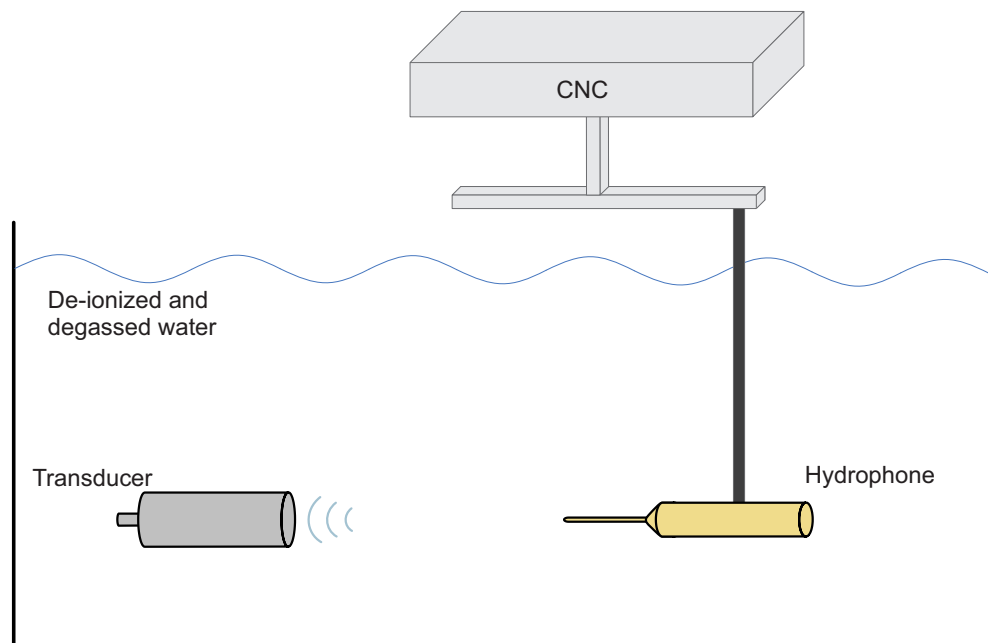
Figure 7.1: Schematic diagram of the experimental setup. The experiments are performed in a tank filled with de-ionized and degassed water. The alignment of the transducer and the needle hydrophone is performed by a CNC system.

Kim *et al.*, 2001). The fundamental matched filter had a centre frequency of 2.25 MHz and bandwidth of 0.45 MHz and 0.90 MHz for chirps with 20% FBW and 40% FBW, respectively. The second harmonic matched filter was designed by multiplying these parameters by 2 and by using a centre frequency of 4.5 MHz and bandwidth of 0.90 MHz and 1.80 MHz for chirps with 20% FBW and 40% FBW respectively. Similarly, the third, the fourth, and the fifth harmonic matched filters were designed by multiplying the centre frequency and the bandwidth of the fundamental matched filter by 3, 4, and 5, respectively. A Hann window was applied on all harmonic matched filters as used in the excitation signal. Extraction of the harmonic components both with the FChT filtering and without the FChT filtering is explained in Figure 7.2.
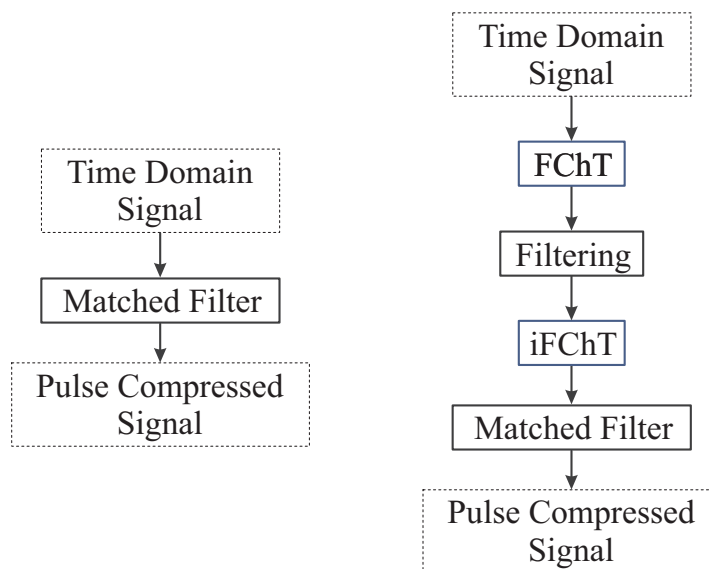
Figure 7.2: (Left) Diagram illustrates the pulse compression method by a matched filter. The time domain signal is convolved with a matched filter to achieve pulse compression. (Right) Diagram illustrates the filtering method by the FChT. First, the time domain signal is transformed into the FChT domain, where the compression is achieved. Second, the harmonic signals are filtered and separated in the FChT domain. Third, the filtered signals are transformed back to the time domain. As the last step, the time domain signals are convolved with harmonic matched filters to achieve pulse compression.

In order to calculate the superharmonic component, the third, the fourth, and the fifth harmonic components of the chirp signal were combined. After pulse compression,

the envelopes of the compressed signals were computed by the Hilbert transform and the individual harmonic components were summed in the time domain. For performance evaluation, the axial pulse width of the compressed time domain signals was measured at -20 dB and the peak sidelobe level of the compressed chirp signals was obtained by measuring the ratio of the highest sidelobe level to the mainlobe level.
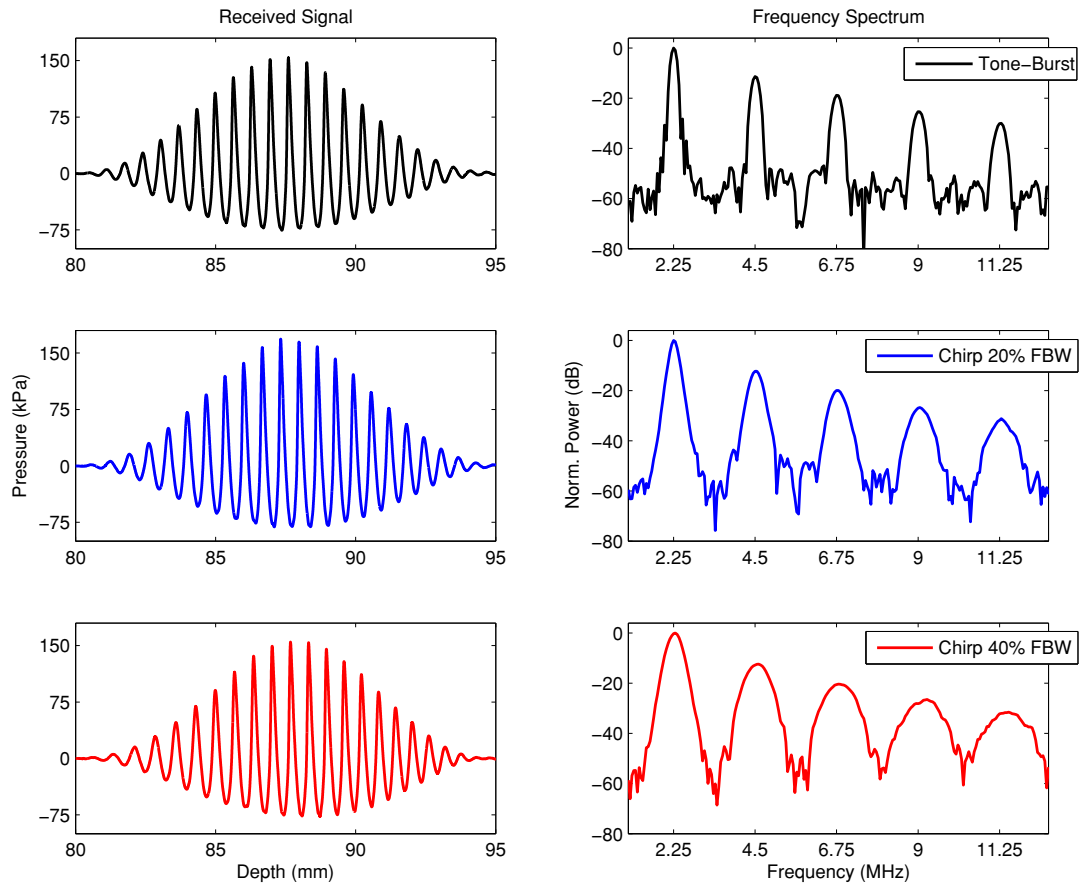
Figure 7.3: Figure shows (Left) the received signals at the same depth for different excitation waveforms and (Right) the associated power spectra showing the harmonic content of the received signals. (Top) Tone-burst excitation, (Middle) chirp excitation with 20% fractional bandwidth, and (Bottom) chirp excitation with 40% fractional bandwidth are shown to point out the difference between the amount of spectral overlapping for higher-order harmonics generated by these excitation waveforms.

7.3 Experimental Results and Discussion

The nonlinear signals were measured at a depth of 8 cm to achieve maximum energy transfer to the higher harmonics as explained in appendix B. Their associated power spectra obtained using the Fourier transform are shown in Figure 7.3. The figure shows the shock-wave formation and the higher order harmonic components. The generation of the harmonics is due to the nonlinear propagation at high acoustic pressure, which yields distortion in signal symmetry at the positive and negative pressure peaks of the received signals. It can also be observed from the figure that increasing the bandwidth of the excitation will increase the bandwidth of the harmonics and will result in the overlapping between higher order harmonic components.

The harmonic signals obtained with a tone-burst excitation is shown in Figure 7.4. All harmonics were filtered by a band-pass filter and normalised with the peak intensity of the fundamental frequency component. A detailed comparison is given in Table 7.1 and Table 7.2 by considering the axial pulse width and peak sidelobe level of the harmonic signals. The results indicate that the superharmonic of a tone-burst improves the axial resolution when compared with the fundamental and second harmonic component. Combining the third, fourth and fifth order harmonics will not only improve the axial resolution but will also improve the SNR, where the SNR of the superharmonic component becomes comparable to the second harmonic component.

The fundamental, harmonics, and superharmonic obtained after pulse compression of chirp excitations with a 20% FBW and with a 40% FBW is shown in Figure 7.5 and Figure 7.6, respectively. The superharmonic extracted from both chirp excitations provided around 60% improvement in axial resolution when compared with their fundamental components. Also around 30% reduction was observed for both chirp excitations in the axial pulse width for the superharmonic when compared with their second harmonic components. The peak sidelobe level of the superharmonic was comparable to the second harmonic component for the chirp excitation with 20% FBW, however the chirp excitation with 40% FBW contained higher peak sidelobe level due to spectral overlapping between the higher order harmonic components.

When the processed superharmonic components were compared, the excitation with larger bandwidth achieved a better compression and an axial resolution, as shown in Figure 7.7. The superharmonic component axial pulse width of the chirp excitation with
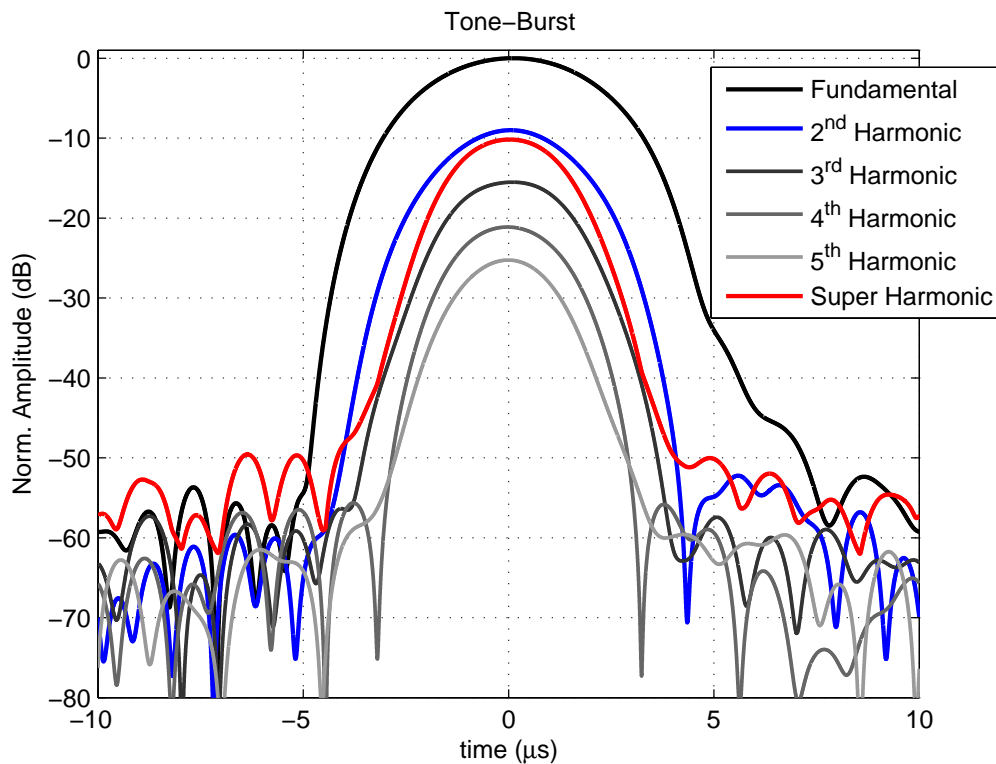
Figure 7.4: The extracted harmonic signals obtained with a tone-burst excitation. The fundamental and harmonic components are individually filtered by a bandpass filter. The superharmonic component is obtained by combining the third, fourth, and fifth harmonic components in time domain.

Table 7.1: Axial pulse width of harmonic signals.

	Pulse Width (μs)		
	Chirp 20%	Chirp 40%	Tone-burst
Fundamental	9.2	5.1	7.9
Second Harmonic	5.6	2.9	6.4
Third Harmonic	4.3	2.1	5.7
Fourth Harmonic	3.3	1.7	5.1
Fifth Harmonic	2.9	1.5	5.0
Superharmonic	3.9	2.0	5.4
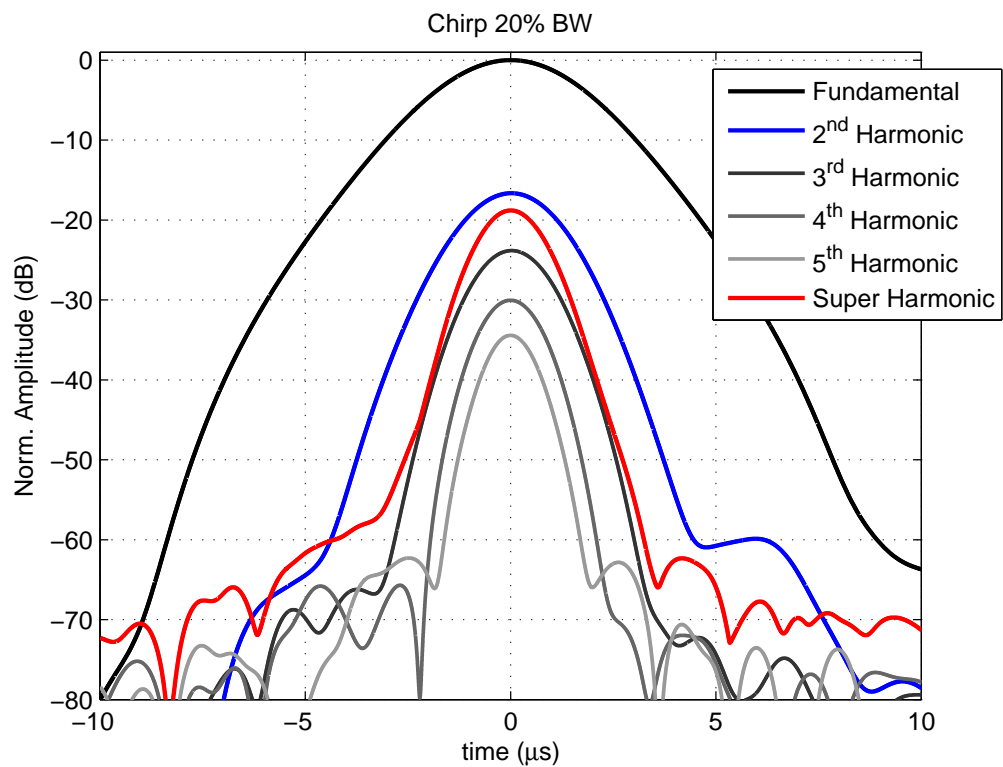
Figure 7.5: The extracted harmonic signals obtained with a 20% FBW chirp excitation. The fundamental and harmonic components are individually compressed by a matched filter or by a bespoke harmonic matched filter. The superharmonic component is obtained by combining the pulse compressed third, fourth, and fifth harmonic components in time domain.
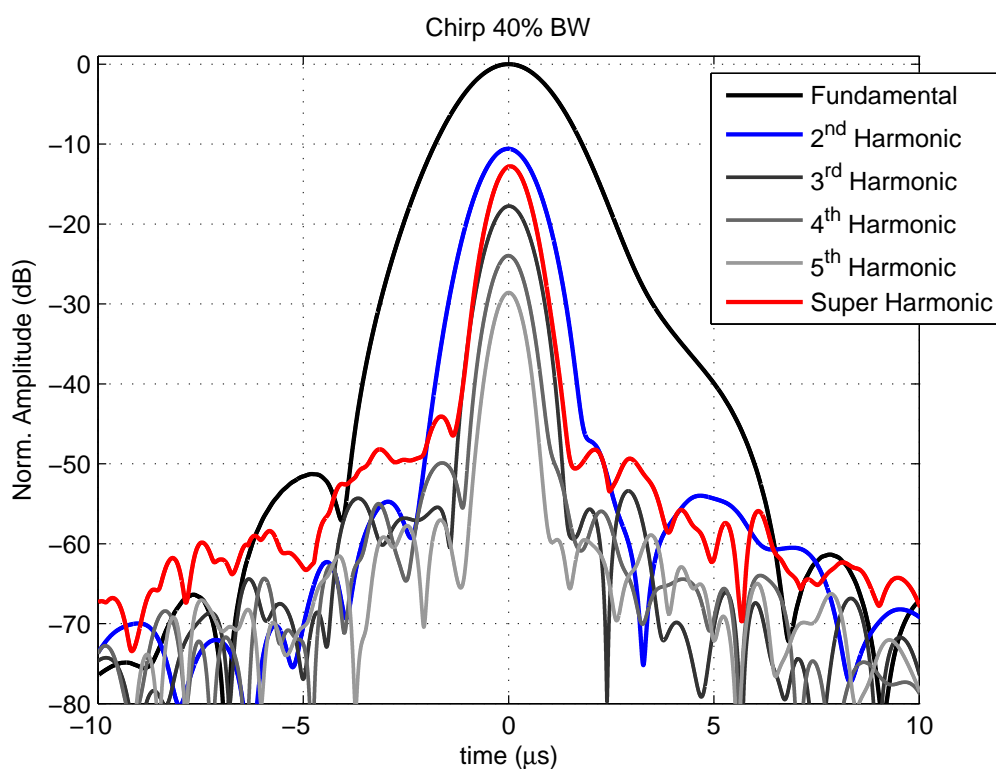
Figure 7.6: The extracted harmonic signals obtained with a 40% FBW chirp excitation. The fundamental and harmonic components are individually compressed by a matched filter or by a bespoke harmonic matched filter. The superharmonic component is obtained by combining the pulse compressed third, fourth, and fifth harmonic components in time domain.

Table 7.2: Peak sidelobe levels of harmonic signals

	Peak Sidelobe Level (dB)		
	Chirp 20%	Chirp 40%	Tone-burst
Fundamental	-64.7	-50.3	-52.3
Second Harmonic	-43.2	-43.3	-43.2
Third Harmonic	-42.3	-35.1	-40.6
Fourth Harmonic	-35.6	-26.4	-34.7
Fifth Harmonic	-27.2	-27.8	-34.4
Superharmonic	-43.5	-31.5	-39.4

40% FBW was nearly half that of the chirp excitation with 20% FBW. The performance of the superharmonic for the chirp excitation with 40% FBW was close to the theoretical expectations, where doubling the signal bandwidth should double the axial resolution. The results indicated that chirp excitation and harmonic matched filters can be used for second harmonic imaging. The only disadvantage of processing the superharmonic component with a harmonic matched filter was the high peak sidelobe level due to spectral overlap between the harmonic components.

7.4 Further Improvement by the FChT

This work has been published in the proceedings of IEEE Ultrasonics with the results presented in the previous section (Arif *et al.*, 2010b). Despite improving the axial resolution for both chirp excitations with 20% and 40% FBW, the result showed that the wideband excitation will always suffer from high sidelobe levels due to spectral overlap between the harmonics.

In order to improve the previous results and reduce the sidelobe levels, the FChT was employed to filter the spectrally overlapped chirps as explained in section 3.3. The time-frequency plane was warped using the FChT and all harmonic components were individually filtered. The received signal in the FChT domain and the window applied on the second harmonic component are shown in Figure 7.8. The window length was calculated by Eq. (3.24) with $n_{win} = 6.75$ and $T = 10$ μs. The extracted harmonics
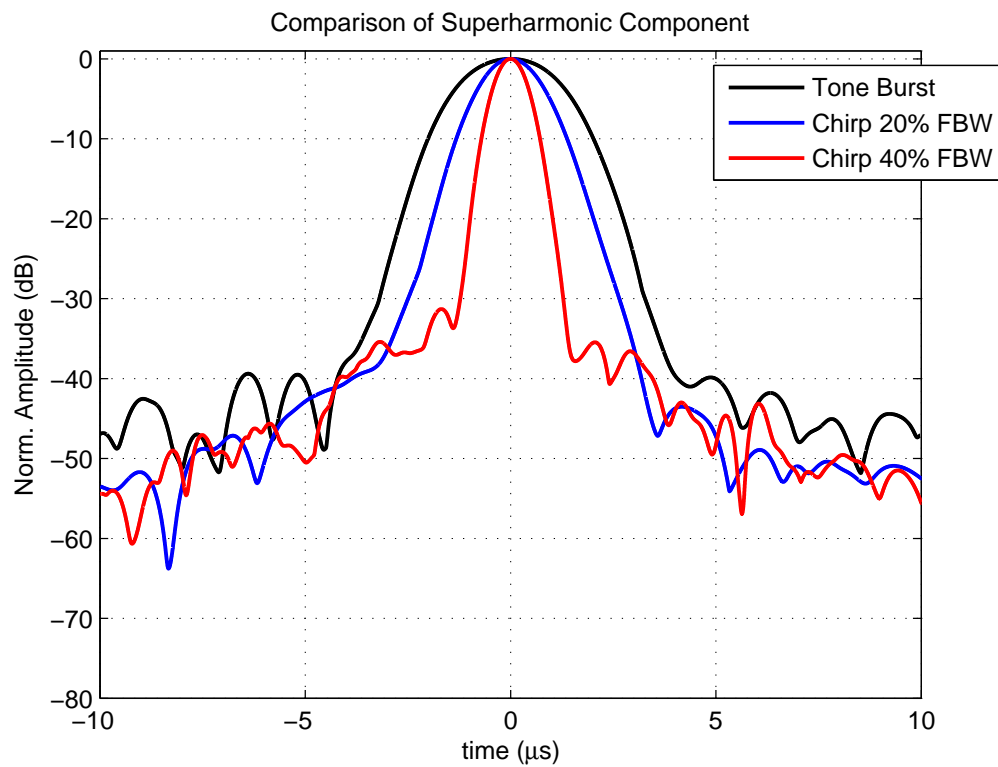
Figure 7.7: Comparison of the superharmonic components given in Figure 7.4, Figure 7.5, and Figure 7.6. Superharmonic components are obtained by a tone-burst excitation, chirp excitation with 20% fractional bandwidth, and chirp excitation with 40% fractional bandwidth.

were transformed back to the time domain by using the inverse FChT and compressed by a harmonic matched filter.
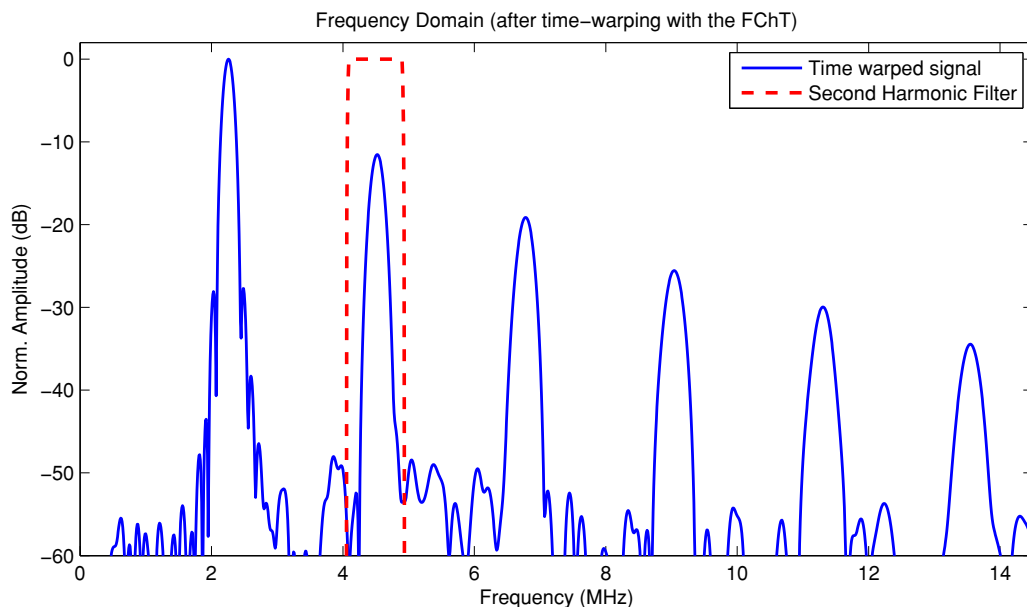
Figure 7.8: Frequency domain representation of the received signal after applying the FChT with a normalised chirp rate that matches with the fundamental and harmonic components. Figure also shows the window applied over the second harmonic. Note that the frequency domain is not the traditional frequency axis, since the time-frequency plane is warped by the FChT.

When Figure 7.5 and Figure 7.9 are compared, the improvement achieved by using the FChT becomes obvious. Similar results were observed for the chirp excitation with 40% FBW after comparing Figure 7.6 and Figure 7.10. The numerical comparison of the results are presented in Table 7.3.

The peak sidelobe level was improved nearly for all harmonics after pulse compression. No improvement was observed on the axial resolution as expected, since the signal bandwidth was not changed. Figure 7.11 clearly shows the improvement on peak sidelobe levels after using the FChT for filtering the spectrally overlapped harmonic chirps without decreasing the resolution.

It is also possible to reduce the sidelobe levels after compression by applying different windows on the matched filter as described in section 2.3.1. In this approach, there is always a trade-off between axial pulse width and sidelobes, where it is not possible
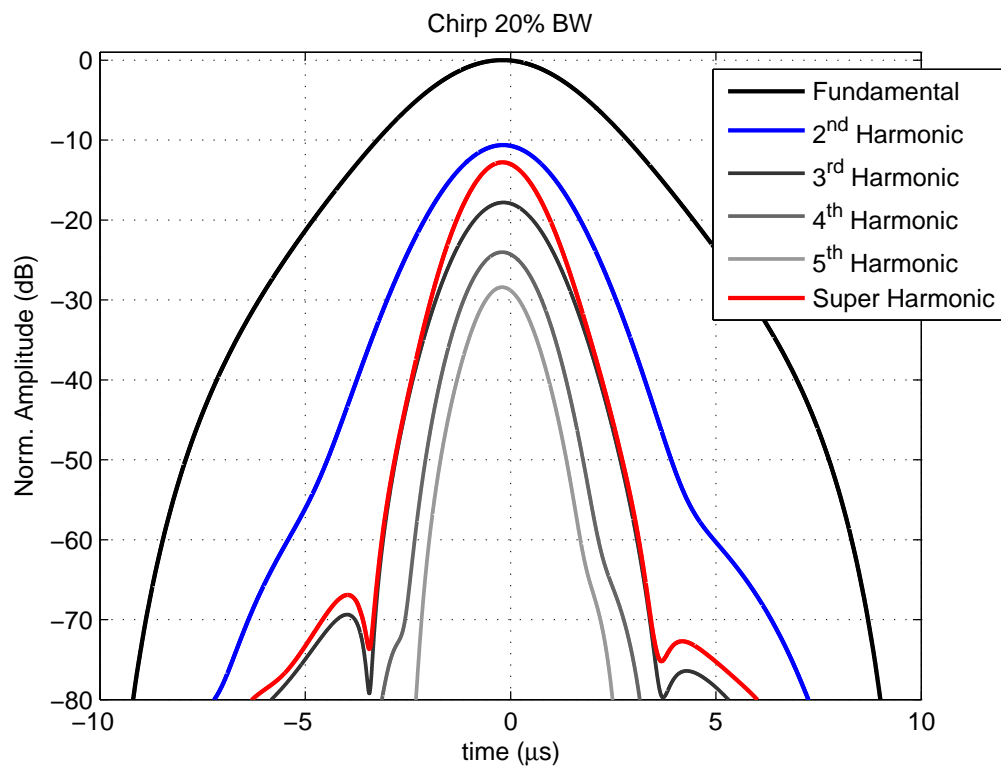
Figure 7.9: The extracted harmonic signals obtained with a 20% FBW chirp excitation, after filtering in the FChT domain. The fundamental and harmonic components are individually compressed by a matched filter or by a bespoke harmonic matched filter. The superharmonic component is obtained by combining the pulse compressed third, fourth, and fifth harmonic components in time domain.
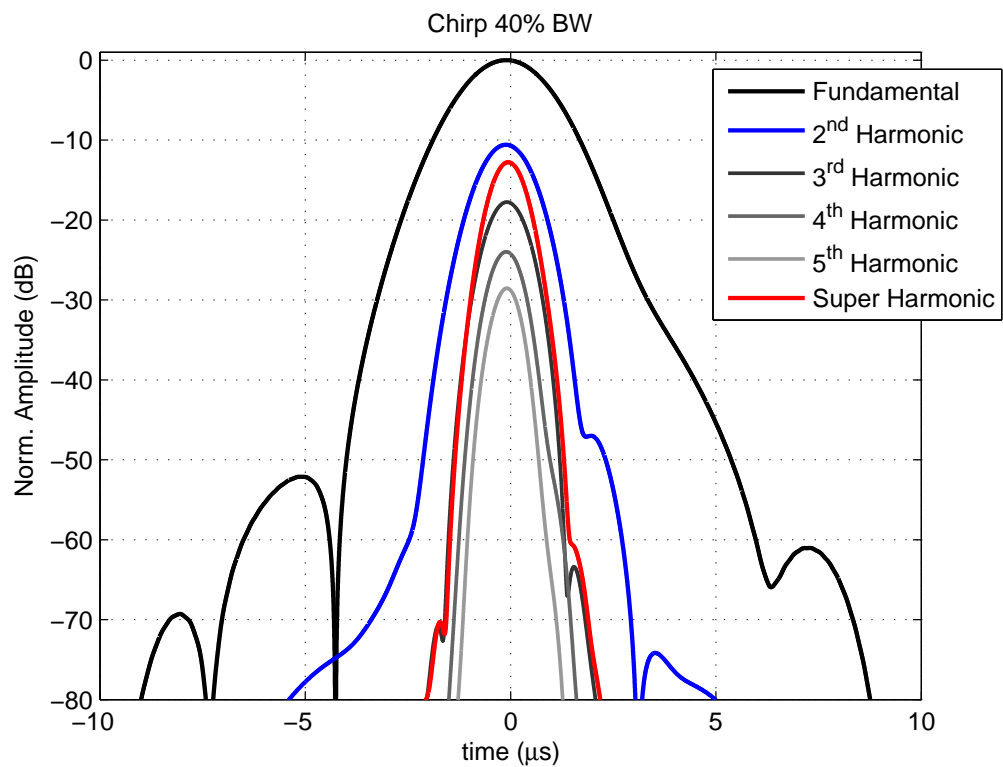
Figure 7.10: The extracted harmonic signals obtained with a 40% FBW chirp excitation, after filtering in the FChT domain. The fundamental and harmonic components are individually compressed by a matched filter or by a bespoke harmonic matched filter. The superharmonic component is obtained by combining the pulse compressed third, fourth, and fifth harmonic components in time domain.

Table 7.3: Peak sidelobe levels of harmonic signals compressed by a matched filter and filtered by the Fan Chirp transform

| | Peak Sidelobe Level (dB) | | | |
| | MF | | FChT + MF | |
	Chirp 20%	Chirp 40%	Chirp 20%	Chirp 40%
Fundamental	-64.7	-50.3	-	-52.1
Second Harmonic	-43.2	-43.3	-71.5	-36.5
Third Harmonic	-42.3	-35.1	-51.6	-45.7
Fourth Harmonic	-35.6	-26.4	-56.4	-70.6
Fifth Harmonic	-27.2	-27.8	-59.9	-70.2
Superharmonic	-43.5	-31.5	-54.1	-57.5

to improve the sidelobe levels without sacrificing the axial resolution. However, the FChT can achieve the optimum compression in terms of both sidelobe level and axial resolution.

7.5 Conclusions

The main advantage of the superharmonic imaging over second harmonic imaging is the enhanced spatial resolution. This improvement on lateral and axial resolution was confirmed with simulations and experiments by Ma *et al.* (2006). The experimental measurements performed in this work verifies the results observed by Ma *et al.* (2006). When the superharmonic components were compared with the second harmonic components, a 30% improvement was observed for the chirp excitation with 20% FBW and a 31% improvement was observed for the chirp excitation with 40% FBW as shown in Table 7.1.

In addition to this improvement on image resolution, the superharmonic imaging also suppresses reverberations, near-field artefacts, and off-axis artefacts similar to the second harmonic imaging. However the suppression rate of off-axis artefacts, which are caused by grating lobes of the fundamental beam, is much higher in superharmonic
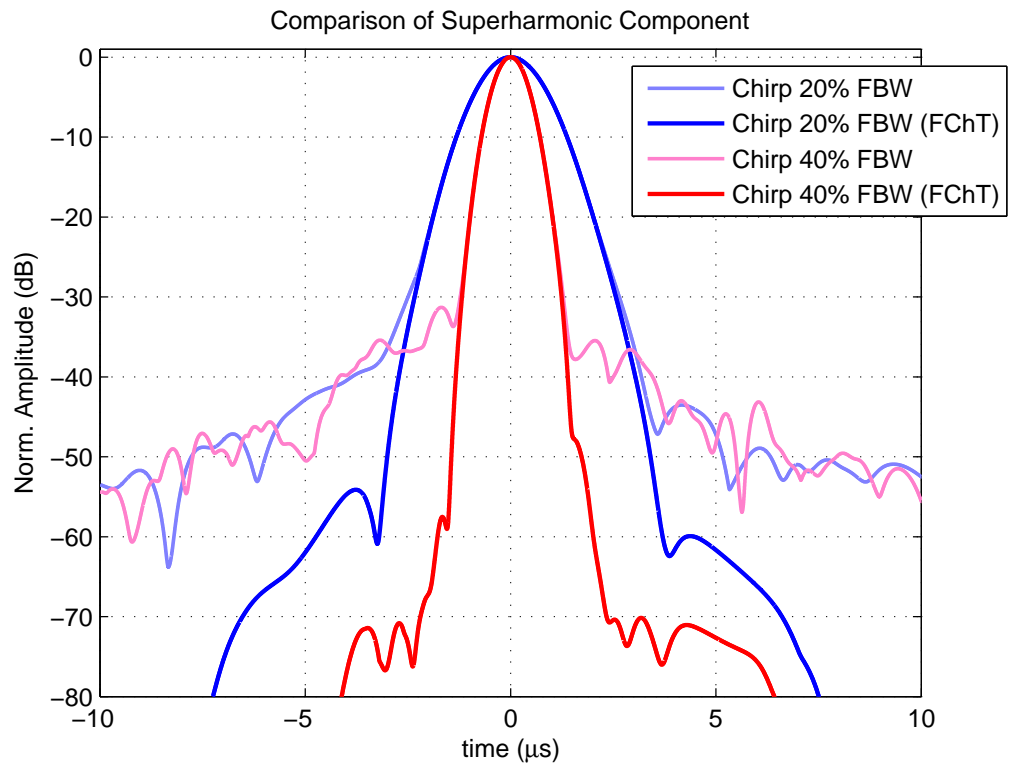
Figure 7.11: Comparison of extracted superharmonic components processed with and without the FChT technique. The superharmonic components, as given in Figure 7.7, processed by the previous method have higher sidelobe levels. The method based on the FChT technique proposed in this section achieves better sidelobe suppression without reducing the axial resolution.

imaging, since three different harmonic components causing three different grating lobe patterns are used for imaging.

Using the third, the fourth and the fifth harmonic does not only improve the image resolution, but also reduces the speckle. Combining different frequency components gives similar benefits with frequency compound imaging (Sanchez & Oelze, 2009). Therefore, significant speckle reduction can be achieved by superharmonic imaging and more details can be visualized. For this reason, superharmonic imaging is a good candidate for all types of medical imaging applications where high image resolution is necessary such as imaging small structures and detection of lesions.

Besides having these advantages, superharmonic imaging has several drawbacks. Reduced sensitivity, signal-to-noise ratio, and penetration depth are the main limitations of the superharmonic imaging. The higher-order harmonics are usually located at a frequency band where the transducer does not work efficiently, therefore causing a reduction in the SNR and sensitivity. The penetration depth is reduced because of frequency-dependant attenuation in tissue. The SNR and penetration can be increased by using coded excitation and increasing the total transmitted energy, but the available transducer bandwidth is the real limitation for the superharmonic imaging. The commercial ultrasound probes do not have sufficient bandwidth; however the research on transducer technology is focusing on increasing the transducer bandwidth and reception sensitivity. With the availability of the wider transducer bandwidth ($<150\%$), the superharmonic imaging can become a standard modality for high resolution imaging in the future.

Superharmonic imaging provides better spatial resolution than conventional B-mode imaging and second harmonic imaging; however without separating the spectrally overlapping harmonics the final ultrasound image cannot be formed. The current research is inclined towards the use of narrow bandwidth excitation signals in order to reduce the sidelobe levels and the harmonic leakage. However, this approach significantly reduces the possible improvement that can be achieved by the superharmonic imaging. Pulse inversion cannot be used to separate the overlapping harmonics, since it will cancel out all the odd harmonics. New multiple excitation methods were proposed specifically for superharmonic imaging such as the "Dual-pulse frequency compounded superharmonic imaging" method offered by van Neer *et al.* (2011). This approach can generate higher-quality harmonic images at the cost of a reduced frame rate, but it cannot be applied to

coded excitation. Conventional bandpass filtering can separate the harmonic components at the expense of reduced bandwidth. However, individual filters must be applied for each harmonic component and the overall reduction in bandwidth to compensate the spectral overlap will be three times more than the reduction in second harmonic imaging. Therefore, the FChT was used as a filtering tool for wideband chirp excitation in order to separate the individual harmonic components without sacrificing the signal bandwidth.

In this work, linear frequency modulated chirp signals were proposed as an excitation method for superharmonic imaging. Chirp coded excitation can potentially enhance the SNR and axial resolution with reduced artefacts in superharmonic imaging when compared to conventional tone-burst excitation. However, the spectral overlap between the higher-order harmonics reduces the image dynamic range. To overcome this problem the Fan Chirp transform was employed to filter the chirp harmonics. To the best of the author's knowledge, this is the first time the FChT is applied to an ultrasound imaging application for filtering and compressing chirp signals. The results showed that the FChT can successfully filter the spectrally overlapped harmonic signals when used with chirp coded excitation.

Part III

Contrast-Enhanced Ultrasound Imaging

It has been presented in chapter 6 and chapter 7 that spectral overlap between the fundamental and harmonic components increase the sidelobe levels of compressed waveforms with matched filters. The spectral overlap is inevitable for wideband excitation, since harmonics exist even at low pressure levels as explained in appendix B.

For the human body, it is possible to measure the acoustic properties of the soft-tissue and have an approximate figure concerning the speed of sound and attenuation values (Culjat *et al.*, 2010; Mast, 2000). A carefully chosen excitation waveform and a matched filter pair that compensates for the depth-dependant attenuation, frequency-dependant attenuation, and transducer response can still achieve reasonable mainlobe width and sidelobe levels which will be sufficient for ultrasound imaging. However, when ultrasound contrast agents are injected into the region of interest to be imaged, both the temporal and the spectral characteristic of the received signal will be considerably different. Contrast agents generate significantly more harmonics than tissue and increase the broadband noise due to microbubble destruction.

From a signal processing aspect, microbubbles alters the phase, the envelope shape, and the frequency content of the scattered echoes that make pulse compression even more challenging for contrast-enhanced ultrasound imaging. Therefore, chapter 8 evaluates the performance of pulse compression by matched filters through simulations and experiments for contrast-enhanced ultrasound imaging and contrast-enhanced second harmonic imaging. The Fan Chirp transform is proposed as a filtering tool to improve the axial resolution and the sidelobe levels of the compressed signals by separating all overlapping harmonics in time and frequency.

After performing simulations and experiments to observe the effects of nonlinear microbubble behaviour on pulse compression, it is decided to further investigate the microbubble response. Third order spectral analysis, also known as the bispectral analysis, is utilized to analyse the microbubble response. The bispectral analysis is explained and results on microbubble behaviour are presented in chapter 9. Chapter 9 also offers a method to separate the second harmonic response of tissue and microbubbles using bispectral analysis.

Chapter 8

Pulse Compression with Microbubbles

8.1 Introduction

The use of microbubbles or ultrasound contrast agents (UCAs) was first reported in 1968, when Gramiak & Shah (1968) performed ultrasound measurements of the aortic root by injecting gas bubbles and observed an enhancement in echoes. It led to an increasing interest in microbubble research and clinical use of UCAs. The first contrast agents were free air bubbles. The second generation contrast agents were encapsulated microbubbles, which were more stable to be carried in the systemic circulation. These bubbles had a lower diffusion rate and longer lifetime in blood than free air bubbles, but they were mostly used to enhance the echo from blood in B-mode and Doppler imaging (Bouakaz *et al.*, 2007).

Nowadays UCAs are encapsulated microbubbles filled with a low solubility gas, small enough to pass lung circulation ($1 - 10$ μm in diameter). UCAs are highly echogenic[1] because of the large difference in density and compressibility between the gas inside the microbubbles and the surrounding tissue. Diagnostic medical ultrasound employs UCAs mostly to enhance the contrast in ultrasound imaging. Microbubbles are more widely used in echocardiography than other imaging applications, since UCAs enable left ventricle opacification and myocardial perfusion imaging. Yet, other medical diagnostic applications such as detection and characterisation of small lesions and

---

[1]The ability of generating an echo.

tumours will also benefit from contrast-enhanced ultrasound imaging (Burns *et al.*, 2000b).

The linear scattering behaviour of microbubbles improves the response from blood pool, vessels, and human heart. Nevertheless, the nonlinear behaviour of the microbubbles must be used to achieve a better separation between tissue and contrast agents. In capillaries or small blood vessels, it is hard to detect microbubbles with their linear scattering response. However, increasing the pressure level will cause the microbubbles to behave nonlinearly, which will allow the differentiation of their response from that of tissue (Borsboom *et al.*, 2005; Harput *et al.*, 2012).

8.1.1   Nonlinear Behaviour of Microbubbles

Current research on ultrasound contrast imaging mostly focuses on exploiting the nonlinear behaviour of the microbubbles (Averkiou *et al.*, 2008; Biagi *et al.*, 2009; Cheung *et al.*, 2008; Sprague *et al.*, 2010). Because of their gas core, microbubbles are highly compressible and echogenic. They are also strong ultrasound scatterers; behaving linear at low pressure levels and nonlinear at higher pressures. It is hard to classify the microbubble behaviour with specific pressure levels, however, three regimes can be defined according to the applied pressure levels (de Jong *et al.*, 2002):

Low acoustic pressure (< 50 kPa)
For very small pressure amplitudes the microbubble response is linear, so the Rayleigh-Plesset equation is accurate in this regime. The resonance frequency of an oscillating bubble is identified in this linear region.

Moderate acoustic pressure ($50 - 300$ kPa)
In this regime, the microbubble response is both linear and nonlinear. The microbubble response is considered to be nonlinear, because the oscillation amplitude and the number of oscillation modes are increased. Nevertheless the bubble can still continue to oscillate stably, where this situation being referred to as "stable acoustic cavitation" (Brennen, 1995). Several nonlinear phenomena can be observed in this regime, including the generation of harmonics. The nonlinear microbubble behaviour can be predicted by using the modified Rayleigh-Plesset equation and similar models such as Marmottant *et al.* (2005).

High acoustic pressure (> 300 kPa)
In this regime, microbubbles experience an explosive cavitation growth and violent col-

lapse, which is referred to as "transient acoustic cavitation". Under such circumstance, the microbubble radius can change by several orders of magnitude during each cycle (Brennen, 1995). In other words, high acoustic pressures can cause microbubble destruction and consequently affect their reflectivity. However, the destruction of UCAs can also be used for imaging purposes (de Jong *et al.*, 2002).

The three regimes are defined with nominal acoustic pressure levels, yet these threshold values directly depend on contrast agent properties and coating. It is also important to note that the excitation frequency is a crucial factor in determining these thresholds. The relationship between the excitation frequency of the driving waveform and resonance frequency of the microbubble will play an important role on the aforementioned classification scheme. When microbubbles are excited near their resonance frequency, the natural oscillation is triggered and therefore the response is stronger.

8.1.2 Motivation

Harput *et al.* (2010) demonstrated that the microbubble response to wideband and long duration excitation is stronger. Microbubbles excited with a chirp waveform generate more harmonics than with a tone burst excitation of same duration. Harput *et al.* (2010) presented their results on SonoVue® (Braco Research SA, Milan, Italy), however most contrast agents will have a stronger response to wideband excitation since the microbubble population is polydisperse. Therefore, using chirps for ultrasound imaging with contrast agents is advantageous as more microbubbles can be excited close to their resonance frequency.

The microbubbles behaviour near resonance increases the scattering from blood and can achieve a better separation between tissue and contrast agents, thus a better contrast-to-tissue ratio (CTR). CTR specifies the ratio between contrast perfused and non-perfused tissue, where a higher CTR is necessary for most clinical applications.

Although chirp excitation amplifies the microbubble response and offers an improved CTR, the resonance behaviour of microbubbles introduce new complications for imaging applications. The resonance behaviour affects the phase, frequency and amplitude of echoes, so the matched filter technique may not work as efficiently with microbubbles as it works with linear reflectors. For this reason, this study investigates the effect of the pulse compression with the matched filter and filtering by the FrFT and the FChT techniques for the simulated and experimental behaviours of microbubbles.

The aim of this work is to improve the image quality of contrast-enhanced ultrasound imaging and contrast-enhanced second harmonic imaging.

8.2 Materials and Methods

8.2.1 Simulations

In this study, the simulations were performed with the Marmottant *et al.* (2005) model for SonoVue® (Braco Research SA, Milan, Italy) microbubbles coated with a thin layer of phospholipid and filled with SF_6. Appendix C explains the simulation model. Table C.1 lists the symbol definitions and values used in the simulations (Tu *et al.*, 2009).

Two different simulations were performed to observe the effect of the excitation frequency on microbubble behaviour and to observe the microbubble response to chirp excitation. The diameter of the simulated microbubble was 3 μm, which was insonated with a peak acoustic pressure of 100 kPa and 500 kPa. For the first simulation, the excitation waveform was a 20 μs duration sinusoidal tone-burst with a centre frequency changing between 2 MHz and 8 MHz. For the second set of simulations, a LFM chirp excitation with 4 MHz centre frequency, 2 MHz bandwidth, and 20 μs duration was used.

8.2.2 Microbubble Preparation and Characterisation

Lipid coated microbubbles were used in the experiments, because of their hyper-echogenicity. The lipids were prepared by mixing 1,2-Dipalmitoyl-*sn*-glycero-3-phosphocholine (DPPC), 1,2-Distearoyl-*sn*-glycero-3-phosphoethanolamine-N-[maleimide(polyethylene glycol)-2000] (DSPE-PEG2000), and 1,2-Dipalmitoyl-*sn*-glycero-3-phosphate (DPPA) from Avanti Polar Lipids (Alabaster, AL) dissolved in chloroform and drying them in a glass vial within a vacuum desiccator. The encapsulated microbubbles were prepared by re-suspending the lipids in Dulbecco's Phosphate-Buffered Saline (DPBS) containing 1% glycerine by volume. The solution was mixed in a 1 mL vial and saturated with C_3F_8, which forms the gas core. The vial was shaken for 45 seconds by a CapMix mechanical shaker (3M ESPE, St. Paul, MN). The microbubble size distribution and concentration were optically measured by Nikon Eclipse Ti-S inverted microscope (Nikon Corp,

Tokyo, Japan) as 1.9 ± 1 μm and 1×10^{10}, respectively. The microbubbles were diluted by 1:5000 to achieve similar concentrations to those observed in the human body.

After producing the microbubbles, their scattering response was measured for the frequency range of $3 - 8$ MHz and peak-negative pressure of 100 kPa. The measurements were conducted in a tank containing deionized and degassed water at 20°C. A cylindrical chamber containing the microbubble suspension was immersed in a water tank. The chamber had an internal diameter of 25 mm and had two windows covered by an acoustically transparent saran wrap, one facing the transmitting transducer and the other facing the receiving hydrophone. The transducer was positioned perpendicular to the hydrophone which was placed at a distance of 10 mm from the chamber in the water tank. The suspension was mixed using a magnetic stirrer (HI-180F, Hanna Instruments Ltd., Bedfordshire, UK) to ensure uniform microbubble distribution during the measurements. A fresh microbubble suspension was used for each set of measurements, which approximately took $5 - 20$ seconds with a total experiment time of less than one hour.

A 20 μs duration sinusoidal tone-burst was used as an excitation signal for which the centre frequency was changed between 3 MHz and 8 MHz with a 0.1 MHz incremental steps. All excitation signals were designed in Matlab (Mathworks Inc., Natick, MA, USA) and then loaded into a 33250A Arbitrary Waveform Generator (Agilent Technologies Inc., Santa Clara, CA, USA). The generated signals were first amplified with an A150 E&I RF Power Amplifier (Electronics & Innovation Ltd., Rochester, NY, USA) and then used to drive a single element V310 immersion transducer (Olympus-NDT Inc., Waltham, MA, USA) with a centre frequency of 5 MHz and a -6 dB bandwidth of 80%. Before the measurements the pressure calibration of the transducer was performed using a Polyvinylidene Difluoride (PVDF) 1 mm needle hydrophone (Precision Acoustics Ltd., Dorchester, UK) for the frequency range of $3 - 8$ MHz.

For each excitation frequency, 150 measurements were taken with a pulse repetition frequency of 100 Hz. The scattered pressure from contrast agents were received using the 1 mm needle hydrophone. The received signals were amplified by 40 dB using a low noise 5072-PR pre-amplifier (Panametrics-NDT, Inc., Waltham, MA, USA) and then digitized at a sampling frequency of 1 GHz using a LeCroy 64xi digital oscilloscope (LeCroy Corporation, Chestnut Ridge, NY, USA). All received signals were corrected in Matlab using the frequency response of the hydrophone with the calibration data

from 0.5 to 20 MHz being supplied by the manufacturer. The received signals spectra were averaged in the frequency domain over the 150 measurements for further noise reduction. The resonance frequency of the microbubble population was measured as 3.8 MHz.

8.2.3 Experimental Setup

Scattering Measurements
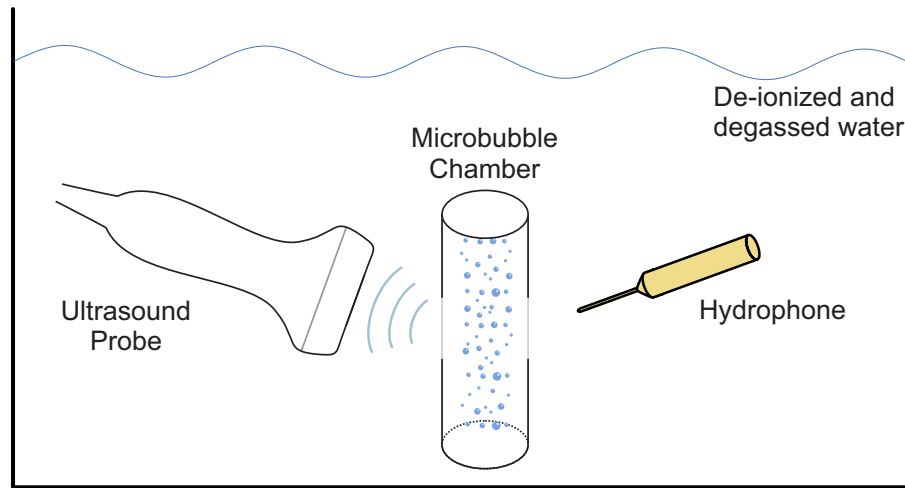
Figure 8.1: Schematic diagram of the experimental setup for microbubble scattering measurements performed in a tank filled with de-ionized and degassed water. Measurements are performed with a commercial ultrasound probe connected to the UARP and a hydrophone.

Scattering measurements were performed to evaluate the microbubble response to linear frequency modulated chirp excitation with different chirp rates and pressure levels. A L3-8/40EP medical probe (Prosonic Co., Korea) was used to excite the microbubbles in a 25 mm diameter cylindrical chamber with two acoustically transparent windows as shown in Figure 8.1. The measurements were conducted in a tank containing deionized and degassed water at 20°C. The medical probe was connected to the Ultrasound Array Research Platform (UARP) to generate three excitation waveforms with a centre frequency of 3.8 MHz and a signal duration of 20 μs. The excitation signals had 10%, 20%, and 40% fractional bandwidths. The medical probe and the

excitations were specifically chosen to replicate imaging conditions and find the noise level of the imaging setup.

The measurements were performed for a peak negative pressure range of $100 - 500$ kPa. For each excitation waveform and pressure level 150 measurements were taken with the microbubble suspension being renewed after every five measurements. Scattered pressure waveforms from the contrast agents were received using the 1 mm needle hydrophone, which was placed perpendicular to the ultrasound probe. All received signals were corrected in Matlab using the frequency response of the hydrophone. The received signals spectra were averaged in the frequency domain over the 150 measurements to reduce the variance of the experimental results due to multiple scattering effects from the microbubble cluster, low signal amplitude, and large fluctuations as a result of microbubble movements (Gorce *et al.*, 2000).

Imaging

The same medical probe was used to scan the wire as shown in Figure 8.2. The wire phantom consisted of a 120 μm thick aluminium wire located at a depth of 60 mm. The medical probe was connected to the UARP to perform a linear scan with a focal depth of 60 mm. For the second measurement, a 20 mm wide chamber with two mylar windows to contain the microbubble solution was introduced as shown in Figure 8.3. The aim of these measurements was to find the point spread function of the system with and without microbubbles for contrast-enhanced ultrasound imaging and contrast-enhanced second harmonic imaging.

For both experiments, the UARP was programmed to generate a Hann windowed linear frequency modulated chirp with a centre frequency of 3.5 MHz, a duration of 20 μs, and a bandwidth of 1 MHz. Since the medical probe bandwidth spans between 3 MHz and 8 MHz, the excitation signal was chosen to be a LFM chirp sweeping the frequency range of $3-4$ MHz so the second harmonic could be received at the frequency range of $6-8$ MHz.

The imaging was performed with a peak negative pressure of 500 kPa. All received signals were corrected using an inverse filter designed in Matlab according to the frequency response of the medical probe. Later, the pulse compression was performed on each beamformed scan line by using either a matched filter or a second harmonic matched filter. The second harmonic matched filter was designed with twice the centre
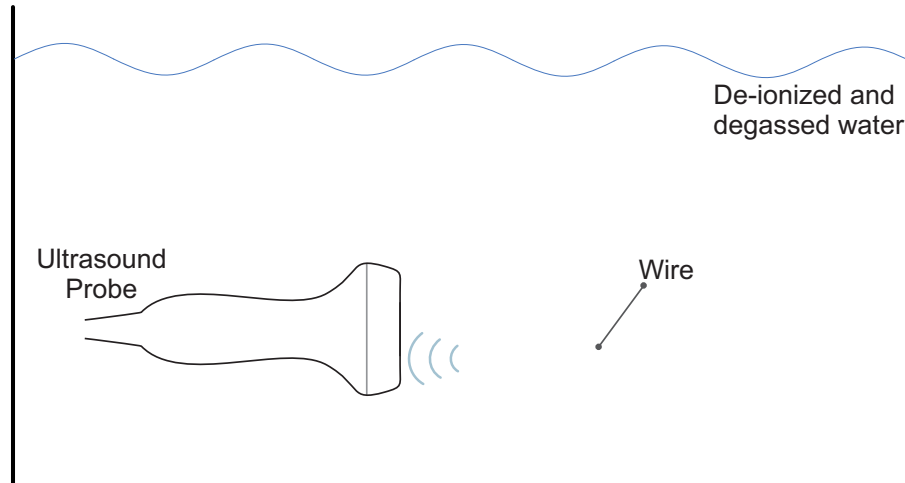
Figure 8.2: Schematic diagram of the experimental setup with a point scatterer. Measurements are performed using a commercial ultrasound probe connected to the UARP in a tank filled with de-ionized and degassed water.
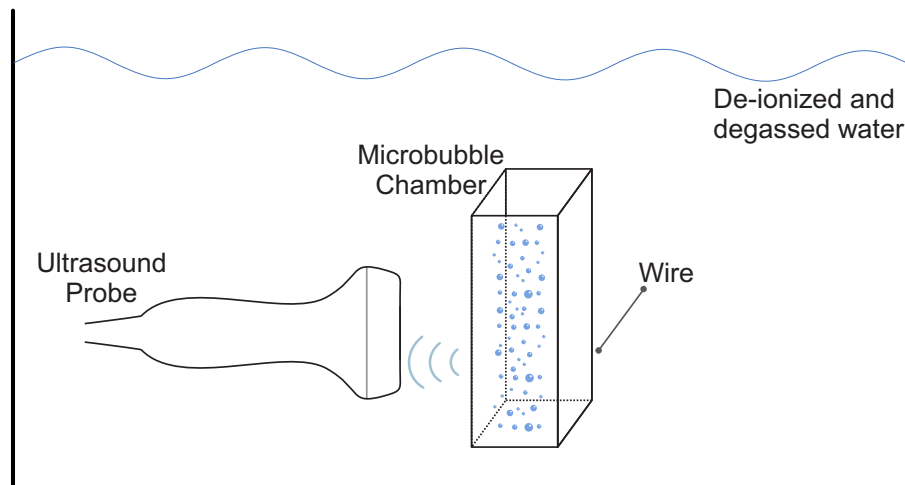
Figure 8.3: Schematic diagram of the experimental setup with a point scatterer shadowed by microbubbles. Measurements are performed with a commercial ultrasound probe connected to the UARP in a tank filled with de-ionized and degassed water.

144

frequency and bandwidth of the fundamental component by using the same window function applied to the excitation signal.

8.3   Simulation Results and Discussion
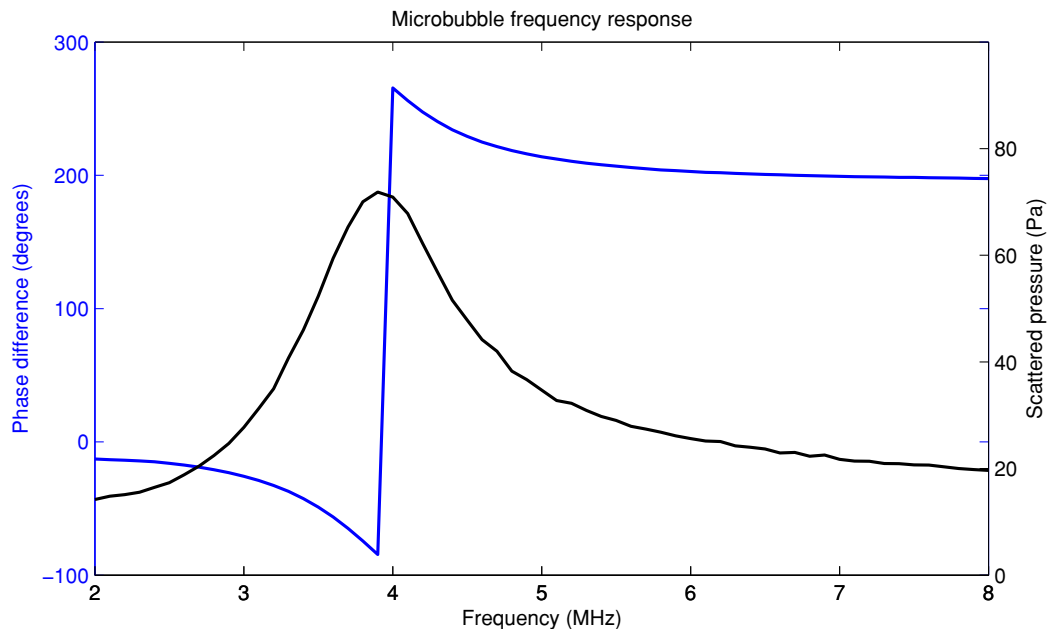
Figure 8.4: Frequency response of a 3 μm microbubble simulated with the Marmottant model.

The simulations were performed with the Marmottant *et al.* (2005) model for a phospholipid coated microbubble as explained in the previous section. The diameter of the simulated microbubble was 3 μm and the peak acoustic pressure was 100 kPa. A 20 μs duration sinusoidal tone-burst was used as an excitation signal. The simulations were repeated for the frequency range of 2 MHz to 8 MHz with 0.1 MHz incremental steps.

Figure 8.4 shows the scattered pressure from microbubbles and the phase difference between the excitation waveform and the microbubble oscillations. When microbubbles are excited with a chirp waveform around their resonance frequency, both the phase and amplitude response will be significantly different than that of the tissue. Microbubbles will oscillate with a different phase for the excitation frequencies below or above their resonance peak. Therefore, the scattered echoes from microbubbles will have sudden

phase variations that may reduce the pulse compression efficiency. For this reason, two different scenarios were tested with a low pressure and a high pressure excitation, to evaluate the effectiveness of the techniques explained in the chapter 3.

8.3.1 Low Pressure Simulations
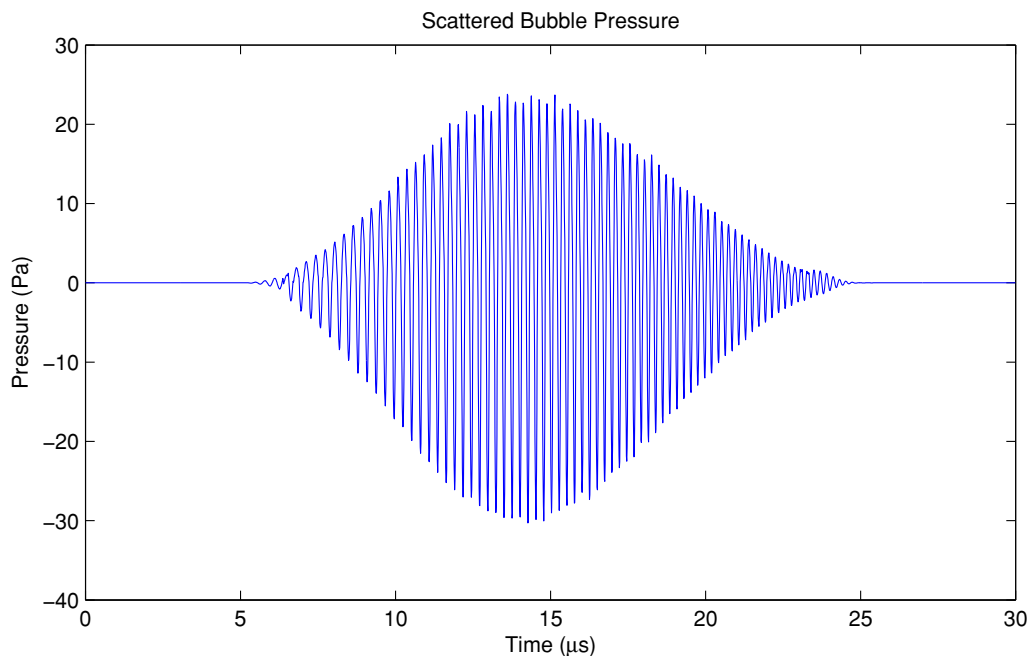
Figure 8.5: Simulated pressure waveform scattered by a 3 μm microbubble excited by a LFM chirp with a peak negative acoustic pressure of 100 kPa, a centre frequency of 4 MHz, a bandwidth of 2 MHz, and a duration of 20 μs.

Figure 8.5 shows the simulated 3 μm microbubble response to a LFM chirp excitation with a 4 MHz centre frequency, a 2 MHz bandwidth, and a 20 μs duration.

Even at pressure levels as low as 100 kPa, microbubbles generated significantly more harmonics than tissue, where the spectrum of the scattered pressure from the 3 μm microbubble is given in Figure 8.6.

Figure 8.7 shows the signal compressed by a matched filter. The mainlobe width of the compressed signal was the same as with the autocorrelation function of the excitation waveform, but an increase in sidelobe levels was observed. Although the sidelobe levels were higher than expected, the waveforms compressed with a matched filter could still be used for imaging applications with 40 dB dynamic range. Since
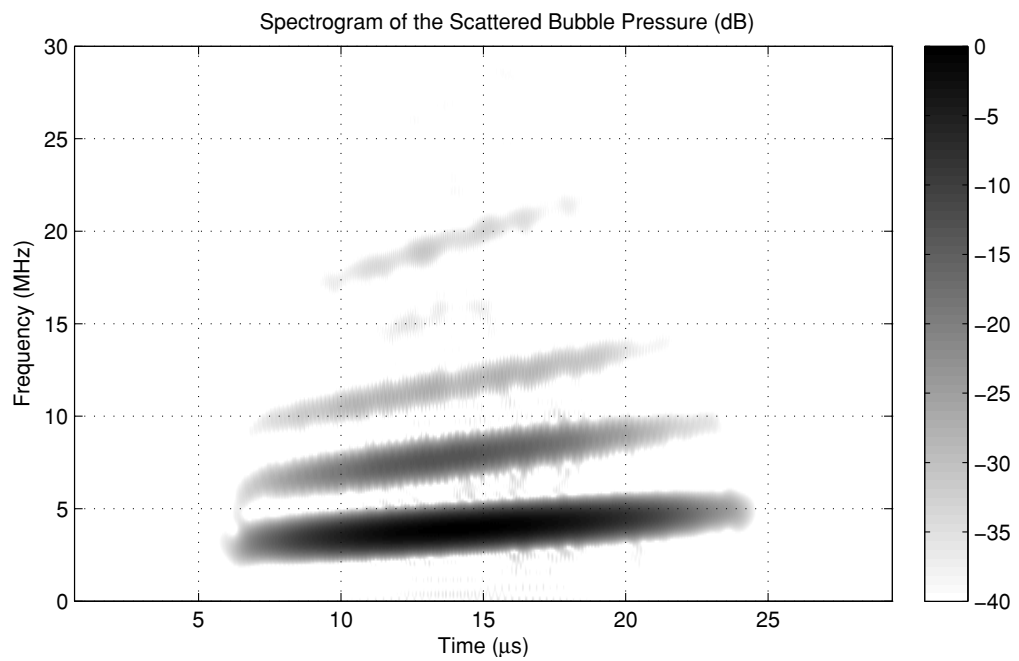
Figure 8.6: Spectrogram of the simulated pressure waveform scattered by a 3 μm microbubble excited by a LFM chirp with a peak negative acoustic pressure of 100 kPa, a centre frequency of 4 MHz, a bandwidth of 2 MHz, and a duration of 20 μs.

there was no spectral overlap between the second harmonic and the fundamental components, the compressed signal did not suffer from compression artefacts as represented in Figure 6.12.
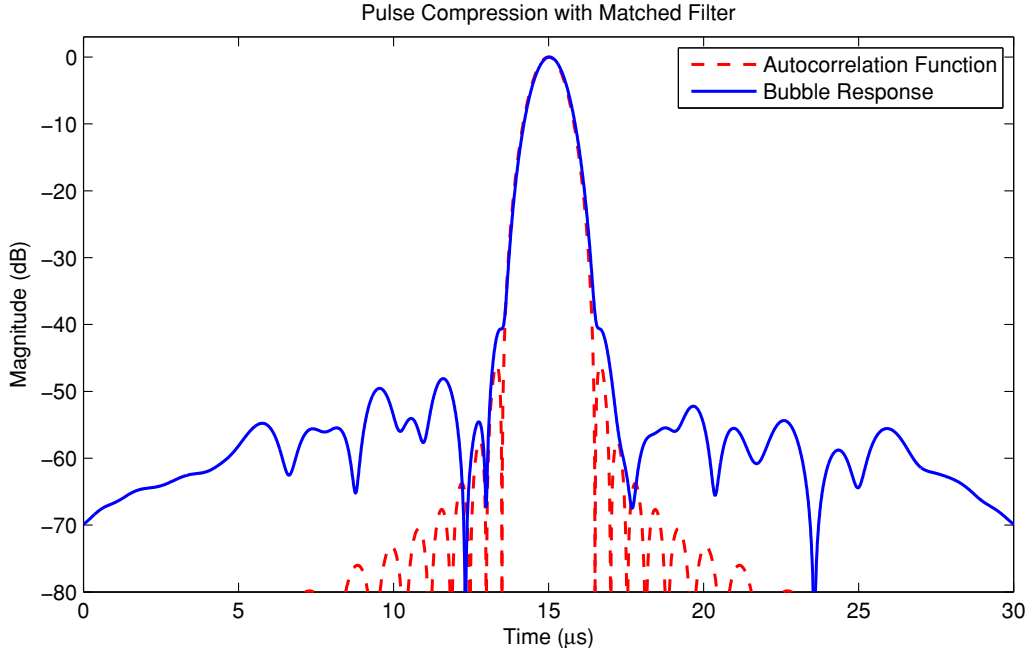
Figure 8.7: Simulated pressure waveform compressed by a matched filter for a 3 μm microbubble excited at 100 kPa. The pulse compression was performed with a matched filter designed with the same parameters of the excitation signal; a centre frequency of 4 MHz, a bandwidth of 2 MHz, and a duration of 20 μs. The red dashed line is the autocorrelation function of the excitation waveform given for comparison.

Figure 8.8 and Figure 8.9 show the signal compressed by a matched filter, after filtering in the FrFT domain and the FChT domain respectively as explained in chapter 3. Even though the final compressed signal benefited from filtering in the FChT domain and the FrFT domain, the differences in the mainlobe width and peak sidelobe level of the compressed signals in Figure 8.7, Figure 8.8, and Figure 8.9 were negligible.

Figure 8.10 shows the signal compressed with a second harmonic matched filter before and after filtering in the FrFT domain and the FChT domain. The pulse compression was performed with a second harmonic matched filter designed with twice the parameters of the excitation signal; centre frequency of 8 MHz, bandwidth of 4 MHz, and duration of 20 μs. As expected, the compressed second harmonic component
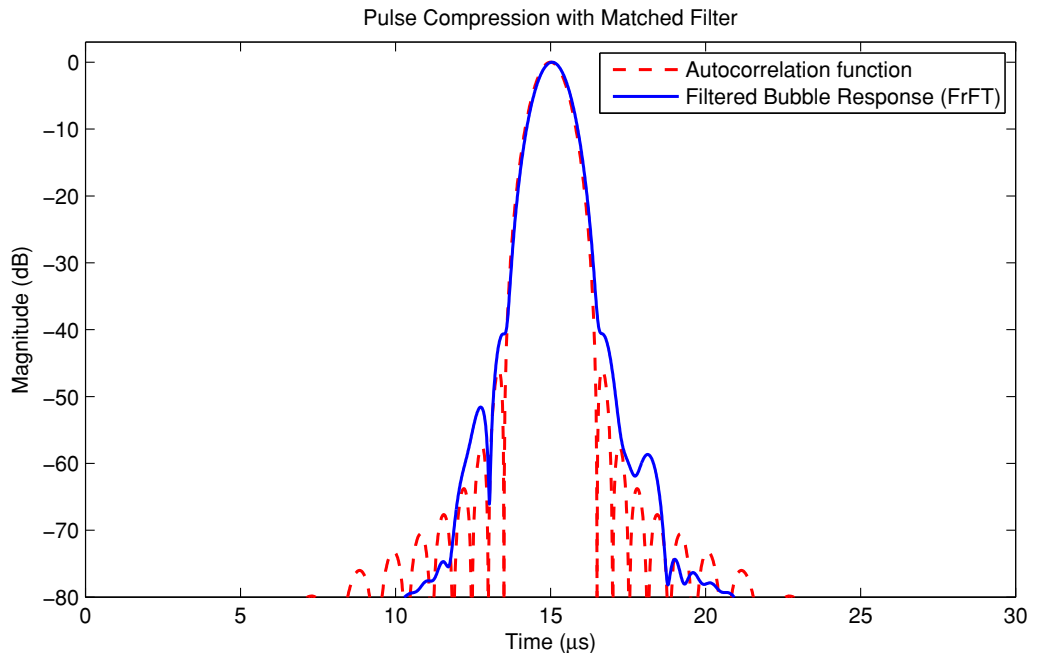
Figure 8.8: Simulated pressure waveform compressed by a matched filter after filtering in the FrFT domain for a 3 μm microbubble excited at 100 kPa. The pulse compression was performed with a matched filter designed with the same parameters of the excitation signal; a centre frequency of 4 MHz, a bandwidth of 2 MHz, and a duration of 20 μs. The red dashed line is the autocorrelation function of the excitation waveform given for comparison.
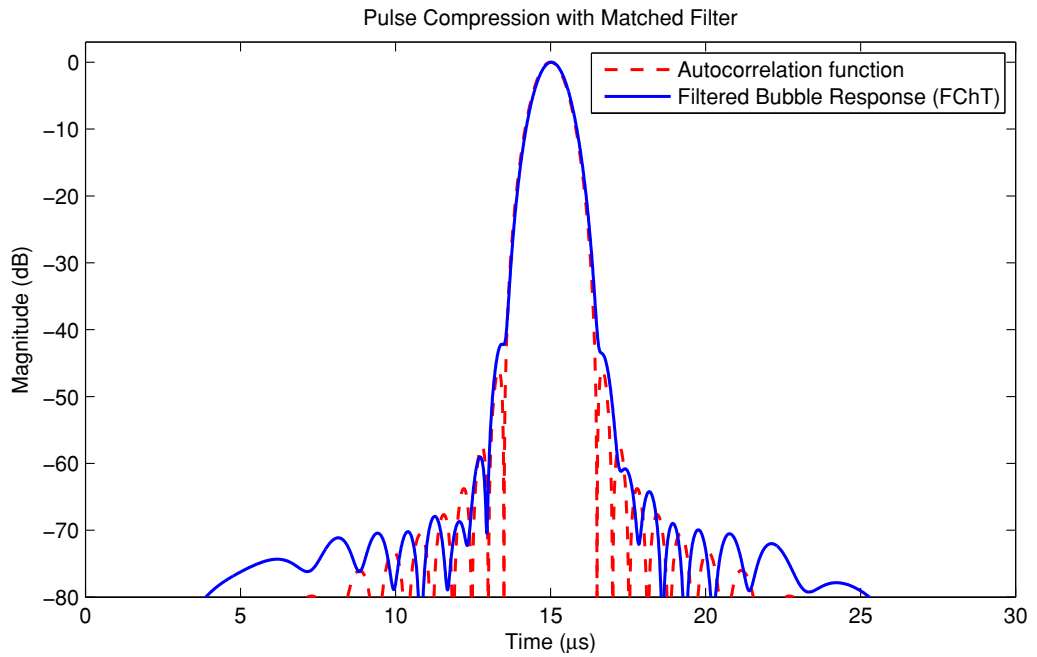
Figure 8.9: Simulated pressure waveform compressed by a matched filter after filtering in the FChT domain for a 3 μm microbubble excited at 100 kPa. The pulse compression was performed with a matched filter designed with the same parameters of the excitation signal; a centre frequency of 4 MHz, a bandwidth of 2 MHz, and a duration of 20 μs. The red dashed line is the autocorrelation function of the excitation waveform given for comparison.

achieved a better resolution than the fundamental. Also, filtering in the FChT domain and the FrFT domain before pulse compression reduced the sidelobe levels.
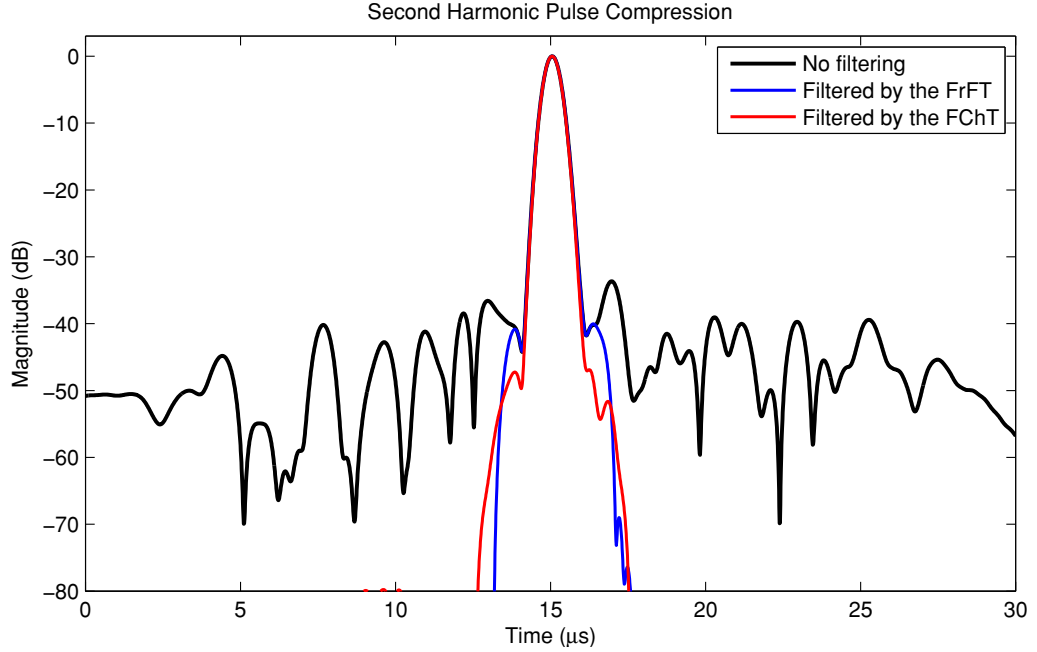
Figure 8.10: Simulated pressure waveform compressed by a second harmonic matched filter without any filtering and after filtering in the FrFT and FChT domains for a 3 μm microbubble excited at 100 kPa. The pulse compression was performed with a second harmonic matched filter designed with twice the parameters of the excitation signal; a centre frequency of 8 MHz, a bandwidth of 4 MHz, and a duration of 20 μs.

8.3.2 High Pressure Simulations

For this set of simulations, all the parameters were the same as the previous simulations but the acoustic pressure was increased. Although microbubbles are highly echogenic and generate more harmonics than tissue at low pressure levels, the use of acoustic pressures as high as 500 kPa is common while imaging with microbubbles Sun *et al.* (2007). Therefore, the simulations were repeated by increasing the excitation pressure to 500 kPa.

The time frequency representation of the scattered pressure waveform at 500 kPa by a 3 μm microbubble is given in Figure 8.11. When compared with Figure 8.6 the
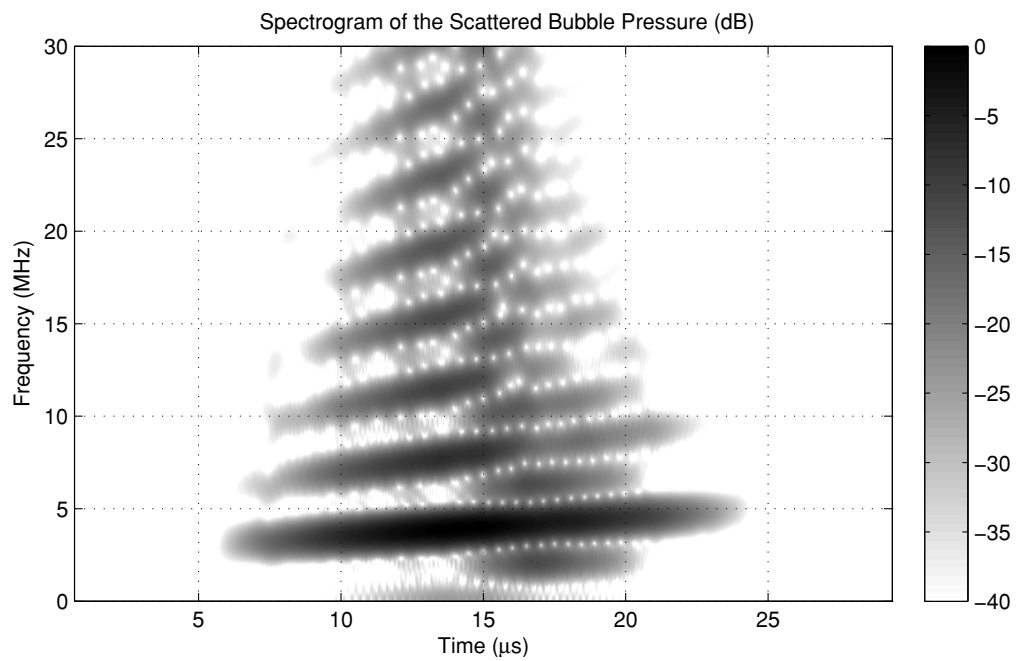
Figure 8.11: Spectrogram of the simulated pressure waveform scattered by a 3 μm microbubble excited by a LFM chirp with a peak negative acoustic pressure of 500 kPa, a centre frequency of 4 MHz, a bandwidth of 2 MHz, and a duration of 20 μs.

harmonic generation was significantly higher than the low pressure excitation with subharmonic[1] and ultraharmonic[2] components being introduced.

Figure 8.12 shows the signal compressed by a matched filter for a 500 kPa excitation. The mainlobe width of the compressed signal was wider than the autocorrelation function of the excitation waveform, especially below -15 dB. Due to the spectral overlap between the subharmonic, ultraharmonic and fundamental components, the compressed signal suffered from high sidelobe levels.
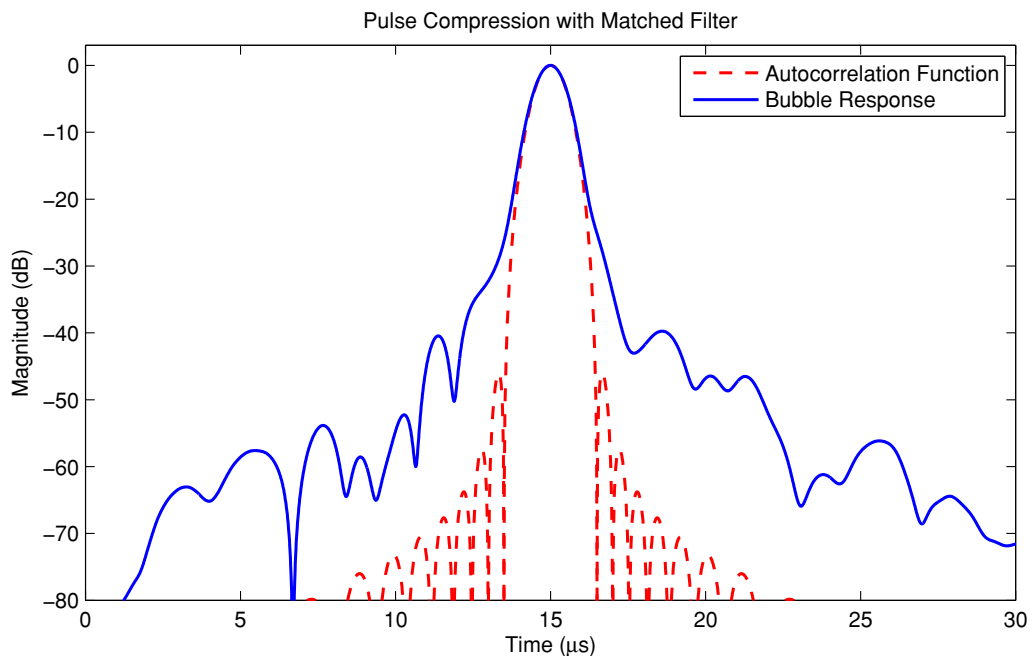
Figure 8.12: Simulated pressure waveform compressed by a matched filter for a 3 μm microbubble excited at 500 kPa. The pulse compression was performed with a matched filter designed with the same parameters of the excitation signal; a centre frequency of 4 MHz, a bandwidth of 2 MHz, and a duration of 20 μs. The red dashed line is the autocorrelation function of the excitation waveform, which is given for comparison.

Figure 8.13 shows the waveform compressed in the FrFT domain. Although the waveform was successfully compressed and separated from its harmonics, the FrFT was not a good candidate for compressing and filtering the microbubble response as explained in chapter 3 and chapter 7. In Figure 8.13, the fundamental component

---

[1] The harmonics generated at $1/n$ multiples of the fundamental frequency for $n = 2, 3, 4...$

[2] The harmonics generated at $(2k + 1)/2$ multiples of the fundamental frequency for $k = 1, 2, 3...$

was successfully compressed at $t = 15$ μs, but the drawback of the FrFT is that the transform must be individually calculated for each harmonic.
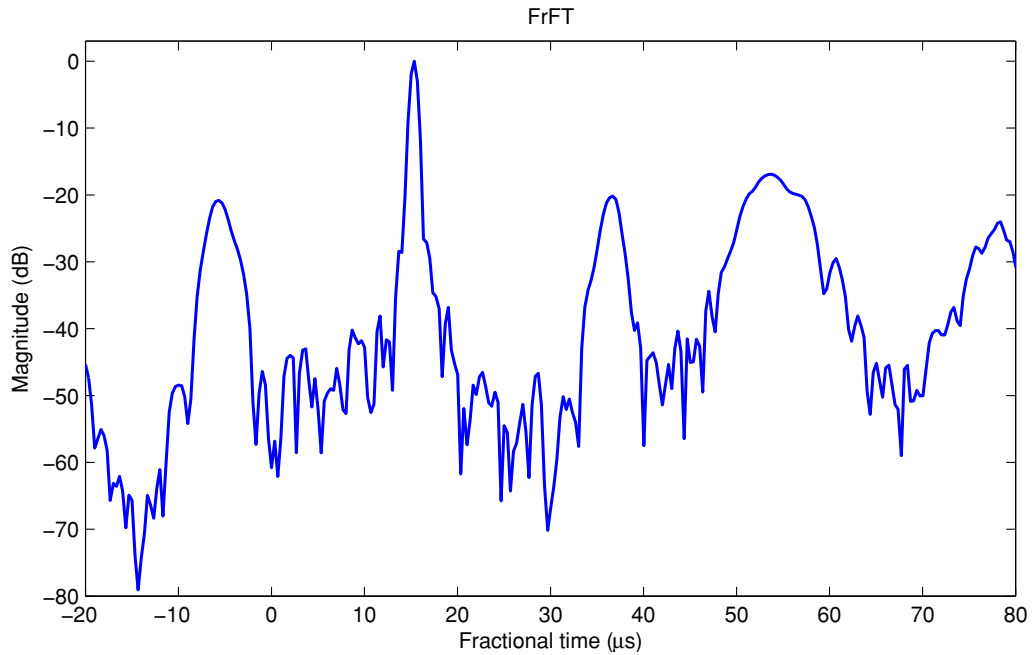
Figure 8.13: The FrFT spectrum of the simulated pressure waveform scattered by a 3 μm microbubble excited by a LFM chirp with a peak negative acoustic pressure of 500 kPa, a centre frequency of 4 MHz, a bandwidth of 2 MHz, and a duration of 20 μs.

Figure 8.14 shows the compressed waveform in the FChT domain. The fundamental and second harmonic components of the scattered waveform appeared exactly at 4 MHz and 8 MHz in the warped-frequency domain, respectively. Therefore, both fundamental and second harmonic components can be filtered in the FChT domain after a single transformation.

Figure 8.15 shows the signal compressed by a matched filter, after filtering in the FChT domain. For this example, the compressed signal significantly benefited from filtering in the FChT domain, where both the mainlobe width and sidelobe levels were improved in comparison with Figure 8.12.

Figure 8.16 shows the signal compressed by a second harmonic matched filter before and after filtering in the FChT domain. Both the mainlobe width and sidelobe levels were improved after filtering in the FChT domain. The compressed second harmonic signal did not give any improvement on the mainlobe width compared to the compressed
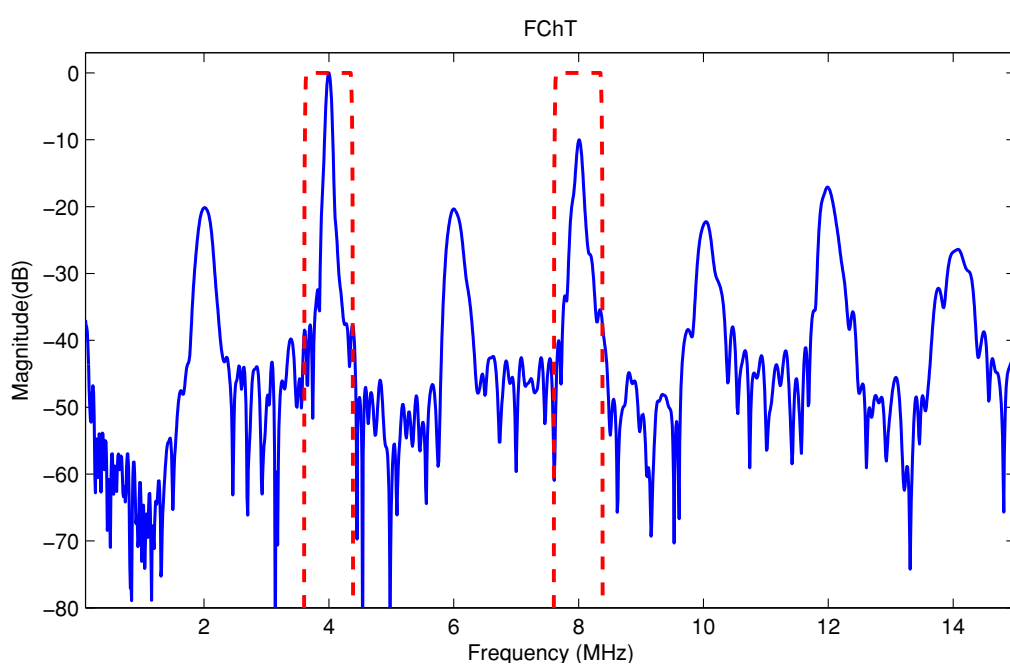
Figure 8.14: The FChT spectrum of the simulated pressure waveform scattered by a 3 μm microbubble excited by a LFM chirp with a peak negative acoustic pressure of 500 kPa, a centre frequency of 4 MHz, a bandwidth of 2 MHz, and a duration of 20 μs. The red dashed lines show the windows applied around the fundamental and second harmonic component for filtering.
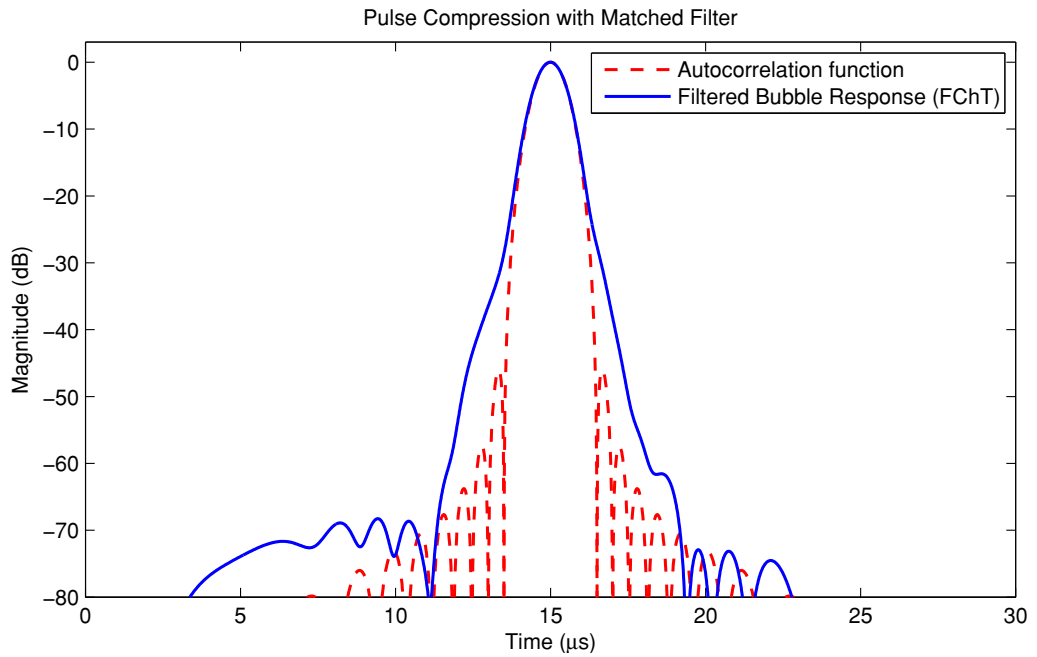
Figure 8.15: Simulated pressure waveform compressed by a matched filter after filtering in the FChT domain for a 3 μm microbubble excited at 500 kPa. The pulse compression was performed with a matched filter designed with the same parameters of the excitation signal; a centre frequency of 4 MHz, a bandwidth of 2 MHz, and a duration of 20 μs. The red dashed line is the autocorrelation function of the excitation waveform given for comparison.

fundamental component. The compressed second harmonic signal after filtering in the FChT domain had a larger mainlobe width than its equivalent at 100 kPa given in Figure 8.10, however it showed improvement over the compressed signal without any filtering.
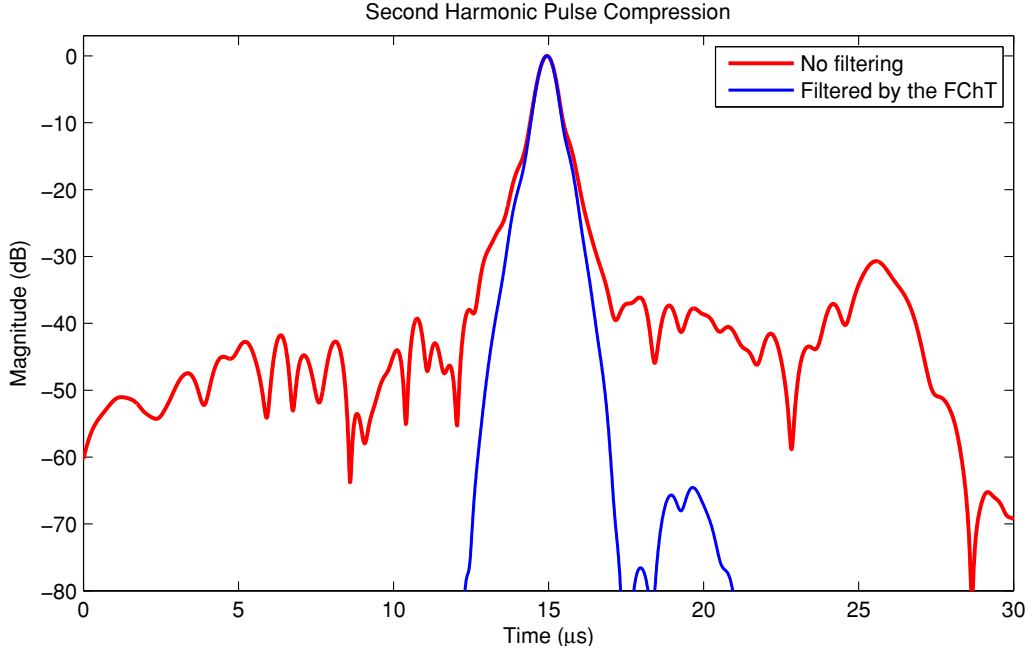
Figure 8.16: Simulated pressure waveform compressed by a second harmonic matched filter without any filtering and after filtering in the FChT domains for a 3 μm microbubble excited at 500 kPa. The pulse compression was performed with a second harmonic matched filter designed with twice the parameters of the excitation signal; a centre frequency of 8 MHz, a bandwidth of 4 MHz, and a duration of 20 μs.

Table 8.1 presents the results achieved from the simulations by comparing the mainlobe width of compressed signals at -20 dB and peak sidelobe level. The simulation results showed that filtering in the FChT domain reduces the sidelobe levels of the compressed waveform both for second harmonic and fundamental components. For the simulations performed at a peak negative pressure of 100 kPa the improvements were not evident, however at 500 kPa the sidelobe levels were reduced significantly after filtering in the FChT domain both for the fundamental and the second harmonic components.

The main reason for this difference in sidelobe levels was the harmonics generated

Table 8.1: Mainlobe widths and peak sidelobe levels of the compressed fundamental and second harmonic components.

FUNDAMENTAL	Mainlobe Width	Peak Sidelobe Level
Autocorrelation function	2.2 μs	-46.0 dB
No filtering (100 kPa)	2.2 μs	-40.7 dB
FrFT (100 kPa)	2.2 μs	-40.7 dB
FChT (100 kPa)	2.2 μs	-42.1 dB
No filtering (500 kPa)	2.5 μs	-39.7 dB
FChT (500 kPa)	2.3 μs	-61.7 dB
SECOND HARMONIC	Mainlobe Width	Peak Sidelobe Level
No filtering (100 kPa)	1.3 μs	-33.7 dB
FrFT (100 kPa)	1.3 μs	-40.0 dB
FChT (100 kPa)	1.3 μs	-46.9 dB
No filtering (500 kPa)	2.2 μs	-30.7 dB
FChT (500 kPa)	1.9 μs	-64.5 dB

by the microbubbles. For the high pressure simulations, the microbubbles generated more harmonics that spectrally overlap with each other. In the presence of spectral overlap the performance of the matched filter dropped as presented in the chapter 6. The reasons why FrFT was not chosen for compressing and filtering the microbubble response at high pressure levels were reviewed in the chapter 3 and chapter 7.

8.4 Experimental Results and Discussion

8.4.1 Scattering Measurements
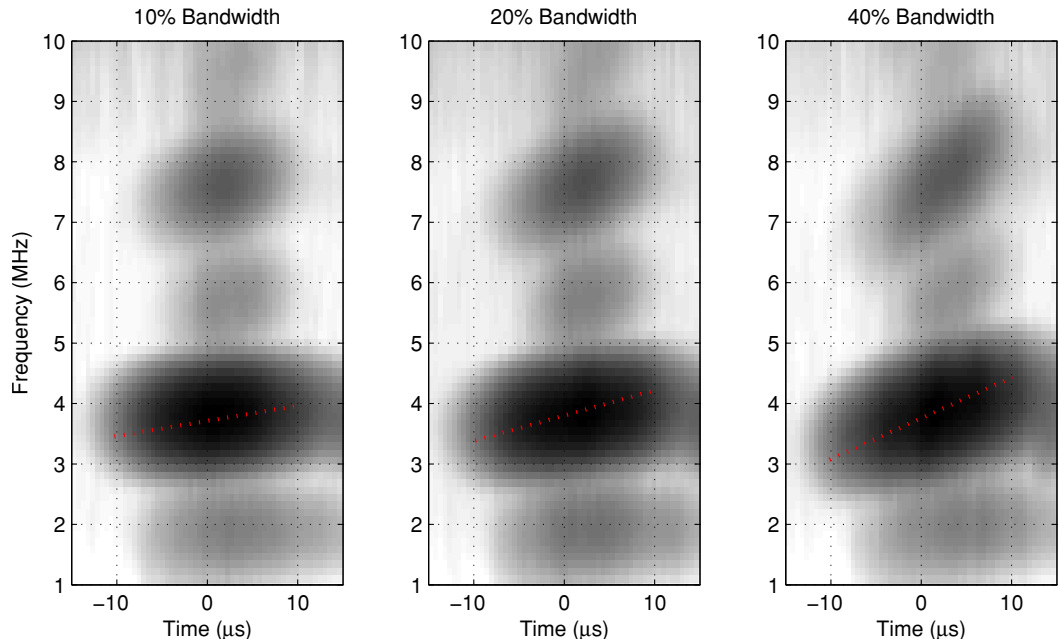
Figure 8.17: Spectrogram of the scattered pressure waveforms from a microbubble population with the chirp excitation of 3.8 MHz centre frequency and 20 μs signal duration at 500 kPa for (Left) 10% fractional bandwidth, (Middle) 20% fractional bandwidth, and (Right) 40% fractional bandwidth. The red dotted lines show the chirp rate of the excitation waveform.

The first experiments were performed to observe the spectral response of the microbubble population. Figure 8.17 shows the scattered pressure waveform from the microbubble cloud for a 10%, 20%, and 40% fractional bandwidth. It was observed that the scattered pressure waves maintained their chirp rates for the fundamental and

harmonic components in all three measurements. Since the chirp rates remained the same, it was expected to observe improvements after filtering in the FChT domain.

Figure 8.18 shows the spectrum of scattered pressure waveform for a chirp excitation with a 3.8 MHz centre frequency, a 20 μs signal duration, and a 20% fractional bandwidth. Similar results were observed for the other measurements with different excitation waveforms. The signals were corrected according to the control measurements performed without microbubbles, therefore 0 dB was the noise level for all measurements. The increase in broadband noise for the high pressure excitations was due to microbubble destruction, which reduced the SNR. The increased noise level also suggests that the compressed signals will benefit from filtering in the FChT domain.
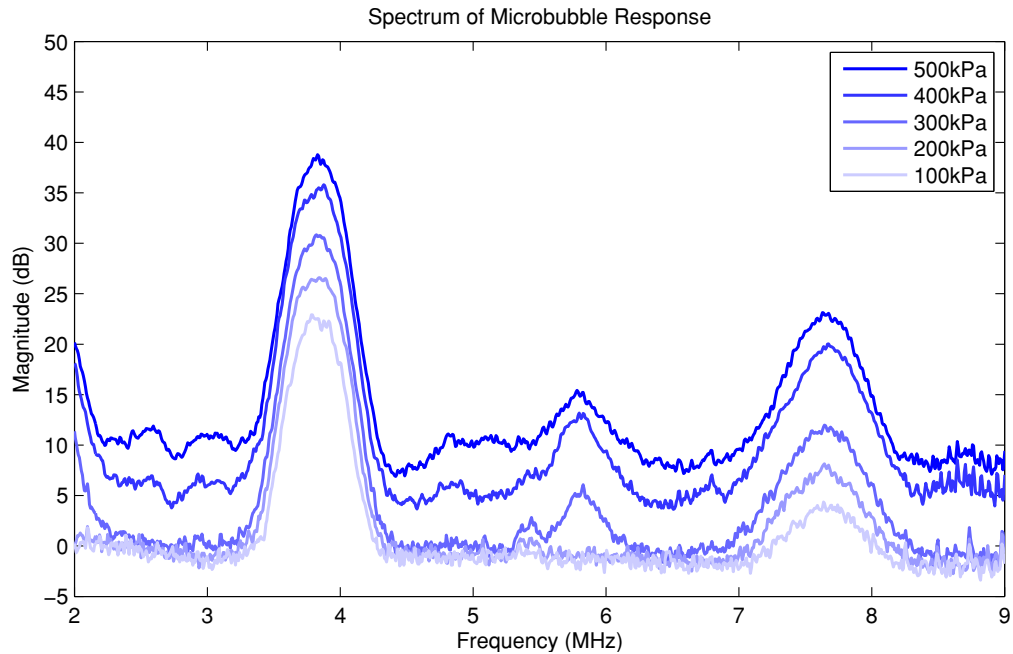
Figure 8.18: Frequency spectrum of the scattered pressure waveforms from a microbubble population for LFM chirp excitation with 3.8 MHz centre frequency, 20 μs signal duration, and 20% fractional bandwidth and a pressure range of $100 - 500$ kPa.

8.4.2   Imaging and Point Spread Function

The performance of the filtering in the FChT domain can be assessed by comparing the spatial impulse responses of the system with and without filtering stages. The spatial impulse response is also referred to as the point spread function for imaging

applications. Figure 8.19 shows the point spread function for the ultrasound images formed at the fundamental frequency and processed with the FChT and without the FChT. After filtering in the FChT domain the sidelobe level was reduced as expected by simulations.

Figure 8.21 shows the point spread function of the ultrasound images at second harmonic frequency processed by the FChT and without the FChT. Similar results observed for the second harmonic image, where filtering in the FChT domain reduced the sidelobe levels.

When the same experiment was repeated with microbubbles, the fundamental and the second harmonic images filtered with the FChT had lower sidelobe levels as shown in Figure 8.22 and Figure 8.20. After *shadowing* by a cloud of microbubbles, no significant difference was observed on the point spread function of the sub-wavelength scatterer after pulse compression. Nevertheless, the peak sidelobe level was reduced both for the fundamental and the second harmonic images when they were processed with the FChT.

Table 8.2 shows the results measured from the fundamental and second harmonic images in Figure 8.19, 8.20, 8.21, and 8.22 by comparing the point spread function dimensions at -20 dB and peak sidelobe level. The experimental measurements showed similar results with the simulations performed in the previous section. Dimensions of the point spread function did not change after filter with the FChT. However, filtering in the FChT domain significantly reduced the sidelobe levels of the compressed waveform in the presence of microbubbles both for second harmonic and fundamental components by 20.4 dB and 8 dB, respectively.

Although the image quality was improved for a point scatterer, the microbubble response was observed to be weaker after filtering in the FChT domain. Figure 8.18 may explain the difference between the images filtered in the FChT and not filtered in the FChT domain. For the images processed without using the FChT, as shown in the Figure 8.22(left) and Figure 8.20(left), the matched filter did not only compress the waveforms scattered with the same chirp rate, but also the broadband noise and harmonics that were within the bandwidth of the matched filter. Yet, the FChT ignored them due to the peak detection method used for separating the maximally compressed and partially compressed waveforms as explained in the section 3.3. The CTR being one of the most important metrics in measuring the microbubble response and the
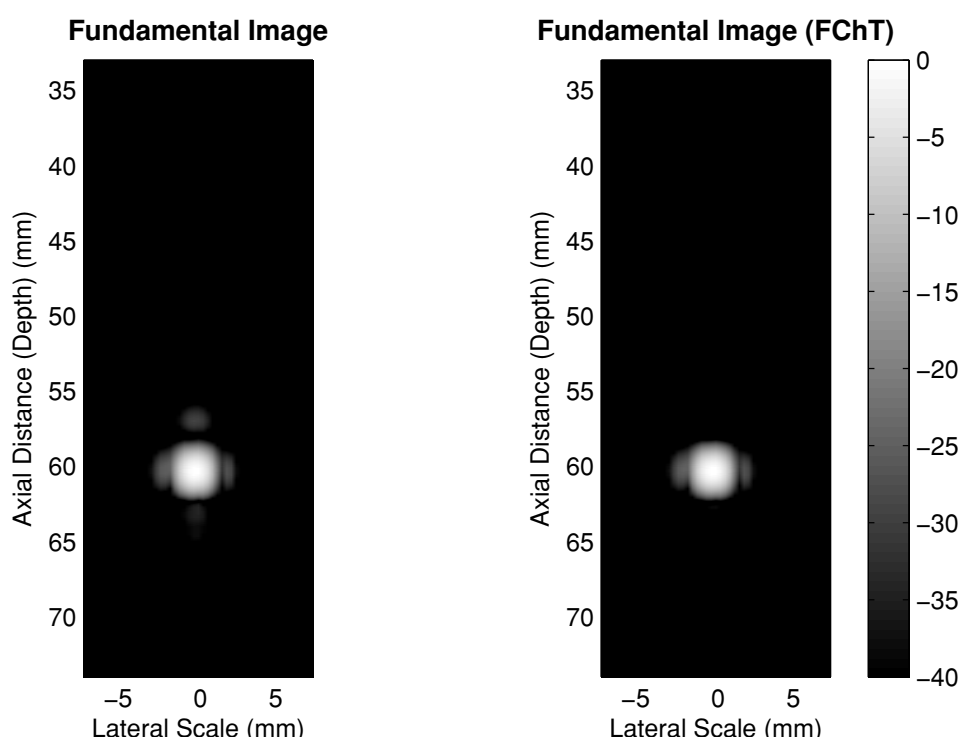
Figure 8.19: The fundamental image of the experimental setup given in Figure 8.2 (Left) compressed with a match filter, and (Right) compressed with a match filter after filtering by the FChT. The sub-wavelength scatterer is located at 60 mm.
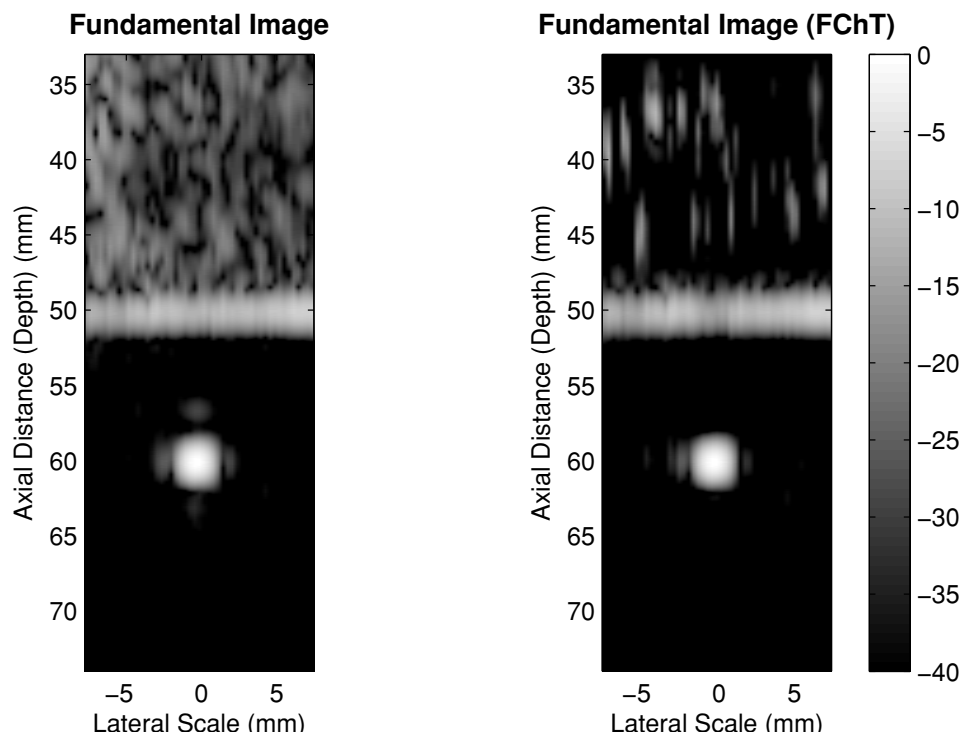
Figure 8.20: The fundamental image of the experimental setup given in Figure 8.3 (Left) compressed with a match filter, and (Right) compressed with a match filter after filtering by the FChT. The sub-wavelength scatterer is located at 60 mm. The microbubble chamber is positioned between 30 mm and 50 mm.
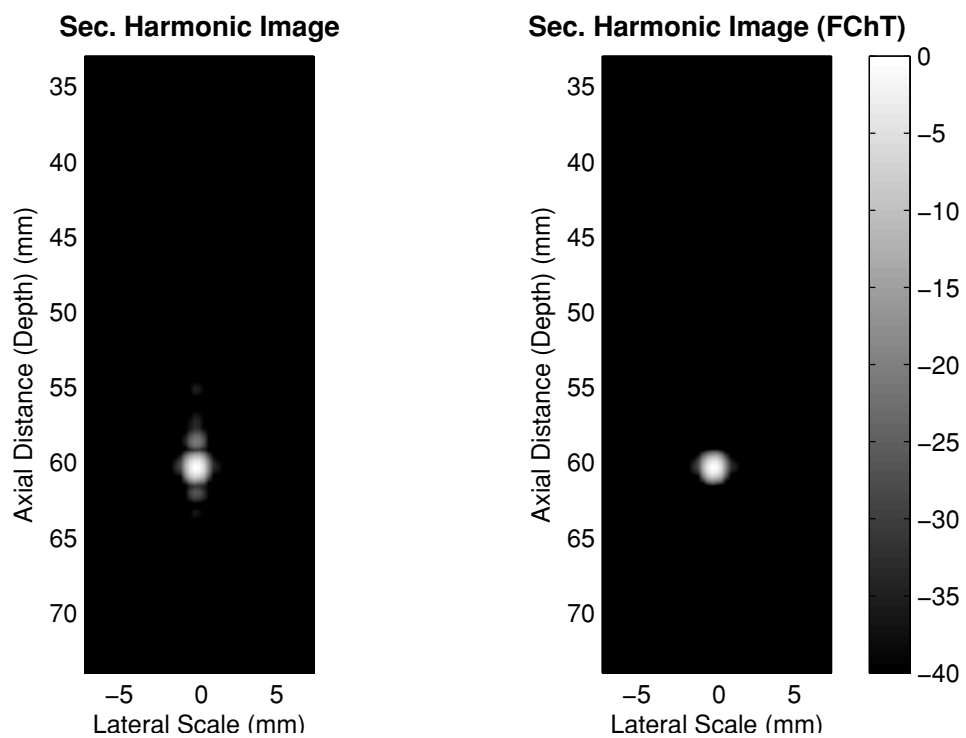
Figure 8.21:   The second harmonic image of the experimental setup given in Figure 8.2 (Left) compressed with a match filter, and (Right) compressed with a match filter after filtering by the FChT. The sub-wavelength scatterer is located at 60 mm.
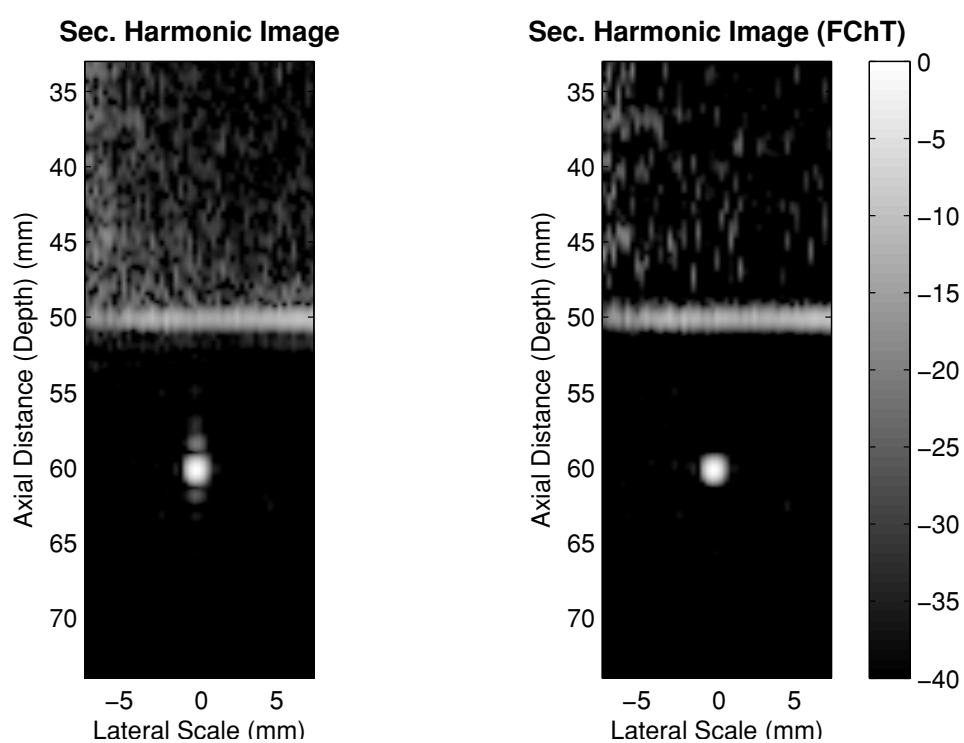
Figure 8.22:   The second harmonic image of the experimental setup given in Figure 8.3 (Left) compressed with a match filter, and (Right) compressed with a match filter after filtering by the FChT. The sub-wavelength scatterer is located at 60 mm. The microbubble chamber is positioned between 30 mm and 50 mm.

Table 8.2: Point spread function dimensions and peak sidelobe levels (PSLL) of the fundamental and second harmonic images filtered with and without the FChT.

	without MB		with MB	
FUNDAMENTAL	MF	FChT + MF	MF	FChT + MF
Axial (mm)	3.23	3.22	3.27	3.23
Lateral (mm)	2.90	2.90	2.99	2.99
PSLL (dB)	-29.5	-38.1	-29.1	-37.1
SECOND HARMONIC	MF	FChT + MF	MF	FChT + MF
Axial (mm)	1.94	1.86	1.97	1.85
Lateral (mm)	1.64	1.64	1.64	1.64
PSLL (dB)	-20.7	-39.0	-20.5	-40.9

quality of the ultrasound image, the results achieved by the FChT method may not be considered as an improvement by radiologists.

8.5 Conclusions

Any dispersive media exhibits nonlinear behaviour and generates harmonics, as explained in the appendix B. Yet, the mechanisms responsible for the nonlinear behaviour of microbubbles are completely different. Water always generates harmonics in an expected manner as given in Figure 7.3, but microbubbles have unique acoustic signatures that change with bubble size, bubble encapsulation, bubble gas core, excitation pressure, and excitation frequency. However, the scattered response from the microbubble population still have the same chirp rate as the excitation signal and the chirp rate of the harmonics generated by the microbubbles are scaled by a ratio of n for the nth-harmonic as presented in Figure 8.18. Therefore, it is possible to use the FChT as a filtering tool for contrast-enhanced ultrasound imaging and contrast-enhanced second harmonic imaging.

In this study, one of the possible worst case scenario for pulse compression was created by depth and frequency dependant attenuation, high level of harmonic gener-

ation, variation on the phase information due to resonance behaviour of microbubbles, increased broadband noise by microbubble destruction and limited transducer bandwidth. Nevertheless, filtering in the FChT domain reduced the compression artefacts and successfully improved the image quality.

Chapter 9

Separating the Second Harmonic Response of Tissue and Microbubbles using Bispectral Analysis

The second harmonic generation in medical ultrasound is either caused by tissue or ultrasound contrast agents. The conventional signal processing techniques cannot separate the harmonic response from microbubbles and tissue. The second order spectral analysis, commonly known as the frequency analysis, is the most common way of evaluating the microbubble response. Although frequency analysis can estimate the power spectrum effectively, it suppresses the phase relation between the frequency components.

In this work, the third order spectral analysis (bispectral analysis) is used to evaluate the second harmonic response of tissue and microbubbles. The power spectrum shows the magnitude of energy existing at different frequencies, but fails to show the relation between their phases. Higher-order spectral analysis can display the phase-coupling between different frequency components, *i.e.* between fundamental and harmonics. Thus, bispectral analysis can be utilized to evaluate the microbubble response and separate the second harmonic generated by tissue and microbubbles using the phase coupling between fundamental and harmonic components.

This work has been accepted for publication as (Harput *et al.*, 2012).

9.1 Introduction

The nonlinear behaviour of the ultrasound contrast agents (UCAs) is utilized in medical ultrasound imaging to distinguish blood from the surrounding tissue by enhancing the blood echogenicity (de Jong *et al.*, 2000; Frinking *et al.*, 2000). The nonlinear harmonic components generated by microbubbles are used in ultrasound contrast imaging to improve the image contrast and allow a selective detection during perfusion (de Jong *et al.*, 2009).

One of the most common techniques to improve the contrast-to-tissue ratio (CTR) is second harmonic imaging. Most commercial ultrasound imaging systems offer second harmonic imaging and it is widely used in clinical applications, such as myocardial perfusion, tumour detection, and blood flow measurements (Porter & Xie, 2010; Tranquart *et al.*, 1999; Wei *et al.*, 1998). Quantitative evaluation of blood perfusion is clinically valuable in many situations (Schrope & Newhouse, 1993). Contrast-enhanced perfusion imaging, the qualitative and the quantitative assessment is based on (i) pixel-wise evaluation of the region of interest, e.g. wash-in curves plotted according to change in pixel intensity values of the ultrasound video, or (ii) visual inspection of the B-mode images (Wiesmann *et al.*, 2004). These assessment techniques may causes inconsistent quantification of the perfusion for different scenarios. The problem becomes more evident if usage of different UCAs, the variability in the scanning conditions and the tissue generated second harmonic are considered.

This study focuses on the assessment of the second harmonic to improve the CTR in harmonic imaging and increase the accuracy of perfusion imaging by distinguishing between the second harmonic response generated by the tissue and UCAs. It is usually assumed that at low pressure levels, tissue does not generate harmonics and CTR is improved by microbubble generated second harmonic. However, harmonics are generated even at low pressure levels, thus causing the misinterpretation of harmonic response from microbubbles (Duck, 2002; Hamilton & Blackstock, 2008). For example, human soft tissue generates second harmonic as high as -20 dB compared to the fundamental for an excitation pressure of 140 kPa, a 4 MHz centre frequency and at a depth of 3.5 cm as described in appendix B.

Nonlinear propagation in tissue generates harmonics that are in phase with the fundamental component. The variation in phase velocity at different points on the

wave progressively steepens the waveform. The distortion of the wave happens in an expected manner, where the shape turns from sinusoidal to sawtooth (Duck, 2002). However, the harmonics generated by a polydisperse population of microbubbles are not necessarily in phase with the fundamental component. In this work, bispectral analysis is used to separate the second harmonic response of tissue and microbubbles via the phase relations of fundamental and harmonic components. The degree of phase coherence, the bicoherence index, is calculated by using the phase coupling between fundamental and second harmonic components for a set of measurements.

9.2 Bispectral Analysis

The second order spectral analysis, commonly known as the frequency analysis, is the most common way of evaluating the microbubble response. Most power spectrum estimation techniques, including the conventional Fourier type methods, estimate the power distribution of the signal by suppressing the phase relation between the frequency components.

For a time domain zero-mean stationary signal $s(t)$ with a duration of T[1], the Fourier transform of the signal can be represented as

$$S(f) = \lim_{T \to \infty} \frac{1}{T} \int_{-T/2}^{T/2} s(t) \, e^{-j2\pi ft} dt. \tag{9.1}$$

The power spectral density of the signal is estimated as

$$P(f) = E\left\{S(f) \, S^*(f)\right\} = \lim_{T \to \infty} \frac{1}{T} \int_{-T/2}^{T/2} s(t)^2 \, dt. \tag{9.2}$$

where $E\left\{\cdot\right\}$ represents the expected value, and $*$ denotes the complex conjugate.

The Fourier analysis can only represent the complete statistics of a Gaussian process, where any finite linear combination of samples has a joint Gaussian distribution (Kim & Powers, 1979; Nikias & Raghuveer, 1987). However, higher order spectral techniques are necessary to characterize the signals in the presence of nonlinearities and identification of non-Gaussian behaviour (Nikias & Raghuveer, 1987). These nonlinearities may create new phase coherent spectral components. The third-order spectrum or bispectrum can be used for the detection of such phase coherence.

---

[1]Record length of the signal $s(t)$.

170

The third-order spectrum can be generalised by considering higher-order products of the signal, where the power spectrum is defined as the mean squared value of the signal for a zero-mean random process. To explain the third-order spectrum, the moments and the cumulants must be defined first. The r-th moment of signal $s(t)$ is defined as

$$m_r = E\left\{s^r(t)\right\}. \tag{9.3}$$

Cumulants can be defined as moments in which the dependence on lower order moments has been removed, where the moments of a random variable are related to its cumulants by (Nikias & Petropulu, 1993)

$$
\begin{aligned}
c_1 &= m_1 \\
c_2 &= m_2 - m_1^2 \\
c_2 &= m_3 - 3m_2 m_1 + 2m_1^3
\end{aligned}
\tag{9.4}
$$

The first moment, m_1, is the mean and it is assumed to be zero since the process has a zero mean.

$$m_1 = c_1 = E\left\{s(t)\right\} = 0. \tag{9.5}$$

The second moment, m_2, is the variance or the spread of the data around the mean. The second order moment is also known as the autocorrelation function since

$$R_{ss}(\tau) = E\left\{s(t)\, s(t-\tau)\right\}. \tag{9.6}$$

The Wiener-Khinchin theorem states the relation between the autocorrelation function and the power spectral density as the Fourier transform. Therefore, the second order spectrum, power spectral density, of a signal is the Fourier transform of its autocorrelation function,

$$P(f) = \int_{-\infty}^{\infty} R_{ss}(\tau)\, e^{-j2\pi f\tau} d\tau. \tag{9.7}$$

For a zero-mean signal ($m_1 = 0$), the second order cumulant is equal to second order moment, $c_2 = m_2$. Therefore, the second order cumulant spectrum represents the power spectrum;

$$P(f) = \int_{-\infty}^{\infty} c_2(\tau)\, e^{-j2\pi f\tau} d\tau. \tag{9.8}$$

The third moment, m_3, is a measure of asymmetry that shows the skewness of the process's probability density function. The third moment is zero, $m_3 = 0$, for

all symmetric distributions such as a Gaussian distribution. Therefore, higher-order cumulants are necessary for the identification of Gaussian and non-Gaussian behaviour.

The bispectrum is equal to third order cumulant spectrum for a zero-mean signal since $c_3 = m_3$.

$$B(f_1, f_2) = \int_{-\infty}^{\infty} \int_{-\infty}^{\infty} c_3(\tau_1, \tau_2) \, e^{-j2\pi(f_1\tau_1 + f_2\tau_2)} d\tau_1 d\tau_2. \tag{9.9}$$

The third order spectrum, bispectrum, can also be calculated for f_1 and f_2 using the Fourier transform of the signal as (Kim & Powers, 1979; Nikias & Raghuveer, 1987);

$$B(f_1, f_2) = E\left\{S(f_1)\, S(f_2)\, S^*(f_1 + f_2)\right\}, \tag{9.10}$$

where the bispectrum contains additional information about the statistical dependence of frequencies f_1 and f_2 at the coupled frequency $f_1 + f_2$.

The bicoherence index, $b(f_1, f_2)$, normalizes the bispectrum by the power spectrum as

$$b(f_1, f_2) = \frac{B(f_1, f_2)}{\sqrt{P(f_1)\, P(f_2)\, P(f_1 + f_2)}}, \tag{9.11}$$

where $b^2(f_1, f_2)$ is the measure of the quadratic phase coupling. For $b^2(f_1, f_2) = 0$, no phase coherence exists between the harmonic component at the coupled frequency $f_1 + f_2$, and fundamental component at f_1 and f_2. When the bicoherence index is equal to 1, it indicates 100% phase coherence.

9.2.1 Discrete Bispectral Analysis

The computation of the bispectrum was performed on the discrete signal $s[n]$, after sampling the continuous signal $s(t)$ with a record length of T. The duration $T = N \cdot \Delta t$ was large enough to have sufficient frequency resolution and the sampling interval Δt was small enough to ensure that any spectral component is smaller than the Nyquist frequency. For the discrete signal $s[n]$ the Fourier amplitudes are calculated by the discrete Fourier transform as (Kim & Powers, 1979)

$$S_k = \frac{1}{N} \sum_{n=1}^{N} s[n] \, e^{-j2\pi kn/N}, \tag{9.12}$$

for $k = 1, 2, ..., N/2$, where N is the total number of samples in the measurement.

The power spectrum estimation of the discrete signal $s[n]$ can be performed by

$$P(k) = |S_k|^2 .$$ (9.13)

The bispectrum for M sets of data records of length N can be estimated by

$$B(k,l) = \frac{1}{M} \sum_{i=1}^{M} S_k^{\{i\}} S_l^{\{i\}} S_{k+l}^{*\{i\}},$$ (9.14)

for $i = 1, 2, ..., M$, where M is total number of independent measurements and k and l corresponds to frequency components f_1 and f_2 in Eq. (9.10).

By reformulating the Eq. (9.11) in discrete form, the bicoherence index can be estimated for M number of independent measurements as

$$b(k,l) = \frac{\left| \frac{1}{M} \sum_{i=1}^{M} S_k^{\{i\}} S_l^{\{i\}} S_{k+l}^{*\{i\}} \right|}{\sqrt{\left[\frac{1}{M} \sum_{i=1}^{M} \left| S_k^{\{i\}} S_l^{\{i\}} \right|^2 \right] \left[\frac{1}{M} \sum_{i=1}^{M} \left| S_{k+l}^{\{i\}} \right|^2 \right]}} .$$ (9.15)

The variance of the bicoherence may be expressed as (Chandran & Elgar, 1991; Kim & Powers, 1979)

$$\mathrm{var}(\, b(k,l)\,) \approx \frac{1}{M} \left[1 - b^2(k,l) \right],$$ (9.16)

where the variance of the higher-order spectral analysis can be reduced by increasing the number of measurements since $\mathrm{var}(\, b(k,l)\,) \approx 0$ for $M \to \infty$.

9.3 Materials and Methods

9.3.1 Ultrasound Phantom

The tissue mimicking material (TMM) was prepared by mixing 3% (36 gr.) high strength Agar powder (Acros Organics, Geel, Belgium), 10 gr. Germall plus (ISP Chemicals LLC, Chatham, NJ), 25 gr. soda-lime glass microspheres with a diameter $\leq 25\ \mu$m (MO-SCI Corp., Rolla, MO), 8% glycerine, and 87% de-ionized water by volume. After the TMM was set, attenuation and average sound velocity were measured as 0.56 dB/cm·MHz and 1524 m/s, respectively.

Phantom #1 was built by placing a chamber for UCAs behind a 2 cm thick TMM block. The chamber was also 2 cm thick and had two mylar windows to contain the

microbubble solution. Phantom #2 was the mirrored version of Phantom #1, where microbubbles were shadowing the TMM during the ultrasound measurements. The microbubbles used in these phantoms were prepared and characterised as explained in section 8.2.2.

9.3.2 Experimental Setup

The 96-channel Ultrasound Array Research Platform (UARP) was used to scan the phantom using a L3-8/40EP medical probe (Prosonic Co., Korea) (Smith *et al.*, 2010, 2012). A linear frequency modulated chirp sweeping between $3 - 4$ MHz was used as excitation signal and the second harmonic was received by the same probe at $6 - 8$ MHz. The duration of the excitation waveform was $10~\mu$s. A Hamming window was applied on the chirp signal in order to reduce spectral leakage. Long duration and wideband signals perform better while calculating the phase correlation, because their phase signature is easier to follow both in the time and frequency domains. In order to compensate for the poor axial resolution caused by long signal duration, coded excitation was preferred in this work.

Two sets of measurements were performed at 300 kPa and 600 kPa using the ultrasound phantoms with the probe facing the TMM or UCA chamber, as shown in Figure 9.1 and Figure 9.2. The probe was electronically focused to 60 mm and a linear scan was performed by the UARP, where the mechanical index (MI) values of 0.16 and 0.32 were calculated at the focal point. The UCA suspension was renewed after every 5 measurements, since microbubble destruction was observed during the experiments. The captured data from the UARP was transferred to a personal computer and processed in Matlab (Mathworks Inc., Natick, MA, USA).

9.3.3 Estimation of the Bispectrum

Raw RF data for 100 B-mode images were recorded to ensure a sufficient sample size and achieve statistical convergence. Although a hundred B-mode frames are needed in order to perform the bispectral analysis, it does not increase the total imaging duration when compared with the existing perfusion imaging techniques. Usually a few seconds to minutes of video recording is necessary in order to evaluate the contrast perfusion by measuring the peak video intensity, calculating the time-to-peak, and plotting the wash-in curves.
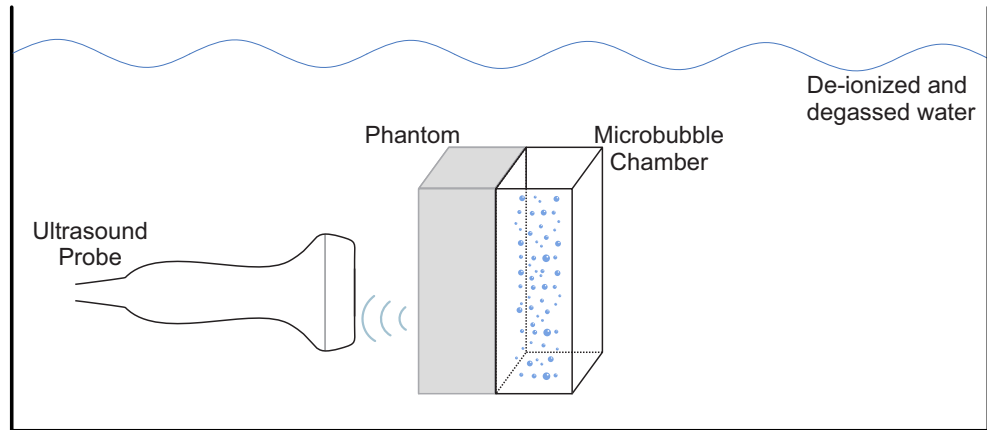
Figure 9.1:   Experimental setup referred to as Phantom #1. Measurements are performed with a commercial ultrasound probe connected to the UARP.
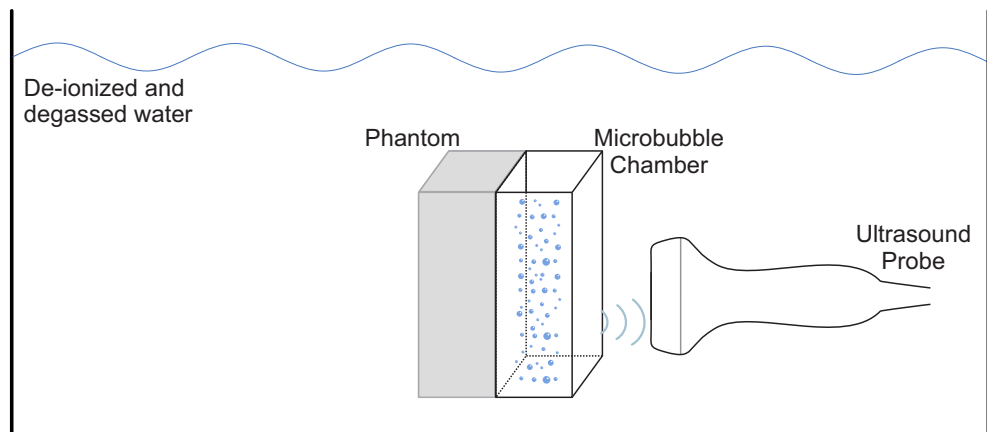
Figure 9.2:   Experimental setup referred to as Phantom #2. Measurements are performed with a commercial ultrasound probe connected to the UARP.

After capturing the RF data, the signal processing was performed as described by Kim & Powers (1979). A single RF line was selected from each frame for processing. The mean value was subtracted from each record to eliminate the DC components. A window was applied to each signal to reduce spectral leakage. The Fourier transform of each signal was calculated using the fast Fourier transform (FFT) technique. The bispectrum was estimated for a single line selected from each frame for different regions of the phantom. The bicoherence index was calculated by using Eq. (9.15) for the region with TMM and the region with UCAs separately for $M = 100$ sets of data.

9.4 Experimental Results and Discussion

It was observed in the measurements that glass microspheres increase the echogenicity of the TMM substantially when compared to the ultrasound phantom used in chapter 6. Figure 9.3 shows the fundamental and the second harmonic images of the Phantom #1 without microbubbles. The perfusion of the microbubbles can be followed by comparing Figure 9.3 to Figure 9.4. However, for Figure 9.4 the CTR value is still below 0 dB, where it is hard to distinguish between TMM and microbubbles.

Although both Phantom #1 and Phantom #2 have the same TMM, same scanning pressure, and same microbubble concentration; the B-mode images shown in Figure 9.4 and Figure 9.6 have different CTR values. A similar problem was reported by Tang *et al.* (2010), where the effects of non-linear propagation on the CTR was analysed.

In order to resolve the issues arising due to the low CTR, bispectral analysis can be used as an auxiliary tool. The square of the bicoherence index, $b^2(f_1, f_2)$, represents the phase coherence between nonlinear coupled waves at a frequency of interest $f_1 + f_2$. For the LFM excitation used in this work, the observer should focus on the frequencies between 3 and 4 MHz for f_1 and f_2 in the bispectral domain, where the phase coupling between the frequency range of $3 - 4$ MHz and $6 - 8$ MHz will be observed.

When the RF data, which forms the B-mode images in Figure 9.4, was processed in the bispectral domain, a phase coherence between fundamental and second harmonic as high as 83% was observed for the TMM as shown in Figure 9.5(a). The value dropped to 71%, when the TMM was shadowed by the microbubbles as shown in Figure 9.7(a). No significant correlation between second harmonic and fundamental components was observed for microbubbles. A maximum $b^2(f_1, f_2)$ value of 10% was calculated, which
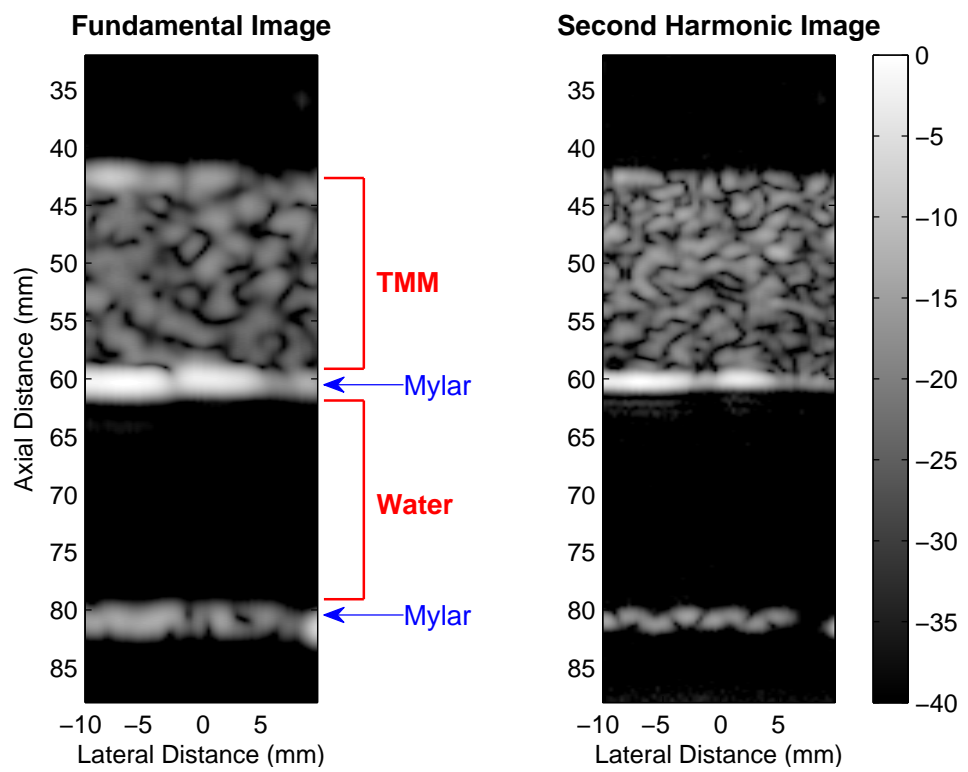
Figure 9.3: The fundamental and second harmonic images of Phantom #1 for a MI of 0.32 with tissue mimicking material (TMM) and a chamber filled with water.
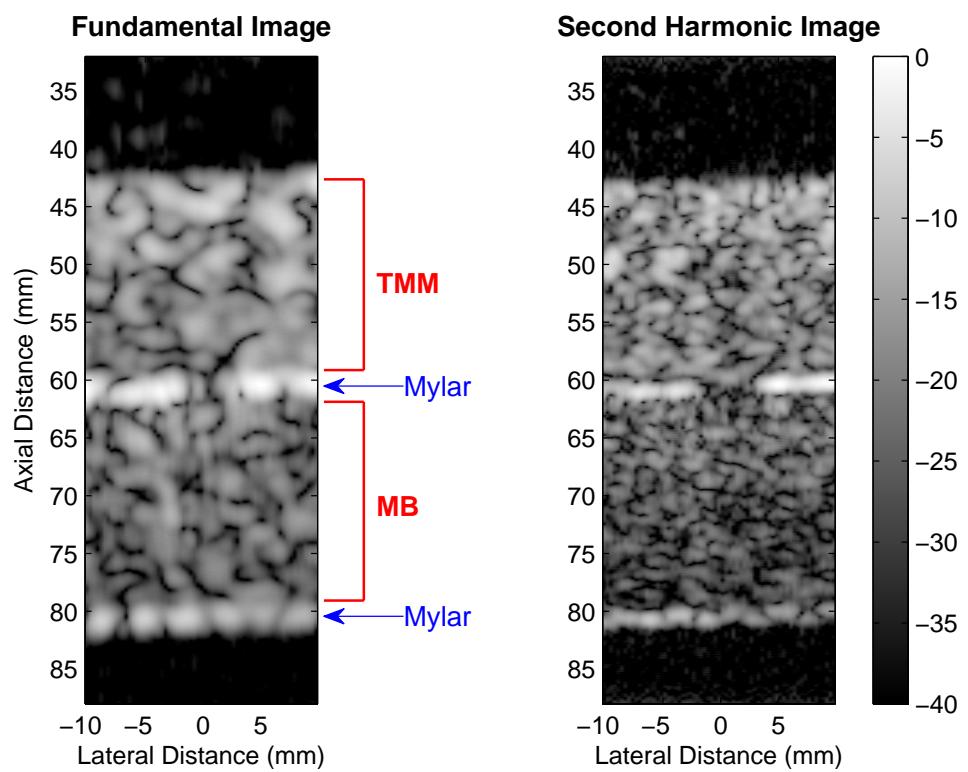
Figure 9.4:   The fundamental and second harmonic images of Phantom #1 for a MI of 0.32 with the tissue mimicking material (TMM) and the chamber filled with microbubbles (MB). CTR for the second harmonic image is −7.3 dB.
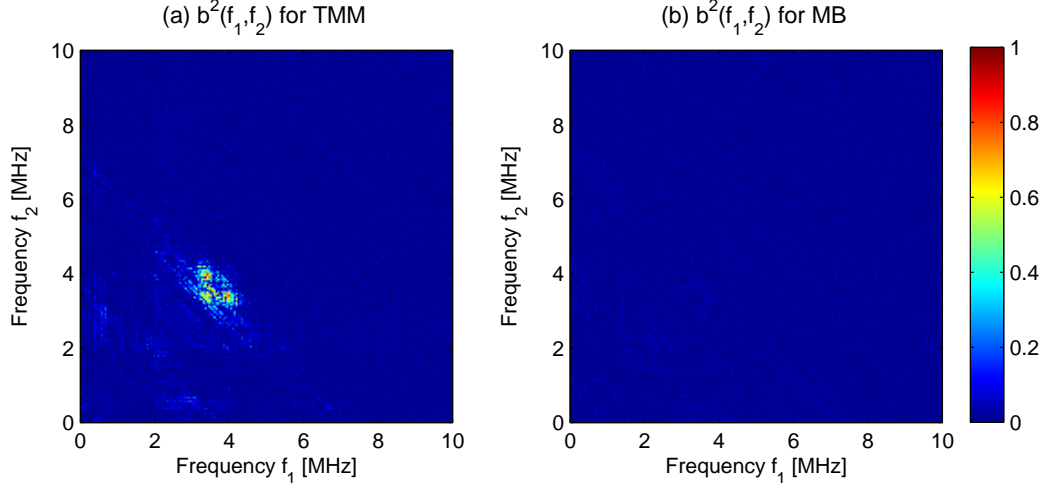
Figure 9.5: Phase coherence for Phantom #1 at MI of 0.32 is shown for (a) the TMM and (b) the microbubbles. A maximum $b^2(f_1, f_2)$ value of 83% was calculated for the TMM, and 10% for the MB.

shows that frequencies f_1 and f_2 have low statistical dependence with the coupled frequency $f_1 + f_2$, as shown in Figure 9.5(b) and Figure 9.7(b).

The phase correlation values for different measurements are listed in Table 9.1. For Phantom #2 at 300 kPa the phase coherence value for the TMM was lower than for the other measurements. The reason for this is the poor second harmonic generation by the TMM and the noise, where the SNR for the TMM after shadowing by microbubbles drops as low as 5 dB for the second harmonic image. The bicoherence index becomes inaccurate for low SNR measurements, since the white Gaussian noise is a random process with a bicoherence value of zero. Although bispectral analysis does not perform well under low SNR, one can still separate the harmonic response. For the experiments performed at lower MI the CTR value was always above 10 dB, where the TMM and UCAs were clearly distinguishable in the B-mode ultrasound image and bispectral analysis is not necessary, as shown in Figure 9.8.

Results show that bispectral analysis can successfully find the phase coherence and separate the harmonics generated by microbubbles and tissue. Another advantage of higher-order spectral analysis is the robustness of the estimates against bubble motion and change in bubble population. Bispectral analysis is not affected by the microbubble motion since movement does not change the phase relation between fundamental and
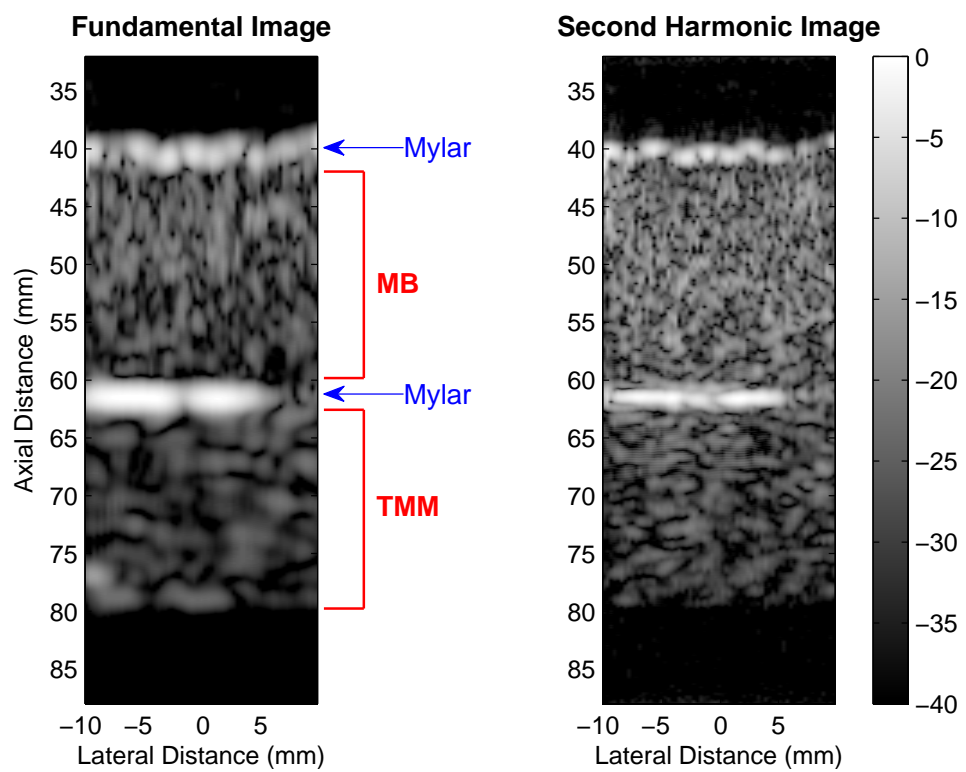
Figure 9.6: The fundamental and second harmonic images of Phantom #2 for a MI of 0.32 with the tissue mimicking material (TMM) and the chamber filled with microbubbles (MB). CTR for the second harmonic image is 7.1 dB.
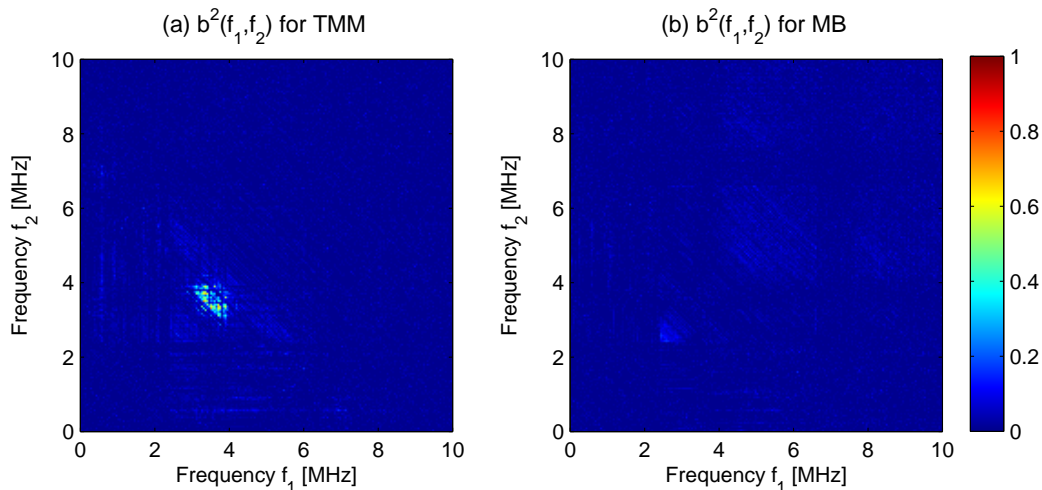
Figure 9.7: Phase coherence for Phantom #2 at MI of 0.32 is shown for (a) the TMM and (b) the microbubbles. A maximum $b^2(f_1, f_2)$ value of 71% was calculated for the TMM, and 7% for the MB.

harmonic components. Most of the commercially available microbubbles have polydisperse size distribution, such as Sonuvue, Bracco BR14, Definity, Sonazoid, and Optison. Therefore, in a statistical point of view these microbubbles can be considered as independent and identically distributed random variables. Since the Gaussian-ness of a process can be identified by higher-order statistics, the acoustic response of a polydisperse microbubble population can be differentiated from tissue response. However, the microbubble population being monodisperse and all microbubbles having the same acoustic signature, the scattering and harmonic generation from microbubbles would not be a random process.

Although, the microbubble size distribution has no major impact on higher-order spectral estimates, the microbubble concentration might have. Tang *et al.* (2008) suggested that nonlinear propagation may still occur even at low acoustic pressure levels and can affect the imaging results in the presence of high concentration of microbubbles on the acoustic path. The impact of the acoustic attenuation caused by high concentration of microbubbles reduces both the CTR and the SNR. Bispectral analysis performs well under low CTR, however the low SNR values will change the bicoherence index as explained through Figure 9.8 and Table 9.1. The bispectral response of the microbubbles will not be affected by the acoustic attenuation, but the bispectrum of
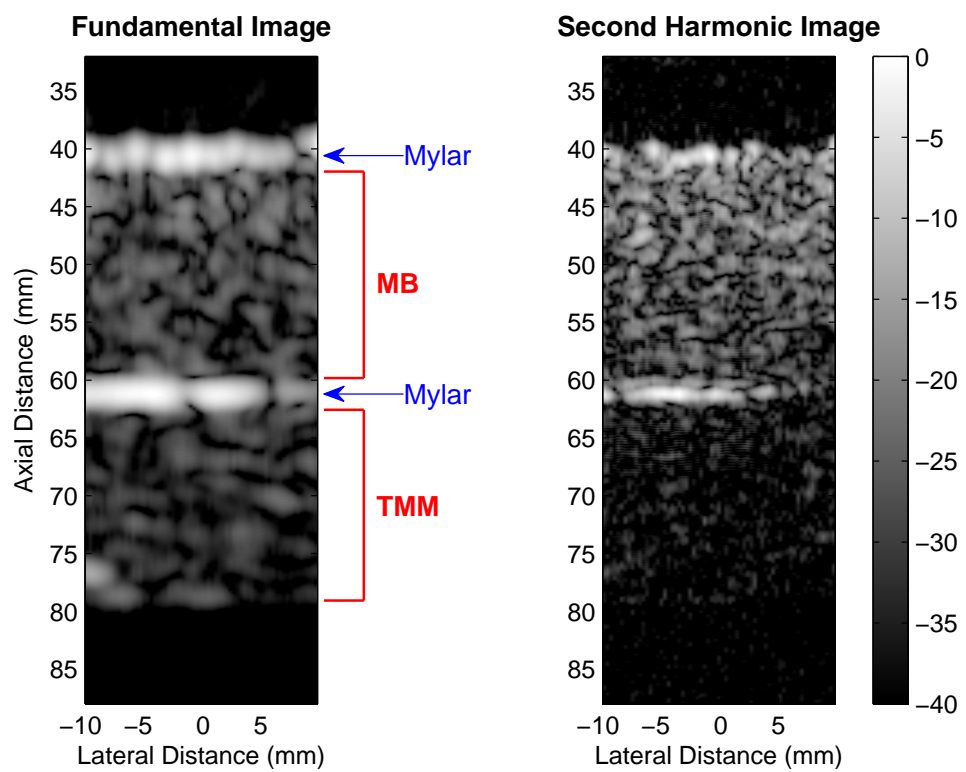
Figure 9.8: The fundamental and second harmonic images of Phantom #2 for a MI of 0.16 with the tissue mimicking material (TMM) and the chamber filled with diluted microbubbles (MB). CTR for the second harmonic image is -7.3 dB.

tissue will due to the loss in SNR when the contrast agent concentration is too high. Especially for the regions shadowed by microbubbles, the acoustic attenuation makes the bispectral analysis impractical for evaluation of microbubble and tissue response.

Table 9.1: Maximum phase coherence values and thier standard deviations at $3-4$ MHz frequency range for different experimental measurements.

	MB		TMM	
	Max.	Std.	Max.	Std.
Phantom #1 (MI 0.16)	4%	0.4% [*0.39%]	67%	5.6% [*3.8%]
Phantom #1 (MI 0.32)	10%	0.7% [*0.95%]	83%	4.1% [*3.4%]
Phantom #2 (MI 0.16)	5%	0.5% [*0.49%]	17%	1.7% [*1.5%]
Phantom #2 (MI 0.32)	7%	0.6% [*0.68%]	71%	6.2% [*3.8%]

Max.: Maximum bicoherence index.

Std.: Standard deviation calculated from experiments.

*Std.: Theoretical standard deviation calculated by Eq. (9.16).

9.5 Conclusions

The bispectral analysis has been used for analysing non-Gaussian processes and evaluating nonlinearities. In statistics and signal processing the bispectral analysis has many applications, although there are only a few examples in ultrasound (Hillis *et al.*, 2006). In this study, the bispectral analysis was used for the first time to evaluate the harmonic generation of ultrasound contrast agents.

The main advantage of using higher-order spectral estimation techniques to second order estimation techniques, such as correlation and power spectrum, is presence of the phase information. The second order statistics suppresses the phase relation between the frequency components. Higher-order spectral analysis maintain the phase information and can reveal the phase coherent spectral components of a non-Gaussian process, because the cumulants of a Gaussian random process are identically zero for orders higher than 2.

The higher-order spectral estimation techniques are usually criticised because of the amount of data required to produce low variance estimates and the amount of computational complexity involved. The requirement for large data lengths to reduce the variance of the estimate makes bispectral analysis impractical for many applications. Similarly, the computational complexity also reduces the practicality of this method, where the fast Fourier transform (FFT) has a computational complexity in the order of $(N \log N)$ and the bispectrum has a computational complexity of a two-dimensional FFT in the order of $(N \log N)^2$. Another complication for ultrasound imaging applications is the necessity for using image registration algorithms to follow the region of interest from the B-mode images.

The possible applications for the bispectral analysis to medical ultrasound imaging are myocardial perfusion imaging and carotid imaging, where the boundaries between the chambers of the hearth, arteries and tissue are easily distinguishable. In this study, a similar experimental setup was created using a tissue phantom, where 100 B-mode images were captured and processed to ensure a sufficient sample size and to reduce the variance. Although a 100 B-mode frames were used to calculate the bicoherence index, it does not increase the total imaging duration when compared with the existing perfusion imaging techniques. Usually a few seconds to minutes of video recording is necessary in order to evaluate the contrast perfusion by measuring the peak video intensity, calculating the time-to-peak, and plotting the wash-in curves. Therefore, there is no extra overhead for perfusion imaging of hearth and carotid imaging since clinicians usually need more than tens of ultrasound frames to observe the behaviour of the hearth or flow in the arteries.

Results show that higher-order spectral analysis allows separation of the harmonics generated by microbubbles and tissue at low CTR. Unlike other tissue harmonic suppression techniques based on multiple-excitations (Couture *et al.*, 2008; Pasovic *et al.*, 2011), bicoherence is not susceptible to motion artefacts since movement does not affect the phase relation between fundamental and harmonic components. The bispectral analysis was proposed as an auxiliary tool for the second harmonic ultrasound imaging applications with high SNR and low CTR. For low SNR values, the bispectral analysis cannot differentiate between noise and the tissue response. For the second harmonic images with high CTR, the tissue and the microbubble response can be visually separated and there is no need for the bispectral analysis.

184

Chapter 10

Conclusions

Ultrasound imaging is an indispensable modality for medical diagnostics, because of its non-invasive and non-ionizing nature. To assess the quality of an ultrasound image; the spatial resolution, the dynamic range, and the sensitivity of the image must be considered. The spatial resolution determines the minimum distinguishable spacing between two point targets. The dynamic range is the ratio between the largest and the smallest echoes can be represented in the image. More targets are simultaneously detectable with a larger image dynamic range. The image sensitivity can be described as the signal-to-noise ratio. The penetration depth, which was not considered as an image quality metric, can be categorized within the image sensitivity.

To form a high resolution image, higher ultrasonic frequencies are preferable. However, high frequencies result in poor image sensitivity, since the penetration depth and the SNR are reduced due to high attenuation. Both the SNR and penetration can be improved by using chirp coded excitation. The resolution and the dynamic range of an ultrasound image with chirp excitation are determined after the pulse compression by the main lobe width and the peak sidelobe level, respectively. Therefore, this work was focused on improving the compression ratio and decreasing the sidelobe level for ultrasound imaging with chirp coded excitation.

The Fractional Fourier transform and the Fan Chirp transform were proposed as filtering and compression tools to enhance the performance of pulse compression with chirps. Examples were given through the applications on different problems encountered in chirp coded excitation for medical ultrasound imaging, including hard-tissue

ultrasound imaging, soft-tissue ultrasound imaging and contrast-enhanced ultrasound imaging.

10.1 Dental Imaging

Ultrasound is widely used for medical diagnostic imaging of soft-tissue, since it is cheaper than other modalities, it does not use ionizing radiation, and it is safe and painless for the patient. However, radiography is currently the most dominant diagnostic imaging technique in dentistry. Dental X-ray scanners can achieve better resolution than ultrasound imaging. However, ultrasound is a non-ionizing modality and can be safely used for dental measurements. For this reason, an ultrasound contact imaging method was developed as a diagnostic tool for dental imaging.

The preliminary study was performed on a tooth phantom built by materials with similar acoustic impedances to human teeth. After achieving satisfactory results with a tooth phantom, a human molar tooth was burrowed from the Leeds Dental Institute Skeletal Tissues Bank to repeat the measurements on a real tooth sample. However, the noise levels were $2-3$ orders of magnitude higher mostly because of the attenuation. Therefore, the linear frequency modulated chirp signals were proposed as an excitation method for dental imaging to improve the SNR. Because the tooth layers were highly attenuating, the detection of small cracks and weak echoes would not be possible without using long duration signals carrying high energy. However, using chirps for dental imaging introduced new problems on the receiver side, where the performance of pulse compression with a matched filter was decreased.

For the tooth measurements, the received echoes were attenuated not only because of depth and frequency dependant attenuation, but also because of scattering, dispersion and absorption. The structure of the dental tissues absorbs and scatters the sound wave due to roughness and the irregular curved shape of the tooth. Therefore, the change in the envelope shape and reduced bandwidth resulted in a discrepancy between the matched filter and received chirp signal. To overcome this pulse compression problem, the FrFT was used to analyse the received echoes by separating chirp signals overlapping in both the time and the frequency domains. The proposed technique was used to measure the thickness of the enamel layer and for the evaluation of restorations in human teeth. The results obtained with the proposed method was compared with

a Gaussian pulse, which is the *de facto* standard in thickness measurements, and with a chirp excitation processed by a matched filter for pulse compression. The proposed method achieved more accurate results with an average error of 1.6%, where the Gaussian pulse and the chirp waveform processed by a matched filter had an average error of 3.6%.

In this study, a contact imaging method was developed and a single element transducer was used to transmit an ultrasound wave and to receive the reflections from tooth layers, cracks, cavities, and flaws. The amplitude of the return echo was used to obtain a rough estimate of the thickness of the tooth layer or the location of a cavity or a crack. This method is commonly used for non-destructive testing (NDT) applications and known as the amplitude scan or the A-scan.

The current measurement setup cannot be practically used to image a tooth since the transducer was moved by a CNC system. The final scanning instrument must be a hand-held ultrasound probe that can be used in clinical application. Therefore, the future work and the development stage include embedding position encoders on the transducer, so a single element can be used to perform multiple A-scans. By moving the transducer along the surface of the tooth being examined and combining these individual A-scan lines with the spatial information an ultrasound image can be formed. After these adjustments, the proposed contact imaging method and the coded excitation technique can be used as a diagnostic tool in dentistry to measure the enamel thickness, locate small cracks and discontinuities and detect possible restoration faults in human teeth.

10.2 Second Harmonic Imaging and Superharmonic Imaging

The main advantages of the second harmonic and superharmonic imaging over fundamental B-mode imaging are the increased spatial resolution and suppressed reverberations, near-field artefacts, and off-axis artefacts. Therefore, harmonic imaging significantly improves the image quality. Besides increasing the spatial resolution, second harmonic and superharmonic imaging have some drawbacks. Increased sidelobe levels due to the spectral overlap between the harmonic and fundamental components, decreased penetration depth and sensitivity, and reduced signal-to-noise ratio are the

main limitations of the ultrasound harmonic imaging. To overcome these limitations, this study employed the coded excitation technique in conjunction with the FrFT and FChT.

Lower excitation frequencies can be used in soft-tissue imaging, since the features of the internal organs are larger than that of the human teeth. However, the penetration is still an issue, since a penetration depth of up to 300 mm may be necessary for soft-tissue imaging. Therefore, the linear frequency modulated chirp signals were proposed as an excitation method to improve the penetration depth and the SNR.

Harmonic imaging provides better spatial resolution; however without separating the spectrally overlapping harmonics a high-quality image cannot be formed. The pulse compression with a matched filter introduces image artefacts due to the spectral overlap between the fundamental and harmonic components. Conventional filtering techniques such as a bandpass filter can be used to separate the harmonic components with a cost of reduced bandwidth. Pulse inversion can remove the fundamental component by halving the image frame rate. Filtering in the FrFT domain performs better than the band-pass approach, because the received signals are transformed into another domain where the second harmonic component is not overlapping with the fundamental component. Therefore the FrFT was used as a filtering tool with wide bandwidth chirp excitation in order to extract the overlapped second harmonic component without reducing the bandwidth.

Using the FrFT to separate the harmonic chirps however may not be practical for superharmonic imaging. Filtering process must be repeated individually for each harmonic component, which will increase the redundancy, computation time and accumulated error. Instead of computing several Fractional Fourier transforms, the FChT was used to compress all spectrally overlapping harmonic chirp components with one transformation. The final results showed that filtering methods based on the FrFT and the FChT can reduce the high sidelobe levels of the compressed harmonic components caused by the spectral overlap.

The second harmonic and superharmonic imaging are suitable for all types of medical imaging applications where high image resolution is necessary such as imaging small structures and detection of lesions. For high resolution imaging applications superharmonic imaging outperforms the second harmonic imaging by offering significant speckle reduction. Combining different frequency components reduces the speckle and

increases the amount of detail can be visualized. However, the main issue for the superharmonic imaging is the limited transducer bandwidth. The higher-order harmonics are usually located at a frequency band where the transducer does not work efficiently, therefore causing a reduction in the SNR and sensitivity. Currently, it is not possible for the superharmonic imaging to become an imaging standard with the commercially available probes and equipment. The ultrasound probes in the market are insufficient for superharmonic imaging, because they do not have a large bandwidth and sensitivity to accommodate fundamental to fifth order harmonics of the received echoes. However, the current research on transducer technology is focusing on increasing the transducer bandwidth. The recent developments in interleaved phased array transducers and CMUT arrays showed improved transmission efficiency and reception sensitivity, which will make them suitable for superharmonic imaging applications in the near future.

Another drawback of this harmonic imaging study was that the results were presented with measurements performed in water and agar based tissue mimicking materials. It was not possible to perform ultrasonic measurements on human tissue or animal tissue, since the instruments used in this work was not clinically or pre-clinically approved. This problem has been experienced by many researchers, so the use of ultrasound phantoms is common in medical imaging research. Therefore, the use of ultrasound phantoms can be legitimised for this study since the aim of the presented work was to filter and to compress harmonic chirp components in second harmonic and superharmonic imaging. The rate of harmonic generation, absorption and attenuation are different for tissue, tissue mimicking materials and water, but the dynamics of harmonic generation are the same. For this reason, to simulate the harmonic generation in tissue, the ultrasound phantoms were made based on the previous research performed on the tissue substitutes for ultrasound (Culjat *et al.*, 2010; Rickey *et al.*, 1995).

10.3 Microbubble Response to Chirp Excitation and its Effects on Pulse Compression

Three major problems were addressed for chirp excitation in the presence of microbubbles that reduced the performance of the pulse compression with a matched filter.

10.3 Microbubble Response to Chirp Excitation and its Effects on Pulse Compression

First, it was proven by simulations that the amplitude and the phase of the scattered pressure wave from a microbubble were different than that of the excitation signal. The shape of signal envelope and the phase was corrupted due to microbubble resonance.

Second, it was presented that the mechanisms responsible for the nonlinear behaviour of microbubbles were different than that of tissue. Tissue generates only higher order harmonics in a predictable manner, but microbubbles have unique acoustic signatures that change with bubble size, encapsulation, gas core, excitation pressure, and excitation frequency. Also generation of subharmonics and ultraharmonics increases the sidelobe levels after compression, due to the increased amount of spectral overlap.

Third, an increase in noise level was observed for the experimental measurements performed at high acoustic pressures. The reason for the increase in broadband noise was the microbubble destruction, which reduced the SNR.

After addressing these problems, it was proven that the chirp rate was not corrupted and the pulse compression in the existence of microbubbles was possible. The scattered response from the microbubble population had the same chirp rate as the excitation signal and the chirp rate of the harmonics generated by the microbubbles were scaled by a ratio of n for the nth-harmonic. Therefore, filtering in the FChT domain was performed to reduce the compression artefacts and improve the image quality for contrast-enhanced ultrasound imaging and contrast-enhanced second harmonic imaging.

However, the drawback of using the FChT as a filtering tool was a reduction in image contrast. The CTR being one of the most important metrics in measuring the microbubble response and the quality of the contrast-enhanced ultrasound image, the results achieved by the FChT method may not be considered as an improvement by radiologists. The reason for this was the pulse compression artefacts caused by the aforementioned problems. The matched filter did not only compress the waveforms scattered from microbubbles with the same chirp rate, but also the broadband noise and the harmonics that were within the bandwidth of the matched filter. Yet, the FChT filtered the broadband noise due to the peak detection method used for separating the maximally compressed and partially compressed waveforms.

10.4   Bispectral Analysis

Nonlinear propagation in tissue generates harmonics that are in phase with the fundamental component. The distortion of the wave happens in a predictable manner, where the shape turns from sinusoidal to sawtooth. However, the harmonics generated by a polydisperse population of microbubbles are not necessarily in phase with the fundamental component. The second order spectral analysis, such as power spectrum, suppresses the phase relation between the frequency components. Higher-order spectral analysis maintains the phase information and can be used to reveal the phase coherent spectral components of a non-Gaussian process. Therefore, in this study a higher-order spectral analysis method was proposed to analyse the nonlinear microbubble behaviour. After observing non-correlated phase behaviour between microbubble generated harmonics and the fundamental component, the bispectral analysis was used to separate the second harmonic response of tissue and microbubbles.

The bispectral analysis requires high amount of data to produce an estimate with a low variance. The application of a higher-order spectral estimation technique in ultrasound imaging must satisfy the requirement of > 50 samples depending on the application. Therefore, the computational complexity and the demand for large data lengths make bispectral analysis impractical for many applications. However, the bispectral analysis can still be beneficially used in medical ultrasound imaging applications such as myocardial perfusion imaging and carotid imaging, where clinicians require a few seconds to minutes of ultrasound video to evaluate the contrast perfusion. In this study, experimental measurements were performed with a tissue phantom, where 100 B-mode images were captured and processed to reduce the variance. The bicoherence index was calculated for the regions with tissue and microbubbles, and used to measure the phase coupling between fundamental and second harmonic components.

Results showed that higher-order spectral analysis allows separation of the harmonics generated by microbubbles and tissue for ultrasound images with low CTR and high SNR. For low SNR values, the bispectral analysis cannot differentiate between noise and the tissue response. For the second harmonic images with high CTR, the tissue and the microbubble response can be visually separated and there is no need for the bispectral analysis.

Appendix A

Time-Frequency Analysis

The Fourier analysis for a discrete signal can be summarised as the decomposition of the function into sinusoids of different frequencies. The repetition of each sample of the finite duration time series is mapped into discrete frequency bins by using the discrete Fourier transform. This frequency information can be used to calculate the distribution of the signal's energy on the time-frequency plane, which will be explained in the following sections.

The sampling frequency, f_s, of the time domain signal plays an important role on the Fourier analysis, since the largest frequency component that can be analysed without aliasing is determined by the Nyquist-Shannon sampling theorem as $f_n = f_s/2$. However, in this study the sampling frequency was always chosen to be considerably larger than the Nyquist frequency, e.g. $f_s > 20 f_n$. The reason for the oversampling of the time domain signal was to increase the SNR, where the dynamic range is increased by 3 dB for each 2 fold increase of the sampling frequency. If the quantisation noise is assumed to be white Gaussian noise and evenly spread across the range of $[0, f_s/2]$, increasing the sampling frequency will spread the noise across a wider frequency range.

A.1   Definition and Estimation of the Power Spectral Density

Let the real valued discrete time signal $s[n]$ denote a sequence of random variables with zero mean, $E\{s[n]\} = 0$. The autocovariance sequence of $s[n]$ is defined as

$$R[k] = E\{s[n]\,s[n-k]\}.$$

(A.1)

The relationship between the autocovariance sequence, $R[k]$, and the spectral density function, $P(f)$, is the discrete time Fourier transform (DTFT) that can be expressed as (Oppenheim & Schafer, 1975)

$$P(f) = \sum_{k=-\infty}^{\infty} R[k]\, e^{-j2\pi fk}. \tag{A.2}$$

Most of the spectral estimation methods, such as Blackman-Tukey method, exploit this relationship to estimate the spectrum by using the autocorrelation function, $R_{ss}[k]$. The autocorrelation reveals the similarities between the observations performed at different times and the existing frequencies in the signal can be estimated by using these time delays between the observations. Since the autocorrelation is just the autocovariance divided by the variance of the process, using the autocorrelation function results in a normalised spectrum. Therefore, the following definition based on the autocorrelation can be used to estimate the normalised power spectral density;

$$P(f) = \sum_{k=-\infty}^{\infty} R_{ss}[k]\, e^{-j2\pi fk}. \tag{A.3}$$

For an ergodic process[1] the autocorrelation function can be defined as

$$R_{ss}[k] = \lim_{N\to\infty} \frac{1}{N} \sum_{n=1}^{N} s[n]\, s[n-k], \tag{A.4}$$

A second definition for the power spectral density can be given as (Nikias & Petropulu, 1993)

$$P(f) = \lim_{N\to\infty} \frac{1}{N} \left| \sum_{n=1}^{N} s[n]\, e^{-j2\pi fn} \right|^2, \tag{A.5}$$

To estimate the power spectral density (PSD), methods based on Fourier transform as given in Eq. (A.5) can be used such as; raw periodogram, smoothed periodogram, modified periodogram, Bartlett's method, Welch's method, and Blackman-Tukey method. These methods are some of the most commonly used spectral estimation techniques, but not the all. The list can be extended by adding Multi-taper method, Singular spectrum analysis, Maximum entropy, and parametric methods; such as Autoregressive (AR), Moving Average (MA) and ARMA. For the sake of clarity, only some of the non-parametric methods are explained in this section.

---

[1]A process is ergodic if all its moments can be determined from a single observation.

Periodogram: The periodogram PSD estimates were computed from a finite-length discrete sequence using the fast Fourier transform (FFT) as

$$P(f) = \frac{1}{N} \left| \sum_{n=1}^{N} s[n] \, e^{-j2\pi fn} \right|^2 , \tag{A.6}$$

where N is the total number of samples in the measurement. For long duration signals with a large value of N the raw periodogram is a good PSD estimate, however for short data lengths the frequency resolution is poor. Periodogram also suffers from large sidelobes that can mask low amplitude signals. The main disadvantage of the raw periodogram is the spectral bias and the fact that the variance does not decrease as the N increases.

Smoothed Periodogram: The variance problem can be reduced by smoothing the periodogram. Smoothing of the periodogram can be achieved by applying a filter in the frequency domain. As the spectrum is smoothed the variance of the periodogram is reduced, however it is also biased towards the local mean. Another disadvantage of the smoothing is the reduction in resolution. Two closely spaced frequency components might not be resolved, because the narrow peaks are spread out over a wider frequency range after smoothing. Therefore, the capability of identifying individual peaks and the ability of measuring the signal bandwidth accurately are significantly lower for the smoothed spectrum.

Bartlett's Method: The time domain signal is split into non-overlapping segments as

$$s[n] = \underbrace{s_1, s_2, ...s_K}_{s_1[n]}, \underbrace{s_{K+1}, s_{K+2}, ...s_{2K}}_{s_2[n]}, ..., \underbrace{s_{N-K+1}, s_{N-K+2}, ...s_N}_{s_L[n]}. \tag{A.7}$$

where $N = K \cdot L$ is the total number of samples, K is number of samples in each segment and L is the number of segments. Then, the periodogram is calculated for each independent segment as

$$P_{\{i\}}(f) = \frac{1}{K} \left| \sum_{n=1}^{K} s_{\{i\}}[n] \, e^{-j2\pi fn} \right|^2 . \tag{A.8}$$

The final estimate of the spectrum is obtained by averaging the estimates from these periodograms

$$P_B(f) = \frac{1}{L} \sum_{i=1}^{L} P_{\{i\}}(f). \tag{A.9}$$

Bartlett's method reduces the variance of the periodogram at the expense of increased bias and decreased spectral resolution, compared to raw periodogram (Oppenheim & Schafer, 1975).

Welch's Method: This method is similar to the Bartlett's method, but the segments contributing to each periodogram are allowed to overlap. If non-overlapping windows are used, a significant part of the signal is ignored due to the small values of the windows near the edges. To avoid this loss of information, Welch's method uses overlapping windows.

The periodograms are not independent due to the overlap, but the variance is lower than the Bartlett's method since there are more periodograms to be averaged. The Welch's method can be defined as the averaged periodograms of overlapped and windowed segments of the discrete signal $s[n]$ as (Welch, 1967)

$$P_{w,\{i\}}(f) = \frac{1}{K} \left| \sum_{n=1}^{K} w[n]\, s_{\{i\}}[n]\, e^{-j2\pi fn} \right|^2, \tag{A.10}$$

where $P_{w,\{i\}}(f)$ is the windowed periodogram of the segment i, $w[n]$ is the windowing function, and K is number of samples in each segment. The final estimate of the spectrum is obtained by averaging L estimates from Eq. (A.10)

$$P_W(f) = \frac{1}{L} \sum_{i=1}^{L} P_{w,\{i\}}(f). \tag{A.11}$$

Blackman-Tukey Method: The spectrum is estimated by the smoothed and truncated autocorrelation function. The autocorrelation function, $R_{ss}[k]$ in Eq. (A.4), is windowed before calculating the periodogram as (Blackman & Tukey, 1958)

$$P_{BT}(f) = \sum_{k=-K}^{K} w[k]\, R_{ss}[k]\, e^{-j2\pi fk}, \tag{A.12}$$

where $w[k]$ is the windowing function and $2K + 1$ is the size of the window. The bias, resolution and variance of the spectral estimates are controlled by the choice of windowing function, which is explained in the next section. To minimise the bias, large window size is preferable, but using large windows increases the variance. The variance is reduced for smaller window size, but the resolution is decreased and the bandwidth is increased.

Modified Periodogram: The smoothness, resolution and variance of the spectral estimates can be controlled by using filters, averaging and windowing. However, there is always a trade-off between these parameters. In this study, the intended use of the periodogram was to verify the spectral overlap between the fundamental and harmonic frequency components. For this reason, a modified periodogram was chosen by focusing on increasing the resolution and reducing the bias.

The spectral bias can be reduced by avoiding the sharp truncation of the $s[n]$. The signal $s[n]$ can be truncated gradually by using an appropriate window, which will be explained in the next section. The windowing can be applied as

$$s_w[n] = \frac{1}{U} w[n] \, s[n].$$
(A.13)

where U is the windowing gain that can be calculated by summation of all window coefficients

$$U = \sum_{n=1}^{N} w[n].$$
(A.14)

Windowing also reduces the sidelobes in the periodogram that can mask low amplitude signals.

When the FFT is used to process a discrete signal of length N, the spectral resolution of the FFT is defined as

$$\Delta f = f_s/N,$$
(A.15)

where f_s is the sampling frequency. Increasing the length of the time domain signal N, also increases the frequency resolution. Therefore, *zero padding* in time domain was performed on the recorded signals in order to increase spectral resolution after FFT for all recordings. The zero padded signal

$$\bar{s}_w[n] = [0, 0, 0...., \ s_w[n], ..., 0, 0, 0] \, ,$$
(A.16)

was used to calculated the modified periodogram as

$$P_M(f) = \frac{1}{N'} \left| \sum_{n=1}^{N'} \bar{s}_w[n] \, e^{-j2\pi f n} \right|^2 ,$$
(A.17)

where N' is the size of the windowed and zero padded signal $\bar{s}_w[n]$.

In this study, the spectral plots regarding to signal's estimated power spectrum was a modified periodogram with a 100% tapered Tukey window or a Hann window. This

window was chosen to keep the widening of the frequency components at minimum, to maintain the spectral resolution, to reduce the bias of the estimate, and to reduce the spectral leakage. Averaging and smoothing of the periodogram was not used in this work, since smoothing changes the bandwidth of the signal and averaging reduces the resolution and increases the bias.

Example: To illustrate the differences between the aforementioned methods, the received echo for the measurement performed in chapter 6 Figure 6.5 was processed with the raw periodogram, the modified periodogram (100% tapered Tukey window), the Blackman-Tukey method (100% tapered Tukey window), and the Welch's method ($L = 8$, 50% overlap and Hamming window). The resulting spectral plots are shown in Figure A.1, Figure A.2, Figure A.3, and Figure A.4.

To compare the spectral resolution of each method the -6 dB bandwidth of the fundamental frequency component located around 2.25 MHz was measured. The -6 dB bandwidth is 0.804 MHz for the raw periodogram, which has the worst variance that can clearly be observed in the Figure A.1. The raw periodogram was expected to perform better in terms of resolution, but due to the high variance there is a significant fluctuation in the values. The -6 dB bandwidth is 0.962 MHz for the Welch's method, which has the worst resolution when compared to the other methods due to averaging. The -6 dB bandwidth is 0.772 MHz for the Blackman-Tukey method, which performs better than Welch's in terms of resolution and better than the raw periodogram in terms of variance. The modified periodogram achieves a -6 dB bandwidth of 0.713 MHz thanks to zero padding and elimination of sharp truncation errors by windowing in time domain. None of these methods are superior than another, however the modified periodogram was chosen in this study since it achieves a reasonable performance for all important metrics; resolution, variance and bias.
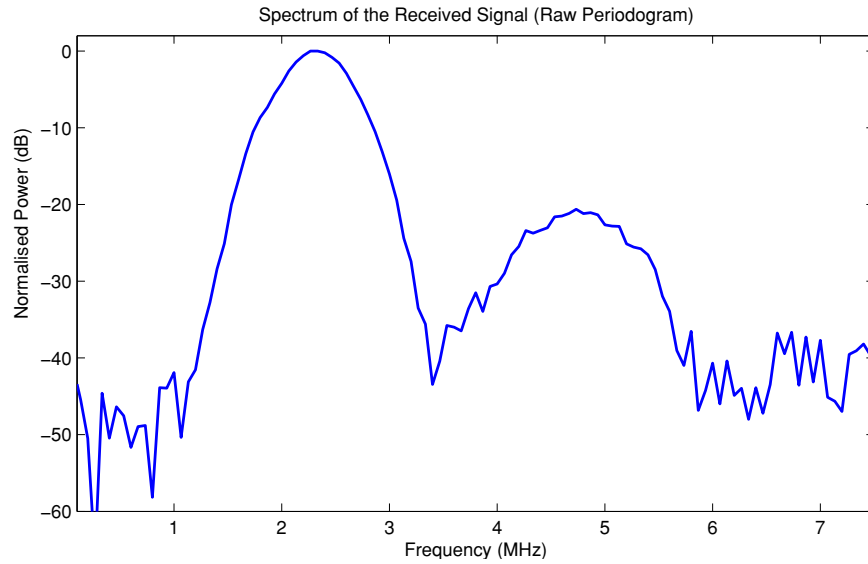
Figure A.1: Raw periodogram of the received signal.
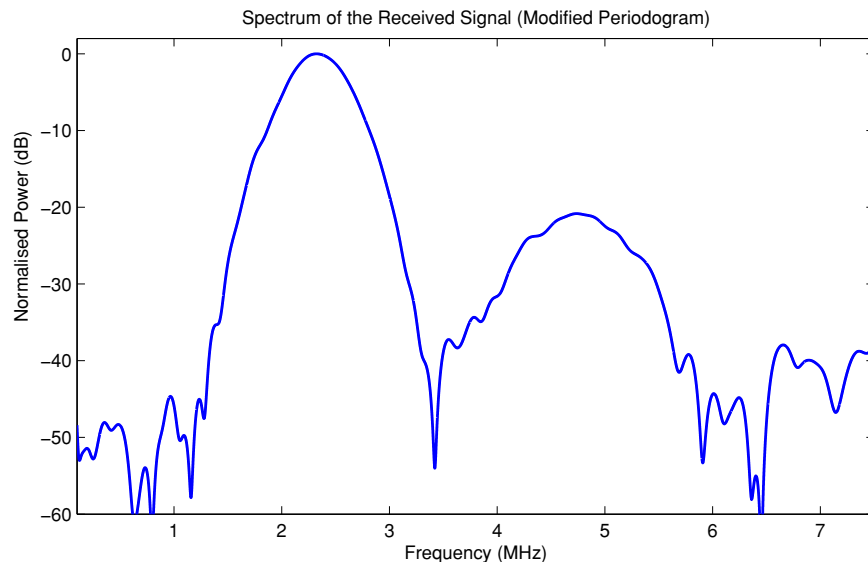
Figure A.2: Periodogram of the received signal processed by the modified periodogram method.
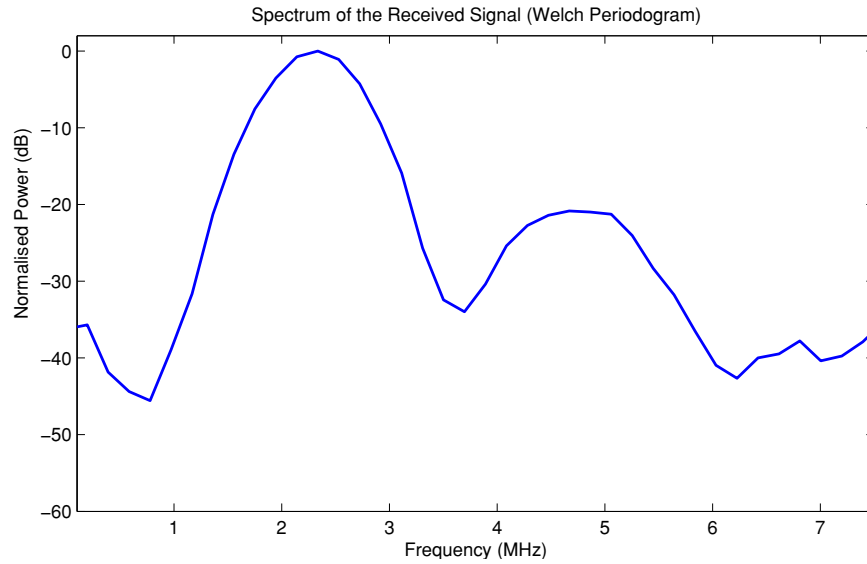
Figure A.3: Periodogram of the received signal processed by the Welch's method.
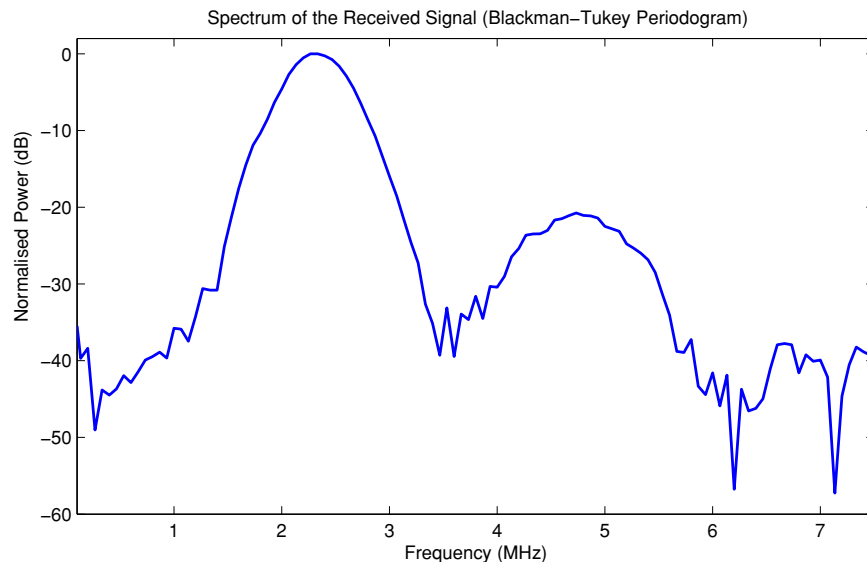
Figure A.4: Periodogram of the received signal processed by the Blackman-Tukey method.

A.2   Windowing

In this study, the periodograms were mostly used for the visual representation of the fundamental and harmonic frequency components and the spectral overlap between them, rather than detection and estimation of signal's power. For this reason, reducing the spectral leakage while maintaining a high resolution was the main purpose of using windows. The effects of negative frequency components are not mentioned, because the harmonics are located closer to the fundamental frequency component and affected more due to the spectral leakage and resolution problems

Some of the widely used window functions such as; rectangular, Bartlett, Hamming, Hann (100% tapered Tukey window), Tukey, Blackman, Gaussian, Dolph-Chebyshev, and Kaiser-Bessel were compared in terms of sidelobe characteristics, bandwidth and worst case processing loss. The numerical comparison of these figures of merits are listed in Table A.1. Some of these window functions are plotted in Figure A.5 to illustrate the difference between various window shapes.

Minimum Resolution Bandwidth: The contribution of different signals can be described as the coherent summation of signal's energy in the frequency domain. In order to be able to distinguish between closely spaced frequency components, the separation between their frequency peaks must be at least as wide as the -3 dB width of their main lobe. However, when two frequency components with same amplitude are separated by less than their -3 dB bandwidth, they will appear as a single lobe in the frequency domain (Harris, 1978). Therefore, the crossover points between the spectral peaks must be less than 0.5, which corresponds to -6 dB points. For this reason, the -6 dB bandwidth of the windows are chosen as a comparison metric.

Table A.1 shows the comparison between various windows in frequency bins, which corresponds to the discrete intervals of the frequency domain. The widow functions with narrower bandwidths results in better resolution, but higher sidelobes. E.g. the rectangular window achieves the best resolution with a -6 dB bandwidth of 1.21 discrete Fourier transform (DFT) bins, but it has the worst sidelobe performance with a highest sidelobe level of -13 dB. As the main lobe width narrows, the more energy leaks into the sidelobes. Therefore, the window functions such as rectangular, Bartlett and 50% tapered Tukey with narrower bandwidth have higher sidelobe levels.

Table A.1: Comparison of various windows

WINDOW		Highest Sidelobe Level (dB)	Sidelobe Roll-off (dB/octave)	-6.0 dB Bandwidth (DFT Bins)	Worst Case Process Loss (dB)
Rectangular		-13	-6	1.21	3.92
Bartlett		-27	-12	1.78	3.07
Hamming		-43	-6	1.81	3.10
Hann		-32	-18	2.00	3.18
Tukey	$a = 0.5$	-15	-18	1.57	3.11
Blackman		-58	-18	2.35	3.47
	$a = 2.5$	-42	-6	1.86	3.14
Gaussian	$a = 3.0$	-55	-6	2.18	3.40
	$a = 3.5$	-69	-6	2.52	3.73
	$a = 2.5$	-50	0	1.85	3.12
Dolph-	$a = 3.0$	-60	0	2.01	3.23
Chebyshev	$a = 3.5$	-70	0	2.17	3.35
	$a = 4.0$	-80	0	2.31	3.48
	$a = 2.0$	-46	-6	1.99	3.20
Kaiser-	$a = 2.5$	-57	-6	2.20	3.38
Bessel	$a = 3.0$	-69	-6	2.39	3.56
	$a = 3.5$	-82	-6	2.57	3.74

Values in this table are taken from Harris (1978).

Spectral Leakage: The main reason of spectral leakage is the discontinuities in the sampled signal either due to the truncation of the signal or due to sampling of non-integer number of periods. The latter case is important for the periodograms processed with Bartlett's and Welch's method and for spectrograms, which will be described in the next section. Main indicators of a good spectral leakage suppression are low *sidelobe roll-off* and low *highest sidelobe level*, which also reduces the bias.

Discontinuities in the sampled signal cause the signal's energy to leak from the frequency bins, where the actual signal's energy exists, to adjacent frequency bins. The spectral leakage results in amplitude and positional errors in the periodogram estimate, especially for the harmonics with lower power levels (Harris, 1978). To reduce the effects of spectral leakage, window functions are used: 1-) to assign a smaller weighting factor to the samples of the signal that cause spectral leakage, 2-) to reduce the sampled values to zero at the beginning and end so that the discontinuities in the sampled signal are eliminated. Figure A.5 was plotted to point out this capability of cancelling discontinuities, which is not clear in Table A.1. The windows with shoulders such as Hamming, Gaussian, Kaiser-Bessel, Dolph-Chebyshev achieve low sidelobe levels, but they cannot completely cancel these discontinuities.

In Figure A.5, it can be observed that only Hann and Blackman does not have shoulders and they are better candidates to prevent spectral leakage. These two windows also have the highest sidelobe roll-off value of -18 dB when compared with the other window functions in Table A.1 thanks to the decrease of the window coefficients to zero at the beginning and end of the function. A similar observation was performed in Figure 2.3, where the spectral leakage at the second harmonic frequency was lower for the window functions without shoulders.

Scallop Loss: Scallop loss can be described as the error in signal's peak power, because of its position in the discrete frequency domain. A frequency peak centred exactly at one of the discrete frequency bins will be displayed correctly. However, when the peak is not at the centre of a frequency bin, there is an error between the displayed and the actual level. As the worst case scenario; if the peak is centred at half a DFT bin away from equally spaced frequency bins, this error can be larger than 3 dB. However, the scallop loss can be significantly reduced by oversampling and zero padding, where both techniques are used in this work to minimise the scallop loss. Therefore, scallop loss was not taken into consideration while choosing a window function.
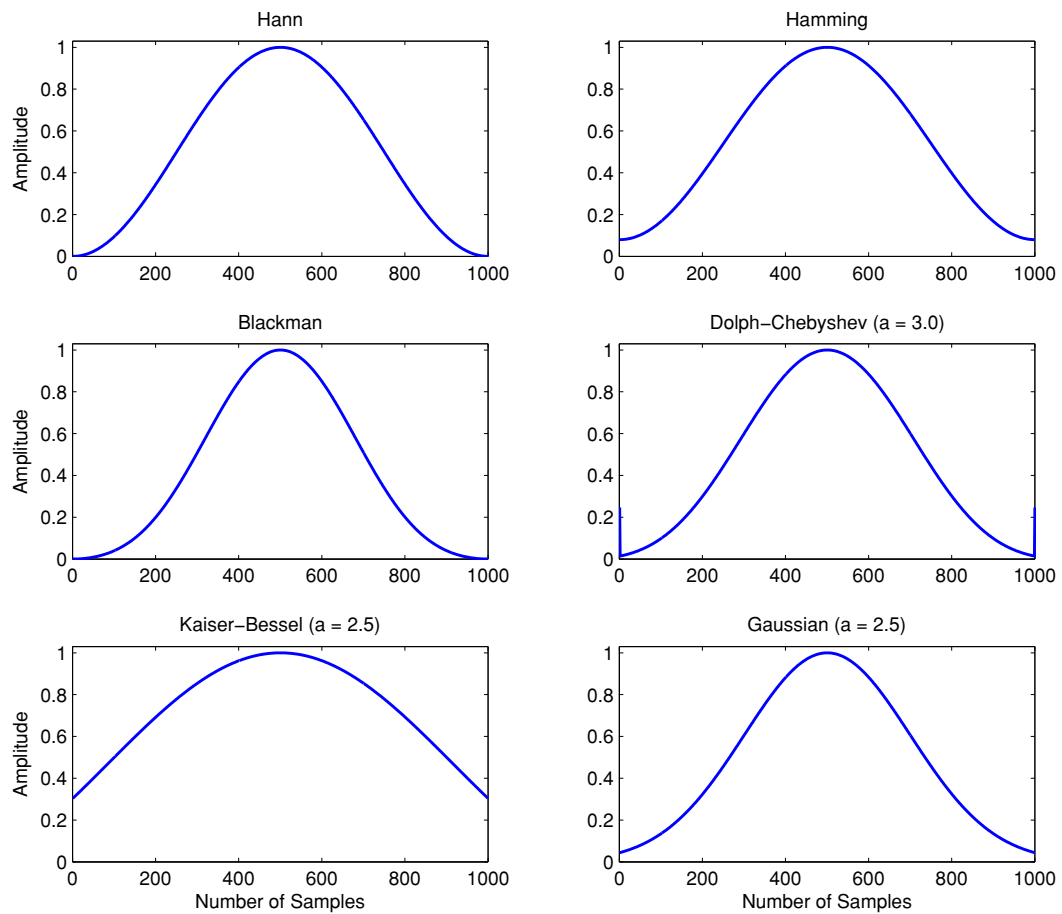
Figure A.5: Figure shows the shape of window functions for some of the windows stated in this section. (Top-Left) the Hann window, (Top-Right) the Hamming window, (Middle-Left) the Blackman window, (Middle-Right) the Dolph-Chebyshev window ($a = 3.0$), (Bottom-Left) the Kaiser-Bessel window ($a = 2.5$), and (Bottom-Right) the Gaussian window ($a = 2.5$).

Worst Case Processing Loss: The processing loss is due to zero values of the window function near the boundaries. The worst case processing loss is the combination of the maximum scalloping loss and the processing loss. This metric shows the total reduction in SNR due to windowing and location of the frequency peak. For this reason, minimising the worst case processing loss maximises the detectability. As Harris (1978) stated that the window functions with a worst case processing loss larger than 3.8 dB are very poor windows and should not be used. Therefore, the windowing functions exceeding 3.8 dB level are not mentioned in this section. Note that the rectangular window is an exception and it is only used for comparison purposes.

The choice of window function used in this study was result of a compromise between resolution and spectral leakage. With 2.0 DFT bins, the Hann window does not have the best resolution, however in terms of spectral leakage, it has a reasonable performance with a highest sidelobe level of -32 dB and a sidelobe roll-off of -18 dB. The Hann window also has a worst case processing loss of 3.18 dB, which is better than most of the window functions listed in the Table A.1. Therefore, the Hann window was preferred for most of the applications while tapering the time domain signal or estimating the power spectrum.

A.3 Time-Frequency Distributions

The time analysis and frequency analysis by themselves cannot completely describe the nature of the signal, therefore there is a need for combined time-frequency representation. E.g. for a chirp signal with an instantaneous frequency function of $f_c + (B/T)t$ as given in Eq. (2.3), the frequency spectrum can only show the intensities of the existing frequencies. The time-frequency representation of the same chirp however precisely shows when these frequency components exist in time.

Short Time Fourier Transform (STFT): The STFT performs a time-localized Fourier transform of the signal $s(t)$ within a sliding window $w(t)$ as

$$S_{STFT}(\tau, f) = \int_{-\infty}^{\infty} s(t)\, w(t - \tau)\, e^{-j2\pi ft} dt, \qquad (A.18)$$

or in discrete form as

$$S_{STFT}[m, f] = \sum_{n=1}^{N} s[n]\, w[n - m]\, e^{-j2\pi fn}. \qquad (A.19)$$

The final spectrogram can be represented as the magnitude squared STFT as $|S_{STFT}|^2$.

The achievable resolution by the window function is limited due to the uncertainty principle. The time and frequency resolutions of the STFT cannot be chosen arbitrarily at the same time. However, by increasing the window length and ratio of overlaps between the windows a reasonable resolution can be achieved. Increasing the ratio of the overlap significantly increases the computational load for long windows and signals, but also the resolution of the spectrogram.

Wigner-Ville Distribution: This approach uses the autocorrelation function to calculate the power spectrum by comparing the signal to itself for all possible time lags as

$$S_{WV}(t,f) = \frac{1}{2\pi} \int_{-\infty}^{\infty} s\left(t - \frac{\tau}{2}\right) s\left(t + \frac{\tau}{2}\right) e^{-j2\pi f\tau} d\tau, \qquad (A.20)$$

or in discrete form as

$$S_{WV}[n,f] = \frac{1}{2\pi} \sum_{m=1}^{M} s[n-m]\, s[n+m]\, e^{-j4\pi fm}. \qquad (A.21)$$

The Wigner-Ville distribution is not a linear transform, therefore *cross-terms* will occur when there is more than one chirp (Martin & Flandrin, 1985). Therefore, the final time-frequency distribution will show the contributions from auto-terms and cross-terms, which is the interaction between different components.

Wavelet Transform: In contrast to traditional techniques such as the STFT spectrogram, the wavelet transform allows the use of variable window lengths. By varying the window length or by scaling and shifting the wavelet function, different frequency components of the signal can be analysed with a different resolution. The wavelet transform has a higher time resolution for high frequency components and lower time resolution for slowly changing low frequency components. For this reason, it is also referred to as multi-resolution signal analysis. The wavelet transform can be defined as (Daubechies, 1990)

$$W_\psi(\upsilon, \tau) = \frac{1}{\sqrt{\upsilon}} \int_{-\infty}^{\infty} s(t)\, \psi\left(\frac{t - \tau}{\upsilon}\right) dt, \qquad (A.22)$$

where υ is the scaling that modulates the width, τ shifts the time and ψ is the mother wavelet.

The basic idea behind the multi-resolution analysis is based on the uncertainty principle. Since $\Delta t \cdot \Delta f \leq 1/2$, it is not possible to achieve a good time and frequency resolution simultaneously. The wavelet transform however, scales time window by modifying the wavelet function and can achieve varying time and frequency resolutions in the spectrogram, which is also referred to as the *scalogram*.

For the case of LFM chirps, the estimation of the instantaneous frequency is dependent on the wavelet function. The instantaneous frequency can appear with a varying slope through different sections of the scalogram, since the spectrum has different resolutions for different frequencies. For this reason, the wavelet transform was not preferred in this study.

Example: To illustrate the difference between these method a waveform was designed similar to the example given in Figure 3.10. The waveform was superposition of three different chirps. The first component of the simulated linear frequency modulated chirp has an amplitude of 1, a duration of 20 μs, centre frequency of 5 MHz, and bandwidth of 5 MHz. The second component has an amplitude of $1/4$, a duration of 20 μs, centre frequency of 10 MHz, and bandwidth of 10 MHz. The third component has an amplitude of $1/9$, a duration of 20 μs, centre frequency of 15 MHz, and bandwidth of 15 MHz.

Figure A.6 shows the STFT spectrogram of the simulated chirp signal processed by a Hann window with 50% overlap, which is one of the common techniques for spectrum estimation. For this example the signal length was 4096 samples and the window length was 256 samples. For this window size, a satisfactory frequency resolution can be achieved by sacrificing the time resolution. However, by increasing the window overlap to 99% as shown in Figure A.7, the time resolution can be increased with a cost of reduced frequency resolution due to the smoothing effect of averaging and increased bias on the spectral estimation.

When the Kaiser-Bessel window is used to calculate the modified periodogram instead of the Hann window, the effect of windowing on spectral leakage becomes clear, as shown in Figure A.8. The fundamental and harmonic signals are stretched in frequency domain and they have higher sidelobes when compared with the Figure A.7. The reason for this is the high shoulders of the Kaiser-Bessel window ($a = 2.5$), which makes is less effective than Hann window for suppression of spectral leakage.
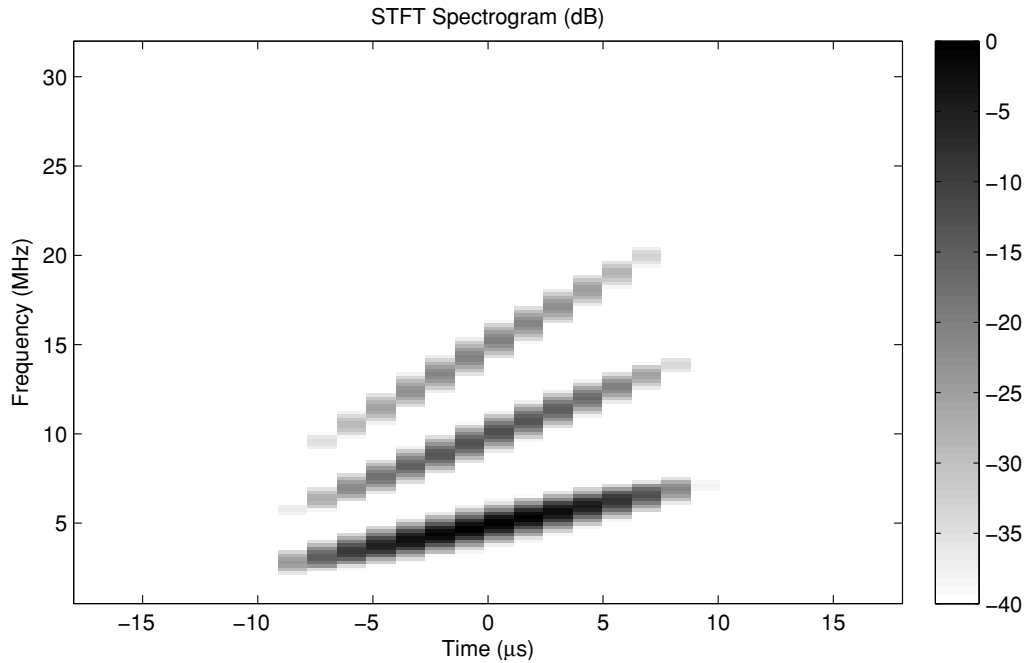
Figure A.6: Spectrogram of the simulated chirp signal processed with the STFT and a Hann window with 50% overlap.

The contour plot of the Wigner-Ville distribution is given in Figure A.9, which is the most preferred way of plotting distribution curves. The cross-terms, which are causing the misinterpretation of the harmonic content of the signal, are clearly visible in the figure. Therefore, the Wigner-Ville distribution was not used in this study for spectrogram estimation.

In order to plot the scalogram of the simulated chirp, the continuous wavelet transform, *cwt* function in Matlab, was used with second order Daubechies wavelets, as shown in Figure A.8. Because the resolution is different for different frequency components, the instantaneous frequency is not linear. The distribution of the signal's energy in time-frequency domain is significantly different than Figure A.7. This error can be reduced by using different wavelet functions and scaling, but the problem cannot be completely eliminated.
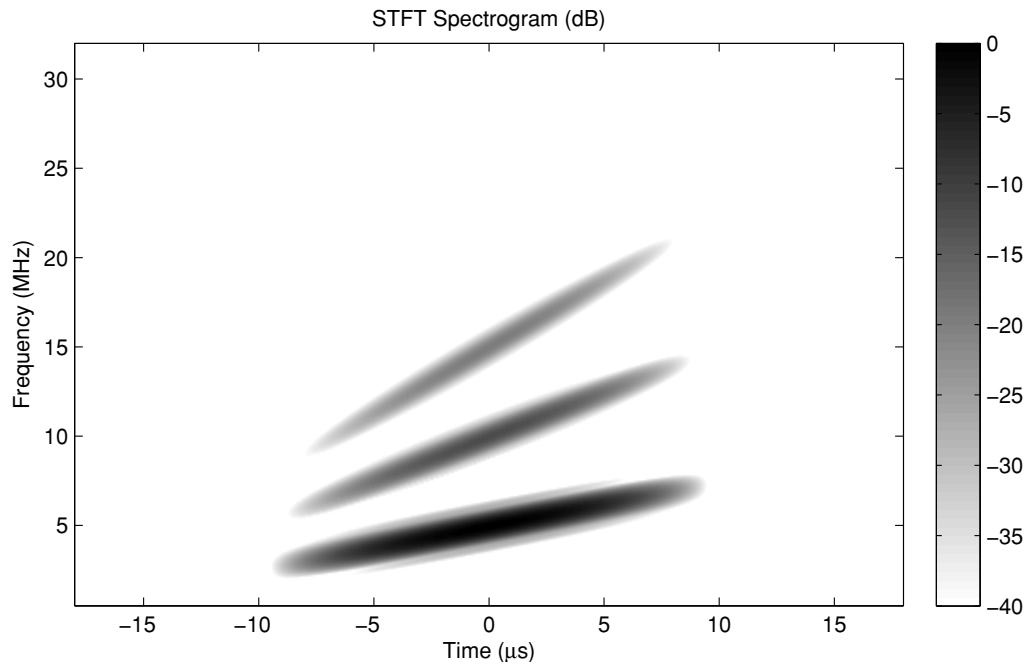
Figure A.7: Spectrogram of the simulated chirp signal processed with the STFT and a Hann window with 99% overlap
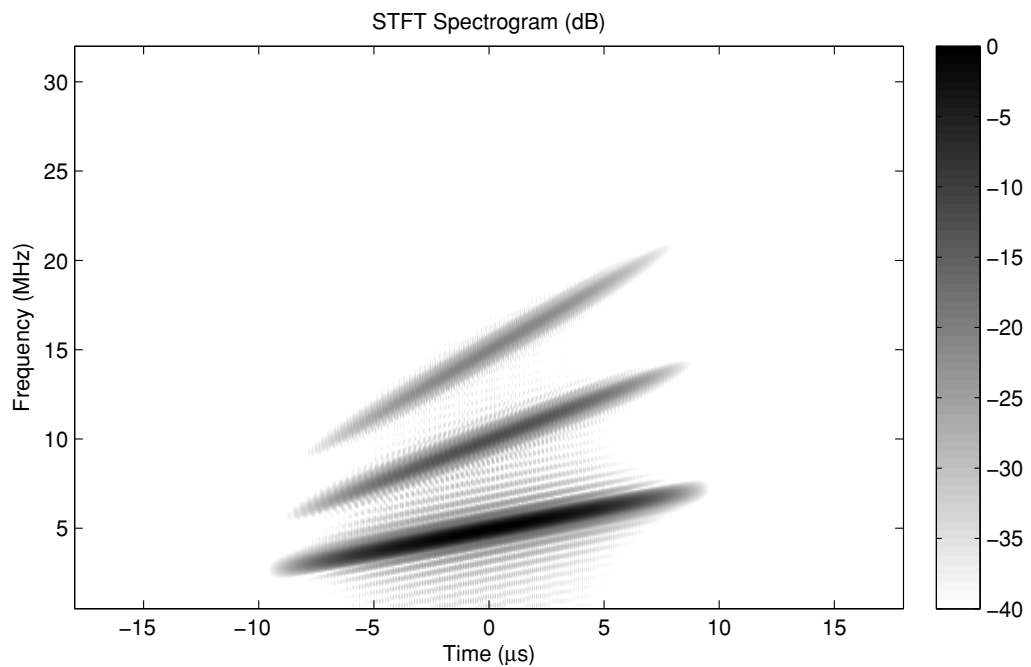
Figure A.8: Spectrogram of the simulated chirp signal processed with the STFT and a Kaiser-Bessel window ($a = 2.5$).
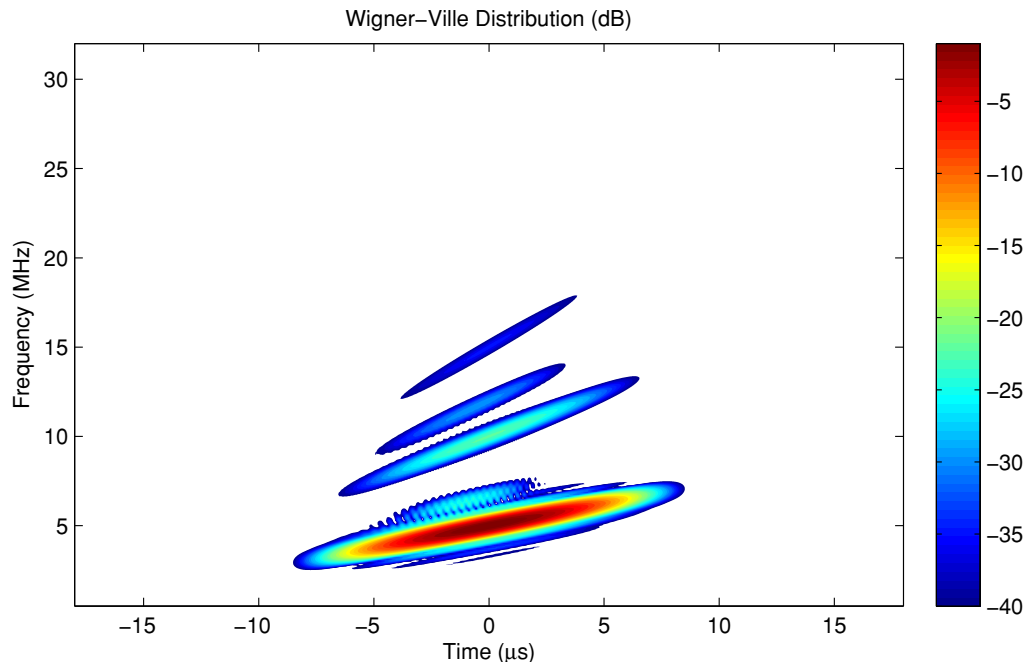
Figure A.9: Wigner-Ville distribution of the simulated chirp signal.
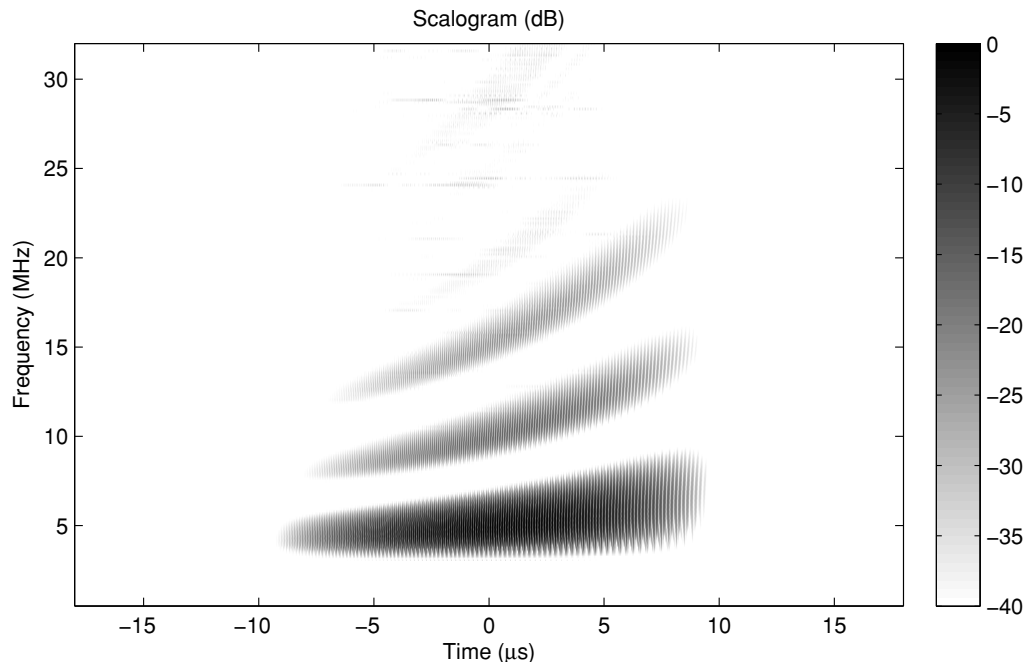
Figure A.10: Scalogram of the simulated chirp signal processed with the continuous wavelet transform by using second order Daubechies wavelets.

Appendix B

Harmonic Generation Through Nonlinear Propagation

The propagation of ultrasonic waves is nonlinear. This nonlinearity engenders a progressive distortion of the wave shape resulting in acoustic shocks and generation of high-order harmonics. This phenomenon is usually referred to as "nonlinear propagation".

The shock wave generation is due to the variation in phase velocity, which is caused by two physical mechanisms; convection and nonlinearity of pressure-density relation (Duck, 2002). Propagation speed of the ultrasound wave is different for the compression and expansion phases, because waveform peaks travel faster than troughs. At the compression phase of the wave the speed is higher, since compression increases the density of the medium. It is slower during the rarefaction phase, where the density is lower as shown in Figure B.1. Since $(c_0 + \Delta V_+) > (c_0 - \Delta V_-)$, the initial sinusoidal waveform progressively deforms and becomes a sawtooth wave.

Figure B.2(left) shows the generation of a shock wave and higher-order harmonics due to nonlinear propagation. The measurements were performed in de-ionized and degassed water at a distance of $z = 20$ mm, $z = 40$ mm, and $z = 90$ mm for a 20 cycle sinusoidal waveform with a centre frequency of 2.25 MHz. The waveform steepens and the sinusoidal wave turns into a sawtooth wave as the ultrasound wave propagates. This progressive distortion of the waveform shape gives rise to higher-order harmonics as given in Figure B.2(right).
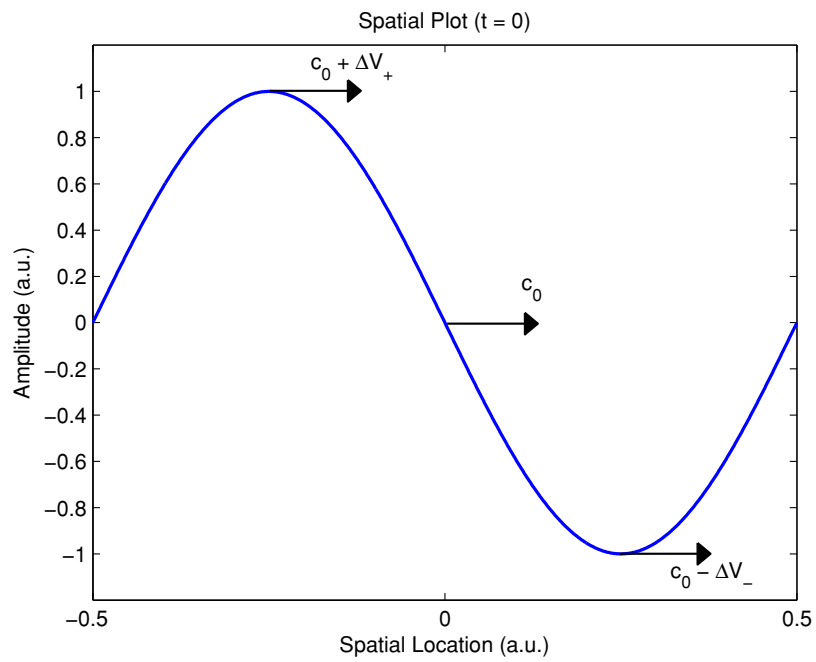
Figure B.1: Spatial plot of the initial waveform at $t = 0$. Propagation speed of the ultrasound wave is different for the compression phase $(c_0 + \Delta V_+)$ and the expansion phase $(c_0 - \Delta V_-)$.
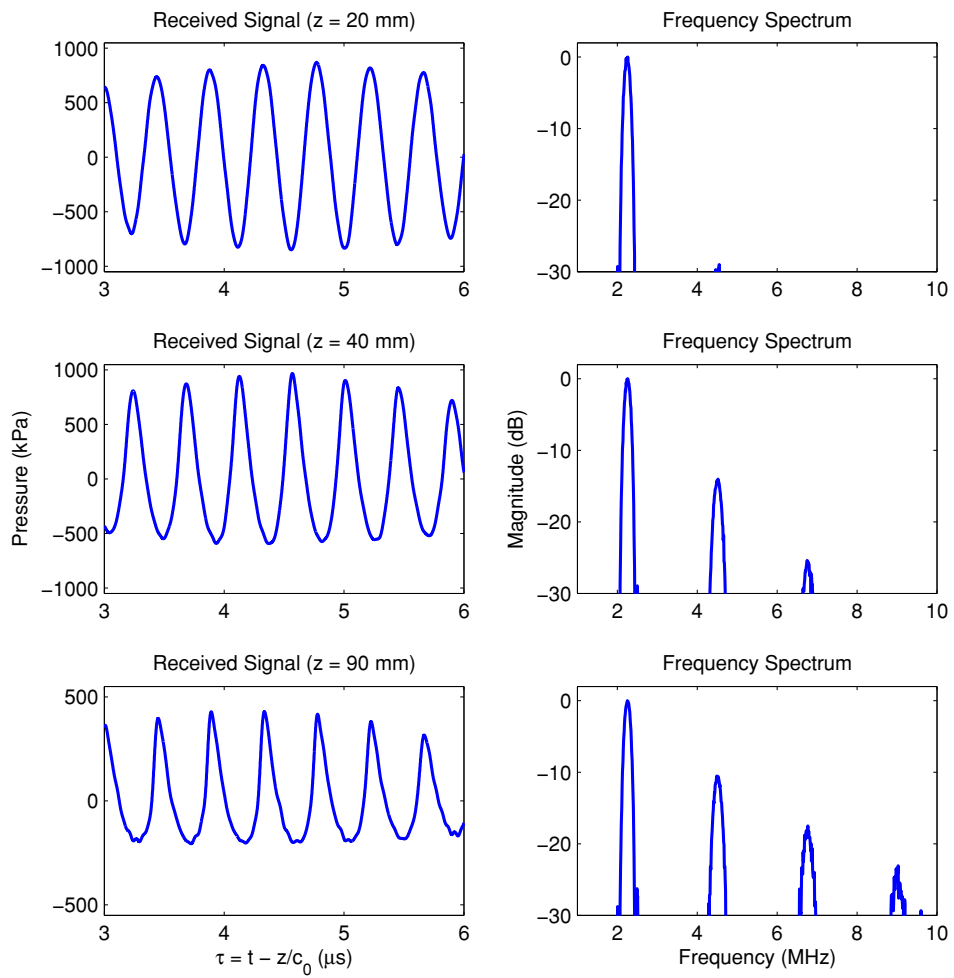
Figure B.2: (Left) Temporal plot of the ultrasound wave and (Right) the associated frequency spectra for (Top) $z = 20$ mm, (Middle) $z = 40$ mm, and (Bottom) $z = 90$ mm.

This relation between the variations in propagation speed and shock wave generation was modelled and formulated by Hamilton & Blackstock (2008). The shock wave parameter as defined by Hamilton & Blackstock (2008) and Duck (2002) can be expressed as;

$$\sigma_{sw} = \frac{2\pi}{\rho_0 \, c_0^3} \left[\, p_0 \, zf(1 + B/2A) \, \right] \tag{B.1}$$

where ρ_0 is the density of the medium, c_0 is the speed of the sound wave, p_0 is the acoustic pressure at the source, f is the frequency, z is the distance, $\beta = 1 + B/2A$ is usually referred to as the nonlinearity coefficient of the medium.

For $\sigma_{sw} \geq 1$ shock wave formation starts. For example, to achieve shock formation ($\sigma_{sw} = 1$) in degassed and de-ionized water at room temperature, one needs a $p_0 \cdot z \cdot f$ product of 14.8 MPa·MHz·cm. However, it doesn't mean that there is no harmonic generation taking place below this threshold.

Hamilton & Blackstock (2008) combined the Fubini and Fay solutions including pre and post-shock regions. Their results showed that the harmonic generation occurs even for $\sigma_{sw} \leq 1$. For $\sigma_{sw} \geq 3$ all harmonics decay due to absorption as shown in Figure B.3.
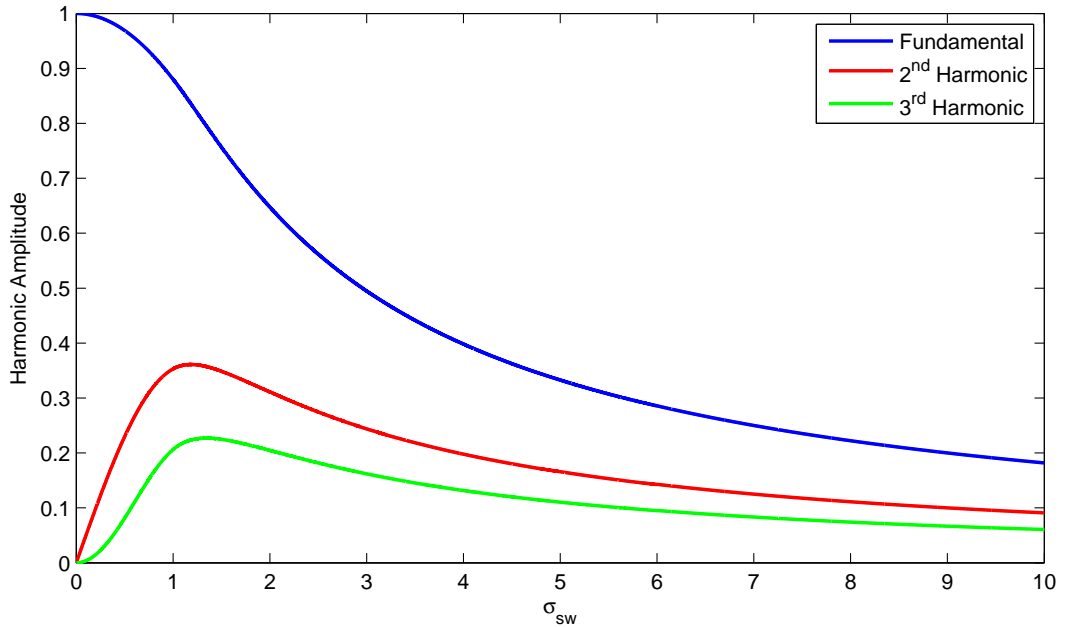
Figure B.3: Spectral amplitudes of fundamental and harmonic components as a function of the shock wave parameter, σ_{sw}.

In this work the shock wave parameter is calculated according to Eq. (B.1), and the power levels of generated harmonics are estimated using Figure B.3 and the harmonic amplitudes are referred to as $\mathcal{B}_n$ for the n-th harmonic.

Appendix C

Microbubble Simulation Model

The bubble dynamics and cavitation was first analysed by Rayleigh (1917) for air bubbles in liquids. After culminating with the work done by Plesset (1949), the Rayleigh-Plesset equation is obtained as

$$\rho \left(R\ddot{R} + \frac{3}{2}\dot{R}^2 \right) = p_L - p_\infty, \tag{C.1}$$

where R is the bubble radius as a function of time, ρ is density of the liquid, p_∞ is the pressure in the liquid at infinity, p_L is the pressure in the liquid at the bubble boundary. The pressure at infinity can be expressed as

$$p_\infty = P_0 + P_{\text{drive}}(t), \tag{C.2}$$

where P_0 is the hydrostatic pressure and $P_{\text{drive}}(t)$ is the acoustic driving pressure.

The equation is further extended to model the bubble behaviour more accurately as given in Eq.(C.3). In the literature this equation is sometimes known as Rayleigh-Plesset-Noltingk-Neppiras-Poritsky (RPNNP), named after its developers Neppiras (1980); Neppiras & Noltingk (1951); Noltingk & Neppiras (1950); Plesset (1949); Rayleigh (1917).

$$\rho \left(R\ddot{R} + \frac{3}{2}\dot{R}^2 \right) = \left(P_0 + \frac{2\sigma}{R_0} \right) \left(\frac{R_0}{R} \right)^{3\gamma} - \frac{2\sigma}{R} - \frac{4\mu\dot{R}}{R} - (P_0 + P_{\text{drive}}(t)), \tag{C.3}$$

where R_0 is the initial bubble radius at equilibrium,γ is the polytropic index, σ is the surface tension between liquid and bubble interface and μ is the viscosity of the liquid.

Ultrasound contrast agents are coated microbubbles, so different models are developed to simulate the effect of the shell. The Sarkar model is one of the simplistic

models, which often used to calculate the radial oscillations of coated microbubbles. This model is basically an extension of the Rayleigh-Plesset equation (Chatterjee & Sarkar, 2003)

$$\rho \left(R\ddot{R} + \frac{3}{2}\dot{R}^2 \right) = \left(P_0 + \frac{2\sigma}{R_0} \right) \left(\frac{R_0}{R} \right)^{3\gamma} - \frac{2\sigma}{R} - \frac{4\mu\dot{R}}{R} - \frac{4\kappa_S\dot{R}}{R^2} - p_\infty \qquad \text{(C.4)}$$

where κ_S is the dilatational viscosity of the shell.

Marmottant et al. (2005) further extended Eq. (C.4) by defining the surface tension to be radius dependent to compensate for the effect of shell elasticity, χ.

$$\rho \left(R\ddot{R} + \frac{3}{2}\dot{R}^2 \right) = \left(P_0 + \frac{2\sigma(R_0)}{R_0} \right) \left(\frac{R_0}{R} \right)^{3\gamma} - \frac{2\sigma(R)}{R} - \frac{4\mu\dot{R}}{R} - \frac{12\mu_S\varepsilon\dot{R}}{R^2} - p_\infty \quad \text{(C.5)}$$

where μ_S is the shear viscosity of the phospholipid shell, ε is the shell thickness, and the radius-dependant surface tension is defined as

$$\sigma(R) = \begin{cases} 0 & \text{if } R \leq R_{\text{buckling}} \\ \chi \left(\dfrac{R^2}{R_{\text{buckling}}^2} - 1 \right) & \text{if } R_{\text{buckling}} \leq R \leq R_{\text{rupture}} \\ \sigma & \text{if } R \geq R_{\text{rupture}} \end{cases} \qquad \text{(C.6)}$$

The buckling and rupture radii of the microbubble are defined as $R_{\text{buckling}} = R_0$ and $R_{\text{rupture}} = R_0\sqrt{1 + \sigma/\chi}$.

C.1 Simulation Parameters

Table C.1 lists the symbol definitions and their values used in the simulations.

Table C.1: Parameter values used in the simulations

Symbol	Parameter Definition	Value	Unit
R	bubble radius (function of time)		m
$\dot{R}$	bubble wall velocity		m/s
$\ddot{R}$	bubble wall acceleration		m/s^2
R_0	initial bubble radius at equilibrium (constant)		m
p_∞	pressure in the liquid at infinity		Pa
p_L	pressure in the liquid at the bubble boundary		Pa
$P_{\mathrm{drive}}(t)$	acoustic driving pressure		Pa
p_i	pressure inside the bubble at equilibrium		Pa
P_0	hydrostatic pressure	101325	Pa
ρ	density of the liquid (water)	998	kg/m^3
σ	surface tension of water	0.0728	N/m
μ	shear viscosity of the liquid (water)	0.001	Pa·s
μ_S	shear viscosity of the shell (phospholipid)	0.5	Pa·s
γ	polytropic gas index for SF$_6$ (adiabatic)	1.095	-
G_S	shear modulus of the shell	20×10^6	Pa
ε	shell thickness	4×10^{-9}	m
κ_S	dilatational viscosity of shell ($\kappa_S \approx 3\varepsilon\mu_S$)	6×10^{-9}	Pa·m·s
χ	shell elasticity ($\chi \approx 3\varepsilon G_S$)	0.3	N/m

References

ABBOTT, J.G. (1999). Rationale and derivation of mi and ti - a review. *Ultrasound in Medicine & Biology*, **25**, 431–441. 12

ALMEIDA, L.B. (1994). The fractional Fourier transform and time-frequency representations. *Signal Processing, IEEE Transactions on*, **42**, 3084–3091. 32

ARIF, M., COWELL, D.M.J. & FREEAR, S. (2010a). Pulse compression of harmonic chirp signals using the fractional Fourier transform. *Ultrasound in Medicine & Biology*, **36**, 949–956. i, 90

ARIF, M., HARPUT, S. & FREEAR, S. (2010b). Experimental investigation of chirp coded excitation in ultrasound superharmonic imaging. In *Ultrasonics Symposium, 2010 IEEE*, 2187–2190. 126

ARIF, M., HARPUT, S., SMITH, P.R., COWELL, D.M.J. & FREEAR, S. (2011). Extraction of an overlapped second harmonic chirp component using the fractional Fourier transform. In *Ultrasonics Symposium, 2011 IEEE*, 405–408. i, 89, 106

ARSHADI, R., YU, A.C.H. & COBBOLD, R.S.C. (2007). Coded excitation methods for ultrasound harmonic imaging. *Canadian Acoustics*, **35**, 35–46. 3, 15, 17, 92, 93, 118

AVERKIOU, M.A., MANNARIS, C., BRUCE, M. & POWERS, J. (2008). Nonlinear pulsing schemes for the detection of ultrasound contrast agents. *The Journal of the Acoustical Society of America*, **123**, 915–920. 138

BARBER, F.E., LEES, S. & LOBENE, R.R. (1969). Ultrasonic pulse-echo measurements in teeth. *Archives of Oral Biology*, **14**, 745–760. 13, 52, 54, 61, 67, 71, 75, 81

BENNETT, M., MCLAUGLIN, S., ANDERSON, T. & MCDICKEN, N. (2004). Filtering of chirped ultrasound echo signals with the fractional Fourier transform. In *IEEE Ultrasonics Symposium*, vol. 3, 2036–2040. 72

BIAGI, E., BRESCHI, L., VANNACCI, E. & MASOTTI, L. (2009). Multipulse technique exploiting the intermodulation of ultrasound waves in a nonlinear medium. *Ultrasonics, Ferroelectrics and Frequency Control, IEEE Transactions on*, **56**, 520–535. 138

BLACKMAN, R.B. & TUKEY, J.W. (1958). *The Measurement of Power Spectra*. Dover Publications. 5, 195

BORSBOOM, J.M.G., CHIN, C.T. & DE JONG, N. (2003). Nonlinear coded excitation method for ultrasound contrast imaging. *Ultrasound in Medicine & Biology*, **29**, 277–284. 3, 97

BORSBOOM, J.M.G., CHIN, C.T., BOUAKAZ, A., VERSLUIS, M. & DE JONG, N. (2005). Harmonic chirp imaging method for ultrasound contrast agent. *Ultrasonics, Ferroelectrics and Frequency Control, IEEE Transactions on*, **52**, 241–249. 3, 13, 14, 138

BOUAKAZ, A., FRIGSTAD, S., CATE, F.J.T. & DE JONG, N. (2002). Super harmonic imaging: a new imaging technique for improved contrast detection. *Ultrasound in Medicine & Biology*, **28**, 59–68. 117

BOUAKAZ, A., VERSLUIS, M., BORSBOOM, J. & DE JONG, N. (2007). Radial modulation of microbubbles for ultrasound contrast imaging. *Ultrasonics, Ferroelectrics and Frequency Control, IEEE Transactions on*, **54**, 2283–2290. 137

BRENNEN, C.E. (1995). *Cavitation and Bubble Dynamics*. Oxford University Press. 138, 139

BURNS, P.N., SIMPSON, D.H. & AVERKIOU, M.A. (2000a). Nonlinear imaging. *Ultrasound in Medicine & Biology*, **26**, 19–22. 95

BURNS, P.N., WILSON, S.R. & SIMPSON, D.H. (2000b). Pulse inversion imaging of liver blood flow: Improved method for characterizing focal masses with microbubble contrast. *Investigative Radiology*, **35**, 58–71. 92, 138

CANCELA, P., LÓPEZ, E. & ROCAMORA, M. (2010). Fan chirp transform for music representation. In *Proc of the 13th Int Conference on Digital Audio Effects*, 1–8. 6, 36

CANDAN, Ç., KUTAY, M.A. & OZAKTAS, H.M. (2000). The discrete fractional Fourier transform. *Signal Processing, IEEE Transactions on*, **48**, 1329–1337. 29, 32

CAPUS, C. & BROWN, K. (2003). Short-time fractional Fourier methods for the time-frequency representation of chirp signals. *Journal of the Acoustical Society of America*, **113**, 3253–3263. 30, 31

CHANDRAN, V. & ELGAR, S.L. (1991). Mean and variance of estimates of the bispectrum of a harmonic random process-an analysis including leakage effects. *Signal Processing, IEEE Transactions on*, **39**, 2640–2651. 173

CHATTERJEE, D. & SARKAR, K. (2003). A newtonian rheological model for the interface of microbubble contrast agents. *Ultrasound in Medicine & Biology*, **29**, 1749–1757. 216

CHETTY, K., HAJNAL, J.V. & ECKERSLEY, R.J. (2006). Investigating the nonlinear microbubble response to chirp encoded, multipulse sequences. *Ultrasound in Medicine & Biology*, **32**, 1887–1895. 3

CHEUNG, K., COUTURE, O., BEVAN, P.D., CHÉRIN, E., WILLIAMS, R., BURNS, P.N. & FOSTER, F.S. (2008). In vitro characterization of the subharmonic ultrasound signal from definity microbubbles at high frequencies. *Physics in Medicine and Biology*, **53**, 1209–1223. 138

CHIAO, R. & HAO, X. (2005). Coded excitation for diagnostic ultrasound: a system developer's perspective. *Ultrasonics, Ferroelectrics and Frequency Control, IEEE Transactions on*, **52**, 160–170. 2, 12, 14, 15, 60, 93

CHOI, H. & WILLIAMS, W.J. (1989). Improved time-frequency representation of multicomponent signals using exponential kernels. *Acoustics, Speech and Signal Processing, IEEE Transactions on*, **37**, 862–871. 5, 6

CHOMAS, J., DAYTON, P., MAY, D. & FERRARA, K. (2002). Nondestructive subharmonic imaging. *Ultrasonics, Ferroelectrics and Frequency Control, IEEE Transactions on*, **49**, 883–892. 13

COBBOLD, R.S.C. (2007). *Foundations of Biomedical Ultrasound*. Oxford University Press. 93

COHEN, L. (1989). Time-frequency distributions-a review. *Proceedings of the IEEE*, **77**, 941–981. 4, 5

COOK, C.E. & BERNFELD, M. (1967). *Radar signals: An introduction to theory and application*. New York: Academic Press. 12, 14

COUTURE, O., AUBRY, J., MONTALDO, G., TANTER, M. & FINK, M. (2008). Suppression of tissue harmonics for pulse-inversion contrast imaging using time reversal. *Physics in Medicine and Biology*, **53**, 5469–5480. 95, 184

COWELL, D.M.J. & FREEAR, S. (2008). Quinary excitation method for pulse compression ultrasound measurements. *Ultrasonics*, **48**, 98–108. 96

COWELL, D.M.J. & FREEAR, S. (2010). Separation of overlapping linear frequency modulated (LFM) signals using the fractional Fourier transform. *Ultrasonics, Ferroelectrics and Frequency Control, IEEE Transactions on*, **57**, 2324–2333. 31, 72, 80

CULJAT, M., SINGH, R., YOON, D. & BROWN, E. (2003). Imaging of human tooth enamel using ultrasound. *Medical Imaging, IEEE Transactions on*, **22**, 526–529. 54, 61, 72, 75, 87

CULJAT, M.O., SINGH, R.S., BROWN, E.R., NEURGAONKAR, R.R., YOON, D.C. & WHITE, S.N. (2005a). Ultrasound crack detection in a simulated human tooth. *Dentomaxillofac Radiology*, **34**, 80–85. 54, 72, 75, 87

CULJAT, M.O., SINGH, R.S., WHITE, S.N., NEURGAONKAR, R.R. & BROWN, E.R. (2005b). Evaluation of gallium-indium alloy as an acoustic couplant for high-impedance, high-frequency applications. *Acoustics Research Letters Online*, **6**, 125–130. 59

CULJAT, M.O., GOLDENBERG, D., TEWARI, P. & SINGH, R.S. (2010). A review of tissue substitutes for ultrasound imaging. *Ultrasound in Medicine & Biology*, **36**, 861–873. 136, 189

DAUBECHIES, I. (1990). The wavelet transform, time-frequency localization and signal analysis. *Information Theory, IEEE Transactions on*, **36**, 961–1005. 4, 6, 205

DE JONG, N., FRINKING, P.J.A., BOUAKAZ, A. & CATE, F.J.T. (2000). Detection procedures of ultrasound contrast agents. *Ultrasonics*, **38**, 87–92. 169

DE JONG, N., BOUAKAZ, A. & FRINKING, P. (2002). Basic acoustic properties of microbubbles. *Echocardiography*, **19**, 229–240. 138, 139

DE JONG, N., EMMER, M., VAN WAMEL, A. & VERSLUIS, M. (2009). Ultrasonic characterization of ultrasound contrast agents. *Medical and Biological Engineering and Computing*, **47**, 861–873. 169

DUCK, F.A. (2002). Nonlinear acoustics in diagnostic ultrasound. *Ultrasound in Medicine & Biology*, **28**, 1–18. 117, 169, 170, 210, 213

DUGMORE, C.R. & ROCK, W.P. (2004). A multifactorial analysis of factors associated with dental erosion. *British Dental Journal*, **196**, 283–286. 55

DUNN, R.B., QUATIERI, T.F. & MALYSKA, N. (2009). Sinewave parameter estimation using the fast fan-chirp transform. In *IEEE Workshop on Applications of Signal Processing to Audio and Acoustics*, 349–352. 36, 38

DUSSIK, K.T., DUSSIK, F. & WYT, L. (1947). Auf dem wege zur hyperphonographie des gehirnes. *Wien. med. Wschr.*, **97**, 425–429. 1

ECKERSLEY, R.J., TANG, M.X., CHETTY, K. & HAJNAL, J.V. (2007). Microbubble contrast agent detection using binary coded pulses. *Ultrasound in Medicine & Biology*, **33**, 1787–1795. 15

EVANS, J.A. & TAVAKOLI, M.B. (1990). Ultrasonic attenuation and velocity in bone. *Physics in Medicine and Biology*, **35**, 1387–1396. 52

FARMAN, A.G. & FARMAN, T.T. (2005). A comparison of 18 different x-ray detectors currently used in dentistry. *Oral Surg Oral Med Oral Pathol Oral Radiol Endod.*, **99**, 485–489. 86

FDA (30-09-1997). Information for manufacturers seeking marketing clearance of diagnostic ultrasound systems and transducers. Tech. rep., FDA. 12

FRINKING, P.J.A., BOUAKAZ, A., KIRKHORN, J., CATE, F.J.T. & DE JONG, N. (2000). Ultrasound contrast imaging: current and new potential methods. *Ultrasound in Medicine & Biology*, **26**, 965–975. 169

GHORAYEB, S.R. & VALLE, T. (2002). Experimental evaluation of human teeth using noninvasive ultrasound: echodentography. *Ultrasonics, Ferroelectrics and Frequency Control, IEEE Transactions on*, **49**, 1437–1443. 54, 59, 61, 71, 75, 87

GHORAYEB, S.R., XUE, T. & LORD, W. (1997). Ultrasonic imaging of teeth for early detection of abscesses. In *IEEE Ultrasonics Symposium, 1997.*, 1511–1515. 61

GHORAYEB, S.R., PETRAKIS, P. & MCGRATH, M. (2003). Experimental determination of ultrasonic phase velocities in human teeth along arbitrary symmetry directions. In *Proceedings of IEEE Engineering in Medicine and Biology Society, 2003.*, vol. 3, 2382–2385. 71

GHORAYEB, S.R., BERTONCINI, C.A. & HINDERS, M.K. (2008). Ultrasonography in dentistry. *Ultrasonics, Ferroelectrics and Frequency Control, IEEE Transactions on*, **55**, 1256–1266. 13, 54, 56, 75, 81

GORCE, J., ARDITI, M. & SCHNEIDER, M. (2000). Influence of bubble size distribution on the echogenicity of ultrasound contrast agents: A study of sonovue. *Investigative Radiology*, **35**, 661–671. 143

GRAMIAK, R. & SHAH, P.M. (1968). Echocardiography of the aortic root. *Investigative Radiology*, **3**, 356–366. 137

GRIFFITH, J.M. & HENRY, W.L. (1974). A sector scanner for real time two-dimensional echocardiography. *Circulation*, **49**, 1147–1152. 1

HAMILTON, M.F. & BLACKSTOCK, D.T. (2008). *Nonlinear Acoustics*. Acoustical Society of America. 45, 169, 213

HARPUT, S., COWELL, D.M.J., EVANS, T., BUBB, N. & FREEAR, S. (2009). Tooth characterization using ultrasound with fractional Fourier transform. In *Ultrasonics Symposium, 2009 IEEE*, 1906–1909. i, 52, 72, 78

HARPUT, S., ARIF, M. & FREEAR, S. (2010). Experimental investigation of the subharmonic emission from microbubbles using linear and nonlinear frequency modulated signals. In *Ultrasonics Symposium, 2010 IEEE*, 1724–1727. 139

HARPUT, S., EVANS, T., BUBB, N. & FREEAR, S. (2011a). Detection of restoration faults under fillings in human tooth using ultrasound. In *Ultrasonics Symposium, 2011 IEEE*, 1443–1446. i, 52

HARPUT, S., EVANS, T., BUBB, N. & FREEAR, S. (2011b). Diagnostic ultrasound tooth imaging using fractional Fourier transform. *Ultrasonics, Ferroelectrics and Frequency Control, IEEE Transactions on*, **58**, 2096–2106. i, 52, 78

HARPUT, S., MCLAUGHLAN, J., SMITH, P.R., COWELL, D.M.J., EVANS, S.D. & FREEAR, S. (2012). Separating the second harmonic response of tissue and microbubbles using bispectral analysis. In *Ultrasonics Symposium, 2012 IEEE*, In Press. i, 138, 168

HARRIS, F.J. (1978). On the use of windows for harmonic analysis with the discrete Fourier transform. *Proceedings of the IEEE*, **66**, 51–83. 21, 200, 201, 202, 204

HILLIS, A.J., NEILD, S.A., DRINKWATER, B.W. & WILCOX, P.D. (2006). Global crack detection using bispectral analysis. *Proceedings of the Royal Society A: Mathematical, Physical and Engineering Science*, **462**, 1515–1530. 183

HUA, J., CHEN, S. & KIM, Y. (2009). Refining enamel thickness measurements from b-mode ultrasound images. In *Proceedings of IEEE Engineering in Medicine and Biology Society*, 440–443. 54, 55

HUGHES, D., GIRKIN, J., POLAND, S., LONGBOTTOM, C., BUTTON, T., ELGOYHEN, J., HUGHES, H., MEGGS, C. & COCHRAN, S. (2008). Investigation of dental samples

using a 35 mhz focussed ultrasound piezocomposite transducer. *Ultrasonics*, **49**, 212–218. 54

HUYSMANS, M.C.D.N.J.M. & THIJSSEN, J.M. (2000). Ultrasonic measurement of enamel thickness: a tool for monitoring dental erosion? *Journal of Dentistry*, **28**, 187–191. 70, 71, 72

IRIEA, T., OHDAIRA, E. & ITOH, K. (2003). Study for imaging of inside bone using fm-chirp pulse compression system. *Ultrasonics*, **24**, 713–716. 3

JAYNES, E.T. (1996). Bayesian spectrum and chirp analysis. 4, 5

JENSEN, J.A., NIKOLOV, S.I., GAMMELMARK, K.L. & PEDERSEN, M.H. (2006). Synthetic aperture ultrasound imaging. *Ultrasonics*, **44**, e5–e15. 2

JOHN, C. (2005). Directing ultrasound at the cemento-enamel junction (cej) of human teeth: I. asymmetry of ultrasonic path lengths. *Ultrasonics*, **43**, 467–479. 59, 61

JOHN, C. (2006). Lateral distribution of ultrasound velocity in horizontal layers of human teeth. *The Journal of the Acoustical Society of America*, **119**, 1214–1226. 61

KÉPESI, M. & WERUAGA, L. (2006). Adaptive chirp-based timefrequency analysis of speech signals. *Speech Communication*, **48**, 474–492. 6, 36

KIM, D.Y., LEE, J.C., KWON, S.J. & SONG, T.K. (2001). Ultrasound second harmonic imaging with a weighted chirp signal. In *Ultrasonics Symposium, 2001 IEEE*, 1477–1480. 15, 89, 120

KIM, Y.C. & POWERS, E.J. (1979). Digital bispectral analysis and its applications to nonlinear wave interactions. *Plasma Science, IEEE Transactions on*, **PS-7**, 120–131. 170, 172, 173, 176

KINO, G.S. (1987). *Acoustic Waves:Devices, Imaging, and Analog Signal Processing*. Prentice-Hall, Inc. 2, 56, 81

KOÇ, A., OZAKTAS, H.M., CANDAN, C. & KUTAY, M.A. (2008). Digital computation of linear canonical transforms. *Signal Processing, IEEE Transactions on*, **56**, 2383–2394. 28, 29

KOSSOFF, G. & SHARPE, C.J. (1966). Examination of the contents of the pulp cavity in teeth. *Ultrasonics*, **4**, 77–83. 13, 54, 59, 75, 81

KUTAY, A., OZAKTAS, H.M., ARIKAN, O. & ONURAL, L. (1997). Optimal filtering in fractional Fourier domains. *Signal Processing, IEEE Transactions on*, **45**, 1129–1143. 32

LEAVENS, C., WILLIAMS, R., FOSTER, F.S., BURNS, P.N. & SHERAR, M.D. (2007). Golay pulse encoding for microbubble contrast imaging in ultrasound. *Ultrasonics, Ferroelectrics and Frequency Control, IEEE Transactions on*, **54**, 2082–2090. 14, 15

LEES, S. & ROLLINS, J.F.R. (1972). Anisotropy in hard dental tissues. *Journal of Biomechanics*, **5**, 557–566. 71

LÖST, C., IRION, K.M., JOHN, C. & NÜSSLE, W. (1992). Two-dimensional distribution of sound velocity in ground sections of dentin. *Dental Traumatology*, **8**, 215–218. 54, 59, 61, 75, 87

LOUWERSE, C., KJAELDGAARD, M. & HUYSMANS, M.C.D.N.J.M. (2004). The reproducibility of ultrasonic enamel thickness measurements: an in vitro study. *Journal of Dentistry*, **32**, 83–89. 55, 60, 70

MA, Q., MA, Y., GONG, X. & ZHANG, D. (2005). Improvement of tissue harmonic imaging using the pulse-inversion technique. *Ultrasound in Medicine & Biology*, **31**, 889–894. 95

MA, Q., ZHANG, D., GONG, X. & MA, Y. (2006). Investigation of superharmonic sound propagation and imaging in biological tissues in vitro. *The Journal of the Acoustical Society of America*, **119**, 2518–2523. 131

MAEV, R.G., DENISOVA, L.A., MAEVA, E.Y. & DENISSOV, A.A. (2002). New data on histology and physico-mechanical properties of human tooth tissue obtained with acoustic microscopy. *Ultrasound in Medicine & Biology*, **28**, 131–136. 54

MAMOU, J., ARISTIZÁBAL, O., SILVERMAN, R.H., KETTERLING, J.A. & TURNBULL, D.H. (2009). High-frequency chirp ultrasound imaging with an annular array for ophthalmologic and small-animal imaging. *Ultrasound in Medicine & Biology*, **35**, 1198–1208. 3

MANN, S. & HAYKIN, S. (1995). The chirplet transform: physical considerations. *Signal Processing, IEEE Transactions on*, **43**, 2745–2761. 4, 6

MARANGOS, O., MISRA, A., SPENCER, P. & KATZ, J.L. (2011). Scanning acoustic microscopy investigation of frequency-dependent reflectance of acid-etched human dentin using homotopic measurement. *Ultrasonics, Ferroelectrics and Frequency Control, IEEE Transactions on*, **58**, 585–595. 70

MARESCA, D., JANSEN, K., RENAUD, G., VAN SOEST, G., LI, X., ZHOU, Q., DE JONG, N., SHUNG, K.K. & VAN DER STEEN, A.F.W. (2012). Intravascular ultrasound chirp imaging. *Applied Physics Letters*, **100**, 1–3. 3

MARMOTTANT, P., VAN DER MEER, S., EMMER, M., VERSLUIS, M., DE JONG, N., HILGENFELDT, S. & LOHSE, D. (2005). A model for large amplitude oscillations of coated bubbles accounting for buckling and rupture. *The Journal of the Acoustical Society of America*, **118**, 3499–3505. 138, 140, 145, 216

MARTIN, W. & FLANDRIN, P. (1985). Wigner-ville spectral analysis of nonstationary processes. *Acoustics, Speech and Signal Processing, IEEE Transactions on*, **33**, 1461–1470. 5, 205

MAST, T.D. (2000). Empirical relationships between acoustic parameters in human soft tissues. *Acoustics Research Letters Online*, **1**, 37–42. 136

MATTE, G.M., VAN NEER, P.L.M.J., BORSBOOM, J.M.G., VERWEIJ, M.D. & DE JONG, N. (2008). A new frequency compounding technique for super harmonic imaging. In *Ultrasonics Symposium, 2008 IEEE*, 357–360. 117

MCBRIDE, A.C. & KERR, F.H. (1987). On Namias's fractional Fourier transforms. *IMA Journal of Applied Mathematics*, **39**, 159–175. 6, 29

MCDICKEN, W., BRUFF, K. & PATON, J. (1974). An ultrasonic instrument for rapid b-scanning of the heart. *Ultrasonics*, **12**, 269–272. 1

MISARIDIS, T. & JENSEN, J.A. (2005a). Use of modulated excitation signals in medical ultrasound. part i: Basic concepts and expected benefits. *Ultrasonics, Ferroelectrics and Frequency Control, IEEE Transactions on*, **52**, 177–191. 2, 12, 20, 41, 60, 61, 78, 81, 97

MISARIDIS, T. & JENSEN, J.A. (2005b). Use of modulated excitation signals in medical ultrasound. part ii: Design and performance for medical imaging applications. *Ultrasonics, Ferroelectrics and Frequency Control, IEEE Transactions on*, **52**, 192–207. 2, 14, 15

MISARIDIS, T. & JENSEN, J.A. (2005c). Use of modulated excitation signals in medical ultrasound. part iii: High frame rate imaging. *Ultrasonics, Ferroelectrics and Frequency Control, IEEE Transactions on*, **52**, 208–219. 2

MISARIDIS, T.X., GAMMELMARK, K., JORGENSEN, C.H., LINDBERG, N., THOMSEN, A.H., PEDERSEN, M.H. & JENSEN, J.A. (2000). Potential of coded excitation in medical ultrasound imaging. *Ultrasonics*, **38**, 183–189. 2, 12

MOSHINSKY, M. & QUESNE, C. (1971). Linear canonical transformations and their unitary representations. *Journal of Mathematical Physics*, **12**, 1772–1780. 28

NAMIAS, V. (1980). The fractional order Fourier transform and its application to quantum mechanics. *IMA Journal of Applied Mathematics*, **25**, 241–265. 29

NEPPIRAS, E.A. (1980). Acoustic cavitation. *Physics Reports*, **61**, 159–251. 215

NEPPIRAS, E.A. & NOLTINGK, B.E. (1951). Cavitation produced by ultrasonics: Theoretical conditions for the onset of cavitation. *Proceedings of the Physical Society. Section B*, **64**, 1032–1038. 215

NIKIAS, C.L. & PETROPULU, A.P. (1993). *Higher-Order Spectra Analysis : A Nonlinear Signal Processing Framework*. Prentice-Hall. 171, 193

NIKIAS, C.L. & RAGHUVEER, M.R. (1987). Bispectrum estimation: A digital signal processing framework. *IEEE Proceedings*, **75**, 869–891. 170, 172

NOLTINGK, B.E. & NEPPIRAS, E.A. (1950). Cavitation produced by ultrasonics. *Proceedings of the Physical Society. Section B*, **63**, 674–685. 215

NOVELL, A., DER MEER, S., VERSLUIS, M., JONG, N. & BOUAKAZ, A. (2009). Contrast agent response to chirp reversal: simulations, optical observations, and acoustical verification. *Ultrasonics, Ferroelectrics and Frequency Control, IEEE Transactions on*, **56**, 1199–1206. 3

O'DONNELL, M. (1992). Coded excitation system for improving the penetration of real-time phased-array imaging systems. *Ultrasonics, Ferroelectrics and Frequency Control, IEEE Transactions on*, **39**, 341–351. 2, 12

OPPENHEIM, A.V. & SCHAFER, R.W. (1975). *Digital Signal Processing*. Prentice-Hall. 27, 193, 195

OZAKTAS, H.M., BARSHAN, B., MENDLOVIC, D. & ONURAL, L. (1994). Convolution, filtering, and multiplexing in fractional Fourier domains and their relation to chirp and wavelet transforms. *Journal of the Optical Society of America A*, **11**, 547–559. 6, 32

OZAKTAS, H.M., ARIKAN, O., KUTAY, M.A. & BOZDAĞI, G. (1996). Digital computation of the fractional Fourier transform. *Signal Processing, IEEE Transactions on*, **44**, 2141–2150. 29, 32

PARK, J., LI, X., ZHOU, Q. & SHUNG, K.K. (2013). Combined chirp coded tissue harmonic and fundamental ultrasound imaging for intravascular ultrasound: 2060 mhz phantom and ex vivo results. *Ultrasonics*, **53**, 369–376. 4

PASOVIC, M., DANILOUCHKINE, M., FAEZ, T., VAN NEER, P.L.M.J., CACHARD, C., VAN DER STEEN, A.F.W., BASSET, O. & DE JONG, N. (2011). Second harmonic inversion for ultrasound contrast harmonic imaging. *Physics in Medicine and Biology*, **56**, 3163–3180. 184

PASSMANN, C. & ERMERT, H. (1996). A 100-mhz ultrasound imaging system for dermatologic and ophthalmologic diagnostics. *Ultrasonics, Ferroelectrics and Frequency Control, IEEE Transactions on*, **43**, 545–552. 2

PECK, S.D. & BRIGGS, G.A.D. (1987). The caries lesion under the scanning acoustic microscope. *Advances in Dental Research*, **1**, 50–63. 54

PEDERSEN, M.H., MISARIDIS, T.X. & JENSEN, J.A. (2003). Clinical evaluation of chirp-coded excitation in medical ultrasound. *Ultrasound in Medicine & Biology*, **29**, 895–905. 2

PLESSET, M.S. (1949). The dynamics of cavitation bubbles. *ASME J. Appl. Mech.*, **16**, 228–231. 215

PORTER, T.R. & XIE, F. (2010). Myocardial perfusion imaging with contrast ultrasound. *J. Am. Coll. Cardiol.: Cardiovascular Imaging*, **3**, 176–187. 169

RAO, N.A.H.K. (1994). Investigation of a pulse compression technique for medical ultrasound: a simulation study. *Medical and Biological Engineering and Computing*, **32**, 181–188. 2

RAUM, K., KEMPF, K., HEIN, H.J., SCHUBERT, J. & MAURER, P. (2007). Preservation of microelastic properties of dentin and tooth enamel in vitroa scanning acoustic microscopy study. *Dental Materials*, **23**, 1221–1228. 54, 70, 71

RAYLEIGH, L. (1917). On the pressure developed in a liquid during the collapse of a spherical cavity. *Phil. Mag.*, **34**, 94–98. 215

RICKEY, D.W., PICOT, P.A., CHRISTOPHER, D.A. & FENSTER, A. (1995). A wallless vessel phantom for doppler ultrasound studies. *Ultrasound in Medicine & Biology*, **21**, 1163–1176. 189

ROSE, E.C., HAGENMÜLLER, M., JONAS, I.E. & RAHN, B.A. (2005). Validation of speed of sound for the assessment of cortical bone maturity. *European Journal of Orthodontics*, **27**, 190–195. 71

ROSENBERG, B., MURRAY, P.E. & NAMEROW, K. (2007). The effect of calcium hydroxide root filling on dentin fracture strength. *Dental Traumatology*, **23**, 26–29. 55

ROSENTHAL, S.J., JONES, P.H. & WETZEL, L.H. (2001). Phase inversion tissue harmonic sonographic imaging: A clinical utility study. *American Journal of Roentgenology*, **176**, 1393–1398. 89

SANCHEZ, J.R. & OELZE, M.L. (2009). An ultrasonic imaging speckle-suppression and contrast-enhancement technique by means of frequency compounding and coded excitation. *Ultrasonics, Ferroelectrics and Frequency Control, IEEE Transactions on*, **56**, 1327–1339. 133

SATIR, S. & DEGERTEKIN, F.L. (2012). Harmonic reduction in capacitive micromachined ultrasonic transducers by gap feedback linearization. *Ultrasonics, Ferroelectrics and Frequency Control, IEEE Transactions on*, **59**, 50–59. 117

SCHROPE, B.A. & NEWHOUSE, V.L. (1993). Second harmonic ultrasonic blood perfusion measurement. *Ultrasound in Medicine & Biology*, **19**, 567–579. 169

SHEN, C. & CHIU, Y. (2009). Design of chirp excitation waveform for dual-frequency harmonic contrast detection. *Ultrasonics, Ferroelectrics and Frequency Control, IEEE Transactions on*, **56**, 2198–2206. 3

SHEN, C. & LI, P. (2002). Motion artifacts of pulse inversion-based tissue harmonic imaging. *Ultrasonics, Ferroelectrics and Frequency Control, IEEE Transactions on*, **49**, 1203–1211. 93

SIEMENS AG (2007). *Abdominal Imaging, ACUSON Antares system*. Siemens Medical Solutions USA, Inc. 89

SINGH, R.S., CULJAT, M., NEURGAONKAR, R.R., WHITE, S.N., GRUNDFEST, W.S. & BROWN, E.R. (2006). Single-element plzt transducer for wide-bandwidth imaging of solid materials. In *IEEE Ultrasonics Symposium*, 1926–1930. 54

SINGH, R.S., CULJAT, M.O., CHO, J.C., NEURGAONKAR, R.R., YOON, D.C., GRUNDFEST, W.S., BROWN, E.R. & WHITE, S.N. (2007). Penetration of radiopaque dental restorative materials using a novel ultrasound imaging system. *American Journal of Dentistry*, **20**, 221–226. 72, 75, 78

SINGH, R.S., CULJAT, M.O., GRUNDFEST, W.S., BROWN, E.R. & WHITE, S.N. (2008). Tissue mimicking materials for dental ultrasound. *The Journal of the Acoustical Society of America*, **123**, EL39–EL44. 13, 57

SKOLNIK, M.I. (1981). *Introduction to Radar Systems*. McGraw-Hill. 12, 60

SMITH, P.R. (2013). *Ultrasonic Phased Array Techniques Using Switched-Mode Excitation*. Ph.D. Thesis, University of Leeds, UK. 96

SMITH, P.R., COWELL, D.M.J., RAITON, B., KY, C.V., PHAM, T.H., BUI, B.Q. & FREEAR, S. (2010). A PLL-based phased array method to minimize phase quantization errors and reduce phasing-lobes. In *Ultrasonics Symposium, 2010 IEEE*, 1837–1840. 96, 174

Smith, P.R., Cowell, D.M.J., Raiton, B., Ky, C.V. & Freear, S. (2012). Ultrasound array transmitter architecture with high timing resolution using embedded phase-locked loops. *Ultrasonics, Ferroelectrics and Frequency Control, IEEE Transactions on*, **59**, 40–49. 96, 174

Song, J., Kim, S., Sohn, H., Song, T. & Yoo, Y.M. (2010). Coded excitation for ultrasound tissue harmonic imaging. *Ultrasonics*, **50**, 613–619. 3, 92

Song, J., Chang, J.H., Song, T. & Yoo, Y. (2011). Coded tissue harmonic imaging with nonlinear chirp signals. *Ultrasonics*, **51**, 516–521. 4

Sprague, M.R., Chérin, E., Goertz, D.E. & Foster, F.S. (2010). Nonlinear emission from individual bound microbubbles at high frequencies. *Ultrasound in Medicine & Biology*, **36**, 313–324. 138

Sun, Y., Zhao, S., Dayton, P.A. & Ferrara, K.W. (2006). Observation of contrast agent response to chirp insonation with a simultaneous optical-acoustical system. *Ultrasonics, Ferroelectrics and Frequency Control, IEEE Transactions on*, **53**, 1130–1137. 3

Sun, Y., Kruse, D.E. & Ferrara, K.W. (2007). Contrast imaging with chirped excitation. *Ultrasonics, Ferroelectrics and Frequency Control, IEEE Transactions on*, **54**, 520–529. 3, 13, 151

Szabo, T.L. (2004). *Diagnostic Ultrasound Imaging: Inside Out*. Elsevier Academic Press. 2, 12

Takeuchi, Y. (1979). An investigation of a spread energy method for medical ultrasound systems: Part one: Theory and investigation. *Ultrasonics*, **17**, 175–182. 2, 14

Tang, M.X., Mari, J.M., Wells, P.N.T. & Eckersley, R.J. (2008). Attenuation correction in ultrasound contrast agent imaging: elementary theory and preliminary experimental evaluation. *Ultrasound in Medicine & Biology*, **34**, 1998–2008. 181

Tang, M.X., Kamiyama, N. & Eckersley, R.J. (2010). Effects of nonlinear propagation in ultrasound contrast agent imaging. *Ultrasound in Medicine & Biology*, **36**, 459–466. 176

TOTAH, V.P. (1942). Increase in hardness of dentin on drying. *Journal of Dental Research*, **21**, 99–101. 71

TRANQUART, F., GRENIER, N., EDER, V. & POURCELOT, L. (1999). Clinical use of ultrasound tissue harmonic imaging. *Ultrasound in Medicine & Biology*, **25**, 889–894. 89, 169

TU, J., GUAN, J., QIU, Y. & MATULA, T.J. (2009). Estimating the shell parameters of sonovue microbubbles using light scattering. *The Journal of the Acoustical Society of America*, **126**, 2954–2962. 140

VAN NEER, P.L.M.J., MATTE, G., DANILOUCHKINE, M.G., PRINS, C., VAN DEN ADEL, F. & DE JONG, N. (2010). Super-harmonic imaging: development of an interleaved phased-array transducer. *Ultrasonics, Ferroelectrics and Frequency Control, IEEE Transactions on*, **57**, 455–468. 117

VAN NEER, P.L.M.J., DANILOUCHKINE, M.G., MATTE, G.M., VAN DER STEEN, A.F.W. & DE JONG, N. (2011). Dual-pulse frequency compounded superharmonic imaging. *Ultrasonics, Ferroelectrics and Frequency Control, IEEE Transactions on*, **58**, 2316–2324. 117, 133

WEI, K., JAYAWEERA, A.R., FIROOZAN, S., LINKA, A., SKYBA, D.M. & KAUL, S. (1998). Quantification of myocardial blood flow with ultrasound-induced destruction of microbubbles administered as a constant venous infusion. *Circulation*, **97**, 473–483. 169

WELCH, P.D. (1967). The use of fast fourier transform for the estimation of power spectra: A method based on time averaging over short, modified periodograms. *Audio and Electroacoustics, IEEE Transactions on*, **15**, 70–73. 195

WERUAGA, L. & KÉPESI, M. (2007). The fan-chirp transform for non-stationary harmonic signals. *Signal Processing*, **87**, 1504–1522. 6, 36, 38

WIESMANN, M., MEYER, K., ALBERS, T. & SEIDEL, G. (2004). Parametric perfusion imaging with contrast-enhanced ultrasound in acute ischemic stroke. *Stroke*, **35**, 508–513. 169

YAMANER, F.Y., OLCUM, S., OGUZ, H.K., BOZKURT, A., KOYMEN, H. & ATALAR, A. (2012). High-power cmuts: Design and experimental verification. *Ultrasonics, Ferroelectrics and Frequency Control, IEEE Transactions on*, **59**, 1276–1284. 117

YANIKOĞLU, F., ÖZTÜRK, F., HAYRAN, O., ANALOUI, M. & STOOKEY, G.K. (2000). Detection of natural white spot caries lesions by an ultrasonic system. *Caries Research*, **34**, 225–232. 70

ZHANG, D., GONG, Y., GONG, X., LIU, Z., TAN, K. & ZHENG, H. (2007). Enhancement of subharmonic emission from encapsulated microbubbles by using a chirp excitation technique. *Physics in Medicine and Biology*, **52**, 5531–5544. 3